

# Generically Orthogonal Event Decompositions and Measurement Combinations in Standard Model $VH$ ( $b\bar{b}$ ) Searches with the ATLAS Detector

A DISSERTATION PRESENTED  
BY  
STEPHEN K. CHAN  
TO  
THE DEPARTMENT OF PHYSICS

IN PARTIAL FULFILLMENT OF THE REQUIREMENTS  
FOR THE DEGREE OF  
DOCTOR OF PHILOSOPHY  
IN THE SUBJECT OF  
PHYSICS

HARVARD UNIVERSITY  
CAMBRIDGE, MASSACHUSETTS  
2018

<sup>18</sup> ©2017 – STEPHEN K. CHAN

<sup>19</sup> ALL RIGHTS RESERVED.

20                   **Generically Orthogonal Event Decompositions and**  
21                   **Measurement Combinations in Standard Model  $VH(b\bar{b})$**   
22                   **Searches with the ATLAS Detector**

23                   **ABSTRACT**

24         This thesis describes variations on the two lepton channel of the Run-2 search for the SM Higgs  
25         boson produced in association with a vector boson using different variable sets for multivariate anal-  
26         ysis (MVA) training. The three variable sets in question are the set of variables from the fiducial anal-  
27         ysis, a set based on the Lorentz Invariants (LI) concept, and a set based on a combination of masses  
28         and decay angles derived using the RestFrames (RF) package. Aside from the variable sets used for  
29         MVA training and discriminant distributions, the analysis is otherwise identical to the fiducial an-  
30         laysis. Both the LI and RF sets perform competitively on the basis of significances, with the RF set  
31         showing a  $\sim 3.5\%$  improvement in expected fits to Asimov and data, though neither set boosts ob-  
32         served significance. Both sets also reduce the observed error on  $\hat{\mu}$ , with the LI set reducing the error  
33         due to systematics by 7.5% and the RF set doing so by 16%.

34         The issue of combining multiple results from different channels and datasets is also examined  
35         through the combination of the fiducial Run 1 and Run 2 ATLAS  $VH(b\bar{b})$  results, which results in  
36         an observed signal strength of  $0.90^{+0.18}_{-0.18}(\text{stat.})^{+0.21}_{-0.19}(\text{syst.})$  and an observed (expected) significance  
37         of 3.6 (4.0) standard deviations, the first ever evidence of this process.

# Contents

38

39	o	INTRODUCTION	I
40	I	THE STANDARD MODEL HIGGS AND COLLIDER EVENT VARIABLES	4
41	1.1	The Standard Model Higgs Boson . . . . .	5
42	1.2	Higgs Boson Production and Decay at the Large Hadron Collider . . . . .	8
43	1.3	Collider Events and Event Level Variables . . . . .	II
44	1.4	Characterization with Event-Level Variables . . . . .	13
45	1.5	Lorentz Invariants . . . . .	16
46	1.6	RestFrames Variables . . . . .	18
47	1.7	Extensions to the $\ell$ and $\tau$ Lepton Channels . . . . .	20
48	2	THE LARGE HADRON COLLIDER AND THE ATLAS DETECTOR	24
49	2.1	The CERN Accelerator Complex . . . . .	25
50	2.2	The Large Hadron Collider . . . . .	25
51	2.3	ATLAS at a Glance . . . . .	31
52	2.4	The Inner Detector . . . . .	37
53	2.5	The ATLAS Calorimeters . . . . .	41
54	2.6	The Muon Spectrometer . . . . .	49
55	3	DATA AND SIMULATED SAMPLES	55
56	4	SIGNAL AND BACKGROUND MODELING	58
57	4.1	Event Generation In a Nutshell . . . . .	59
58	4.2	Description of Modeling Uncertainty Categories . . . . .	61
59	4.3	Process Specific Systematic Summaries . . . . .	72
60	5	OBJECT AND EVENT RECONSTRUCTION AND SELECTION	81
61	5.1	Triggers . . . . .	83
62	5.2	Electrons . . . . .	85
63	5.3	Muons . . . . .	87
64	5.4	Missing Transverse Energy . . . . .	89
65	5.5	Jets . . . . .	89
66	5.6	Flavor Tagging . . . . .	99
67	5.7	Miscellania and Systematics Summary . . . . .	109
68	5.8	Event Selection and Analysis Regions . . . . .	109

69	<b>6 MULTIVARIATE ANALYSIS CONFIGURATION</b>	112
70	6.1 Training Samples and Variable Selection . . . . .	113
71	6.2 MVA Training . . . . .	124
72	6.3 Statistics Only BDT Performance . . . . .	129
73	<b>7 STATISTICAL FIT MODEL AND VALIDATION</b>	135
74	7.1 The Fit Model . . . . .	136
75	7.2 Fit Inputs . . . . .	139
76	7.3 Systematic Uncertainties Review . . . . .	140
77	7.4 The VZ Validation Fit . . . . .	142
78	7.5 Nuisance Parameter Pulls . . . . .	146
79	7.6 Postfit Distributions . . . . .	154
80	7.7 VH Fit Model Validation . . . . .	161
81	<b>8 FIT RESULTS</b>	176
82	<b>9 MEASUREMENT COMBINATIONS</b>	182
83	9.1 The Combined Fit Model . . . . .	183
84	9.2 Combined Fit Results . . . . .	198
85	<b>10 CLOSING THOUGHTS</b>	206
86	<b>APPENDIX A MICROMEGAS TRIGGER PROCESSOR SIMULATION</b>	209
87	A.1 Algorithm Overview . . . . .	210
88	A.2 Monte Carlo Samples . . . . .	215
89	A.3 Nominal Performance . . . . .	215
90	A.4 Fit Quantities . . . . .	216
91	A.5 Efficiencies . . . . .	222
92	A.6 Incoherent Background . . . . .	225
93	A.7 BCID . . . . .	230
94	A.8 Charge Threshold . . . . .	230
95	A.9 Misalignments and Corrections . . . . .	234
96	A.10 Individual Cases . . . . .	239
97	A.11 $ds \neq 0$ . . . . .	240
98	A.12 $dz \neq 0$ . . . . .	240
99	A.13 $dt \neq 0$ . . . . .	240
100	A.14 $\alpha \neq 0$ . . . . .	241
101	A.15 $\beta \neq 0$ . . . . .	241
102	A.16 $\gamma \neq 0$ . . . . .	241
103	A.17 Simulation Correction of the Algorithm Under Nominal Conditions . . . . .	244
104	A.18 Translation Misalignments Along the Horizontal Strip Direction ( $\Delta s$ ) . . . . .	247

105	A.19 Translation Misalignments Orthogonal to the Beamline and Horizontal Strip Direction ( $\Delta z$ ) . . . . .	249
106	A.20 Translation Misalignments Parallel to the Beamline ( $\Delta t$ ) . . . . .	251
107	A.21 Chamber Tilts Towards and Away from the IP ( $\gamma_s$ Rotation) . . . . .	252
108	A.22 Rotation Misalignments Around the Wedge Vertical Axis ( $\beta_z$ ) . . . . .	254
109	A.23 Rotation Misalignments Around the Axis Parallel to the Beamline ( $\alpha_t$ ) . . . . .	255
110	A.24 Conclusion . . . . .	257
112	<b>APPENDIX B TELESCOPING JETS</b>	259
113	B.1 Monte Carlo Simulation . . . . .	260
114	B.2 Jet Reconstruction and Calibration . . . . .	261
115	B.3 Event Reconstruction and Selection . . . . .	262
116	B.4 Validation of Jet Calibration . . . . .	265
117	B.5 Truth-Level Analysis . . . . .	268
118	B.6 Errors on Telescoping Significances . . . . .	271
119	B.7 Counting . . . . .	271
120	B.8 Multiple Event Interpretations . . . . .	272
121	B.9 $t(z) = z$ . . . . .	273
122	B.10 $t(z) = \rho_S(z) / \rho_B(z)$ . . . . .	274
123	B.11 Reconstructed-Level Analysis . . . . .	279
124	B.12 Conclusions and Prospects . . . . .	285
125	<b>APPENDIX C PROGRESS IN PARTICLE PHYSICS AND EXISTENTIAL THREATS TO THE</b>	
126	<b>AMERICAN WORLD ORDER</b>	286
127	<b>REFERENCES</b>	299



# Acknowledgments

<sup>130</sup> THIS THESIS WOULD NOT HAVE BEEN POSSIBLE without large amounts of espresso.

*Your life has a limit but knowledge has none...if you  
understand this and still strive for knowledge, you will  
be in danger for certain!*

Zhuangzi

# 0

131

132

## Introduction

133 SINCE THE DISCOVERY of a Standard Model (SM) like Higgs boson at the LHC in 2012[7][6], one  
134 of the main outstanding physics goals of the LHC has been to observe the primary SM Higgs decay  
135 mode,  $H \rightarrow b\bar{b}$ , with efforts primarily targeted at searching for Higgs bosons produced in associ-  
136 ation with a leptonically decaying vector ( $W$  or  $Z$ , denoted generically as  $V$ ) boson. This primary

<sup>137</sup> Higgs decay mode also offers the best opportunity to observe direct Higgs coupling to quarks. As  
<sup>138</sup> the integrated luminosity of data collected at the LHC increases,  $H \rightarrow b\bar{b}$  searches will increasingly  
<sup>139</sup> become limited by the ability to constrain systematic uncertainties, with the latest result from AT-  
<sup>140</sup> LAS at  $\sqrt{s} = 13$  TeV using  $36.1\text{ fb}^{-1}$  of  $pp$  collision data already approaching this regime, having a  
<sup>141</sup>  $VH(b\bar{b})$  signal strength of  $1.20^{+0.24}_{-0.23}(\text{stat.})^{+0.34}_{-0.28}(\text{syst.})$  at  $m_H = 125$  GeV [42].

<sup>142</sup> While this effort will likely require a combination of several different methods at various differ-  
<sup>143</sup> ent stages in the analysis chain, one possible avenue forward is to revise the multivariate analysis  
<sup>144</sup> (MVA) discriminant input variables used, as various schemes offer the promise of reducing system-  
<sup>145</sup> atic uncertainties through more efficient use of both actual and simulated collision data. This the-  
<sup>146</sup> sis discusses two such alternate MVA schemes, the RestFrames (RF) and Lorentz Invariants (LI)  
<sup>147</sup> variables, in the context of the 2-lepton channel of the Run 2 analysis in [42] and [65], henceforth  
<sup>148</sup> referred to as the “fiducial analysis,” before a brief discussion of combinations across channels and  
<sup>149</sup> datasets.

<sup>150</sup> Electroweak symmetry breaking, Standard Model Higgs production and decay, and event level  
<sup>151</sup> variables are treated in Chapter 1. The Large Hadron Collider and ATLAS detector are the subject  
<sup>152</sup> of Chapter 2. Data and simulation samples used are described in Chapter 3. Signal and background  
<sup>153</sup> modeling with accompanying systematics are defined in Chapter 4. Object and event reconstruction  
<sup>154</sup> definitions and event selection requirements are outlined in Chapter 5. The multivariate analysis, in-  
<sup>155</sup> cluding a description of the LI and RF variable sets and a summary of performance in the absence of  
<sup>156</sup> systematic uncertainties, is described in Section 6. The statistical fit model and systematic uncertain-  
<sup>157</sup> ties are described in Section 7, and the fit results may be found in Chapter 8. Combining channels

<sup>158</sup> and datasets at different  $\sqrt{s}$  values is discussed in the context of the Run 1 + Run 2 SM  $VH(b\bar{b})$

<sup>159</sup> combination in Chapter 9. Finally, conclusions and closing thoughts are presented in Chapter 10.

<sup>160</sup> Editorial notes:

<sup>161</sup> 1. pdf will be *probability* distribution function

<sup>162</sup> 2. PDF will be *parton* distribution function

<sup>163</sup> 3. Unless otherwise stated, ATLAS and LHC/CERN images are from public available material  
<sup>164</sup> from experiment webpages. Copyright terms may be found here [https://atlas.cern/  
<sup>165</sup> copyright](https://atlas.cern/copyright).

*The relationship between theorists and experimentalists  
is like that between a truffle farmer and his pig*

Howard Georgi

# 1

166

167

## The Standard Model Higgs and Collider

168

### Event Variables

169 MUCH HAS BEEN SAID about the so-called Standard Model (SM) of particle physics, so only the  
170 bare essentials of electroweak symmetry breaking and Higgs production relevant to SM  $VH(b\bar{b})$  will

<sup>171</sup> be addressed here. This discussion follows [66] Chapter II in both content and notation. We then  
<sup>172</sup> move onto the treatment of kinematic variables in collider events, including the two novel schemes  
<sup>173</sup> considered in this thesis, the Lorentz Invariants (LI) and RestFrames (RF) concepts.

## <sup>174</sup> I.I THE STANDARD MODEL HIGGS BOSON

<sup>175</sup> The generic scalar Lagrangian potential (the kinetic term will be addressed later) for a scalar in the  
<sup>176</sup> SM is:

$$V(\Phi) = m^2 \Phi^\dagger \Phi + \lambda (\Phi^\dagger \Phi)^2 \quad (I.1)$$

<sup>177</sup> where  $\Phi$  is a complex scalar doublet field under  $SU(2)$  from which the physical Higgs emerges after  
<sup>178</sup> symmetry breaking. Its four degrees of freedom are typically decomposed as follows:

$$\Phi = \frac{1}{\sqrt{2}} \begin{pmatrix} \sqrt{2}\phi^+ \\ \phi^0 + i\alpha^0 \end{pmatrix} \quad (I.2)$$

<sup>179</sup>  $\phi^+$  is the complex charged component of the Higgs doublet, and  $\phi^0$  and  $\alpha^0$  are the CP-even and  
<sup>180</sup> CP-odd neutral components, respectively.

<sup>181</sup> If the sign of  $m^2 \Phi^\dagger \Phi$  is negative,  $\Phi$  acquires a *vacuum expectation value* or VEV:

$$\langle \Phi \rangle = \frac{1}{\sqrt{2}} \begin{pmatrix} 0 \\ \sqrt{\frac{2m^2}{\lambda}} \end{pmatrix} \quad (I.3)$$

<sup>182</sup> with this value typically denoted  $v = \sqrt{2m^2/\lambda} = (\sqrt{2}G_F)^{-1/2} \approx 246$  GeV (with the coupling

<sup>183</sup> of the 4-Fermi effective theory of weak interactions measured through experiments involving muon  
<sup>184</sup> decay), and  $\phi^0$  is rewritten as  $\phi^0 = H + v$ .

<sup>185</sup> This non-zero VEV induces spontaneous symmetry breaking in the SM's gauge (local) symme-  
<sup>186</sup> try group of  $SU(3)_C \times SU(2)_L \times U(1)_Y$  since the VEV does not respect the  $SU(2)_L \times U(1)_Y$   
<sup>187</sup> symmetry of the Lagrangian (i.e.  $\langle \Phi \rangle$  is not invariant under a gauge transformation of this group).

<sup>188</sup> Three of the four generators of this subgroup are spontaneously broken, which implies the existence  
<sup>189</sup> of three massless Goldstone bosons, which are in turn “eaten” by linear combinations of the  $W^a$   
<sup>190</sup> (with coupling strength  $g$ ) and  $B$  (with coupling strength  $g'$ ) bosons to form the longitudinal polar-  
<sup>191</sup> izations of the familiar  $W^\pm$  and  $Z$  bosons, with the last generator giving rise to the usual, unbroken  
<sup>192</sup>  $U(1)_{EM}$  symmetry and its massless photon,  $A$ , as well as the scalar Higgs boson  $H$ . To see this, one  
<sup>193</sup> starts with the full Higgs SM Lagrangian (kinetic minus potential only)

$$\mathcal{L}_{Higgs} = (D_\mu \Phi)^\dagger (D_\mu \Phi) - V(\Phi), \quad D_\mu \Phi = (\partial_\mu + ig\sigma^a W_\mu^a + ig' Y B_\mu / 2) \Phi \quad (1.4)$$

<sup>194</sup> One simply plugs in the reparametrized  $\Phi$  with  $\phi^0 = H + v$ , collects the terms involving  $v$  together  
<sup>195</sup> with the appropriate  $W$  and  $B$  kinetic terms to extract:

$$M_W^2 = \frac{g^2 v^2}{4}, \quad M_Z^2 = \frac{(g'^2 + g^2) v^2}{4} \quad (1.5)$$

<sup>196</sup> This is left as an exercise for the reader; this exercise also makes manifest that the Higgs couples with  
<sup>197</sup> the  $W^\pm$  and  $Z$  with strength quadratic in the gauge boson masses. Since the Higgs field also respects

<sup>198</sup> the  $SU(3)_C$  color symmetry, the eight gluons are also left massless, and the  $H$  is left interacting with  
<sup>199</sup> photons and gluons primarily through heavy quark loops (i.e. no tree-level interactions).

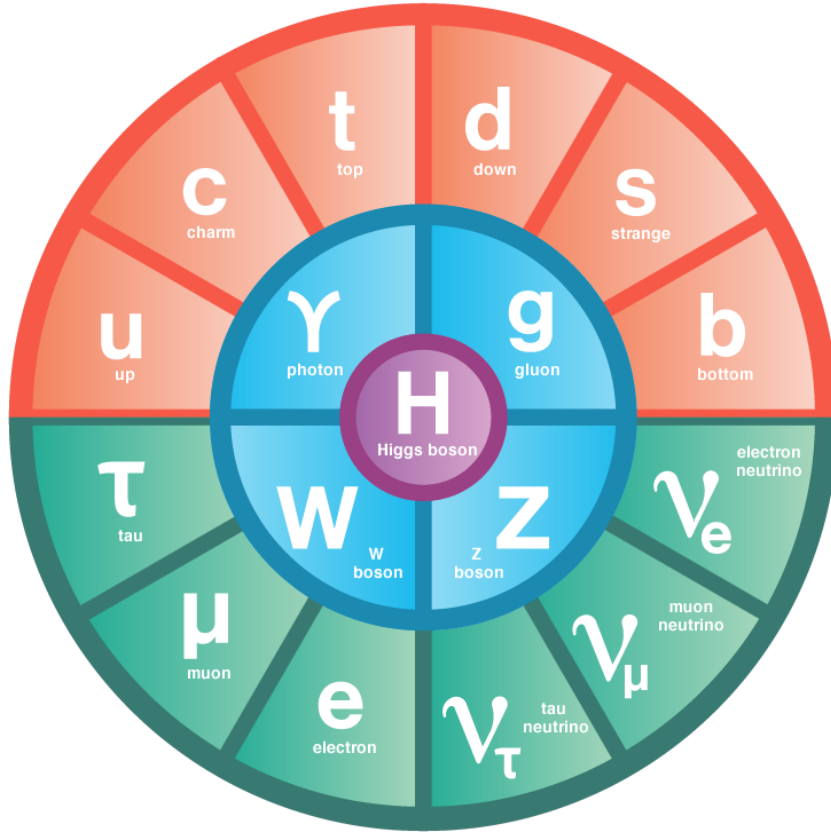


Figure 1.1: The fundamental particles of the Standard Model. IC: [75]

<sup>200</sup> The Higgs is often introduced to the public at large as the mechanism through which fundamen-  
<sup>201</sup> tal fermions (enumerated in Figure 1.1) acquire mass—this is through the Yukawa interactions of the  
<sup>202</sup> Higgs:

$$\mathcal{L}_{Yukawa} = -\hat{h}_{d_{ij}} \bar{q}_{L_i} \Phi d_{R_j} - \hat{h}_{u_{ij}} \bar{q}_{L_i} \tilde{\Phi} u_{R_j} - \hat{h}_{l_{ij}} \bar{l}_{L_i} \Phi e_{R_j} + h.c. \quad (1.6)$$

<sup>203</sup> where  $\tilde{\Phi} = i\sigma_2 \Phi^*$ ,  $q_L$  ( $l_L$ ) and  $u_R$ ,  $d_R$  ( $e_R$ ) are the quark (lepton) left-handed doublets and right

204 handed singlets of the weak  $SU(2)_L$  group, with each term parametrized by a  $3 \times 3$  matrix in family  
205 space (also known as the fermion generations). The neutrinos have been purposely omitted since  
206 the mechanism that generates their mass is as of yet unknown, though these Yukawa interactions  
207 could have a non-zero contribution to neutrino masses. Once the Higgs VEV value is known and  
208 the Yukawa interaction matrices  $\hat{b}_{f_i j}$  (with  $i, j \in \{1, 2, 3\}$ ) are diagonalized, the fermion masses  
209 can simply be written as  $m_{f_i} = b_{f_i} v / \sqrt{2}$ . The SM has no motivation for any of these mass values,  
210 instead leaving them as empirically determined free parameters.

211 Note that from  $\mathcal{L}_{Yukawa}$ , it is easy to see that the Higgs couplings with fermions scale linearly with  
212 fermion mass. Higgs self-couplings and beyond the standard model (BSM) Higgs scenarios are be-  
213 yond the scope of this thesis.

## 214 I.2 HIGGS BOSON PRODUCTION AND DECAY AT THE LARGE HADRON COLLIDER

215 The leading order Feynman diagrams for the four dominant modes of Higgs production at the LHC  
216 are shown in Figure 1.2, each described briefly in turn. The dominant process, accounting for some  
217 87% of Higgs production at the nominal LHC center of mass energy of 14 TeV, is gluon-gluon fu-  
218 sion (ggF), shown at top left in Figure 1.2. At high center of mass energies, most of a proton's mo-  
219 mentum is predominantly carried by gluons (as opposed to the constituent valence quarks associ-  
220 ated with the hadron's identity). This, along with the difficulties associated with high luminosity  
221 antiproton beam production, is why the LHC was designed as a proton-proton collider instead of  
222 a proton-antiproton collider (like the Tevatron or SppS). As mentioned above, the Higgs does not  
223 couple directly to gluons but must instead be produced through the fermion loop shown in the fig-

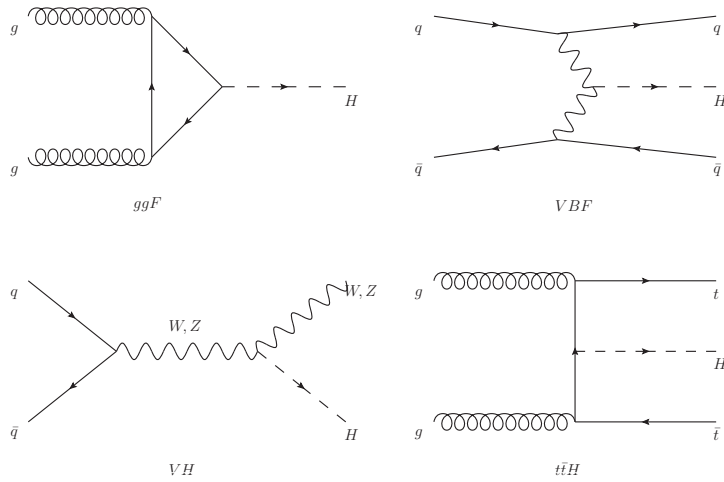


**Figure 1.2:** Dominant Higgs production modes.

ure. The heaviest fundamental fermion by far is the top quark, with  $m_t = 173$  GeV, so top loops dominate this process. While not particularly relevant for this thesis, about 14% of events in the lepton channel of the  $H \rightarrow b\bar{b}$  analysis are ggF initiated.

The next most prevalent process is vector boson fusion (VBF), where vector bosons ( $W$  or  $Z$ , denoted generically as  $V$ ) from quarks in the colliding protons “fuse” to form a Higgs. These quarks typically form jets in the forward region, which provide a unique signature for this process. This process is not relevant for this thesis.

The third leading process is “Higgsstrahlung” or Higgs production in association with a vector boson, often simply  $VH$  production. In this process, a quark-antiquark pair in the colliding protons forms an energetic vector boson, which then radiates a Higgs (this is similar to photon emission of accelerating electrons, called “Bremsstrahlung,” hence the name). Some fraction of the time (about 21% of the time for  $WH$  and 6.7% of the time for  $ZH$ ), the energetic  $V$  will decay leptonically (i.e.

236 into a decay involving an electron or a muon), which provides a unique and triggerable signature  
 237 for this process. Another 20% of the time for  $ZH$  production, the  $Z$  will decay to neutrinos, which  
 238 are not absorbed by detectors and show up as missing transverse energy ( $\vec{E}_T^{\text{miss}}$ ), another triggerable  
 239 signature. This ability to trigger on leptons and  $\vec{E}_T^{\text{miss}}$  and the requirement that this leptonic signa-  
 240 ture be consistent with a  $V$  allow one to significantly reduce the impact of multijet background (a  
 241 very common generic processes at the LHC) on analysis. Hence, this is the process of primary impor-  
 242 tance to this thesis.

243 The final important Higgs production process is  $t\bar{t}H$  production, the box diagram in the lower  
 244 right of Figure 1.2. Again, the top pair provides a useful signature for analysis. This, like VBF, is also  
 245 not considered in this thesis.

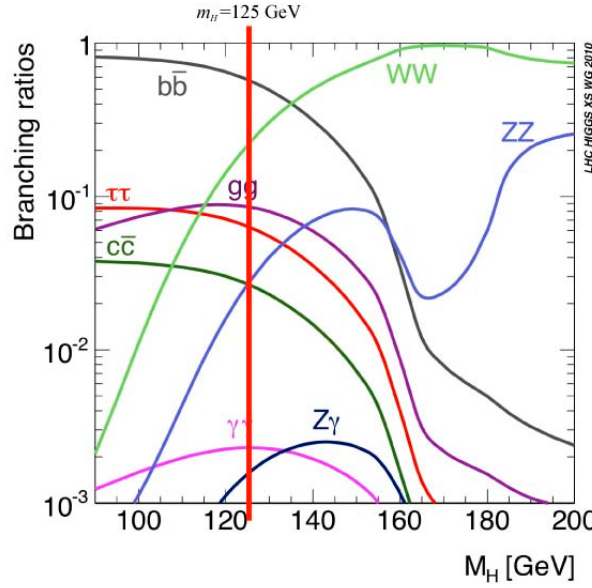


**Figure 1.3:** Higgs decay mode branching fractions as a function of its mass; a line has been drawn at the observed Higgs mass of 125 GeV.

Once the Higgs has been produced, it can decay in a number of ways, as shown in Figure 1.3. By far the most dominant decay mode of the Higgs is to  $b\bar{b}$  with a branching fraction of 58%. This  $b$ -quark pair then hadronizes into two  $b$ -jets (for a more thorough discussion of jets and  $b$ -jets in particular, see Section 5.5). However, many processes at the LHC create pairs of  $b$ -jets with invariant masses consistent with the Higgs and have much higher production rates ( $t\bar{t}$  production at the LHC is in the neighborhood of hundreds of pb, compared to Higgs cross sections of a few pb), so a clear process signature is necessary to study  $H \rightarrow b\bar{b}$  production at the LHC. This is why the bulk of search efforts have focused on  $VH$  production. A summary of Higgs production cross sections and simple extrapolations to raw numbers of Higgs bosons produced for  $VH$  for leptonically decaying  $V$  is shown in Table 1.1

$\sqrt{s}$ (TeV)	ZH	WH	ggF	total $\sigma$	$N_{V \rightarrow \ell^+ \nu} H$
7	$0.34^{+4\%}_{-4\%}$	$0.58^{+3\%}_{-3\%}$	$15.3^{+10\%}_{-10\%}$	17.5	$4.7 \text{ fb}^{-1} \rightarrow 589$
8	$0.42^{+5\%}_{-5\%}$	$0.70^{+3\%}_{-3\%}$	$19.5^{+10\%}_{-11\%}$	22.3	$20.3 \text{ fb}^{-1} \rightarrow 3100$
13	$0.88^{+5\%}_{-5\%}$	$1.37^{+2\%}_{-2\%}$	$44.1^{+11\%}_{-11\%}$	50.6	$36.1 \text{ fb}^{-1} \rightarrow 11100$
14	$0.99^{+5\%}_{-5\%}$	$1.51^{+2\%}_{-2\%}$	$49.7^{+11\%}_{-11\%}$	57.1	$1000 \text{ fb}^{-1} \rightarrow 343000$

**Table 1.1:** Cross sections (in pb) for processes important to the SM  $VH$  ( $b\bar{b}$ ) analysis and the total Higgs cross section as a function of center of mass energy. Also given are the total number of Higgs bosons produced for given luminosities through both  $WH$  and  $ZH$  processes. Uncertainties are theoretical.

### 1.3 COLLIDER EVENTS AND EVENT LEVEL VARIABLES

Collision data in experiments like ATLAS is structured using what is known as the *event data model*. In this model, one collision corresponds to one event. Since each bunch crossing contains more than one proton, there can be more than one collision per event and more than one hard scatter per col-

260 lision. For each collision, tracks in an experiment's inner detector are used to identify the most ener-  
 261 getic collision, which is taken to be the event. The raw data, the various tracks, energy deposits, and  
 262 hits in the detector, undergo reconstruction (described at length in Chapter 5) both through auto-  
 263 mated, experiment-wide, standardized production and through analysis-specific level selections, cor-  
 264 rections, and calibrations. The result of this considerable effort is a collection of labeled 4-vectors,  
 265 representing the final state objects. This is shown in Figure 1.4.

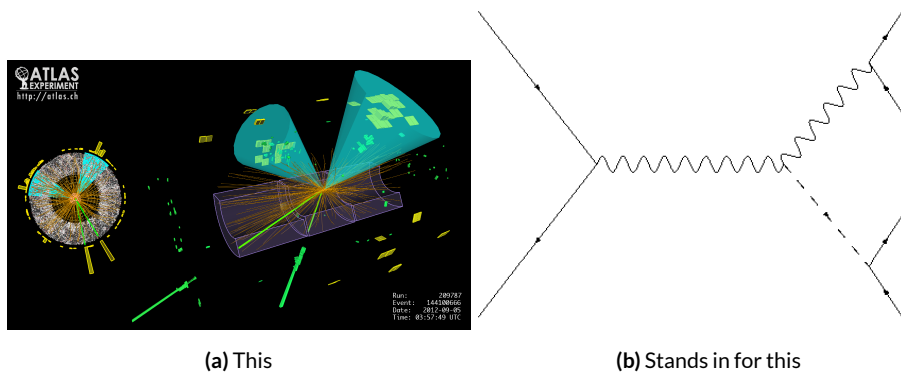


**Figure 1.4:** Reconstruction in a nutshell

266 In the process that is the focus of this thesis, every event ultimately is condensed into a lepton pair  
 267 (two electrons or two muons), two or three jets\*, all 4-vectors, and a  $\vec{E}_T^{\text{miss}}$  vector in the transverse  
 268 plane. Further selection then takes place to winnow down events into interesting regions of phase  
 269 space hopefully more rich in signal-like events. Once events are selected in a search like the one in  
 270 this thesis, one then analyzes the data to test its consistency with some background only hypothesis  
 271 to produce the usual statistical results. This can be done in various ways, with principal approaches

---

\*Sometimes more, though this is a small fraction of events, and the wisdom of this choice may be questioned

272 being: a simple counting experiment (often referred to as the “cut and count” approach), a func-  
273 tional fit for excesses over a falling background spectrum (the so-called “bump hunt” used in anal-  
274 yses like the  $H \rightarrow \gamma\gamma$  discovery channel), or the use of discriminant distributions as PDF’s in a  
275 likelihood fit (the approach of this analysis). These distributions can be simple counts (i.e. single bin  
276 distributions) in analysis regions, quantities of interest (the distribution of the invariant mass of the  
277 two  $b$ -jets in selected events with the greatest transverse momenta,  $m_{bb}$ , is used as a validation), or a  
278 multivariate analysis (MVA) discriminant.

279 **I.4 CHARACTERIZATION WITH EVENT-LEVEL VARIABLES**

280 Traditionally, particle physicists have favored the approach of using distributions of physical vari-  
281 ables since it is easier to develop physical intuition for what these distributions should look like  
282 during validation, so it is no surprise that as many LHC analyses have transitioned to using MVA  
283 techniques that these variables form the basis of many very robust physics results. These variables  
284 do quite well summarize many of the main physics features of an event for the signal topology, cer-  
285 tainly much better than feeding all 18–22 4-vector components directly into a machine learning algo-  
286 rithm. In  $ZH \rightarrow \ell\ell b\bar{b}$  events, for example, one wishes to characterize the  $ZH$  system by using the  
287 lepton pair as a stand-in for the  $Z$  and the  $b$ -jet pair as a stand-in for the  $H$ , and composite variables  
288 like  $m_{bb}$  and  $m_{\ell\ell}$  can be used to check whether events are consistent with these objects. There are  
289 also variables like  $\vec{p}_T^V$  that characterize the momentum scale of the event, angles like  $\Delta R(b_1, b_2)$  and  
290  $\Delta\phi(V, H)$  that can be further used to characterize the overall “shape” of these events, and variables  
291 like  $\vec{E}_T^{\text{miss}}$  that can discriminate against backgrounds like  $t\bar{t}$  that do not have a closed topology.

292 Nevertheless, the intuition based approach, with incremental addition of variables as they prove  
293 useful in the lifetime of an analysis's iterations, does beg the question of whether there is a more sys-  
294 tematic way to treat this information. There are clearly patterns to which variables are useful: these  
295 correspond to important information about the hypothesized physics objects and their relation-  
296 ships, and there have been many attempts to systematize the way these variables are found. Such  
297 systematic, top-down approaches often promise to increase performance in two ways. The first is by  
298 having higher descriptive power, often through some sophisticated treatment of the missing trans-  
299 verse energy in an event,  $\vec{E}_T^{\text{miss}}$ .  $\vec{E}_T^{\text{miss}}$  is just a single quantity, and if there is just one invisible object  
300 in a desired event topology, using  $\vec{E}_T^{\text{miss}}$  on its own often provides sufficient sensitivity. In more com-  
301 plicated topologies with multiple invisible particles in the final state, for example in many supersym-  
302 metry searches, a more careful treatment of the missing energy is often necessary.

303 The second means of improvement is through using a more orthogonal basis of description,  
304 which allows one to more efficiently use data and simulation samples. A more orthogonal basis im-  
305 plies that variables contain less overlapping information with each other and so allow for a more  
306 efficient exploration of parameter space. This means one can gain higher sensitivity from equivalent  
307 datasets using a more orthogonal basis. To see why this might be the case, take an MVA discrimi-  
308 nant for  $ZH \rightarrow \ell\ell b\bar{b}$  formed using only the classic variables  $\Delta R(b_1, b_2)$  and  $p_T^V$ . In the  $ZH \rightarrow$   
309  $\ell\ell b\bar{b}$  topology, the transverse mass of the  $Z$  and  $H$  (and hence the lepton pair and jet pair) are equiv-  
310 alent. This means that at higher  $p_T^V$  the  $p_T$  of  $b$ -jets will also be higher, which in turn implies that  
311 they will have a smaller angle of separation and hence a smaller  $\Delta R(b_1, b_2)$ . This correlation is not  
312 unity—each variable still does have information the other does not—but is still very high. Hence,

313 when training an MVA, which in principle knows nothing about these variables other than some  
314 set limits, an undue number of training events will be wasted converging upon relations that could  
315 be known *a priori*, and while this might be easy to hard code in for a two variable toy example, the  
316 dimensionality of any real discriminant makes this prohibitive. An MVA that uses data (both ac-  
317 tual and simulated) more efficiently will also tend to be have lower variance, offering a potential av-  
318 enue for reduction in the error on quantities of interest due to systematic uncertainties. Details of  
319 how this plays out in a likelihood fit will be deferred to the discussion of the fit model used in the  
320  $VH(b\bar{b})$  search in Chapter 7.

321 Many of these novel schemes are designed to explicitly address the first issue of invisibles in the  
322 final state in channels where it is of paramount importance while having the second issue as some-  
323 thing of a fringe benefit. However, as the amount of data taken at the LHC grows, analyses will in-  
324 creasingly become systematics limited, so an exploration to the veracity of the second claim has great  
325 potential for the high luminosity era of the LHC. The  $ZH \rightarrow \ell\ell b\bar{b}$  process offers a great setting for  
326 investigating this issue on its own since its closed topology largely mitigates any improvement from  
327 more sophisticated treatments of  $\vec{E}_T^{\text{miss}}$ . We introduce two of these more top-down approaches to  
328 event-level variables below: the “Lorentz Invariant” (LI) [53] and “RestFrames inspired” (RF) [56]  
329 variable schemes. A broad overview of the concepts behind these schemes will be given here, with a  
330 more in-depth discussion of their implementation deferred until Chapter 6.

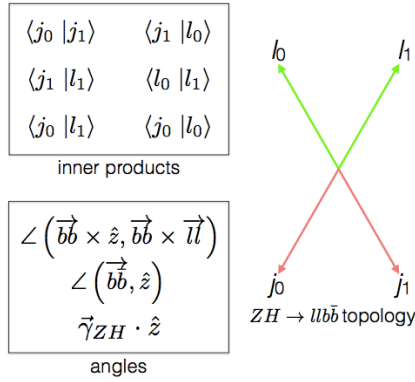


**Figure 1.5:** Summary of LI variables in the  $ZH \rightarrow \ell\ell b\bar{b}$  topology.

331 **I.5 LORENTZ INVARIANTS**

332 The LI variables, first put forth by S. Hagebeck and others [53], are based upon the concept that  
333 once the 4-vectors of an event are determined, all of the information in an event are encoded into  
334 their inner products (Lorentz invariant quantities, hence the name) and the angles between them.  
335 This makes for 16 quantities in all: the ten inner products of the 4-vectors, the three Euler angles,  
336 and the three parameters specifying the boost of the  $ZH$  system. The masses of the four final state  
337 objects are not considered very useful and so can be removed to leave six meaningful inner products  
338 (the  ${}_4C_2$  combinations<sup>†</sup> between distinct final state 4-vectors). Since these inner products can have  
339 an ill-defined physical interpretation and in order to help MVA training, each inner product is scaled

---

<sup>†</sup> ${}_nC_r = \frac{n!}{r!(n-r)!}$ , read “ $n$  choose  $r$ ” and known as the binomial coefficient, is the number of unique possible ways to choose combinations of  $r$  objects from a total set of  $n$  without regard to ordering within combinations.

<sup>340</sup> by:

$$x \rightarrow \frac{x}{x + c} \quad (1.7)$$

<sup>341</sup> where  $c$  is the mean of the distribution in the signal MC distribution. These inner products are de-  
<sup>342</sup> noted  $x_i y_j$ , where  $x$  and  $y$  are either  $j$  (for jet) or  $l$  (for lepton) and the indices are either  $o$  ( $i$ ) for  
<sup>343</sup> the leading (subleading) object by  $p_T$  in the event.

<sup>344</sup> The number of useful angles can be reduced by recognizing some symmetries inherent in the fi-  
<sup>345</sup> nal state. The symmetry around the beam axis eliminates one angle. Furthermore, the boost of the  
<sup>346</sup>  $VH$  system is primarily in the beam direction ( $z$ ) direction, marginalizing the utility of the trans-  
<sup>347</sup> verse boost angles. This leaves the boost in the  $z$  direction, denoted `gamma_ZHz`, and two angles  
<sup>348</sup> chosen to be the angle between the  $b\bar{b}$  system and the beam (`angle_bb_z`) and the angle between  
<sup>349</sup>  $(\vec{b}_1 + \vec{b}_2) \times \hat{z}$  and  $(\vec{b}_1 + \vec{b}_2) \times (\vec{l}_1 + \vec{l}_2)$  (`angle_bbz_bbll`).

<sup>350</sup> These variables do contain a lot of information similar to the usual set: there are mass equivalents  
<sup>351</sup> ( $j_0 \leftrightarrow m_{bb}$ , and  $l_0 \leftrightarrow m_{\ell\ell}$ ) and angles. Instead of individual final state object scales, there  
<sup>352</sup> are the four jet/lepton inner products, though this correspondence (and indeed any physical inter-  
<sup>353</sup> pretation) is far from clear. An important advantage of the LI variable set is that all of the variables  
<sup>354</sup> are in it are orthogonal in the signal case by construction. A drawback of this framework in a com-  
<sup>355</sup> pletely closed final state is that there is no way to treat  $E_T^{miss}$  in a Lorentz invariant way.

<sup>356</sup> There is also no prescription for any additional jets in the event beyond the two  $b$ -tagged jets.  
<sup>357</sup> They are simply ignored in these variable calculations since the fiducial analysis requirement of ex-

358 actly two  $b$ -tagged jets eliminates any combinatoric ambiguity, and additional, untagged jets are as-  
359 sumed (not entirely rigorously) to be unrelated to the signal-like hard scatter.

360 1.6 RESTFRAMES VARIABLES

361 The RestFrames variables [56], calculated using the software package of the same name, is based  
362 upon the idea that the most natural frame in which to analyze objects of the signal decay tree is in  
363 their individual production (rest) frames. The signal decay tree for  $ZH \rightarrow \ell\ell b\bar{b}$  is show in Figure  
1.6. Generally, one does not typically have enough information to determine exactly each of the in-

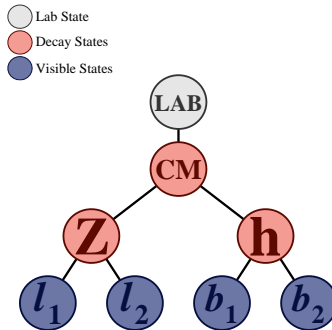


Figure 1.6: The  $ZH \rightarrow \ell\ell b\bar{b}$  decay tree.

364  
365 termediate rest frames or the boosts between the frames, but in a completely closed final state like  
366  $ZH \rightarrow \ell\ell b\bar{b}$ , this can be done in the usual way by adding the 4-vectors of the final state objects and  
367 solving the usual equations from special relativity (RestFrames does this automatically for each  
368 event).

369 Each frame has associated with it the boost from its immediate parent and a mass scale; that mass  
370 (in this case the correspondence between RF mass variables and standard mass variables is exact) and  
371 the angles between the Euclidean three vector associated with boost and the axis of the decay prod-

372   ucts provide useful variables. In general, the polar angle (typically given as a cosine) is considered  
 373   more useful than the azimuthal angle (typically just a  $\Delta\phi$ ), though this is dependent on the candi-  
 374   date decay tree. The  $Z$  frame, for example, has  $MZ$ , which is just the usual  $m_{\ell\ell}$ ,  $\cos Z$ , the cosine of  
 375   the polar angle between the lepton momentum axis in their production frame and the boost from  
 376   the  $ZH$  center of mass (CM) frame, and the angle  $d\phi_{hCMZ}$ .

377   In addition to the masses and angles attached to individual object rest frames, energy scales associ-  
 378   ated with the CM frame can be used to contextualize other event level quantities. In particular, one  
 379   can use the mass of the CM frame as a natural scale to evaluate the momentum of the CM frame,  
 380   and the  $p_T$  of the CM frame as a natural scale for the event's  $E_T^{miss}$ , yielding the variables:

$$R_{p_T} = \frac{p_{T,CM}}{p_{T,CM} + M_{CM}}, \quad R_{p_z} = \frac{p_{z,CM}}{p_{z,CM} + M_{CM}}, \quad R_{met} = \frac{E_T^{miss}}{E_T^{miss} + p_{T,CM}} \quad (1.8)$$

381   denoted  $R_{pT}$ ,  $R_{pZ}$ , and  $R_{met}$ . These can be thought of as behaving like significance based variables  
 382   in particle physics, like METHT or impact parameter significances, or event level defined versions  
 383   of the scalings applied to the LI inner products. These are used instead of the final state object scales  
 384   and standard  $E_T^{miss}$  of the standard variable set.

385   Unlike the LI variables, the physical interpretation of RF variables is very clear. Everything has  
 386   physical units, and these are variables one might have introduced in the usual process of develop-  
 387   ing an MVA with the traditional mindset. The solution to the issue of additional jets in an event is  
 388   not immediately clear. In order to keep the two non-standard MVA's on as equal footing as possi-  
 389   ble, the approach of simply ignoring additional jets is taken in this thesis. Nevertheless, it would be

390 easy enough to redefine the  $H$  intermediate frame to have, for example, the two  $b$ -tagged jets and the  
 391 highest  $p_T$  untagged jet for any subset of events. This flexibility is not a feature of the Lorentz Invari-  
 392 ants framework. Of course, `RestFrames` cannot tell you what approach to take, but it is capable of  
 393 handling more flexible topologies once optimization studies have been completed.

### 394 1.7 EXTENSIONS TO THE 1 AND 0 LEPTON CHANNELS

395 Both the LI and RF variable concepts are readily extendable to the 1-lepton channel. In this topol-  
 396 ogy, one of the leptons in the  $ZH \rightarrow \ell\ell b\bar{b}$  diagram is replaced by a neutrino, the lone invisible  
 397 particle in this final state. We can assume that the neutrino has zero mass and transverse momentum  
 398 equal to the  $\vec{E}_T^{\text{miss}}$  in the event, leaving one undetermined degree of freedom, the longitudinal mo-  
 399 mentum of the neutrino,  $p_z^\nu$ .

400 The LI concept was in fact initially formulated to improve sensitivity in the 1-lepton channel,  
 401 with the same orthogonality of variables described in the 2-lepton case being the main draw. The LI  
 402 approach to estimating the neutrino longitudinal momentum is outlined in [53], which we repro-  
 403 duce here. We first guess the neutrino energy in its rest frame and then boost to the lab frame:

$$\langle E_\nu \rangle = \frac{1}{4} m_{WH} \implies \langle p_z^\nu \rangle = \beta \gamma \langle E_\nu \rangle = \frac{p_z^{WH}}{m_{WH}} \langle E_\nu \rangle = \frac{1}{4} p_z^{WH} \quad (1.9)$$

404 Finally, assuming energy and momentum in aggregate are equally shared among final state con-  
 405 stituents, we arrive at

$$\langle p_z^\nu \rangle = \frac{1}{4} \times \frac{4}{3} (p_z^l + p_z^{j0} + p_z^{j1}) \quad (1.10)$$

406 The RF approach for the 1-lepton case amounts to replacing the  $Z \rightarrow \ell\ell$  in 1.6 with  $W \rightarrow \ell\nu$ .  
407 As alluded to in the 2-lepton discussion, when there is missing information in the final state from  
408 invisible particles and/or combinatoric ambiguities, recursive jigsaw reconstruction (RJR) offers a  
409 standard toolkit for deriving estimated boosts between rest frames by analytically minimizing on  
410 unknown quantities. While in more exotic final states with multiple invisible particles and combi-  
411 natoric ambiguities the choice of jigsaw rule can be subjective, the case of  $W$  is well-studied and out-  
412 lined in detail in Section V.A. of [56]. It reproduces the usual transverse mass of the  $W$  in place of  
413 MZ in the 2-lepton case. Not surprisingly, the underlying calculation is also much the same as the LI  
414 case (where rest frames and boost were explicitly invoked); again, information is the same, only its  
415 decomposition is different.

416 The 0-lepton channel would appear to present some difficulty as two neutrinos in the final state  
417 introduce extra degrees of freedom, but both concepts may be extended by treating the invisibly de-  
418 caying  $Z$  as a single invisible particle and requiring the  $Z$  to be on-shell. Both of these requirements  
419 may be folded into the 1-lepton framework to produce similar sets of variables.

420 While the precise variables that would be included in 0- and 1-lepton LI and RF MVA discrimi-  
421 nants is beyond the scope of this thesis, looking at Table 1.2, we can see the dimensionality and in-  
422 puts of the discriminants of the fiducial analysis. The correspondence for LI/RF variables and stan-  
423 dard variables extends nicely to the other lepton channels. The reduction in multiplicity of variables  
424 owing the lower number of degrees of freedom provided by treating the  $Z$  as a single invisible par-  
425 ticle in the 0-lepton channel would likely not be an issue, as one would just be able to use a greater  
426 fraction of available variables in the MVA discriminant.

Variable	Name	0-lepton	1-lepton	2-lepton
$\vec{p}_T^V$	pTV		✓	✓
$\vec{E}_{\text{T}}^{\text{miss}}$	MET	✓	✓	✓
$\vec{p}_T^{\text{jet}1}$	pTB1	✓	✓	✓
$\vec{p}_T^{\text{jet}2}$	pTB2	✓	✓	✓
$\text{MV}_{2\text{C10}}(\text{jet}_1)^*$	$\text{MV}_{2\text{C10B1}}$	✓	✓	✓
$\text{MV}_{2\text{C10}}(\text{jet}_2)^*$	$\text{MV}_{2\text{C10B2}}$	✓	✓	✓
$m_{jj}$	mBB	✓	✓	✓
$\Delta R(\text{jet}_1, \text{jet}_2)$	dRBB	✓	✓	✓
$ \Delta\eta(\text{jet}_1, \text{jet}_2) $	dEtaBB	✓		
$\Delta\phi(V, H)$	dPhiVBB	✓	✓	✓
$\Delta\eta(V, H)$	dEtaVBB			✓
$M_{\text{eff}}(M_{\text{eff}3})$	HT	✓		
$\min(\Delta\phi(\ell, \text{jet}))$	dPhiLBmin		✓	
$m_{\text{T}}^W$	mTW		✓	
$m_{ll}$	mLL			✓
$\Delta Y(W, H)$	dYWH		✓	
$m_{\text{top}}$	mTop		✓	
Only in 3 Jet Events				
$\vec{p}_T^{jet3}$	pTJ3	✓	✓	✓
$\text{MV}_{2\text{C10}}(\text{jet}_3)^*$	$\text{MV}_{2\text{C10B3}}$	✓	✓	✓
$m_{jjj}$	mBBJ	✓	✓	✓

**Table 1.2:** Variables used to train the multivariate discriminant. Starred variables ( $b$ -tag scores) are not included in current versions of the standard discriminants, but have traditionally been included and most likely will be reintroduced as soon as their accompanying systematics are available.

<sup>427</sup>     *Maybe do the o-lep calculation and o/1-lep RF cartoons*

*Noli turbare circulos meos*

Archimedes

# 2

<sup>428</sup>

## <sup>429</sup> The Large Hadron Collider and the ATLAS

### Detector

<sup>430</sup>

<sup>431</sup> THE CERN ACCELERATOR COMPLEX AND ITS EXPERIMENTS stand as a testament to human in-  
<sup>432</sup> genuity and its commitment to the pursuit of fundamental knowledge. In this chapter, we give a

<sup>433</sup> cursory overview of the CERN accelerator complex, including the Large Hadron Collider (LHC),  
<sup>434</sup> before moving on to a more detailed review of the ATLAS detector.

## <sup>435</sup> 2.1 THE CERN ACCELERATOR COMPLEX

<sup>436</sup> The journey of protons from hydrogen canister to high energy collisions through the CERN ac-  
<sup>437</sup> celerator complex, illustrated in Figure 2.1, is also one through the history of CERN’s accelerator  
<sup>438</sup> program. After being ionized in an electric field, protons are first accelerated in a linear accelera-  
<sup>439</sup> tor, LINAC 2<sup>\*</sup>, to a kinetic energy of 50 MeV. From there, they are fed into the Proton Synchotron  
<sup>440</sup> Booster<sup>†</sup>, which further accelerates them to 1.4 GeV and, as its name implies, feeds them to the 628  
<sup>441</sup> m Proton Synchotron (PS, 1959[8]) and up to 25 GeV. The penultimate stage is the 7 km Super  
<sup>442</sup> Proton Synchotron (SPS, 1976; responsible for the discovery of the  $W$  and  $Z$  bosons and the 1983  
<sup>443</sup> Nobel Prize [10]), which accelerates the protons to a kinetic energy of 450 GeV. Finally, these 450  
<sup>444</sup> GeV protons are injected into the LHC[50], a proton-proton collider housed in the 27 km circumfer-  
<sup>445</sup> ence tunnel that housed the Large Electron Positron Collider (LEP) before its operations ceased in  
<sup>446</sup> 2000.

## <sup>447</sup> 2.2 THE LARGE HADRON COLLIDER

<sup>448</sup> The LHC was designed to function primarily as a proton-proton collider with a center of mass en-  
<sup>449</sup> ergy  $\sqrt{s} = 14$  TeV and an instantaneous luminosity of  $1 \times 10^{34} \text{ cm}^{-2} \cdot \text{s}^{-1}$ , though it is also capable

---

<sup>\*</sup>1978’s LINAC 2 is the successor to 1959’s LINAC 1; it will be replaced in 2020 by LINAC 4; LINAC 3 is responsible for ion production.

<sup>†</sup>Protons can be directly from a LINAC into the PS, but the higher injection energy allows for approximately 100 times more protons to be used at once[9], 1972.

## CERN's Accelerator Complex

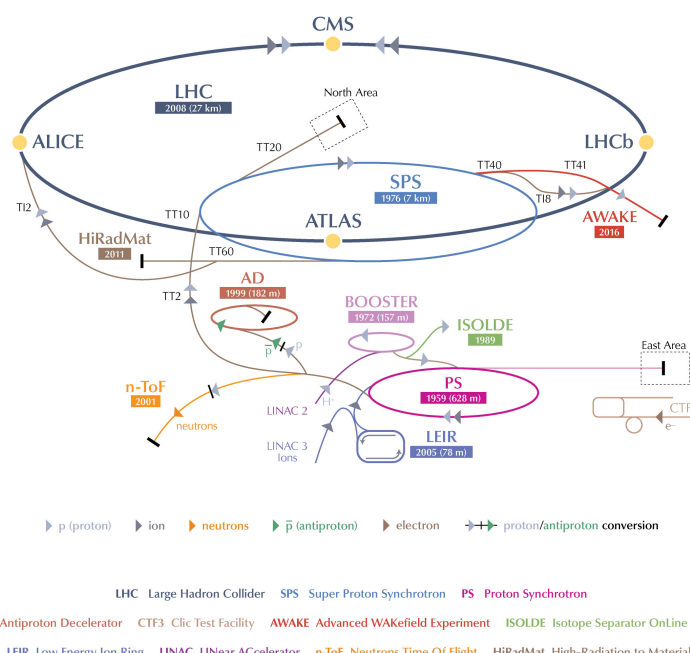
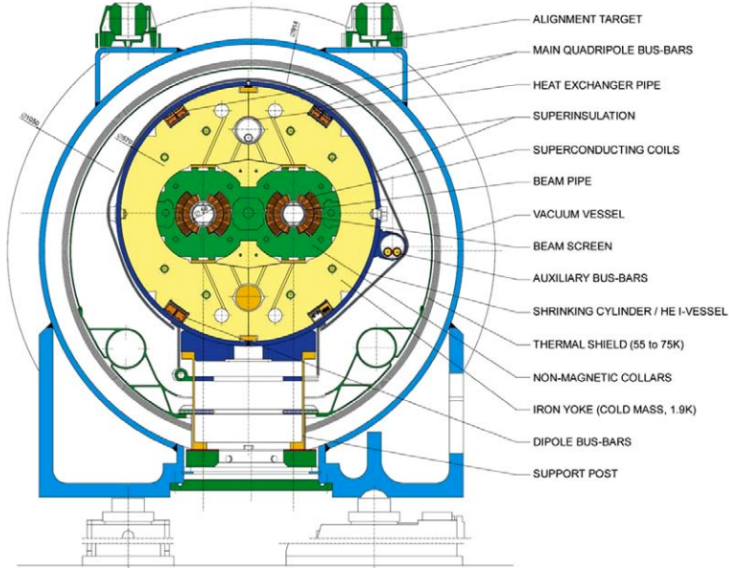


Figure 2.1: The CERN Accelerator Complex [64]

<sup>450</sup> of producing heavy ion (Pb-Pb) collisions, which it does for approximately one month in a typical  
<sup>451</sup> year of physics collisions. Owing to an accident at the beginning of the LHC's initial run, the acceler-  
<sup>452</sup> ator has operated at center of mass energies of 7, 8, and now 13 TeV.

<sup>453</sup> One of the major cost-saving features of the he LHC is that, unlike the defunct Superconducting  
<sup>454</sup> Supercollider (SSC), its construction did not call for a purpose built tunnel, with the LHC instead  
<sup>455</sup> being housed in the old LEP tunnel. LEP, however, like the Tevatron, was a particle-antiparticle  
<sup>456</sup> collider, which meant that both beams could circulate within the same beam pipe, so the LEP tun-  
<sup>457</sup> nel was never built to house two separate storage rings and magnet systems (as the SSC would have  
<sup>458</sup> had). To accomplish the technically challenging task of housing two storage rings and sets of mag-  
<sup>459</sup> nets in one system, the LHC magnets feature a "twin bore" design. The magnets themselves make  
<sup>460</sup> use of superconducting NbTi cables and are cooled using superfluid helium to a temperature of 2  
<sup>461</sup> K, which allows for operational field strengths in excess of 8 T. A stable design is achieved by having  
<sup>462</sup> the magnets share a common cold mass (a 27.5 ton iron yoke for each dipole kept at 1.9 K in which  
<sup>463</sup> the magnets and beam pipes are embedded) and cryostat and by arranging the superconductor wind-  
<sup>464</sup> ings so that the magnetic fluxes of the two systems rotate in opposite directions. This results in an  
<sup>465</sup> extremely complicated magnetic structure. The design layout of an LHC dipole magnet is shown  
<sup>466</sup> in Figure 2.2. These dipole magnets are responsible for bending the LHC's proton beams, and their  
<sup>467</sup> strength is the principal limiting factor in the center of mass energy achievable at a circular collider.

<sup>468</sup> The ideal version of a proton beam in the LHC consists of infinitely small bunches of protons  
<sup>469</sup> of equal momentum equally spaced in the LHC ring (itself not a perfect circle). In reality, the pro-  
<sup>470</sup> tons in the beam deviate from each of these assumptions, with dispersion in both physical space

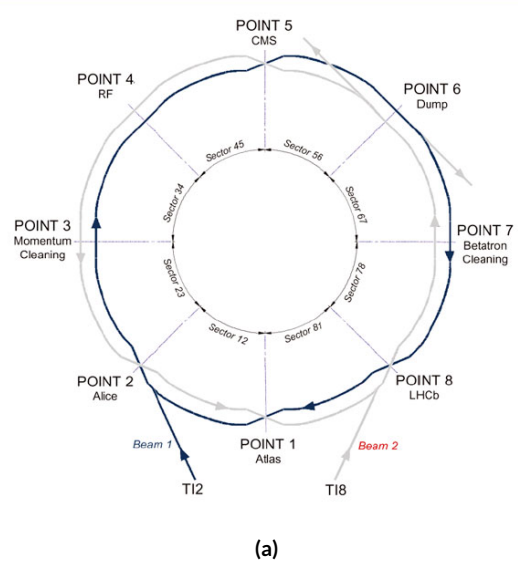


**Figure 2.2:** Schematic drawing of an LHC dipole magnet and cryogenics system.

and momentum space. In general, charged particles in an accelerator ring will demonstrate pseudo-harmonic “betatron” oscillations about the ideal orbit, the amplitude of which gives a characteristic of the beam’s size. In order to get high energy protons to actually collide, different magnets are used to focus the beam and help nudge deviating particles back into more ideal behavior. There are quadrupole magnet assemblies in the short straight sections to accomplish this, as well as quadrupole, octupole, and sextupole magnets interspersed throughout the length of the LHC ring for beam stabilization and other higher order corrections. The interior of the LHC beam pipe operates at a nominal pressure of  $\sim 10^{-7}$  Pa, famously more rarefied than outer space.

The LHC ring itself is between 45 m and 170 m below ground and has a 1.4% incline towards Lac Léman with eight arcs and eight straight sections. In the middle of each of the eight straight sections,

481 there are potential interaction points (each colloquially referred to by its number as “Point  $N$ ”),  
482 with each point housing either accelerator infrastructure or an experiment. A schematic of the con-  
483 tents of each component, as well as a more detailed view of the infrastructure in the LHC ring, can  
484 be found in Figure 2.4.



(a)

Figure 2.3: Schematic and detailed views of the LHC ring. IC: [35], [73]

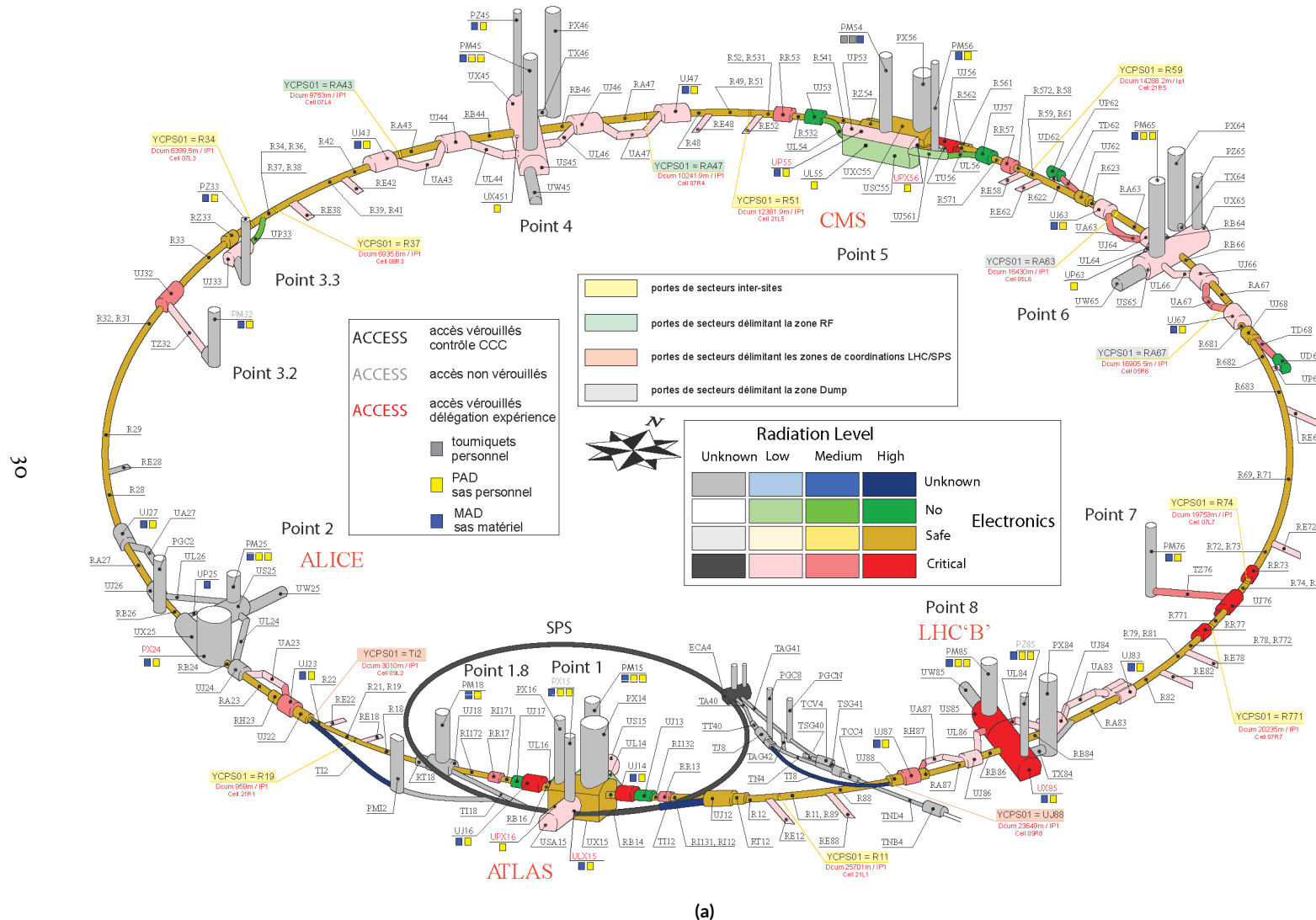


Figure 2.4: Schematic and detailed views of the LHC ring. IC:[35],[73]

485 Points 1, 2, 5, and 8 house the LHC’s experiments, ATLAS (*A Toroidal LHC ApparatuS*, one  
486 of the two general purpose detectors, discussed in detail below), ALICE (A Large Ion Collider Ex-  
487 periment, a dedicated heavy ion experiment), CMS (Compact Muon Solenoid, the other general  
488 purpose detector), and LHCb (LHC beauty, a *B* physics experiment), respectively. Point 3 houses a  
489 series of collimators that scatter and absorb particles in the beam with a large momentum deviation  
490 (which will have different orbital radii) from other particles in the beam (“momentum cleaning”),  
491 while Point 7 has a similar setup to remove particles with large betatron amplitudes (“betatron clean-  
492 ing”). Both of these dedicated cleaning assemblies are in addition to the magnetic focusing assem-  
493 blies discussed above and address the same issues. Point 4 contains the LHC’s RF (radio frequency;  
494 400 MHz) acceleration system, responsible for taking protons from their injection energy of 450  
495 GeV to their collision energy of 3.5, 4, 6.5, or 7 TeV. Point 6 is where the energetic ionizing radiation  
496 of circulating beams can be safely taken out of the collider into a block of absorbing material, either  
497 at the end of a data-taking run or in the event of an emergency (in the event of irregular behavior,  
498 it is essential to do this as quickly as possible to minimize damage to the accelerator and to experi-  
499 ments); this is known as a “beam dump.”

500 2.3 ATLAS AT A GLANCE

501 2.3.1 COORDINATES AND DISTANCES IN THE ATLAS DETECTOR

502 *A Toroidal LHC ApparatuS* is one of the two (the other being CMS) general purpose, high lumi-  
503 nosity detectors at the LHC, located at Interaction Point 1, as described above. With a length of 44

504 m and a height of 25 m, it is the detector with largest physical dimensions at the LHC.<sup>‡</sup>. While pri-  
 505 marily a high luminosity proton-proton collision detector, ATLAS does collect heavy ion collision  
 506 data, typically for one month during a year of typical operation.

507 The ATLAS coordinate system is shown in Figure 2.5. It is a right-handed coordinate system cen-  
 508 tered at the nominal collision point, with the  $x$  axis pointing towards the center of the LHC ring,  
 509 the  $z$  axis pointing up, and the  $y$  axis completing the right-handed coordinate system.

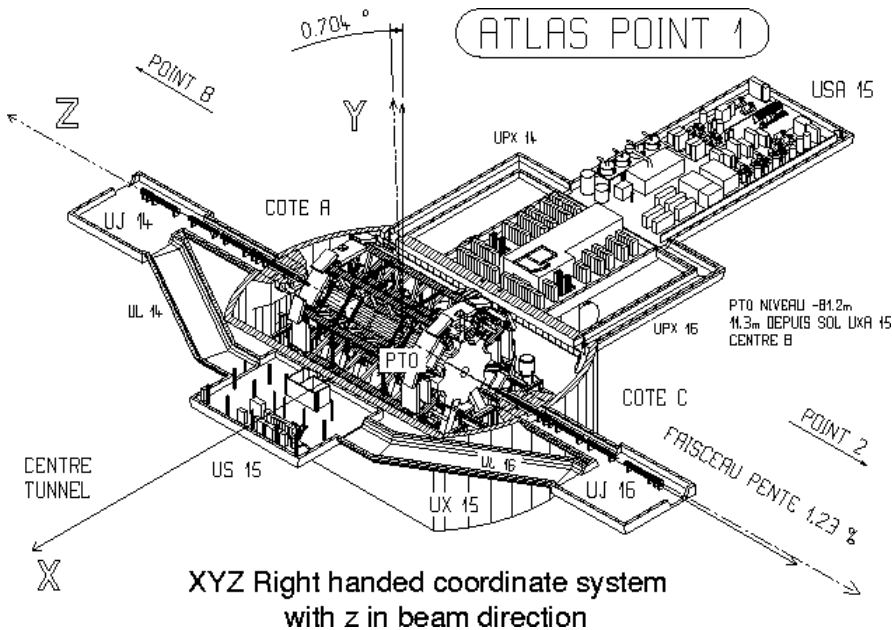


Figure 2.5: The ATLAS coordinate system. "A" side is the airport, and "C" side is "Charlie's," a pub in Saint-Genis, France.

510 While the Cartesian coordinates are useful for specifying the locations of things like detector com-  
 511 ponents and activated calorimeter cells, cylindrical polar coordinates with the same origin,  $z$  axis, and  
 512 handedness are often more suitable, with a point in 3-space expressed as  $(r, \phi, \eta)$ .  $r$  is the perpen-

---

<sup>‡</sup>This is the only reason CMS can call itself “compact.”

513 dicular distance from the beam axis. This differs from the usual spherical  $\rho$ , the distance of a point  
 514 from the origin, because the ATLAS detector is cylindrical<sup>§</sup>, and so detector components are more  
 515 easily located using  $r$  instead of  $\rho$ . In some contexts, the latter is used, though this is (or should be)  
 516 made clear.  $\phi$  is the usual (right-handed) azimuthal angle around the beam axis, with  $o$  at the  $+x$   
 517 axis.

518 In a lepton collider where total momentum is conserved, a useful coordinate is the relativistic  
 519 rapidity of a particle:

$$y = \frac{1}{2} \ln \left[ \frac{E + p_z}{E - p_z} \right] \quad (2.1)$$

520 with  $E$  and  $p_z$  as the energy and longitudinal momentum of the particle, respectively. The rapidity  
 521 is the relativistic analog of a rotation angle; boosts can be added in a manner similar to rotations<sup>¶</sup>,  
 522 and differences in rapidity are invariant under boosts. In a hadronic collider, where the participants  
 523 in the hard scatter are partons inside of the proton of unknown momentum fraction, longitudinal  
 524 momentum is not conserved. Nevertheless, since the incident momentum is entirely longitudinal,  
 525 momentum is still conserved in the transverse plane, so quantities like transverse momentum  $\vec{p}_T$   
 526 or energy ( $E_T$ )<sup>||</sup> are often very useful in analysis. However, in the massless limit<sup>\*\*</sup>, we can take  $E =$

---

<sup>§</sup>“toroidal;” the hole is the beam pipe

<sup>¶</sup>Generally, one need only insert the appropriate factor of  $i$ , the square root of  $-1$ ; this introduces differences in sign and changes all of the trigonometric functions associated with rotations into hyperbolic trigonometric functions.

<sup>||</sup>Energy is not a vector quantity, but one can take the scalar or vectorial sum of vectors formed from energy deposits with their location as the direction and energy value as magnitude. In practice, primitives are almost always assumed to be massless, so transverse energy and momentum may loosely be thought of as equivalent, with  $E_T = |\vec{p}_T| = p_T$

<sup>\*\*</sup>not a terrible one for most particles depositing energy in the calorimeter; pions have masses of  $\sim 130$  MeV, and typical energies of calorimeter objects are  $\sim 10^3$  GeV, making for a boost of roughly 100.

527  $\sqrt{p_T^2 + p_z^2}$ . Hence, with  $\theta$  taken as the zenith angle and  $o$  corresponding to the  $+z$  direction, for a  
 528 massless particle,  $p_z = E \cos \theta$ . Using the usual half angle formula  $\cos \theta = (1 - \tan^2 \theta) / (1 + \tan^2 \theta)$

529

$$\gamma = \frac{1}{2} \ln \left[ \frac{1 + \cos \theta}{1 - \cos \theta} \right] = \frac{1}{2} \ln \left[ \frac{(1 + \tan^2(\theta/2)) + (1 - \tan^2(\theta/2))}{(1 + \tan^2(\theta/2)) - (1 - \tan^2(\theta/2))} \right] = -\ln \left( \tan \frac{\theta}{2} \right) \quad (2.2)$$

530 This last expression, denoted  $\eta$ , is known as the pseudorapidity and is used instead of the polar  
 531 angle as a coordinate in hadron colliders. Moreover, pion production (the most common hadronic  
 532 process) is constant as a function of  $\eta$  in  $p\bar{p}$  collisions.

$$\eta = -\ln \left( \tan \frac{\theta}{2} \right) \quad (2.3)$$

533 Lower values of  $|\eta|$  ( $\lesssim 1.3$ ) correspond to more central areas of the detector known as the “barrel,”  
 534 with the typical layout here being concentric, cylindrical layers. Larger values of  $|\eta|$  (to  $\sim 2.5$  for  
 535 some systems and up to as much as  $\sim 4.5 - 5$  for others) are known as the “end caps,” where ma-  
 536 terial is typically arranged as disks of equal radius centered on the beam pipe stacked to ever greater  
 537 values of  $|z|$ . This terminology will be useful when discussing the various subsystems of the ATLAS  
 538 detector. Since decay products from a collision propagate radially (in the calorimeter portions of  
 539 the detector with no magnetic field), the radial coordinate is not so important for composite physics  
 540 objects like electrons or jets, which are typically expressed as momentum 4-vectors. Hence,  $\eta$  and  $\phi$   
 541 are often the only useful spatial coordinates. Distances between objects are often expressed not as a

542 difference in solid angle, but as a distance,  $\Delta R$ , in the  $\eta - \phi$  plane, where

$$\Delta R_{12} = (\eta_1 - \eta_2)^2 + (\phi_1 - \phi_2)^2 \quad (2.4)$$

543 Two important concepts when discussing particles traveling through matter (e.g. particle detec-

544 tors) are radiation lengths and (nuclear) interaction lengths, which characterize typical lengths for

545 the energy loss of energetic particles traveling through materials. In general, the energy loss is mod-

546 eled as an exponential

$$E = E_0 e^{-l/L} \quad (2.5)$$

547 where  $E_0$  is the initial energy, and  $L$  is a characteristic length. These lengths depend both on the in-

548 cident particle and the material through which they pass. In the case of uniform, composite mate-

549 rials, the length may be found by calculating the reciprocal of the sum of mass fraction weighted

550 reciprocal characteristic lengths of the components. This formula works quite well for modeling the

551 very regular behavior of electromagnetic showers (energetic photons convert into electron/positron

552 pairs, which emit photons...). In this case,  $L$  is denoted  $X_0$ ; this is the radiation length. Hadronic

553 showers are far more complicated, with shower multiplicity and makeup being much more vari-

554 able<sup>††</sup>. Nevertheless, a characteristic length can be tabulated for a standard particle type, typically

555 pions, and is called the nuclear interaction length.

---

<sup>††</sup>Different initial hadrons will shower very differently, and hadronic showers will have phenomena like neutral pions converting to photons (which then shower electromagnetically), making them much trickier to deal with.

556    2.3.2    GENERAL LAYOUT OF ATLAS

557    The ATLAS detector and its main components are shown in Figure 2.6. ATLAS is designed as a  
558    largely hermetic detector, offering full coverage in  $\phi$  and coverage in  $|\eta|$  up to 4.7. The multiple sub-  
559    systems allow for good characterization of the decay products from collisions in the LHC. The in-  
560    nermost system is the inner detector (ID); composed primarily of silicon pixels and strips immersed  
561    in a magnetic field, it is designed to reconstruct the curved trajectories of charged particles produced  
562    in collisions while taking up as little material as possible.

563       Surrounding the ID is the liquid argon based electromagnetic calorimeter (ECAL), which is de-  
564       signed to capture all of the energy of the electromagnetic showers produced by electrons and pho-  
565       tons coming from particle collisions. The ECAL is in turn encapsulated by a scintillating tile and  
566       liquid argon based hadronic calorimeter (HCAL) that captures any remaining energy from the jets  
567       produced by hadronizing quarks and gluons.

568       The outermost layer of ATLAS is the muon spectrometer (MS), which has its own magnetic field  
569       produced by toroidal magnets. Muons are highly penetrating particles that escape the calorimeters  
570       with most of their initial momentum, so the MS and its magnets are designed to curve these charged  
571       particles and measure their trajectories to measure their outgoing momenta. Each of these detector  
572       systems has several principal subsystems and performance characteristics, which will be described in  
573       turn below.

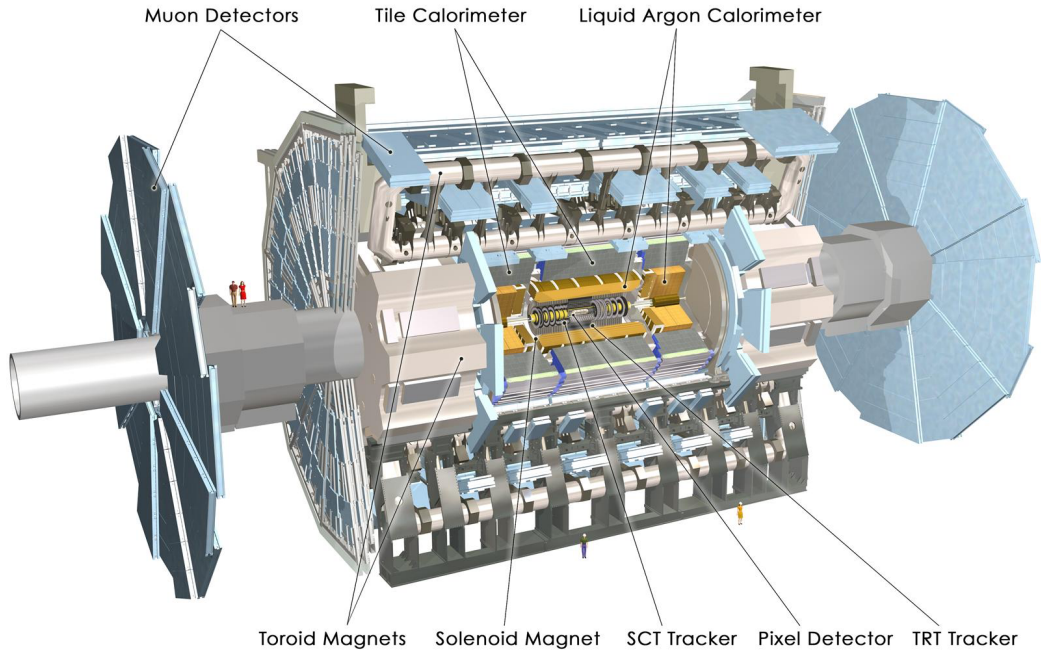


**Figure 2.6:** The ATLAS detector with principal subsystems shown.

#### 574 2.4 THE INNER DETECTOR

575 ATLAS's inner detector (ID) is surrounded by a 2 T superconducting solenoid that is cryogenically  
 576 cooled to a temperature of 4.5 K. The ID uses two silicon detector subsystems (the Pixel and Semi-  
 577 Conductor (strip) Tracker (SCT)) to track the curved trajectories of charged particles emanating  
 578 from particle collisions and a Transition Radiation Tracker (TRT) composed of gas straw detectors  
 579 with filaments for  $e/\pi$  discrimination, as shown in Figure 2.7. The ID offers full coverage in  $\phi$  and  
 580 extends to an  $|\eta|$  of 2.5.

581 Since the components of the ID do not provide an energy measurement, it is desirable for a track-  
 582 ing system to have as small a material budget as possible so that more accurate energy measurements

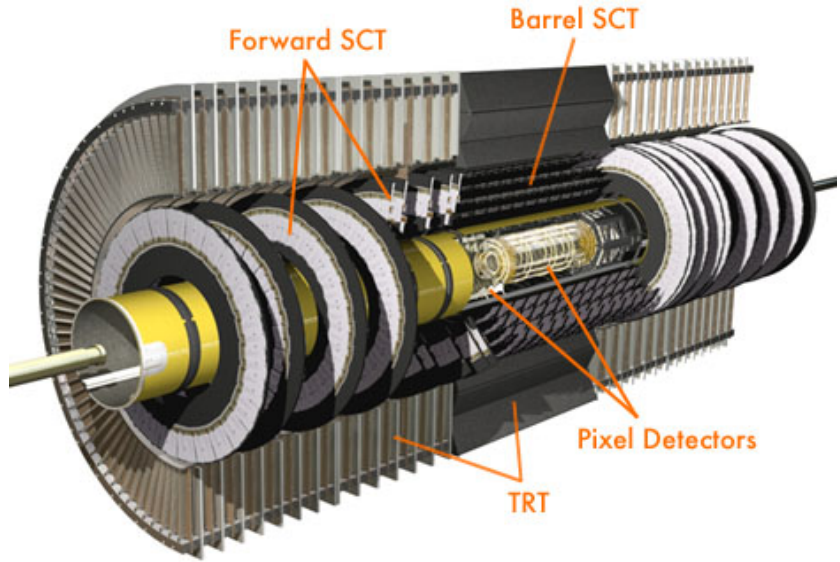


Figure 2.7: The ATLAS inner detector. IC: [44]

583 may be done in the calorimeters. Generally, there are two radiation lengths in the inner detector (the  
 584 precise figure varies with  $\eta$ ); the full material budget, with the layout of the individual layers in each  
 585 subsystem, can be seen in Figure 2.8.

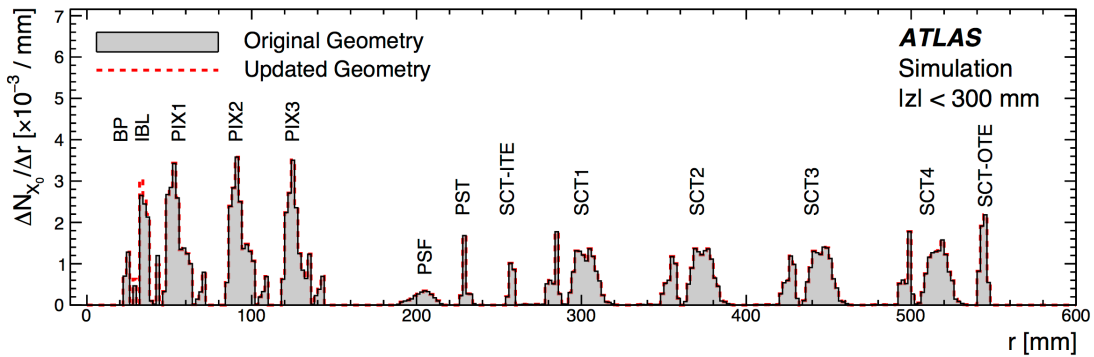


Figure 2.8: The ID material budget. IC: [43]

586    2.4.I    THE PIXEL DETECTOR

587    The innermost part of ATLAS is the Pixel Detector, which, as the name suggests, is comprised of  
588    four layers of silicon pixels in the barrel at 32, 51, 89, and 123 mm from the beam pipe, and three lay-  
589    ers in the end caps at 495, 580, and 650 mm from the beam pipe, with over 80 million channels total.

590    The innermost layer of pixels, the insertable *B* layer (IBL) was installed during the 2013–14 LHC  
591    shutdown. The pixels are cooled to a temperature of  $\sim -5^\circ\text{C}$ , with  $N_2$  gas and operate at 150–600  
592    V. The pixels themselves come in two sizes  $50 \times 400(600) \times 250 \mu\text{m}$ , with the larger pixels in the  
593    outer layers. They provide nominal resolution of  $10(115) \mu\text{m}$  resolution in  $r - \phi(z)$  direction.

594    In order to improve total coverage in the detector and prevent any gaps, pixels are not installed  
595    flush with each other. Pixels in the barrel are tilted at about  $20^\circ$ , with an overlap in  $r - \phi$ , as shown  
596    in Figure 2.9. The disks of the ID end caps are rotated with respect to each other by  $3.75^\circ$ .

597    2.4.2    THE SILICON MICROSTRIP DETECTOR (SCT)

598    The layout of the SCT is similar to that of the Pixel detector, except that, for cost considerations, the  
599    SCT uses silicon strips. These strips are also cooled to  $\sim -5^\circ\text{C}$  with  $N_2$  gas and operate from 150–  
600    350 V. Strip dimensions are  $80 \times 6000 \times 285 \mu\text{m}$ , and provide nominal  $17(580) \mu\text{m}$  resolution in  
601     $r - \phi(z)$ . Barrel strips feature an  $11^\circ$  tilt and come in four layers at 299, 371, 443, and 514 mm. There  
602    are nine end cap disks on each side at  $z$  values varying from 934–2720 mm.

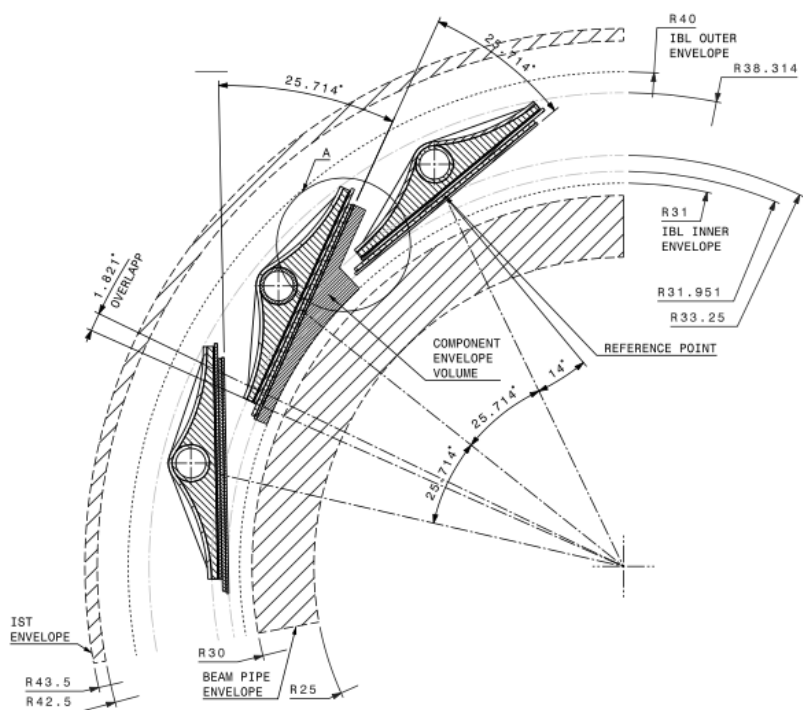


Figure 2.9: Arrangement of pixels in the barrel. IC: [34]

603 2.4.3 TRANSITION RADIATION TRACKER (TRT)

604 The final and outermost subsystem in the ID is the Transition Radiation Tracker (TRT). It provides  
605 coverage for  $|\eta|$  up to 2.0 and is composed of straw detectors with a 4 mm diameter that run the  
606 length of the detector module. The straws provide  $130 \mu\text{m}$  resolution, are filled with a Xe-CO<sub>2</sub>-O<sub>2</sub>  
607 (70-27-3) gas combination, and operate at  $-1500$  V. The filaments and foil lining inside the straws  
608 induce X-ray emission in electrons and pions passing through the TRT as they move from a dielec-  
609 tric to a gas; this “transition radiation” is the source of the TRT’s name. Since the energy deposited  
610 due to transition radiation is proportional to the relativistic boost  $\gamma$ , for constant momentum, this  
611 is inversely proportional to mass. Thus, electrons will have  $\sim 130/0.5 = 260\times$  more transition  
612 radiation than pions, in principle enabling excellent electron/pion discrimination. The TRT will be  
613 replaced by silicon strips in the Phase II upgrade.

614 2.5 THE ATLAS CALORIMETERS

615 ATLAS has four main calorimeter systems: the liquid argon based Electromagnetic Calorimeter  
616 (ECAL), the Hadronic End Cap (HEC), the Forward Calorimeters (FCAL), and the scintillating  
617 tile based hadronic Tile Calorimeter in the barrel. Their layout and material budget in interaction  
618 lengths can be seen in Figure 2.11.

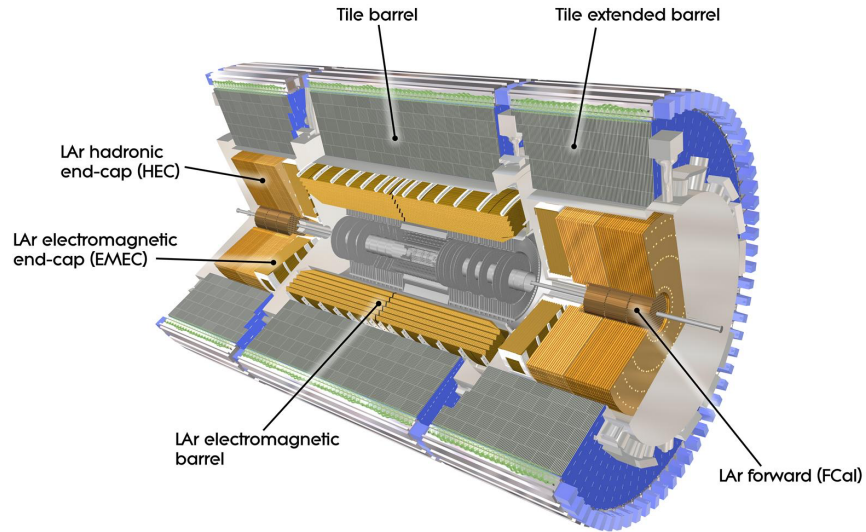


Figure 2.10: The ATLAS calorimeters.

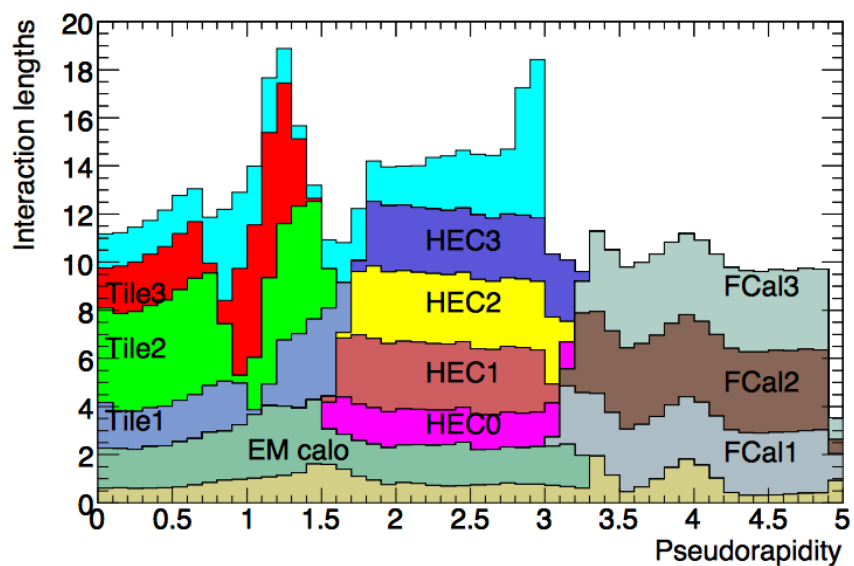


Figure 2.11: Material depth of the ATLAS calorimeters. IC: [44]

619 2.5.1 CALORIMETER RESOLUTION

620 Before diving into the specifics of each of the ATLAS calorimeters, we review some aspects of calorime-  
621 ter energy resolution performance. A calorimeter’s relative energy resolution (a ratio) can be broken  
622 up into three orthogonal components, as shown in Equation 2.6.

$$\frac{\sigma_E}{E} = \frac{S}{\sqrt{E}} \oplus \frac{N}{E} \oplus C \quad (2.6)$$

623  $S$  is the photoelectron statistics or stochastic term and represents the coefficient to the usual count-  
624 ing term (assuming Gaussian statistics);  $N$  is a noise term, which is constant per channel (and hence  
625 comes in as  $1/E$  in the relative energy resolution); and  $C$  is a constant “calibration” term, which re-  
626 flects how well one intrinsically understands a detector (i.e. mismodelling introduces an irreducible  
627 component to the energy resolution). If any detector were perfectly modeled/understood, it’s  $C$   
628 term would be zero.  $N \sim 0.1 - 0.5$  GeV for a typical calorimeter regardless of type, so  $S$  and  $C$   
629 are typically quoted.

630 A typical stochastic term scales as  $S \sim \text{few\%} \sqrt{d_{\text{active}} [\text{mm}] / f_{\text{samp}}}$ , where  $f_{\text{samp}}$  is the sampling  
631 fraction or the ratio of a calorimeter by mass is composed of an active material (i.e. one that regis-  
632 ters energy deposits). The tile calorimeter, for example, has a sampling fraction of about 1/36. There  
633 are several reasons that this fraction is so low. First, many active volumes have insufficient stopping  
634 power; one wants to capture as much energy as possible from electromagnetic and hadronic showers  
635 inside the calorimeter, and this simply is not possible for most active media (one notable exception

636 to this is the CMS crystal-based calorimeter; ATLAS is a more conservative design), so well-behaved  
637 absorbers like lead or iron are necessary to ensure all the energy is contained within a calorimeter.  
638 Another factor is cost; things like liquid argon are expensive. Finally, most active media are unsuit-  
639 able for structural support, so sturdy absorbing materials help relieve engineering constraints.

640 **2.5.2 THE ELECTROMAGNETIC CALORIMETER (ECAL)**

641 The ECAL has liquid argon (LAr) as an active material and lead as an absorber. The ECAL barrel  
642 extends to  $|\eta|$  of 1.475, with three layers at 1150, 1250, and 2050 mm, and its end cap, comprised of  
643 two wheels, covers  $1.375 < |\eta| < 2.5$ , (3.2) for the inner (outer) wheel, with 3 (2) layers out to  
644 3100 mm. There is a 1.1 (0.5) cm thick layer of LAr pre-sampler up to  $|\eta|$  of 1.8 in the barrel (end cap)  
645 of the ECAL, which is designed to aid in correcting for electron and photon energy loss in the ID.

646 The LAr and lead absorber are arranged in alternating, beveled, sawtooth layers in what is known  
647 as an “accordion” geometry, shown in Figure 2.12, which shows the layout of a barrel module in the  
648 ECAL. The absorber thickness is 1.53 (1.13) mm for  $|\eta|$  less (more) than 0.8 to ensure a constant sam-  
649 pling fraction. This arrangement helps provide greater coverage in  $\phi$ .

650 The ECAL overall typically covers 2–4 interaction lengths or about 20–40 radiation lengths. Its  
651 performance corresponds to resolution coefficients  $S = 0.1 \text{ GeV}^{-1/2}$  and  $C = 0.002$  with a 450  
652 ns drift time. In order to optimize the material budget and overall detector construction, the ECAL  
653 barrel infrastructure is integrated with that of the ID’s solenoid. The granularity of the ECAL barrel  
654 middle layer,  $\Delta\eta \times \Delta\phi$  cells of size  $0.025 \times 0.025$ , are used to define the granularity of calorimeter  
655 cluster reconstruction in ATLAS.

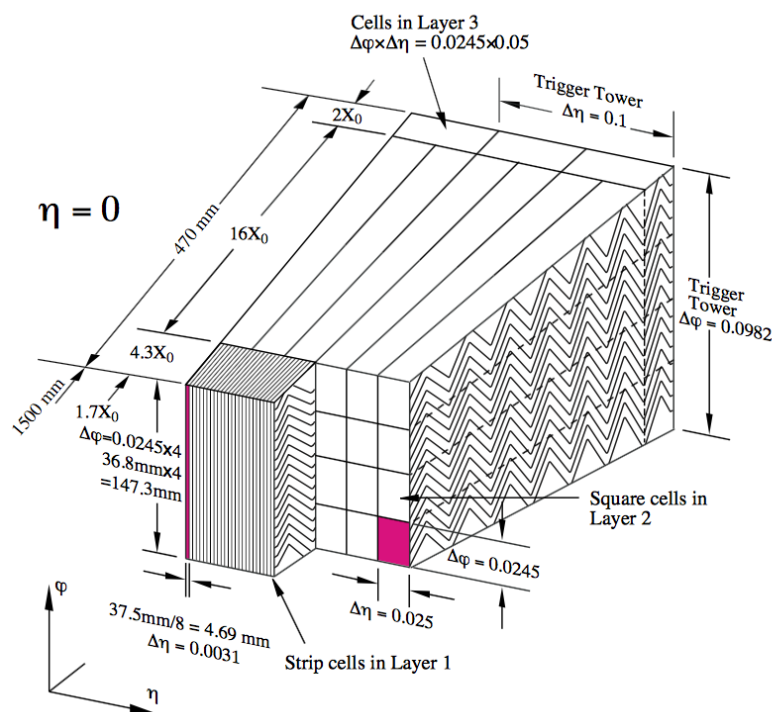


Figure 2.12: The accordion geometry of the LAr electromagnetic calorimeters is prominently shown in this illustration of an ECAL barrel module. IC: [44]

656 2.5.3 HADRONIC END CAPS (HEC)

657 The HEC covers an  $|\eta|$  range of 1.5 to 3.2. Like the ECAL end caps, the HEC consists of two identi-  
658 cal wheels out to a distance from the beam axis of 2030 mm; its layout is shown in Figure 2.13. The  
659 HEC also has LAr as the active material, but instead has flat copper plates as absorbers for sampling  
660 fraction of 4.4% and 2.2% in the first and second wheels, respectively. Its granularity in  $\eta - \phi$  is  
661  $0.1 \times 0.1$  for  $|\eta|$  up to 2.5 and  $0.2 \times 0.2$  in the more forward regions.

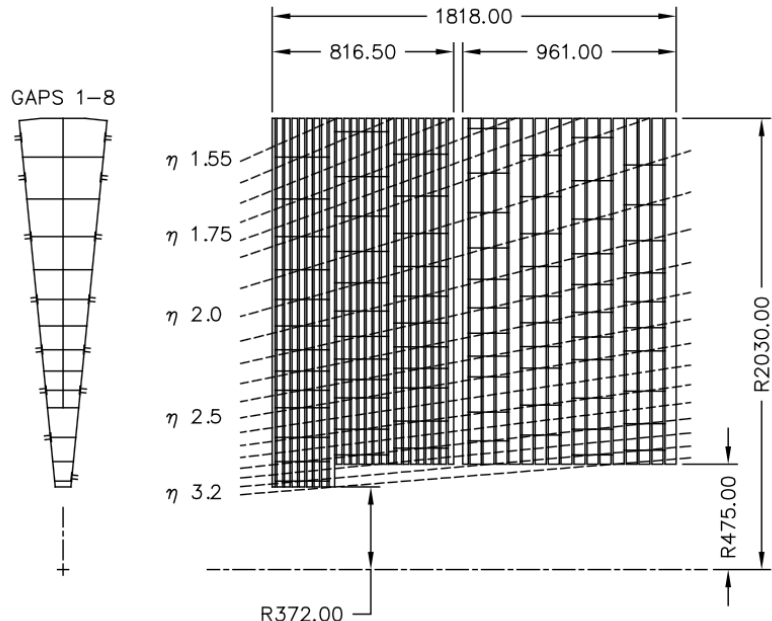


Figure 2.13: The layout of the HEC in  $r - \phi$  and  $r - z$ ; dimensions are in millimeters. IC: [44]

662    2.5.4    THE FORWARD CALORIMETER (FCAL)

663    The FCAL covers an  $|\eta|$  range from 3.1 to 4.9, again using LAr as the active material in gaps between  
664    rods and tubes in a copper-tungsten matrix, as shown in Figure 2.14. These system has characteris-  
665    tic performance corresponding to stochastic term of  $S \approx 1 \text{ GeV}^{-1/2}$ . There are three modules in  
666    the FCAL: one electromagnetic and two hadronic, with the latter two featuring a higher tungsten  
667    content for a larger absorption length.

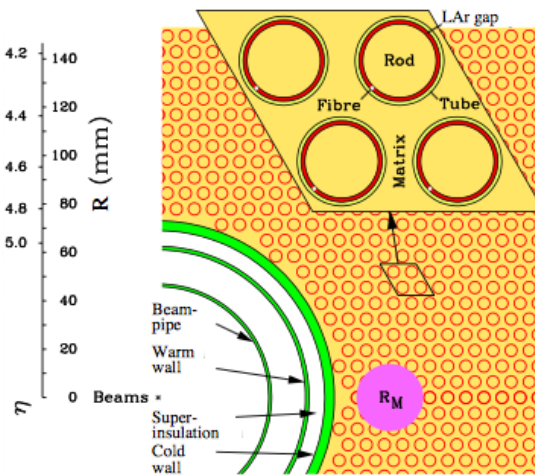
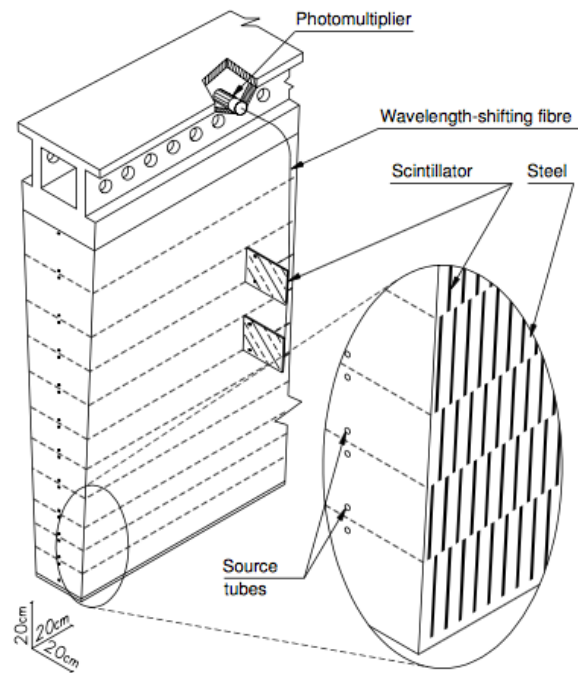


Figure 2.14: The material layout for a typical section of the FCAL in the transverse plane. IC: [44]

668    2.5.5    THE HADRONIC TILE CALORIMETER

669    The tile calorimeter, covering an  $|\eta|$  of up to 1.7 is made up of 64 modules in the barrel (each cover-  
670    ing  $\Delta\phi$  of  $360/64 = 5.625^\circ$ ), each with a layout as in Figure 2.15. It is designed to be self-supporting  
671    for structural reasons, and so is the only calorimeter without LAr as a an active medium, with a stag-  
672    gered matrix of active scintillating polystyrene and supporting steel. It operates at 1800 V with a 400



**Figure 2.15:** The material layout for a typical section of the hadronic tile calorimeter. IC: [44]

673 ns dead time and has a thickness corresponding to 10–20 interaction lengths (2.28–4.25 m). Its cells  
674 have a  $\Delta\eta \times \Delta\phi$  granularity of  $0.1 \times 0.1$  in the first two layers and  $0.2 \times 0.1$  in the last layer. Its  
675 performance corresponds to  $S = 0.5 \text{ GeV}^{-1/2}$  and  $C = 0.05$  (0.03 after calibration).

## 676 2.6 THE MUON SPECTROMETER

677 Since the energy of muons is not captured within the calorimeters, the stations of the ATLAS MS  
678 surround the entire detector and provide tracks of outgoing muons that can be matched to tracks in  
679 the ID. The ATLAS toroids, which provide field strengths of up to 2.5 (3.5) T in the barrel (end cap)  
680 with typical strengths of 0.5–1.0 T, bend the muons, which allows for a muon momentum measure-  
681 ment since the muon mass is known. The relative momentum resolution of a tracker (assuming, as  
682 in ATLAS, that bending primarily happens in the  $\phi$  direction) may be expressed as

$$\frac{\sigma_{p_T}}{p_T} = c_0 \oplus c_1 \cdot p_T \quad (2.7)$$

683 The  $c_0$  term represents a degradation in resolution due to multiple scattering, and is typically 0.5–  
684 2% [78]. The  $c_1$  term describes the phenomenon of, holding magnetic field constant, higher momen-  
685 tum muons curving less. This term has typical values of  $10^{-3} - 10^{-4} \text{ GeV}^{-1}$ . At very high  $p_T$  val-  
686 ues, this is of particular concern since a very small curvature can result in charge misidentification.

687 A cross-sectional view (in  $r-z$ ) of the muon spectrometer with station names, detector types, and  
688 layouts is shown in Figure 2.16. There are three layers of muon detectors in both the barrel (at 5 000,  
689 7 500, and 10 000 mm) and end cap (at 7 000 (11 000), 13 500, and 21 000 mm), with the innermost

690 end cap layer split in two due to the end cap toroid. This corresponds to an  $|\eta|$  range up to 2.4 for both precision and trigger coverage, and up to 2.7 for precision detection only.<sup>††</sup>

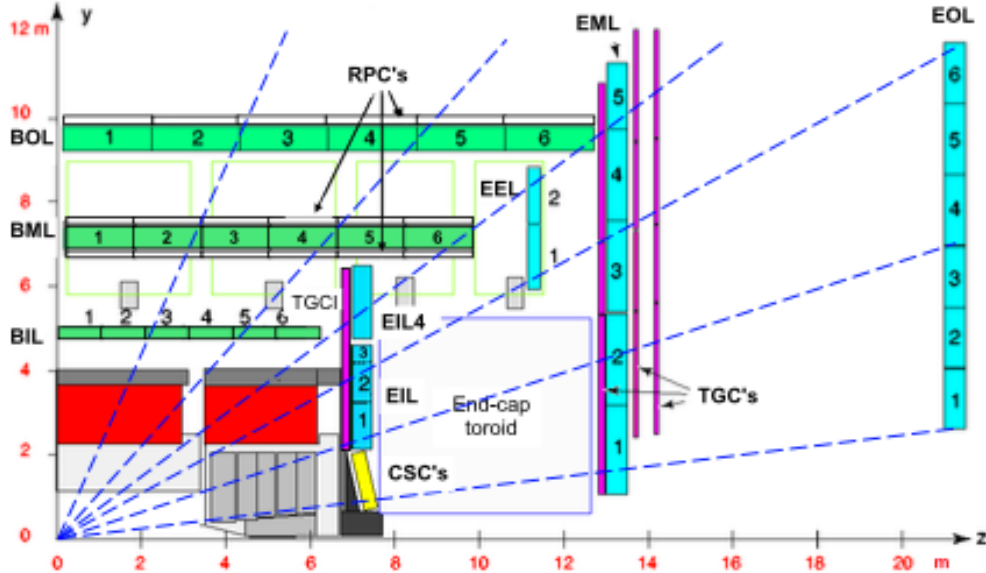


**Figure 2.16:** The ATLAS muon spectrometer. Naming of the MDT stations obeys the following convention [BE] (barrel or end cap) [IEMO] (inner, inner extended (end cap only), middle, or outer layer) [1-6] (increasing in  $z$  ( $r$ ) for the barrel (end cap)), so EI1 is the station in the inner most end cap layer closest to the beam pipe. IC: [44]

691  
692     The MS can reconstruct muons with transverse momenta from 5 GeV up to 3 TeV (with 10% res-  
693     olution at 1 TeV (3% at 100 GeV)). Detectors in the MS fall into two broad headings, precision detec-  
694     tors and trigger detectors, both described below. Nominal performance of the current detector types  
695     in the MS is summarized in Figure 2.17, a table taken from [44]. It should be noted that  $|\eta|$  ranges  
696     quoted below, where applicable, do not include the range 0-0.1, where this a gap in the MS to allow  
697     for cabling and other services to the ATLAS detector; for a discussion of compensatory measures in

---

<sup>††</sup>This will change with the New Small Wheel Phase I Upgrade. cf. Appendix A

<sup>698</sup> muon reconstruction, see Chapter 5.

Type	Function	Chamber resolution (RMS) in			Measurements/track		Number of	
		$z/R$	$\phi$	time	barrel	end-cap	chambers	channels
MDT	tracking	35 $\mu\text{m}$ ( $z$ )	—	—	20	20	1088 (1150)	339k (354k)
CSC	tracking	40 $\mu\text{m}$ ( $R$ )	5 mm	7 ns	—	4	32	30.7k
RPC	trigger	10 mm ( $z$ )	10 mm	1.5 ns	6	—	544 (606)	359k (373k)
TGC	trigger	2–6 mm ( $R$ )	3–7 mm	4 ns	—	9	3588	318k

Figure 2.17: ATLAS MS detector performance. IC: [44]

### <sup>699</sup> 2.6.1 PRECISION DETECTORS

<sup>700</sup> The ATLAS MS has two types of precision detectors: Monitored Drift Tubes (MDT's) and Cathode Strip Chambers (CSC's). An MDT is a tube with a 3 cm diameter with length depending on  
<sup>701</sup> the station in which the tube is located. The tube is filled with an Ar/CO<sub>2</sub> gas mixture and has a  
<sup>702</sup> tungsten-rhenium wire at its center that is kept at 3 000 V when operational. The MDT's provide 35  
<sup>703</sup>  $\mu\text{m}$  resolution (per chamber) in their cross-sectional dimension (there is no sensitivity along the axis  
<sup>704</sup> of the wire). Resolution of this magnitude requires very precise knowledge of the location of the  
<sup>705</sup> wires within the MDT's; this is generally true for detectors in the MS (trigger as well as precision);  
<sup>706</sup> to this end, stations of the MS are aligned using an optical laser system. For a detailed description  
<sup>707</sup> of how misalignment can affect performance, see Appendix A for a detailed discussion of misalign-  
<sup>708</sup> ment's simulated effects on the performance of the proposed Micromegas trigger processor in the  
<sup>709</sup> New Small Wheel (NSW) of the Phase I upgrade. Their 700 ns dead time, however, precludes their  
<sup>710</sup> use as trigger detectors and also in the region of the small wheel (innermost endcap) closest to the  
<sup>711</sup> beam pipe ( $|\eta|$  from 2.0 to 2.7), where rates are highest.

713 In this region, the precision detectors are the CSC's, which have a much lower dead time of  $\sim 40$   
714 ns. These are multiwire proportional chambers with cathode planes that have orthogonal sets of  
715 strips, allowing for a measurement in both principal directions. CSC detector sizes also vary by sta-  
716 tion, coming in both small and large chambers. The CSC strip pitch is 5.31 (5.56) mm for the large  
717 (small) chambers, with position determined from the induced charge distribution in the strips. This  
718 corresponds to a nominal resolution of 60 (5 000)  $\mu\text{m}$  per plane in the bending (non-bending) direc-  
719 tion. These are slated to be replaced by Micromegas detectors in the NSW.

720 **2.6.2 TRIGGER DETECTORS**

721 Trigger detectors have a fundamentally different role than the precision detectors, instead needing to  
722 deliver “good enough” approximate values of muon track positions and  $p_T$  values. The MS has two  
723 types of trigger detectors: Resistive Plate Chambers (RPC’s) in the barrel and Thin Gap Chambers  
724 (TGC’s) in the end caps. They collectively cover an  $|\eta|$  range to 2.4, and their arrangement is shown  
725 in Figure 2.18.

726 The RPC’s are parallel plate detectors with a dead time of 5 ns and a thickness of 2 mm, kept at  
727 a potential of 9 800 V; they are deployed in three layers. RPC’s, too, feature strips with orthogonal  
728 arrangements on the top and bottom planes, with a strip pitch of 23–35 mm.

729 The TGC’s are multiwire proportional chambers with a dead time of 25 ns. Also, featuring or-  
730 thogonal strips, the TGC’s also provide a  $\phi$  measurement to compensate for the lack of MDT sensi-  
731 tivity in this direction. There are four layers of TGC’s in the end cap. TGC’s will be supplanted by  
732 sTGC’s (small thin gap chambers) in the NSW.

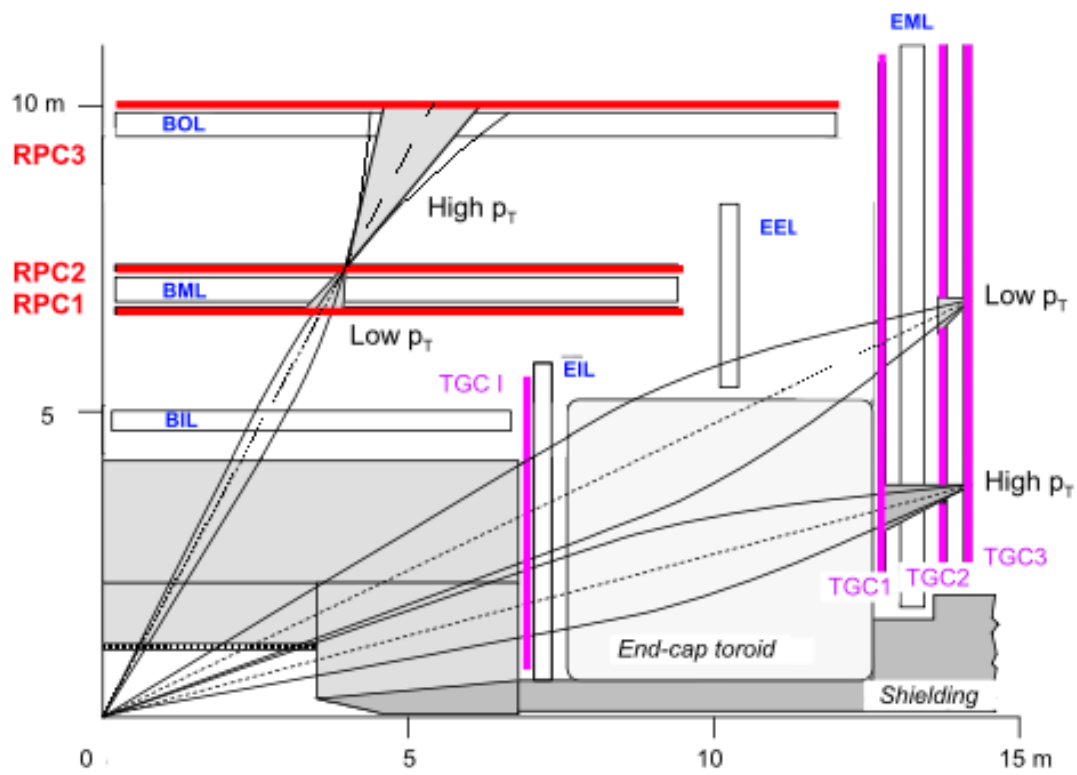


Figure 2.18: ATLAS MS trigger detector arrangement. IC: [44]

<sup>733</sup> For more details on how detector level trigger objects work in the ATLAS MS, see Appendix A

<sup>734</sup> for details on the Micromegas trigger processor algorithm.

*What do you read, my lord?*

*Words, words, words.*

Hamlet, 2:2

# 3

735

736

## Data and Simulated Samples

737 THE DATA AND Monte Carlo simulation (MC) samples used in this thesis are the same as in the fidu-  
738 cial analysis. The data corresponds to  $36.1 \text{ fb}^{-1}$  of  $pp$  collision data collected in 2015+16 at the AT-  
739 LAS detector at  $\sqrt{s} = 13 \text{ TeV}$ . Details of the Run 1 analysis referenced in Chapter 9, may be found  
740 in [20]. Only events recorded with all systems in ATLAS in good working order and passing certain

741 quality requirements, according to a Good Run List (GRL), are analyzed.

742 Details about MC samples may be found in [67], and signal and background modeling are dis-  
743 cussed in the next. The  $ZH \rightarrow \ell\ell b\bar{b}$  process is considered for both multivariate analysis (MVA)  
744 optimization and the final statistical analysis, while  $WH \rightarrow \ell\nu b\bar{b}$  and  $ZH \rightarrow \nu\nu b\bar{b}$  production  
745 are included in the final statistical analysis only. Signal MC samples were generated separately for  $qq$   
746 and  $gg$  initiated  $VH$  processes.  $qqVH$  samples were generated with Powheg MiNLO + Pythia8  
747 [68, 72] with the AZNLO [19] tune set and NNPDF3.0 PDF [28], with alternate samples gener-  
748 ated using MadGraph5\_AMC@NLO [23] for the hard scatter generation and Pythia8 for the  
749 hardronization, parton shower (PS), underlying event (UE), and multiple parton interactions (MPI).  
750 Nominal  $ggZH$  samples were generated using Powheg for the matrix element (ME) and Pythia8  
751 for the parton shower (PS), underlying event (UE), and multiple parton interactions (MPI), again  
752 applying the AZNLO tune and NNPDF3.0 PDF set. [60]

753 The background processes considered in these studies are  $Z+jets$ ,  $t\bar{t}$ , and diboson production for  
754 both MVA optimization and the final statistical analysis with single top production and  $W+jets$   
755 only considered in the final statistical analysis.  $V+jets$  samples are generated using Sherpa 2.2.1 [40]  
756 for both the ME and PS. These samples are generated in different groups, according to the identity  
757 of the  $V$ , the max ( $H_T, p_T^V$ ) of events, with further subdivisions according to the flavor of the two  
758 leading jets in an event,  $b$ ,  $c$ , or  $l$ , for a total of six categories.  $t\bar{t}$  samples are generated using Powheg  
759 with the NNPDF3.0 PDF set interfaced with Pythia8 using the NNPDF2.3 PDF's and the A14  
760 tune [46]. Single top samples use Powheg with the CT10 PDF's interfaced with Pythia6 using  
761 the CTEQ6L1 PDF's [21, 57]. Diboson samples are generated with Sherpa 2.2.1 interfaced with the

762 NNPDF<sub>3.0</sub> NNLO PDF set normalized to NLO cross sections [[33](#)].

*There are certain calculations one simply doesn't do in  
public.*

Alan Blaer

# 4

763

764

## Signal and Background Modeling

765 THIS CHAPTER summarizes the modeling of the dominant signal and background processes in  
766 this analysis, including corrections and systematic uncertainties (systematic uncertainty, also called  
767 nuisance parameter (NP), titles are set in this font) related to each process. Further details on the  
768 specifics of these topics, including in-depth studies for the derivation and definitions of some of the

769 quantities cited, may be found in [67]. We start with a general discussion of modeling and associated  
770 major categories of uncertainties before addressing each of the physics processes.

#### 771 4.1 EVENT GENERATION IN A NUTSHELL

772 Before diving into the specifics of modeling and systematic uncertainties associated with each ma-  
773 jor set of physics processes considered in this analysis, we review at a schematic level\* the problem  
774 of simulation event generation. Once a physics processes of interest has been determined, how one  
775 simulates an ensemble of particle collisions to model the process in question. This is illustrated in  
776 Figure 4.1. Note that the scope of this problem does not include how these generated collision prod-  
777 ucts propagate through one's detector. This problem is left for Chapter 5.

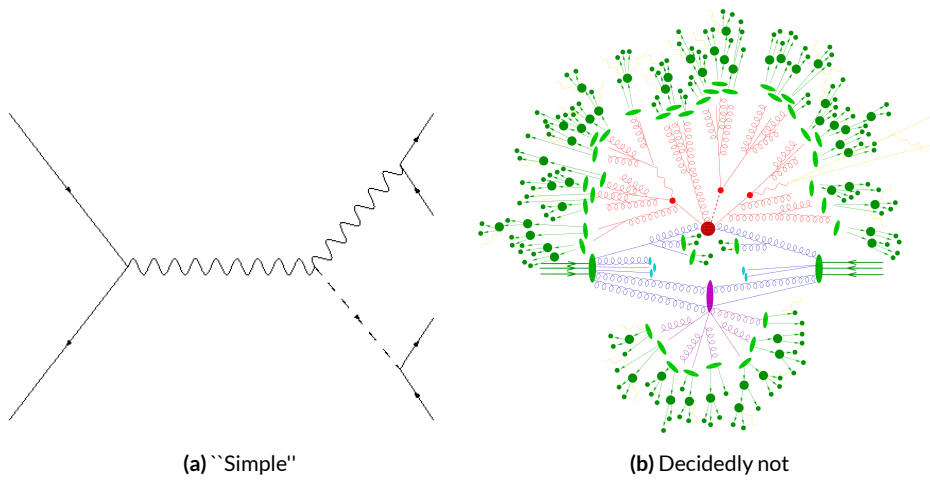


Figure 4.1: The problem here is how to get from (a) to (b).

778 The primary source of complication in event generation comes from dealing with hadronic ob-

---

\*i.e. this will not be a technically rigorous discussion. For a more thorough treatment, the reader is directed to the usual references.

779 jects both in the initial state (the lefthand side of Figure 4.1 (a); the LHC is a hadron collider) and the  
780 final state (this analysis searches for Higgs decays to  $b$ -jets, the lower righthand side of Figure 4.1).

781 Common to all hadronic objects, by definition, are the many considerations that go into calculations  
782 in quantum chromodynamics (QCD). In calculating the hard scatter process itself, one must make  
783 a variety of choices, such as the parton distribution function (PDF) set to use and to what order in  
784 perturbation theory to do the calculation (common choices are leading order (LO), (next to) next to  
785 leading order ((N)NLO), and (next to) next to leading log (NNLL)) [71]. Similar considerations of  
786 ten need to be made for the electroweak parts of an event. These considerations and others in event  
787 generation (broadly called event generator “tuning”) will be discussed in more detail below.

788 The initial state includes not only the hard scatter partons that generate the physics process of in-  
789 terest, but also the rest of the partons in the colliding protons, known as the underlying event (UE).

790 Moreover, the hard scatter partons may not be the only interacting partons in an event, further com-  
791 plicating matters; this phenomenon is known as multiple parton interactions (MPI). Specific to the  
792 final state are the kinematic distributions of the final state objects—what their energies and angular  
793 distributions will be—in addition to the overall cross section of the process that is measurable by the  
794 detector (acceptance effects). Furthermore, one has to model hadronization, the process by which  
795 any free (colored) partons in an event transform into colorless hadrons.

796 Typically, it takes several steps and tools to accomplish this. The hard scatter itself is often mod-  
797 elled with a dedicated event generator like PowHEG [68] or MADGRAPH [23], with events gen-  
798 erated then interfaced with a tool like PYTHIA [72] for the PS, UE, and MPI, though there are ex-  
799 ceptions (SHERPA [51], for example, can do both the hard scatter and hadronization/ for some pro-

800 cesses).

801 4.2 DESCRIPTION OF MODELING UNCERTAINTY CATEGORIES

802 Each of the steps in event generation described above has associated uncertainties. Some uncertain-  
803 ties are inherent in the calculations themselves. The choice of which order in perturbation theory  
804 to do a calculation, for example, comes with it an implicitly defined level of precision<sup>†</sup>. Extrapolat-  
805 ing from one energy/momentum scale to another also introduces uncertainty. Furthermore, there  
806 is no *a priori* correct choice to make at each step in event generation, so each choice (the choice of  
807 generator, PDF set, parton shower calculator, all of their configurable parameters, etc.) implies an  
808 additional layer of uncertainty.

809 In order to quantify these choices, each source of systematic uncertainty is treated separately and  
810 given a unique name. To make this more concrete, take the specific example of the uncertainty asso-  
811 ciated with the  $H \rightarrow b\bar{b}$  branching ratio of 58%, called ATLAS\_BR\_bb, which encapsulates a num-  
812 ber of effects (higher order terms, the mass of the  $b$  quark, and choice of  $\alpha_S$ ). The quoted (in prin-  
813 ciple asymmetric) uncertainty on the Higgs BR is not itself a direct input into the analysis model.  
814 Instead, the effect of varying the branching ratio up and down by one standard deviation is propa-  
815 gated to simulated collision events and recorded (i.e. the analysis is run with the Higgs branching  
816 ratio at  $\pm 1\sigma$ , and the results are recorded alongside the nominal result). The nominal and “up” and  
817 “down” variations are then typically taken to define a normally distributed, freely floating param-

---

<sup>†</sup>though this is less well-defined in QCD calculations than for electroweak calculations since they don’t converge

818 eter in the statistical fit model. Since these parameters associated with systematic uncertainties are  
819 not typically considered interesting quantities, they are often referred to as “nuisance parameters”  
820 (NP’s). The terms “systematic,” “systematic uncertainty,” and “nuisance parameter” are often used  
821 interchangeably.

822 The specifics of exactly how the effects of variations are saved and propagated to the full fit model  
823 are deferred to Chapter 7. The discussion here is confined to how systematic uncertainties for signal  
824 and background modeling and their accompanying variations are defined. Modeling systematics are  
825 derived separately for each physics process (simulation sample). Sometimes, all of the variation for  
826 a given process is encapsulated in a single systematic, but oftentimes the variations from multiple  
827 considerations are distinct enough to be treated separately. Furthermore, each of these separate sys-  
828 tematics for a given sample/process may be treated in a number of ways (e.g. 0-lepton events may  
829 be treated differently from 2-lepton events). An additional subtlety is that a continuous parameter  
830 like a branching ratio lends itself quite naturally to defining Gaussian  $\pm 1\sigma$  variations, while for dis-  
831 crete variations, like choice of PDF set for parton showers, how to proceed is less obvious. This is  
832 addressed on a case-by-case basis, as described below.

833 Before enumerating each of the principal physics processes and their systematics, we begin by  
834 describing considerations and choices that must be addressed for every physics process in order to  
835 make the discussion of individual samples and systematics both clearer and less repetitive.

836 4.2.1 PHYSICS CONSIDERATIONS

837 In general, evaluating the uncertainties arising from the many choices in event generation entails  
838 producing alternate samples of events, which practically means tuning parameters in the various soft-  
839 ware packages and/or using alternate packages/libraries to make new samples. Once these samples  
840 have been created, they are compared at truth-level (particle level) using a package called Rivet [30]  
841 instead of using the full ATLAS detector reconstruction for computational considerations. Given  
842 the nature of the problem and the tools, there are generally three main categories of physics issues,  
843 each described below.

844 UNDERLYING EVENT AND PARTON SHOWER

845 The modeling of the underlying event (UE) and parton shower (PS) are usually handled by the same  
846 package and so are usually treated together. The typical nominal choice in the fiducial analysis is  
847 PYTHIA8. One approach to modeling these uncertainties is simply to see what happens when a  
848 different model is used and then compare this alternate set of events to the nominal set, taking the  
849 difference as the (implicitly one standard deviation) scale of variation. Another approach is to vary  
850 some parameter within a given model, for example, using different tunes in the A14 set for PYTHIA8  
851 with their accompanying variations, to characterize the scale of variation.

852 A natural question is how to treat these two approaches on the same footing. When examining  
853 a set of potential variations related to the same process or effect, oftentimes the largest single varia-  
854 tion in a set is picked as defining the scale for the systematic uncertainty. Another approach is to use

855 the average over a set of variations.<sup>‡</sup> The ATLAS\_UEPS\_VH\_hbb systematic, for example, uses the  
856 Pythia8 + A14 tunes approach to determine the scale of UE variation and compares Pythia8 with  
857 Herwig7 to characterize the PS variation. Each of the A14 tunes comes with an up and down varia-  
858 tion, and the difference between each of these variations and a nominal setup may be expressed as a  
859 ratio,  $R$ , of total events.

860 As is often done when a physical argument can be made for combining related, but ultimately  
861 orthogonal categories/measurements/uncertainties/systematics, the combined UE+PS systematic is  
862 taken to be the sum in quadrature of these two effects:

$$\sum_{tunes} \max_{tune} (|R_{up} - R_{down}|) \oplus \sigma_{PS} \quad (4.1)$$

863 QCD SCALE

864 The term “QCD scale” in the context of modeling uncertainties refers to the choice of renormal-  
865 ization ( $\mu_R$ ) and factorization ( $\mu_F$ ) scales used in QCD calculations. These are typically treated to-  
866 gether. Usually, some multiplicative scale factor,  $f$ , is chosen, and each scale is varied in concert with  
867 the other scale by 1,  $f$ , and  $1/f$  (nine total combinations), sometimes with a cap on how large the  
868 combined variation can be (so ignoring the  $(f, f)$  and  $(1/f, 1/f)$  cases). Just as in the UE+PS, the  
869 largest variation is usually taken as the systematic uncertainty.

870 Another important choice in the context of renormalization, to deal with infinities inherent in

---

<sup>‡</sup>Generally, the maximum is used if it is much larger than other variations, and the average is used if scales are comparable. In general, the historical preference is to be conservative.

871 quantum field theory calculations with loops, is the choice of regularization (to keep track of the  
872 infinities) and subtraction schemes (to eliminate them). A common combination is dimensional reg-  
873 ularization (deforming the four dimensional integral to  $4 - \varepsilon$  dimensions and then taking  $\varepsilon \rightarrow 0$ )  
874 with  $\overline{\text{MS}}$  (“MS-bar” (MS for “minimal subtraction”) subtracts off only the infinities plus some com-  
875 mon factors that always appear in dimensional regularization). For more details, see, for example,  
876 [71]. While each scheme is internally consistent, each can yield different answers at a given order of  
877 calculation (and different subtraction schemes may be used for calculations at different orders).

878 PARTON DISTRIBUTION FUNCTIONS AND  $\alpha_s$

879 Finally, separate uncertainties are often made for the choice of parton distribution function (PDF)  
880 set and associated choice of strong coupling for  $\text{QCD}(\alpha_s)$ . Much as in the previous two cases, one  
881 can vary the parameter  $\alpha_s$  and study what samples of simulation events made using different PDF  
882 sets relative some nominal setup look like. Similarly, one can take the maximum, average, or sum in  
883 quadrature of different variations to characterize a systematic uncertainty.

884 4.2.2 MODELING SYSTEMATIC TYPES

885 With the concept of what type of effect is taken as a single systematic uncertainty and how its varia-  
886 tions are generally evaluated, it is now time to turn to the issue of what exactly is being varied.

887 ACCEPTANCE/NORMALIZATION

888 The most basic type of modeling uncertainty is a normalization uncertainty, often called an accep-  
889 tance uncertainty. This simply denotes the uncertainty on the number of predicted events for a  
890 given process in a given region of phase space (usually delineated by the number of leptons in the  
891 final state and sometimes also by the number of and jets the  $p_T^V$ <sup>§</sup> of an event) and is usually expressed  
892 as a percent.

893 As an example, the uncertainty on the theoretical prediction of the  $H \rightarrow b\bar{b}$  branching ratio,  
894 denoted ATLAS\_BR\_bb (it is an ATLAS-wide systematic), is expressed as a normalization system-  
895 atic with a value of 1.7%, affecting all  $VH$  processes. Now imagine we have an event in a  $VH$  sample  
896 with weight 1.0. The nominal histograms for this region gets filled with this event's relevant informa-  
897 tion with weight 1.0, while the ATLAS\_BR\_bb\_\_1up (\_\_1do) histograms get filled with weight 1.017  
898 (0.983).

899 SHAPE SYSTEMATICS

900 In addition to normalization systematics expressed as single numbers attached to different processes  
901 in different regions, there are also the so-called “shape systematics” and “shape corrections,” heuristi-  
902 cally differences in distributions that exist in distributions even after correcting for normalizations,  
903 which gives distributions a different “shape” even if their integrals are the same (c.f. Figure 4.3).

---

<sup>§</sup>This is the transverse mass of the lepton pair for 2-lepton events, the vectorial sum of the single lepton  
and  $\vec{E}_T^{\text{miss}}$  for 1-lepton events, and the  $\vec{E}_T^{\text{miss}}$  for 0-lepton events.

904 These have the schematic form

$$w_{event} = A_{region} \times f_{region}(event) \quad (4.2)$$

905 where  $w_{event}$  is the simulated event's weight,  $A_{region}$  is the overall normalization (in principle includ-  
906 ing any systematics), and  $f_{region}(event)$  is some function of event-level variables, usually a single vari-  
907 able, like  $p_T^V$  or  $m_{bb}$ . The purpose of these systematics is to take into account (in the case of a system-  
908 atic) or correct (in the case of a correction applied to the event weight) the non-trivial dependence  
909 of a normalization on one of these quantities. Some of these are taken from histograms while others  
910 are parametric functions (in this analysis, usually linear ones).

911 An example of the former case is the quantity  $\delta_{EW}$ , the difference between the nominal  $qqVH$   
912 cross section and the differential cross section as a function of  $p_T^V$  at next to leading order (NLO). As  
a correction, this term is simply used as a correction factor  $k_{EW}^{NLO} = (1 + \delta_{EW})$ .

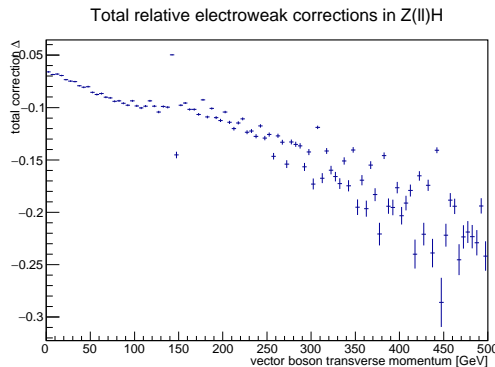


Figure 4.2: The  $\delta_{EW}$  correction term for 2-lepton  $qqZH$ .

913

914 An example of the latter case is the systematic associated with the  $m_{bb}$  dependence of the the

915     $t\bar{t}$  normalization for 2 jet,  $p_T^V \in [75, 150]$  GeV, 2 lepton events. In this case, a variety of effects are  
 916    studied (ME, PS, UE), as shown in Figure 4.3. The top half of the plot is the  $m_{bb}$  plot for this re-  
 917    gion, with the black bars representing the nominal spectrum and spectra generated with different  
 918    ME, PS, and UE choices. The ratio plot in the bottom half of the figure shows the scale of varia-  
 919    tion normalized to bin content. From this ratio plot, it is clear that the choice of ME (pink points)  
 920    was seen to have the largest effect on normalization. The linear fit in the plot reasonably envelopes  
 921    this maximum variation was done, and so is taken as the systematic variation. Hence, in this case,  
 922     $f_{region}(event)$  is a linear function of  $m_{bb}$ , with positive (negative) slope for the up (down) variation.

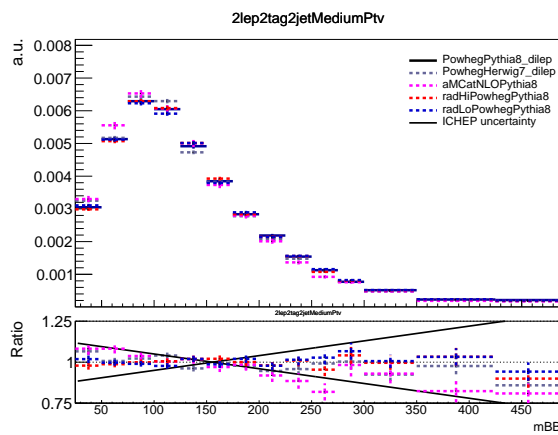


Figure 4.3: The derivation of the 2-lepton  $t\bar{t} m_{bb}$  shape systematic.

### 923 DIVIDING MODELING UNCERTAINTIES: ACCEPTANCE RATIOS

924    In addition to uncertainties on absolute normalizations (both inclusive and region specific), mod-  
 925    eling uncertainties are sometimes introduced for the ratio of normalizations between different re-  
 926    gions. While these can be simple ratios, evaluating a systematic's effect between regions means eval-

927 uating nominal and alternate choices between regions, so the so-called “double ratio” is often taken  
 928 as the scale of variation (plus one). The ATLAS\_UEPS\_VH\_hbb systematic mentioned above, for ex-  
 929 ample, has associated with it, ATLAS\_UEPS\_VH\_hbb\_32JR. This systematic is evaluated by dividing  
 930 the 3 jet to 2 jet ratio in the nominal setup by the same ratio in an alternate setup. These ratios gener-  
 931 ically look like:

$$\frac{\text{Acceptance}[\text{Category}_A(\text{nominalMC})]}{\text{Acceptance}[\text{Category}_B(\text{nominalMC})]} \Big/ \frac{\text{Acceptance}[\text{Category}_A(\text{alternativeMC})]}{\text{Acceptance}[\text{Category}_B(\text{alternativeMC})]} \quad (4.3)$$

932 Double ratio systematics are often included in addition to single systematics when a single system-  
 933 atic could potentially overestimate the total variation due to a single effect. In the above example,  
 934 the choice of UE+PS in signal events may cause different overall variation in 2 jet events as compared  
 935 to events with 3 or more jets due to QCD considerations. However, extrapolating between jet mul-  
 936 tiplicities can be a non-trivial exercise entirely regardless of the choice of generator for UE+PS (cf.  
 937 the discussion of the Stewart-Tackman approach 4.2.2 below), so to include this variation in a single  
 938 systematic would lead to overly conservative systematic uncertainties. Hence, using previous knowl-  
 939 edge of this separate variation between jet multiplicity regions, one can define a double ratio system-  
 940 atic for a more accurate fit model.

941 The three main categories are ratios between different flavor regions, ratios between different lep-  
 942 ton channels<sup>¶</sup>, and ratios between regions with different numbers of jets,  $n_{jet}$ . The first category is  
 943 only relevant for  $V+jets$  systematics and will be treated in that process’s dedicated section below. As

---

<sup>¶</sup>e.g.  $Z+$ heavy flavor jets (at least one  $b$ -jet in the event; often denoted “hf” normalizations in 0- and 2-lepton events

944 this thesis is primarily concerned with the 2-lepton channel, the second category will not be treated  
 945 in detail, though the treatment is much the same as other ratio systematics.<sup>||</sup> In order to discuss the  
 946  $n_{jet}$  ratios in systematics (e.g. the ratios in the double ratio example), we must first describe how ex-  
 947 clusive  $n_{jet}$  cross section calculations are done.

948 THEORETICAL ASIDE: STEWART-TACKMANN A way to calculate uncertainties on processes in re-  
 949 gions with different numbers of jets was developed by Stewart and Tackmann and is implicitly used  
 950 for most  $n_{jet}$  ratio systematics [74]. The problem is how to calculate the cross section and associated  
 951 uncertainty for a process with exclusively  $N$  jets in the final state. Generically:

$$\sigma_{\geq N} = \sigma_N + \sigma_{\geq N+1} \quad (4.4)$$

952 The physical interpretation of one parton to one jet is an idealized case. In order to demarcate  
 953 between jets, one has some quantity that is used as a cutoff in an integral that defines the border be-  
 954 tween jet regions.

$$\sigma_{\geq N} = \int_0^{p_{cut}} \frac{d\sigma_N}{dp} + \int_{p_{cut}} \frac{d\sigma_{\geq N+1}}{dp} \quad (4.5)$$

955 Since these cutoffs (not necessarily constant, etc.) can make calculations more complicated, inclu-  
 956 sive cross sections tend to be easier to calculate. Hence, it is usually much easier to evaluate the two  
 957 inclusive cross sections and find the uncertainties on these by varying  $\alpha_S$  in the usual way (cf. Sec-

---

||Such ratios allow for information in one channel to help constrain other channels, particularly for hard to model processes like  $Z+hf$ . This helps to reduce final overall uncertainties in combined fits. For a discussion of the interplay of nuisance parameters in combined fits, cf. Chapter 9.

<sup>958</sup> tion 4.2.1). One then assumes the inclusive uncertainties are uncorrelated, for a covariance matrix for  
<sup>959</sup>  $\{\sigma_{\geq N}, \sigma_N, \sigma_{\geq N+1}\}$  of (with  $\Delta_x^2$  as the variance associated with  $x$ ):

$$\Sigma = \begin{pmatrix} \Delta_{\geq N}^2 & \Delta_{\geq N}^2 & 0 \\ \Delta_{\geq N}^2 & \Delta_{\geq N}^2 + \Delta_{\geq N+1}^2 & -\Delta_{\geq N+1}^2 \\ 0 & -\Delta_{\geq N+1}^2 & \Delta_{\geq N+1}^2 \end{pmatrix} \quad (4.6)$$

<sup>960</sup> These calculations contain Sudakov double logs of  $\ln^2(p/Q)$ , where  $Q$  corresponds to the scale  
<sup>961</sup> of the hard scatter process ( $m_H$ ), and  $p_{cut}$  is usually something like a  $p_T$  cutoff. When integrating  
<sup>962</sup> over all of the phase space, these terms can come to dominate calculations when  $p \gg Q$ . The  $N+1$   
<sup>963</sup> term in the covariance matrix is an uncertainty associated with the cutoff, but the Sudakov double  
<sup>964</sup> logs will dominate any higher order terms. Stewart and Tackmann give the following reasoning:

<sup>965</sup> “In the limit  $\alpha_S^2 \approx 1$ , the fixed-order perturbative expansion breaks down and the logarithmic  
<sup>966</sup> terms must be resummed to all orders in  $\alpha_S$  to obtain a meaningful result. For typical experimental  
<sup>967</sup> values of  $p_{cut}$  fixed-order perturbation theory can still be considered, but the logarithms cause large  
<sup>968</sup> corrections at each order and dominate the series. This means varying the scale in  $\alpha_S$  in Eq. (9) di-  
<sup>969</sup> rectly tracks the size of the large logarithms and therefore allows one to get some estimate of the size  
<sup>970</sup> of missing higher-order terms caused by  $p_{cut}$ , that correspond to  $\Delta_{cut}$ . Therefore, we can approxi-  
<sup>971</sup> mate  $\Delta_{cut} = \Delta_{\geq 1}$ , where  $\Delta_{\geq 1}$  is obtained from the scale variation for  $\sigma_{\geq 1}$ .”

<sup>972</sup> The above considerations are important for this analysis since phase space is separated into 2 and  
<sup>973</sup>  $\geq 3$  jet regions, and the uncertainties for these regions are anti-correlated.

974    4.3    PROCESS SPECIFIC SYSTEMATIC SUMMARIES

975    Brief descriptions of modeling systematics, including recapitulations of nominal sample generation,  
976    are given in the following sections. The general approach here is to copy the relevant summary tables  
977    and describe any major deviations from the general procedures described in the previous section.  
978    The dominant backgrounds for the 2-lepton channel are  $Z+hf$  and  $t\bar{t}$ , accounting for well over 90%  
979    of all background events. Diboson samples are the next-leading background and are an important  
980    validation sample; others are included for completeness. A summary of all the modeling systematics  
in this analysis are given in Table 4.1.

Process	Systematics
Signal	$H \rightarrow bb$ decay, QCD scale, PDF+ $\alpha_S$ scale, UE+PS (acc, $p_T^V$ , $m_{bb}$ , 3/2 jet ratio)
$Z+jets$	Acc, flavor composition, $p_T^V+m_{bb}$ shape
$t\bar{t}$	Acc, $p_T^V+m_{bb}$ shape
Diboson	Overall acc, UE+PS (acc, $p_T^V$ , $m_{bb}$ , 3/2 jet ratio), QCD scale (acc (2, 3 jet, jet veto), $p_T^V$ , $m_{bb}$ )
Single top	Acc, $p_T^V+m_{bb}$ shape

Table 4.1: Summary of modeling systematic uncertainties, with background samples listed in order of importance.

981

982    4.3.1    SIGNAL PROCESSES

983    Nominal signal  $qqVH$  samples are generated using PowHeg with the MiNLO (multiscale improved  
984    NLO) [62] procedure applied interfaced with PYTHIA8 using the AZNLO tune [19] and NNPDF3.0  
985    PDF set [28]. For the 2-lepton case, gluon fusion initiated Higgs production is also considered (ac-  
986    counting for  $\sim 14\%$  of the total cross section in this channel), with samples generated with PowHeg interfaced

987 with PYTHIA8 using the AZNLO tune. The NNPDF2.3 set [27] is used for both the ME and UE+PS.

988 Alternate samples  $qqVH$  samples are generated using MADGRAPH5\_aMC@NLO [22] for the

989 ME and PYTHIA8 for the UE+PS, hadronization and MPI. The NNPDF2.3\_5f FFN PDF sets and

990 the Al4 tune [13]; the latter has variations included. PowHEG+MINLO+HERWIG7 were samples

991 were also used for systematics.

992 The signal systematics categories are  $H \rightarrow bb$  decay cross section, QCD scale, PDF+ $\alpha_s$  scale, and

993 UE+PS. Additionally, there is the NLOEWK correction described above. The correction scale factor

994 is derived using the HAWK MC software. To encapsulate NNLOEW effects the maximum of 1%,

995 the square of the correction factor, and the photon induced cross section is used as a systematic.

996 Table 4.2, reproduced from [67], summarizes the signal cross section systematics, which are ap-

997 plied uniformly across the analysis channels (as applicable).

Sys Name	source	Norm. effect	applied to
ATLAS_BR_bb	$H \rightarrow bb$ dec. unc, (HO effects, $m_b$ , $\alpha_s$ )	1.7%	all $VH$ processes
ATLAS_QCDscale_VH	QCD scale uncertainty	0.7%	$qq \rightarrow VH$ processes
ATLAS_QCDscale_ggZH	QCD scale uncertainty	27%	$gg \rightarrow ZH$
ATLAS_pdf_Higgs_VH	PDF+ $\alpha_s$ uncertainty	1.9% 1.6%	$qq \rightarrow WH$ $qq \rightarrow ZH$
ATLAS_pdf_Higgs_ggZH	PDF+ $\alpha_s$ uncertainty	5.0%	$gg \rightarrow ZH$

Table 4.2: Summary of all systematic uncertainties on the  $VH$  cross section including their value, source and the corresponding nuisance parameter name.

998 The remaining signal systematics are analysis channel specific and are summarized in Table 4.3.

999 The methodologies match those described in Section 4.2. The UE+PS systematics were derived us-

1000 ing the alternate samples mentioned above; QCD scale uncertainties were derived by varying scales

1001 by 1/3 and 3; and PDF uncertainties were derived by comparing the nominal set with the PDF4LHC15\_30

1002 PDF set [29].

NP name	oL: $ZH \rightarrow \nu\nu b\bar{b}$		iL: $WH \rightarrow \ell\nu b\bar{b}$		zL: $ZH \rightarrow \ell\ell b\bar{b}$	
	2j	3j	2j	3j	2j	$\geq 3j$
ATLAS_UEPS_VH_hbb	10.0%	10.0%	12.1%	12.1%	13.9%	13.9%
ATLAS_UEPS_VH_hbb_32JR	–	13.0%	–	12.9%	–	13.4%
ATLAS_UEPS_VH_hbb_VPT	shape only				shape+norm	
ATLAS_UEPS_VH_hbb_MBB	shape only					
QCDscale_VH_ANA_hbb_J2	6.9%	–	8.8%	–	3.3%	–
QCDscale_VH_ANA_hbb_J3	-7%	+5%	-8.6%	+6.8%	-3.2%	+3.9%
QCDscale_VH_ANA_hbb_JVeto	–	-2.5%	–	3.8%	–	–
QCDscale_VH_ANA_hbb_VPT	shape only				shape+norm	
QCDscale_VH_ANA_hbb_MBB	shape only					
pdf_HIGGS_VH_ANA_hbb	1.1%	1.1%	1.3%	1.3%	0.5%	0.5%
pdf_VH_ANA_hbb_VPT	shape only				shape+norm	
pdf_VH_ANA_hbb_MBB	shape only					

**Table 4.3:** Summary of all systematic uncertainties on the  $VH$  acceptance and shapes originating from altering the PDF and  $\alpha_S$  uncertainties, including their corresponding nuisance parameter name.

### 1003 4.3.2 $V + \text{jets}$

1004 Nominal  $V + \text{jets}$  samples are generated using SHERPA 2.2.1@NLO\*\* [52] for both the ME and PS,  
1005 interfaced with the NNPDF’s and using a five quark flavor scheme, and alternative samples are de-  
1006 rived using MADGRAPH5 interfaced with PYTHIA8. In order to increase statistics in important re-  
1007 gions of phase space, these samples were separated into kinematic slices based on  $p_T^V$  and into bins of  
1008 jet flavor. The kinematic slices were in the quantity  $\max(H_T, P_T^V)$  and had the intervals [0–70, 70–  
1009 140, 140–280, 280–500, 500–1000,  $> 1000]$  GeV. The jet flavor slices were made using flavor vetoes  
1010 and filters:

- 1011 • BFilter: at least 1 b-hadron with  $|\eta| < 4, p_T > 0$  GeV

---

\*\*SHERPA 2.1 is used for some variations not available in SHERPA 2.2.1.

- 1012     • CFilterBVeto: at least 1 c-hadron with  $|\eta| < 3, p_T > 4$  GeV; veto events which pass the  
 1013       BFilter

- 1014     • CVetoBVeto: veto events which pass the BFilter and/or the CFilterBVeto

1015       These in turn are related to the main flavor regions used in the analysis, based on the flavor of  
 1016       the two leading jets in an event (based on  $p_T$ ). These five flavors (with up, down, and strange collec-  
 1017       tively known as “light”) yield six different flavor combinations:  $bb, bc, bl$  (these first three collectively  
 1018       known as “heavy flavor” or  $V+hf$ ),  $cc, cl, ll$  (or just “light” or  $l$ ). Ratio systematics are often made  
 1019       with respect to the acceptance in the  $bb$  region.

1020        $V+jet$  systematics are derived in several steps. The first is to use double ratios of acceptances be-  
 1021       tween analysis regions and nominal versus alternative MC’s (so  $(\text{Region1-nominal}/\text{Region2-nominal})/(\text{Region1-}$   
 1022       alternate}/ $\text{Region2-alternate})$ ). The main region comparisons are 2 jet versus 3 jet (3+ jet for 2-lepton)  
 1023       and then 0-lepton versus 2-lepton (1-lepton) for  $Z+hf$  ( $W+hf^{\dagger\dagger}$ ). The final uncertainty contains the  
 1024       sum in quadrature of four effects:

- 1025       1. Variation of 0.5 and 2 of QCD scales in the SHERPA sample  
 1026       2. Sum in quadrature of half the variation from different resummation and CKKW merging  
 1027       scales <sup>††</sup>  
 1028       3. Maximal variation between nominal setup and SHERPA 2.2.1 with the MMHT2014nnlo68cl  
 1029       and CT14nnlo PDF sets  
 1030       4. Difference between the SHERPA and MADGRAPH<sub>5</sub> sets

---

<sup>††</sup>The  $W+hf$  CR versus the SR is also considered for  $W+hf$

<sup>‡‡</sup>cf. [59], Section 2 for a summary of the CKKW method for different parton multiplicities used in  
 SHERPA

<sup>1031</sup> Summaries of the  $Z$ +jets uncertainties are provided here; the reader is referred to [67] for the  
<sup>1032</sup>  $W$ +jets systematics, as these events are virtually non-existent in the 2-lepton case with which this  
<sup>1033</sup> thesis is almost exclusively concerned. In Table 4.4, from [67] are the normalization systematics.

Process	Name	prior in region					
		2jet			( $\geq$ )3jets		
		2L: low Vpt	2L: high Vpt	oL	2L: low Vpt	2L high Vpt	oL
$Z+1$	SysZclNorm				18%		
$Z+cl$	SysZlNorm				23%		
$Z+hf$	norm_Zbb				Floating Normalization		
$Z+hf$	SysZbbNorm_L2_J3	-	-	-	30%	30%	-
$Z+hf$	SysZbbNorm_J3	-	-	-	-	-	17%
$Z+hf$	SysZbbNorm_0L	-	-	7%	-	-	7%
$Z+hf$	SysZbbPTV				effect on each region obtained from shape rw		

**Table 4.4:** Effect of modelling systematics on  $Z$ +jets normalization in the 2lepton regions. For systematic uncertainties implemented with a prior the effect of  $1-\sigma$  variation is reported. The uncertainties labelled as  $Zbb$  act on the entire  $Z+hf$  background.

<sup>1034</sup> The flavor composition ratio systematics are in Table 4.5, also from [67].

<sup>1035</sup> Finally, the  $p_T^V$  and  $m_{bb}$  shape systematics are derived using control regions in data. The func-  
<sup>1036</sup> tional form for the  $p_T^V$  systematic is  $\pm 0.2 \log 10(p_T^V/50\text{GeV})$ , and that of the  $m_{bb}$  systematic is  $\pm 0.0005 \times$   
<sup>1037</sup>  $(m_{jj} - 100\text{ GeV})$ .

### <sup>1038</sup> 4.3.3 TOP-PAIR PRODUCTION

<sup>1039</sup> Nominal  $t\bar{t}$  samples are produced with POWHEG at NLO for the ME calculation using the NNPDF3.0  
<sup>1040</sup> PDF set interfaced with PYTHIA8.210 using the A14 tune and the NNPDF2.3 PDF set at LO. The

---

These use the same selections as the signal regions except for  $b$ -tags (0, 1, and 2 tags are studied), with the added requirement in 2tag regions that  $m_{bb}$  not be in the range of 110–140GeV.

Category	Nuisance Parameter Name	Prior	Applied to
$Z+bc/Z+bb$	SysZbcZbbRatio	40%	$Z+bc$ events (0-Lepton)
		40%	$Z+bc$ events (2-Lepton 2jet)
		30%	$Z+bc$ events (2-Lepton $\geq 3$ jet)
$Z+bl/Z+bb$	SysZblZbbRatio	25%	$Z+bl$ events (0-Lepton)
		28%	$Z+bl$ events (2-Lepton 2jet)
		20%	$Z+bl$ events (2-Lepton $\geq 3$ jet)
$Z+cc/Z+bb$	SysZccZbbRatio	15%	$Z+cc$ events (0-Lepton)
		16%	$Z+cc$ events (2-Lepton 2jet)
		13%	$Z+cc$ events (2-Lepton $\geq 3$ jet)

**Table 4.5:** The priors on the relative acceptance variations for  $Z+hf$ . The first column details the flavor components across which the acceptance variation is being considered, the second column lists the names of the corresponding nuisance parameter in the Profile Likelihood Fit, the third contains the value of the prior and the fourth column the processes and categories to which this nuisance parameter is applied.

parameters `hdamp` (nominal value  $1.5m_{top}$ , a resummation damping factor for ME/PS matching that can heuristically thought of as tuning high  $p_T$  radiation) in PowHEG and `pThard` (nominal value 0) and `pTdef` (nominal value 2) in PYTHIA (both control merging with PowHEG) are varied to evaluate certain systematics. Alternative  $t\bar{t}$  samples use PowHEG+HERWIG7, MADGRAPH5\_aMC@NLO+PYTHIA8.2, and the nominal setup with varied tunes and parameter values. Uncertainties are taken to cover the largest difference between the nominal and any of these alternate configurations.

The overall  $t\bar{t}$  normalization is a floating normalization, and further systematics attached to the ratio of acceptances between regions (3-to-2 jet, SR-to-WhfCR, and 1-to-0 lepton) are defined using double ratios; these are summarized in Tables 4.6 and 4.7, taken from [67].

Shape systematics for  $\hat{p}_T^V$  and  $m_{bb}$  are linear and taken to cover the largest difference reasonably well, as described above in 4.2.2. These are summarized in Table 4.8, again taken from [67].

The use of a top  $e - \mu$  control region helps constrain this.

	o-lepton		r-lepton			
Systematic	2j	3j	WCR 2j	SR 2j	WCR 3j	SR 3j
norm_ttbar	floating normalization					
SysttbarNorm_L0	8%	8%	-	-	-	-
SysttbarNorm_J2	9%	-	9%	9%	-	-
SysttbarNorm_DWhfCR_L1	-	-	25%	-	25%	-

**Table 4.6:** Effect of modelling systematics on  $t\bar{t}$  normalization in the 0 and 1-lepton analysis region.

	2jet		$\geq 3$ jets	
	low Vpt [SR/CR]	high Vpt [SR/CR]	low Vpt [SR/CR]	high Vpt [SR/CR]
norm_ttbar_J2_L2	floating normalization		-	
norm_ttbar_J3_L2	-		floating normalization	
SysTTbarPTV_L2_L2	effect on each region obtained from shape rw			

**Table 4.7:** Effect of modelling systematics on  $t\bar{t}$  normalization in the 2lepton regions. The SysTTbarPTV\_L2\_L2 systematic is implemented as a shape systematic over the full  $VpT > 75$  GeV range, and as a result has different acceptance effects in the low and high  $VpT$  regions.

Analysis region	Uncertainty	Value	Source	Nuisance Parameter
o,r lepton	$p_T^V$ shape	shape	fit through largest deviation (aMC@NLO+PYTHIA8)	TTbarPTV
2 lepton	$p_T^V$ shape	norm + shape	fit through largest deviation (aMC@NLO+PYTHIA8)	TTbarPTV_L2
o,r lepton	$m_{b\bar{b}}$ shape	shape only	fit through largest deviation (aMC@NLO+PYTHIA8)	TTbarMBB
2 lepton	$m_{b\bar{b}}$ shape	shape only	fit through largest deviation (aMC@NLO+PYTHIA8)	TTbarMBB_L2

**Table 4.8:** Summary of all shape uncertainties for the  $t\bar{t}$  process with short descriptions and the name of the corresponding nuisance parameters.

#### 1052 4.3.4 DIBOSON PRODUCTION

1053 Three diboson production processes (collectively denoted  $VV$ ) are important for these analyses:  $ZZ$ ,  
 1054  $WZ$ , and  $WW$ . Nominal samples are created using SHERPA 2.2.1 using the NNPDF3.0 PDF set. Al-

1055 Alternative samples use PowHEG+PYTHIA8 and PowHEG+HERWIG++. The methodology here is  
 1056 similar to that of the  $t\bar{t}$  systematics, with both overall acceptance and lepton channel specific uncer-  
 1057 tainties, with the exception that UE+PS and QCD scale are treated separately (PDF+ $\alpha_S$  was found  
 1058 to be negligible).  $p_T^V$  shape systematics are described using linear fits, while  $m_{bb}$  shape systematics  
 1059 are described using hyperbolic tangents (third degree polynomials) in the 2 jet (3 jet) regions. Once  
 1060 again, summary tables from [67] are reproduced here.

Sys Name	source	Norm. effect	applied to
SysWWNorm	overall cross section uncertainty	25%	WW in all regions
SysWZNorm	overall cross section uncertainty	26%	WZ in all regions
SysZZNorm	overall cross section uncertainty	20%	ZZ in all regions

**Table 4.9:** Summary of all systematic uncertainties on the diboson cross section including their value, source and the corresponding nuisance parameter name.

NP name	oL: $ZZ \rightarrow \nu\bar{\nu}bb$		1L: $WZ \rightarrow \ell\nu bb$		2L: $ZZ \rightarrow \ell^+\ell^-bb$	
	2j	3j	2j	3j	2j	$\geq 3j$
SysVZ_UEPS_Acc	5.6%	5.6%	3.9%	3.9%	5.8%	5.8%
SysVZ_UEPS_32JR	-	7.3%	-	10.8%	-	3.1%
SysVZ_UEPS_VPT	shape+norm		shape only		shape+norm	
SysVZ_UEPS_MBB				shape only		
SysVZ_QCDscale_J2	10.3%	-	12.7%	-	11.9%	-
SysVZ_QCDscale_J3	-15.2%	+17.4%	-17.7%	+21.2%	-16.4%	+10.1%
SysVZ_QCDscale_JVeto	-	+18.2%	-	+19.0%	-	-
SysVZ_QCDscale_VPT	shape+norm		shape only		shape+norm	
SysVZ_QCDscale_MBB				shape only		

**Table 4.10:** Summary of the systematic uncertainties on the VH acceptance in each analysis region and on the  $p_T^V$  and  $m_{bb}$  shapes originating from altering the QCD scale, including their nuisance parameter name.

<sup>1061</sup> 4.3.5 SINGLE TOP PRODUCTION

<sup>1062</sup> Single top sample are generated separately for the different production channels ( $s$ ,  $t$ , and  $Wt$ ) using  
<sup>1063</sup> Powheg with the CT10 NLO PDF's interfaced with Pythia6 using the PERUGIA2012 PS tune  
<sup>1064</sup> and the corresponding CTEQ6L LO PDF's and PHOTOS (TAUOLA) for QED final state ( $\tau$ ) de-  
<sup>1065</sup> cays.

Production	Uncertainty	Value	Source	Nuisance Parameter
$s$ -channel	overall normalization	4.6%	sum in quadrature of $\mu_R$ , $\mu_F$ , $\alpha_S$ and PDF uncertainties	<code>stopNorm</code>
$t$ -channel	overall normalization	4.4%	sum in quadrature of $\mu_R$ , $\mu_F$ , $\alpha_S$ and PDF uncertainties	<code>stopNorm</code>
$t$ -channel	2 jet region acceptance	17%	sum in quadrature of deviations in alternative generators	<code>stopAcc</code> correlated with 2 jet and 3 jet case
$t$ -channel	3 jet region acceptance	20%	sum in quadrature of deviations in alternative generators	<code>stopAcc</code> correlated with overall and 3 jet case
$Wt$ channel	overall normalization	6.2%	sum in quadrature of $\mu_R$ , $\mu_F$ , $\alpha_S$ and PDF uncertainties	<code>stopWtNorm</code> correlated with 2 jet and 3 jet case
$Wt$ channel	2 jet region normalization	35%	sum in quadrature of deviations in alternative generators	<code>stopWtAcc</code> correlated with overall and 3 jet case
$Wt$ channel	3 jet region normalization	41%	sum in quadrature of deviations in alternative generators	<code>stopWtAcc</code> correlated with overall and 2 jet case
$t$ -channel	$p_T^V$ shape	shape	fit through largest deviation (Powheg+Herwig++) $\pm 0.001 \times p_T^V \mp 0.17 + 1$	<code>StopPTV</code>
$t$ -channel	$m_{b\bar{b}}$ shape	shape	fit through largest deviation (Powheg+Pythia6  radHi-radLo ) $\pm 0.0008 \times m_{b\bar{b}} \mp 0.12 + 1$	<code>StopMBB</code>
$Wt$ channel	$p_T^V$ shape	shape	fit through largest deviation (Powheg+Pythia6 with diagram subtraction) $\pm 0.003 \times p_T^V \mp 0.69 + 1$	<code>StopWtPTV</code>
$Wt$ channel	$m_{b\bar{b}}$ shape	shape	fit through largest deviation (Powheg+Pythia6 with diagram subtraction) $\pm 0.0036 \times m_{b\bar{b}} \mp 0.52 + 1$ ( $m_{b\bar{b}} < 275$ GeV) $\mp 0.47 + 1$ ( $m_{b\bar{b}} \geq 275$ GeV)	<code>StopWtMBB</code>

**Table 4.11:** Summary of all uncertainties for the single top process with short descriptions and the name of the corresponding nuisance parameters, updated for the winter baseline analysis.

*“...what would you do first?”*

*The Master said, “It would have to be rectifying names.”*

Confucius, *The Analects*

1066

# 5

1067

## Object and Event Reconstruction and

1068

## Selection

1069 IN BREAKING WITH THE STANDARD CONVENTION both object definitions and their associated

1070 experimental systematic uncertainties will be defined in this chapter: the hope is that the proximity

1071 of these descriptions will allow them to elucidate each other. Summary tables are almost exclusively  
1072 taken from [31] or [65]. This analysis, like most analyses in ATLAS, use central object definitions  
1073 from collaboration combined performance (CP) groups<sup>\*</sup> using standard analysis tools and recom-  
1074 mendations from these groups for the various objects and their accompanying systematic uncertain-  
1075 ties.

1076 Before proceeding to the objects used in this analysis, we begin with a few remarks on uncertain-  
1077 ties associated with object reconstruction. Event-level variables and selections are discussed more in  
1078 depth in Chapters 1 and 6. As described in Section 4.2, systematics quantify the uncertainty asso-  
1079 ciated with certain effects, and are generally treated in an analysis by saving histograms of discrimi-  
1080 nating distributions corresponding to the nominal analysis except with the systematic in question  
1081 varied by plus and minus one standard deviation each (one histogram each). While for modeling  
1082 systematics this only corresponds to different event weights, for experimental systematics like those  
1083 described in this chapter (with the exception of flavor tagging and certain trigger systematics), this is  
1084 done by varying the parameter in question and re-running reconstruction with the systematic varied  
1085 before recomputing all event level quantities and then saving discriminant values in their appropri-  
1086 ate distributions. This is, in general, a much more computationally intensive process in the analysis,  
1087 which is why an entire software framework, the `CxAODFramework`, was created for this analysis (see  
1088 Section 3 of [31] for more details).

---

\*Teams of physicists within ATLAS dedicated to studying different aspects of reconstruction general to very many analyses. An example is the ATLAS Muon CP group, whose duties include providing definitions for how muons are reconstructed in ATLAS, different quality requirements and thresholds, and muon related systematic uncertainties, as well as software packages to make these definitions and guidelines easier to implement.

<sup>1089</sup> 5.1 TRIGGERS

<sup>1090</sup> Tables of the triggers used with the 2015 and 2016 datasets are given in Tables 5.1 and 5.2.

0 lep	1 lep	2 lep
HLT_xe70	HLT_xe70 HLT_e24_lhmedium_L1EM20VH OR HLT_e60_lhmedium OR HLT_e120_lhloose	HLT_mu20_iloose_L1MU15 OR HLT_mu40 HLT_e24_lhmedium_L1EM20VH OR HLT_e60_lhmedium OR HLT_e120_lhloose

**Table 5.1:** Summary table of triggers used in 2015 Data.

period	0 lep	1 lep	2 lep
A	HLT_xe90_mht_L1XE50	HLT_xe90_mht_L1XE50 HLT_e26_lhtight_nod0_ivarloose OR HLT_e60_lhmedium_nod0 OR HLT_e60_medium OR HLT_e140_lhloose_nod0	HLT_mu24_ilosse(data) HLT_mu24_ilosse_L1MU15(MC) OR HLT_mu40 HLT_e26_lhtight_nod0_ivarloose OR HLT_e60_lhmedium_nod0 OR HLT_e60_medium OR HLT_e140_lhloose_nod0
B-D <sub>3</sub>	HLT_xe90_mht_L1XE50	HLT_xe90_mht_L1XE50 HLT_e26_lhtight_nod0_ivarloose OR HLT_e60_lhmedium_nod0 OR HLT_e60_medium OR HLT_e140_lhloose_nod0	HLT_mu24_ivarmedium OR HLT_mu50 HLT_e26_lhtight_nod0_ivarloose OR HLT_e60_lhmedium_nod0 OR HLT_e60_medium OR HLT_e140_lhloose_nod0
D <sub>4</sub> -E <sub>3</sub>	HLT_xe110_mht_L1XE50	HLT_xe110_mht_L1XE50 HLT_e26_lhtight_nod0_ivarloose OR HLT_e60_lhmedium_nod0 OR HLT_e60_medium OR HLT_e140_lhloose_nod0	HLT_mu24_ivarmedium OR HLT_mu50 HLT_e26_lhtight_nod0_ivarloose OR HLT_e60_lhmedium_nod0 OR HLT_e60_medium OR HLT_e140_lhloose_nod0
$\geq F_1$	HLT_xe110_mht_L1XE50	HLT_xe110_mht_L1XE50 HLT_e26_lhtight_nod0_ivarloose OR HLT_e60_lhmedium_nod0 OR HLT_e60_medium OR HLT_e140_lhloose_nod0	HLT_mu26_ivarmedium OR HLT_mu50 HLT_e26_lhtight_nod0_ivarloose OR HLT_e60_lhmedium_nod0 OR HLT_e60_medium OR HLT_e140_lhloose_nod0

**Table 5.2:** Summary table of triggers used in 2016 Data.

1091 The 0-lepton channel uses a  $\vec{E}_T^{\text{miss}}$  trigger, while the 2-lepton channel uses single lepton triggers,  
 1092 with the 1-lepton analysis using both. Since the 0- and 1-lepton channels are largely beyond the scope  
 1093 of this thesis, the discussion here will be limited to the single lepton triggers; the interested reader is  
 1094 directed towards [31] and its cited sources for an in-depth discussion of the use of the  $\vec{E}_T^{\text{miss}}$  trigger.

1095 The efficiency of triggers is in general different on simulated datasets than in actual data collected  
 1096 in ATLAS, so a scale factor to correct for this difference in efficiency must be applied to simulation  
 1097 events. This scale factor is given by the muon CP group for muons for both the 1- and 2-lepton cases  
 1098 and from the electron CP group for the 1-lepton case. For the two electron case, this was calculated  
 1099 by the analysis team as (details in [31]):

$$\frac{1 - (1 - \epsilon_{\text{MC}}^{e1} \times \text{SF}^{e1}) \times (1 - \epsilon_{\text{MC}}^{e2} \times \text{SF}^{e2})}{1 - (1 - \epsilon_{\text{MC}}^{e1}) \times (1 - \epsilon_{\text{MC}}^{e2})} \quad (5.1)$$

1100 There are also systematic uncertainties associated with these trigger efficiencies. The single elec-  
 1101 tron trigger efficiency systematic uncertainty is encapsulated in a single systematic, `EL_EFF_Trigger_-`  
 1102 `Total_1NPCOR_PLUS_UNCOR`, while the single muon trigger efficiency has two components, one  
 1103 each for the sample statistics, `MUON_EFF_TrigStatUncertainty`, and systematic uncertainties  
 1104 `MUON_EFF_TrigSystUncertainty` associated with that efficiency's measurement.

1105 While the momentum associated with the lowest un-prescaled single lepton triggers changes de-  
 1106 pending on data-taking conditions (the numbers associated with the triggers in the tables can be  
 1107 thought of as nominal  $p_T$  values for trigger level objects), the lowest typical value is  $\sim 25$  GeV. In  
 1108 order to maintain this triggering capability on low  $p_T$  muons in the higher luminosity environment

1109 of the Run 3 LHC and beyond, trigger-capable detectors will be installed in upgraded New Small  
1110 Wheels (NSW) of the ATLAS muon detector during the Phase I upgrade. Detailed studies in sim-  
1111 ulation of the trigger algorithm performance under nominal and misaligned conditions for the Mi-  
1112 cromegas detectors to be installed in the NSW may be found in Appendix A.

1113 **5.2 ELECTRONS**

1114 Electrons in ATLAS are reconstructed using a combination of the ATLAS electromagnetic calorime-  
1115 ter (ECAL) and inner detector (ID). Reconstruction begins by searching for so-called “seed clusters”  
1116 in the ECAL. The ECAL is divided into a  $200 \times 256$  tower grid in the  $\eta - \phi$  plane, with each tower  
1117 having a size of  $0.025$  square in  $\eta$  and  $\phi$ , corresponding to the granularity of the ECAL in its middle  
1118 layer, with all energy in a tower summed longitudinally. A “sliding window” of  $3 \times 5$  cells in the  
1119  $\eta - \phi$  plane is then used to identify EM clusters associated with electrons based on criteria detailed  
1120 in [49]. This comparatively simple algorithm (in contrast to jet reconstruction detailed below) is  
1121 effective since electromagnetic showers have a well defined behavior and shape.

1122 Once seed clusters have been formed, they are associated with tracks in the inner detector. Com-  
1123 bined cluster-tracks pairs form electron candidates. In order for a electron candidate to be consid-  
1124 ered a suitable electron for analysis, it must pass certain quality requirements, based on a cut on the  
1125 value of a likelihood-based (LH) discriminant (cf. [14] for details). This discriminant is given by:

$$d_{\mathcal{L}} = \frac{\mathcal{L}_S}{\mathcal{L}_S + \mathcal{L}_B}, \quad \mathcal{L}_S(\vec{x}) = \prod_{i=1}^n P_{s,i}(x_i) \quad (5.2)$$

1126 where the  $s$  and  $S$  ( $b$  and  $B$ ) subscripts refer to distributions in fiducial signal (background) distri-  
 1127 butions in bins of  $|\eta|$  and  $E_T$ . The  $P(x_i)$  are probability distributions functions (pdf)'s for input  
 1128 variables. Several sets of input variables exist for increasingly stringent quality requirements on elec-  
 1129 trons; this analysis uses Loose LH electrons as the base for electron selection, with the input vari-  
 1130 ables relating to leakage into the hadronic calorimeter (HCAL), shower and energy deposits in each  
 1131 of the ECAL layers, track quality requirements, TRT hits, and track-cluster matching. This analysis  
 1132 adds a LooseTrackOnly isolation requirement (the  $p_T$  sum of tracks within a certain  $\eta - \phi$  distance  
 1133 of the candidate track must be below a certain value), impact parameter significance cuts, and an ex-  
 1134 plicit B-layer hit requirement. The  $ZH$ -signal electrons must further pass a  $27\text{ GeV} p_T$  cut ( $1.05 \times$   
 1135  $p_T^{\text{trigger}}$ ). These requirements are summarized in Table 5.3.

Electron Selection	$p_T$	$\eta$	ID	$d_0^{\text{sig}}$	$ \Delta z_0^{BL} \sin \theta $	Isolation
$VH - \text{loose}$	$>7\text{ GeV}$	$ \eta  < 2.47$	LH Loose + B-layer cut	$< 5$	$< 0.5\text{ mm}$	LooseTrackOnly
$ZH - \text{signal}$	$>27\text{ GeV}$	$ \eta  < 2.47$	LH Loose + B-layer cut	$< 5$	$< 0.5\text{ mm}$	LooseTrackOnly
$WH - \text{signal}$	$>27\text{ GeV}$	$ \eta  < 2.47$	LH Tight	$< 5$	$< 0.5\text{ mm}$	FixedCutHighPtCaloOnly

Table 5.3: Electron selection requirements.

### 1136 5.2.1 ELECTRON SYSTEMATICS

1137 The electron CP group has tabulated standard systematic uncertainties to be associated with the use  
 1138 of reconstructed electrons in ATLAS analyses in two main categories. The first category is related  
 1139 to efficiency corrections and is broken into three components: identification (`EL_EFF_ID_Total-`  
 1140 `CorrUncertainty`), reconstruction (`EL_EFF_Reco_TotalCorrUncertainty`), and isolation  
 1141 (`EL_EFF_Iso_TotalCorrUncertainty`). The second category deals with electron energy scale

1142 (roughly, the uncertainty in taking the energy deposits in an EM cluster and turning them into an  
1143 electron energy) and energy resolution (the width associated with this). This is in practice a very  
1144 complicated procedure, with over 60 systematics associated, but this analysis is not at all sensitive  
1145 to these effects and so a simplified model of two systematics, EG\_RESOLUTION\_ALL and EG\_SCALE-  
1146 \_ALL, is used.

1147 5.3 MUONS

1148 This analysis uses the standard CP muon collection in an event, though these muons in ATLAS are  
1149 constructed in a variety of ways; for full details see [25] and [17]. Most muons are constructed using  
1150 tracks in the chambers of the muon spectrometer (MS), with a variety of algorithms available. MS  
1151 tracks are sufficient to reconstruct a muon (a fit on these tracks can be used to point back to an in-  
1152 teraction point for vertex matching, for example) and, in the  $|\eta| \in (2.5, 2.7)$  interval where there  
1153 is no tracking, these standalone (SA) muons are the default. The most common and robust form  
1154 of muon reconstruction combines tracks in the MS with tracks in the ID (more precisely, a global  
1155 refit with hits from both subsystems is typically done) to form combined (CB) muons. CB and SA  
1156 muons automatically pass the loose reconstruction requirements for the Loose muons used in this  
1157 analysis. Additionally, since there is a gap in the  $|\eta| < 0.1$  range in the MS to make room for cabling  
1158 and other detector services, there are two further muon types used in this range: the segment tagged  
1159 (ST) muons that match ID tracks to segments in the MDT or CSC chambers and the calorimeter  
1160 tagged (CT) muons that match ID tracks to calorimeter clusters consistent with minimum ionizing  
1161 particles (which muons in ATLAS generally are).

1162      Further quality requirements are imposed on Loose muons for the different muon categories  
 1163      used in this analysis. Isolation requirements similar to the electrons in corresponding categories are  
 1164      imposed, and impact parameter requirements are also imposed. The  $ZH$  signal muons also have a  
 1165       $p_T$  cut at 27 GeV and a requirement that the muon fall within the  $|\eta|$  range of the ID.

Muon Selection	$p_T$	$\eta$	ID	$d_0^{\text{sig}}$	$ \Delta z_0^{\text{BL}} \sin \theta $	Isolation
$VH - \text{loose}$	$> 7 \text{ GeV}$	$ \eta  < 2.7$	Loose quality	$< 3$	$< 0.5 \text{ mm}$	LooseTrackOnly
$ZH - \text{signal}$	$> 27 \text{ GeV}$	$ \eta  < 2.5$	Loose quality	$< 3$	$< 0.5 \text{ mm}$	LooseTrackOnly
$WH - \text{signal}$	$> 25 \text{ GeV}$	$ \eta  < 2.5$	Medium quality	$< 3$	$< 0.5 \text{ mm}$	FixedCutHighPtTrackOnly

**Table 5.4:** Muon selection requirements.

### 1166 5.3.1 MUON SYSTEMATICS

1167      Similar to the treatment of systematic uncertainties associated with the electrons, muons have CP de-  
 1168      fined systematics. The muon momentum scale and resolution systematics are divided into three cat-  
 1169      egories associated one for uncertainties related to ID tracks (`MUONS_ID`), one for MS tracks (`MUONS-`  
 1170      `_MS`), one for the overall scale (`MUONS_SCALE`), and two for charge dependent momentum scales  
 1171      (`MUON_SAGITTA_RHO` and `MUON_SAGITTA_RESBIAS`). The remaining systematics have a STAT and  
 1172      SYS component corresponding to the sample statistics and systematic uncertainties for their individ-  
 1173      ual components. Efficiency scale factors use different standard candles in different  $p_T$  ranges ( $J/\psi$ 's  
 1174      ( $Z$ 's) below (above) 15 GeV), and so these systematics are broken up into two categories (`MUON_EFF-`  
 1175      `_STAT` and `MUON_EFF_SYS`; `MUON_EFF_STAT_LOWPT` and `MUON_EFF_SYS_LOWPT`). There are also  
 1176      isolation systematics (`MUON_ISO_STAT`, `MUON_ISO_SYS`) and track to vertex association systematics  
 1177      (`MUON_TTVA_STAT`, `MUON_TTVA_SYS`).

1178 5.4 MISSING TRANSVERSE ENERGY

1179 High precision performance of  $\vec{E}_T^{\text{miss}}$  is not so crucial to the 2-lepton analysis (though it is very im-  
1180 portant to the other channels), so the interested reader is referred to [26].  $\vec{E}_T^{\text{miss}}$  in ATLAS is the neg-  
1181 ative vectoral sum of physics objects (in this analysis just jets and leptons, though in principle also  
1182 including  $\tau$ 's and  $\gamma$ 's) and a so-called track based soft term (TST). The TST is comprised of valid  
1183 ID tracks not associated with any physics objects in an event. These tracks must be associated to an  
1184 event's primary vertex, have a  $p_T > 0.4$  GeV, and pass other quality requirements.

1185 The  $\vec{E}_T^{\text{miss}}$  systematic uncertainties relevant to this analysis are related to track based energy scale  
1186 and resolutions in both the soft term and in the jets and are: MET\_SoftTrk\_ResoPara, MET\_Soft-  
1187 Trk\_ResoPerp, MET\_SoftTrk\_ScaleDown, MET\_SoftTrk\_ScaleUp, MET\_JetTrk\_Scale-  
1188 Down , and MET\_JetTrk\_ScaleUp.

1189 5.5 JETS

1190 Unlike leptons, all analyses considered in this thesis are sensitive to factors regarding jet reconstruc-  
1191 tion and associated systematic uncertainties. A general discussion of jets precedes jet reconstruction  
1192 in ATLAS and associated systematics relevant to this thesis.

1193 5.5.1 JET ALGORITHMS

1194 The hadronic nature of jets makes jet reconstruction a lot more complicated than electron or photon  
1195 reconstruction, where a regular shower shape and track matching (or lack thereof in the case of the

1196 chargeless photon) provide a fairly straightforward and robust approach. The interested reader is

1197 referred to [70] for an excellent survey, from which this discussion is greatly abbreviated.

1198 Looking at an event like the one in Figure 5.1, unambiguous individual jets are particularly easy to

1199 identify, more or less popping out of the  $\eta - \phi$  plane plot, but this is not always the case.

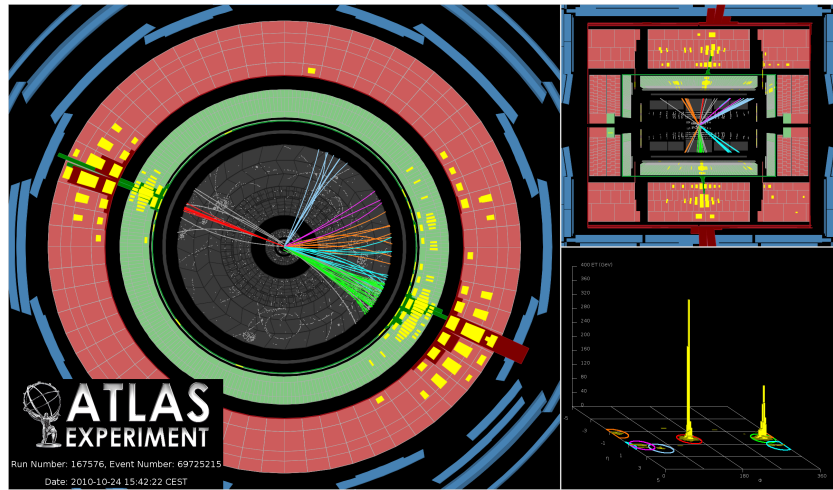


**Figure 5.1:** A clean ATLAS dijet event.

1200 Two general methods of turning particles/calorimeter towers into jets exist: cone-based and se-

1201 quential recombination. The general theme of the former is to find a hard (energetic) particle and

1202 draw a circle around it in the  $\eta - \phi$  plane in an intelligent manner, while the theme of the latter

1203 is to find some metric of distance between particles and then to cluster pairs based on this distance

1204 into jets in an intelligent way. Cone-based algorithms are simple (and therefore generally quite fast)

1205 but generally lack some properties of the sequentially recombined jets (though there are notable ex-

1206 ceptions like SISCone). Cone algorithm reconstructed jets are important for trigger level objects in

1207 ATLAS, though since no jet triggers are used in this analysis, they will not be discussed any further

1208 here.

1209 The general drawback of cone-based algorithms is that they are not infrared and collinear (IRC)  
1210 safe. That is, neither the emission of a soft (IR) quark or gluon during hadronization nor the collinear  
1211 splitting of hard particles during hadronization should not change the final jet collection in an event.  
1212 These are fairly common edge cases and can lead to certain pathologies in QCD calculations. In-  
1213frared and collinear safety are diagrammed schematically in Figures 5.2 (a) and (b), taken from [70].

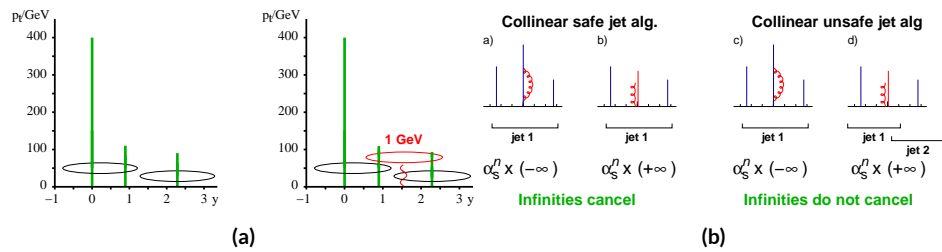


Figure 5.2: Infrared (a) and collinear (b) safety.

1214 Sequential recombination algorithms are generally safe from these effects, as these edge cases are  
1215 very “close” to each other by construction. A sequential recombination algorithm proceeds as fol-  
1216 lows

- 1217 1. Evaluate the set of distances  $d_{ij}$  (for pairs of objects) and  $d_{iB}$  (the “beam distance” for each  
1218 individual object)

$$d_{ij} = \min \left( p_{Ti}^{2p}, p_{Tj}^{2p} \right) \frac{\Delta R_{ij}^2}{R^2}, \quad d_{iB} = p_{Ti}^{2p} \quad (5.3)$$

- 1219 2. Find the minimum distance  
1220 3. If the minimum distance is:

- 1221 • A  $d_{ij}$ : cluster these objects together, and go to step 1  
1222 • A  $d_{iB}$ : call the  $i^{\text{th}}$  object a jet, remove it from the set of objects to be clustered, and go to  
1223 step 1

1224 4. Repeat until all objects are clustered into jets

1225 The choices one must make in sequential recombination are the size parameter  $R$ , akin to a cone  
1226 radius in cone-based algorithms, and the momentum power  $p$ . Common choices and their trade-offs  
1227 are:

- 1228 • +1: the  $k_t$  algorithm; favors the softer particles in an event, so the cluster sequence gives a his-  
1229 tory of hadronization, but jet shapes are irregular (i.e. not circular in the  $\eta - \phi$  plane)
- 1230 • 0: the Cambridge-Aachen algorithm: a pure distance metric; less substructure but jets tend to  
1231 be more circular
- 1232 • -1: the anti- $k_t$  algorithm: clustering begins with hardest particles in an event; regular, localized  
1233 jet shapes, but virtually no substructure in clustering history

1234 Jet reconstruction using all three algorithms on the same event, as well as SISCone, are shown in

1235 Figure 5.3.

1236 All three algorithms have uses for different applications in ATLAS, with anti- $k_t R = 0.4$  jets  
1237 being the default jet collection.<sup>†</sup> These are the jets used in this analysis.

1238 If the choice of jet algorithm seems a little arbitrary, it is. There is no one-size-fits-all jet collection  
1239 perfect for every application, and analyzers have to make these choices for themselves. One interest-  
1240 ing choice is the jet size parameter,  $R$ . A large  $R$  jet will contain more of the radiation coming from a  
1241 final state object, but its large size makes it susceptible to contamination from the underlying event  
1242 and pileup (as well as other analysis objects if  $R$  is sufficiently large or objects sufficiently boosted),  
1243 with small  $R$  jets having the opposite features.  $R = 0.4$  is a fairly middle-of-the-road choice. A natu-  
1244 ral question to ask is whether there needs to be just one jet collection in an analysis. Might there not

---

<sup>†</sup>The other collections find their primary uses in jet substructure techniques. For an example, cf. the discussion of jet trimming in Appendix B.

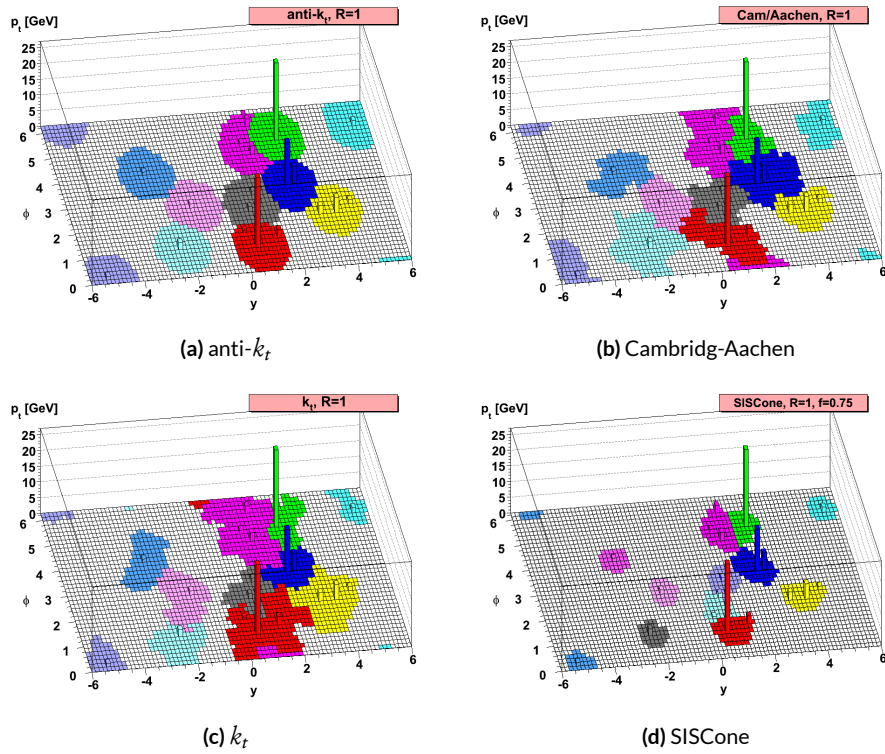


**Figure 5.3:** Different jet algorithms used on the same event. IC:[70]

1245 be more information to be gained from looking at more jet sizes or clusterings? Preliminary studies  
1246 point to this answer being yes and are addressed in Appendix B.

1247 5.5.2 STANDARD ATLAS HBB JETS

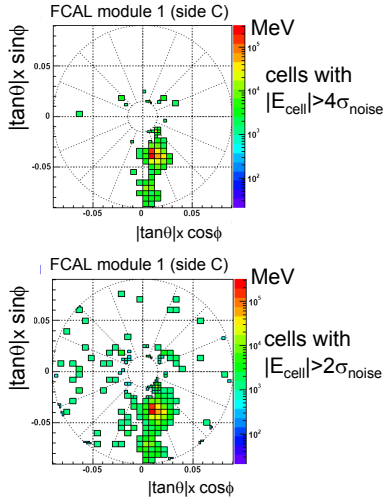
1248 There are a few considerations that arise with jets in physical detectors. The first is what type of ob-  
1249 ject to use as the stand in for “particles” since ATLAS measures energy deposits, not pions. The ap-  
1250 proach ATLAS has settled upon are calorimeter topological clusters (or CaloTopoClusters for short)  
1251 [58]. Unlike the sliding window algorithm used for electron clusters, CaloTopoClusters use a noise  
1252 significance based approach in the “4-2-0” algorithm. Each cell in the electromagnetic and hadronic  
1253 calorimeters (ECAL and HCAL, respectively) has associated with it a characteristic noise level ( $N$  in  
1254 Equation 2.6), with this noise level in each channel, it is possible to construct a “significance” for the  
1255 registered energy deposit in a given channel for a given event by dividing the measured value by its  
1256 characteristic noise. Groups of cells having a significance of 4 are taken as the centers of clusters in  
1257 the  $\eta - \phi$  plane. The second layer in a cluster includes all neighboring cells to the central layer with  
1258 significance of at least 2, and the final layer includes all the nearest neighbors to the second layer.  
1259 This is described in Figure 5.4 from [61].

1260 Once CaloTopoClusters have been formed and clustered into jets, they are calibrated using the  
1261 electromagnetic (EM) scale (the scale for clusters coming form EM showers). Further details may be  
1262 found in [16].

1263 Jets in this analysis fall into two categories, “signal” and “forward” jets, and are required to pass  
1264 certain quality requirements, described in Table 5.5. All jets must pass a series of jet cleaning require-

## Local Hadronic Calibration: Clusters

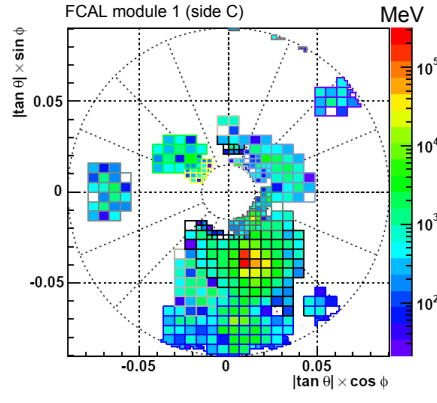
Sven Menke



□ Topological clustering

❖ 4,2,0 clusters in FCal

➢ jets with  $p_T > 50 \text{ GeV}$



3rd Hadronic Calibration Workshop, Milan, Italy, 26-27 April, 2007

M. Lefebvre, P. Loch

33

**Figure 5.4:** A description of the 4-2-0 clustering algorithm.

1265 ments using calorimeter level variables to eliminate jets coming from problematic calorimeter cells  
 1266 and certain backgrounds. Some signal jet candidates also make use of a Jet Vertex Tagger (JVT) that  
 1267 uses primary vertex and jet and track  $p_T$  information to decide whether certain soft jets are likely to  
 1268 have come from the the primary (hard scatter) vertex in an event or are to be considered pileup. Fur-  
 1269 ther details on JVT may be found in [24]. Jets are further corrected using standard CP tools and a  
 1270 dedicated PtReco correction, all outlined in Section 7.3 of [31].

1271 Overlap removal in this analysis is done according to the following precedence, taken from [31]  
 1272 with further steps only taken into account if an object survives previous steps:

- 1273 • tau-electron: If  $\Delta R(\tau, e) < 0.2$ , the  $\tau$  lepton is removed.
- 1274 • tau-muon: If  $\Delta R(\tau, \mu) < 0.2$ , the  $\tau$  lepton is removed, with the exception that if the  $\tau$  lepton

Jet Category	Selection Requirements
Forward Jets	jet cleaning $p_T > 30 \text{ GeV}$ $2.5 \leq  \eta  < 4.5$
Signal Jets	$p_T > 20 \text{ GeV}$ and $ \eta  < 2.5$ jet cleaning $\text{JVT} \geq 0.59$ if ( $p_T < 60 \text{ GeV}$ and $ \eta  < 2.4$ )

**Table 5.5:** `AntiKt4EMTopoJets` selection requirements. The jet cleaning is applied via the `JetCleaningTool`, that removes events in regions corresponding to hot calorimeter cells.

1275 has  $p_T > 50 \text{ GeV}$  and the muon is not a combined muon, then the  $\tau$  lepton is not removed.

1276 • electron-muon: If a combined muon shares an ID track with an electron, the electron is re-  
1277 moved.

1278 If a calo-tagged muon shares an ID track with an electron, the muon is removed.

1279 • electron-jet: If  $\Delta R(\text{jet}, e) < 0.2$  the jet is removed.

1280 For any surviving jets, if  $\Delta R(\text{jet}, e) < \min(0.4, 0.04 + 10 \text{ GeV}/p_T^e)$ , the electron is removed.

1281 • muon-jet If  $\Delta R(\text{jet}, \mu) < 0.2$  or the muon ID track is ghost associated to the jet, then the jet is

1282 removed if the jet has less than three associated tracks with  $p_T > 500 \text{ MeV}$  (`NumTrkPt500PVjet < 3`)

1283 or both of the following conditions are met: the  $p_T$  ratio of the muon and jet is larger than 0.5 ( $p_T^\mu/p_T^{\text{jet}} >$

1284 and the ratio of the muon  $p_T$  to the sum of  $p_T$  of tracks with  $p_T > 500 \text{ MeV}$  associated to the

1285 jet is larger than 0.7 ( $p_T^{\text{muon}}/\text{SumPtTrkPt500PVjet} > 0.7$ ).

1286 For any surviving jets, if  $\Delta R(\text{jet}, \mu) < \min(0.4, 0.04 + 10 \text{ GeV}/p_T^\mu)$ , the muon is removed.

1287 • tau-jet: If  $\Delta R(\tau, \text{jet}) < 0.2$ , the jet is removed.

1288 • electron-fat jet: If  $\Delta R(e, \text{fat jet}) < 1.2$ , the fat jet is removed.

1289 Jets are corrected using a muon-in-jet correction and then a kinematic fitter (Appendix D of [65])  
1290 for the 2-lepton case (PtReco correction for the 0- and 1- lepton case). The muon-in-jet correction  
1291 is designed for  $b$ -jets. Since the decay of a  $b$ -quark to a  $c$ -quark and finally to a light quark (these are  
1292 the multiple vertices for which JetFitter in Section 5.6.1 searches) involves two weak decays, there are  
1293 two  $W$ -bosons involved in the decay. Some of these will decay semileptonically, and, while electron  
1294 and  $\tau$  energy will be captured by the calorimeters, semileptonic  $\mu$ 's will only be registered in the MS,  
1295 which occurs in some 44% of all decays from a theoretical standpoint, which amounts to about 12%  
1296 in practice (due to track isolation requirements for the leptons). This value is about 1–2% for elec-  
1297 trons, which deposit their energy in the calorimeter and so require no correction; any jet with a valid  
1298 lepton associated to it is deemed semileptonic (all others are called hadronic). Any jet with muons  
1299 associated with it has the closest muon's 4-vector (in the  $\eta - \phi$  plane) added to it.

1300 The PtReco correction is a scale factor on the muon-in-jet corrected jet's 4-vector based on the  
1301 jet's  $p_T$  and whether the jet is hadronic or semileptonic. This correction factor is based on particle  
1302 level studies done on a TruthWZ sample. As the 0- and 1-lepton cases are not the focus of this thesis,  
1303 the interested reader is directed to Section 7.3 of [31].

1304 The kinematic fitter used in 2-lepton events with two or three jets takes as its input 12 fit parame-  
1305 ters,

- 1306 • energies of 2 electron or  $p_T$  of 2 muons
- 1307 • energies of 2  $b$ -jets
- 1308 •  $\eta, \phi$  of 2 leptons and 2 jets
- 1309 •  $p_X$  and  $p_Y$  of  $\ell\ell b\bar{b}$  system.

1310 •  $m_{\ell\ell}$

1311 and 3 constraints for the variation of these parameters,

1312 • parameters : Gaussian (b-jet energy : Transfer Functions (TF); these are denoted  $L$ , with an  
1313  $L_{truth}$  as a prior) (the  $\phi$  parameters)

1314 •  $p_x$  and  $p_y$  of  $\ell\ell b\bar{b}$  system : zero with a width of 9 GeV obtained from  $ZH$  signal MC.

1315 •  $m_{ll}$  : Breit-Wigner (BW) distribution of  $Z$  boson (final term, leptons denoted  $\Omega$ )

1316 which leads to test statistic from the usual likelihood formalism to be minimized in each event:

$$\begin{aligned} -2 \ln \mathcal{L} = & \sum_{i=j} \left( \frac{(\phi_i^n - \phi_i^0)^2}{\sigma_\phi^2} \right) + \left( \frac{(\Omega_l^n - \Omega_l^0)^2}{\sigma_\Omega^2} \right) - 2 \ln(L^j) - 2 \ln(L_{truth}^j) \\ & + \sum_{i=x,y} \frac{(\sum p_i^n - \sum P_i)^2}{\sigma_{\sum p_i}^2} + 2 \ln((m_{\ell\ell} - M_X^2)^2 + M_X^2 \Gamma^2) \end{aligned} \quad (5.4)$$

### 1317 5.5.3 JET SYSTEMATICS

1318 As with the electron systematics, jet energy scale (JES) and resolution (JER) are the two principal

1319 considerations for systematic uncertainties, with even more standard. JER, as with the electron en-

1320 ergy resolution, is a single systematic uncertainty, `JET_JER_SINGLE_NP`. There is also a single JVT

1321 efficiency `JET_JvtEfficiency` systematic uncertainty. There are 88 nominal JES systematics, and

1322 this analysis is sufficiently sensitive to these variations that a single systematic is grossly insufficient.

1323 Nevertheless, some simplification is possible, with the 75 of these nuisance parameters (mostly statis-

1324 tical uncertainties related to the  $Z$ +jet and  $\gamma$ +jet calibrations) being reduced to 8, and several explic-

1325 itly named nuisance parameter. These remaining named NP's are: 3 NP's related to the  $\eta$  intercali-

1326 bration used to extrapolate standard calibrations to other jet  $\eta$  regions, 4 NP's related to the flavor

1327 composition of principle background samples ( $W/Z$ +jets, top, and diboson), 4 pileup systematics, a  
1328 single NP for the  $b$ -jet energy scale, a high  $p_T$  jet energy scale systematic, and one for jets that punch  
1329 through the HCAL to leave energy deposits in the MS. These are listed explicitly in Table 5.7.

## 1330 5.6 FLAVOR TAGGING

1331 Given that the final state in this analysis involves pairs of jets originating from  $b$ -quarks, deploying  
1332 effective flavor tagging algorithms is imperative. While flavor tagging in general can be used to isolate  
1333 any flavor ( $b$ ,  $c$ , or light ( $u$ ,  $d$ ,  $s$ , or gluon-initiated jets)), this analysis exclusively looks for  $b$ -jets, so  
1334 this disucssion will focus on  $b$ 's. At truth-level in sumlation, this is fairly straightforward: one need  
1335 only look at the particles contained within a jet and seeing if any include a  $b$ -quark (sometimes a  $B$   
1336 hadron) in the decay chain.

### 1337 5.6.1 DIRECT TAGGING

1338 One of the most distintive features of  $b$ -jets is the presence of secondary vertices, as illustrated in Fig-  
1339 ure 5.5. While most partons created in particle collisions will hadronize promptly,  $b$ -quarks will first  
1340 hadronize into  $B$ -hadrons, which have lifetimes of about a picosecond. This small but finite lifetime  
1341 means that these particles will travel about half a millimeter or so before decaying into a jet in much  
1342 the usual way, and the tracks from this decay will point back to this displaced, secondary vertex.

1343 There are various secondary vertex algorithms used as inputs to the nominal  $b$ -tagging algorithm  
1344 [15], with three main types of algorithms used as inputs

- 1345 i. Track impact parameter based algorithms: L2PD (signed transverse only; more pileup ro-

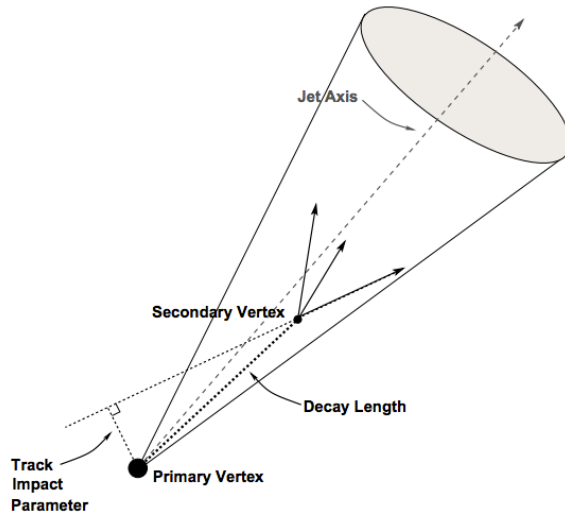


**Figure 5.5:** An illustration of a secondary vertex in a  $b$ -jet. Image credit: [54]

1346 bust),  $I_3PD$  (signed transverse and longitudinal)

- 1347 2. Inclusive secondary vertex reconstruction: SV1 (start with two track vertex pairs and con-  
1348 struct a secondary vertex)
- 1349 3. Multiple vertex reconstruction (decay chain): JetFitter ( $PV \rightarrow b \rightarrow c$  decay chain using Kalman  
1350 filter)

1351 All of these are combined into a boosted decision tree (BDT) and trained on five million  $t\bar{t}$  events  
1352 with an 90%/10% light/ $c$  jet background to form the MV2c10 algorithm, with 10 referring to the per-  
1353 centage of charm events in the training background. The 10% charm ratio was found to be a good  
1354 balance between increased charm rejection capability (as opposed to MV2c00, which has no charm  
1355 in the background training samples) and loss in light jet rejection (compared to MV2c20, which has  
1356 20% charm events in background training samples).

1357 ANALYSIS SPECIFIC CONCERNS AND SYSTEMATIC UNCERTAINTIES In addition to specifying  
 1358 the tagging algorithm, the working point efficiency must be specified. As with selection algorithms  
 1359 in general, there is a trade off between efficiency/recall (identifying all the  $b$ -jets, minimizing type  
 1360 II error) and purity/precision (making sure all jets positively identified are in fact  $b$ -jets, minimiz-  
 1361 ing type I error). Nominal efficiency working points have been calibrated by the flavor tagging CP  
 1362 group and are outlined in Table 5.6.

name	MV2c10 weight cut	$b$ -tagging efficiency [%]	$c$ RR	light RR
FixedCutBEff_60	0.9349	60.03	34.54	1538.78
FixedCutBEff_70	0.8244	69.97	12.17	381.32
FixedCutBEff_77	0.6459	76.97	6.21	134.34
FixedCutBEff_85	0.1758	84.95	3.10	33.53

**Table 5.6:**  $b$ -tagging working points available for MV2c10 for AntiKt4EMTopoJets. RR is the rejection rate (the inverse of efficiency).

1363 These values are aggregate figures, as both the jet's  $p_T$  and  $\eta$  are inputs to the MV2c10 discrim-  
 1364 inant. The working point chosen for this analysis is the 70% FixedCutBEff\_70 working point,  
 1365 with "fixed cut" referring to the fact that this particular usage of the MV2c10 BDT value is a simple  
 1366 cut value.

1367 Just as with the trigger and lepton identification efficiencies, flavor tagging efficiencies differ from  
 1368 their nominal values somewhat depending on what simulation or data sample is being used. To  
 1369 account for this difference, just as in the other cases, scale factors are applied to simulation event  
 1370 weights. It is through these event weights, as with the modeling systematics, that the flavor tagging  
 1371 systematic uncertainties are applied. Given that there are 24 input variables to MV2c10 and that fla-  
 1372 vor tagging is in general a very difficult problem, it is not surprising that, as with the JES, there are

1373 very many systematic uncertainties associated with flavor tagging. However, as with JES, the CP  
1374 group has compacted the full systematic set into a reduced set of 13 systematic uncertainties: 3 each  
1375 associated with  $c$  and light jets, 5 for  $b$ -jets (with the naming convention `FT_EFF_Eigen_(B|C|Light)N`),  
1376 one for the extrapolation of scale factors to different jet  $p_T$  regimes (`FT_EFF_Eigen_extrapolation`),  
1377 and one for the charm to bottom extrapolation (`FT_EFF_Eigen_extrapolation_from_charm`)  
1378 [80]. This schematic is a middle-of-the-road “Medium” set of systematics.

### 1379 5.6.2 TRUTH TAGGING

1380 Since imposing a 2  $b$ -tag requirement overwhelmingly rejects events dominated by  $c$ - and light jets,  
1381 statistics in such MC samples are very low. In order to circumvent this problem and restore full MC  
1382 statistics, the tag rate function, or “truth-tagging” procedure (in contrast to the standard or “direct  
1383 tagging” procedure) is applied, in which all events are kept but given a weight that preserves the over-  
1384 all shape and normalization of underlying distributions. Intuitively, this is done by giving events with  
1385 real  $b$ -jets in MC a much higher weight than events having only  $c$ - or light jets. Truth-tagging is ap-  
1386 plied to all samples when conducting MVA training in order to maximize statistics and reduce the  
1387 risk of overtraining. Truth-tagging is also used for data-MC comparison plots in 2-tag regions and  
1388 for  $V + cc$ ,  $V + c\ell$ ,  $V + \ell$ , and  $WW$  samples used in the final likelihood fit. A detailed description of  
1389 the truth-tagging process is provided below.

1390 Each jet in a given event has associated with it a  $b$ -tagging efficiency, denoted  $\varepsilon$ , that is a function  
1391 of its  $p_T$ ,  $\eta$ , and real flavor ( $b$ ,  $c$ , or light) from truth-level information in MC. Intuitively, this effi-  
1392 ciency can be thought of as the likelihood that a given jet will be  $b$ -tagged. Hence,  $b$ -jets have a much

1393 higher  $b$ -tagging efficiency than  $c$ -jets, which in turn have a higher  $b$ -tagging efficiency than light jets.

1394 We define a truth-tag weight for a given combination of tagged and untagged jets as the product of

1395 the efficiencies of the tagged jets times the product of the complement of the efficiencies of the un-

1396 tagged jets. For example, for an event with three jets, labeled 1, 2, and 3, if jets 1 and 2 are tagged, and

1397 jet 3 is untagged, the truth-tag weight associated with this combination is

$$\varepsilon_1 \varepsilon_2 (1 - \varepsilon_3) \quad (5.5)$$

1398 In order to obtain a truth-tag weight for an event, one takes the sum of the weights for each pos-

1399 sible tag combination. The current analysis requires that all events have exactly two  $b$ -tagged jets, so

1400 the truth-tag weight is the sum of all the weights of all possible pairs of tagged jets (events with fewer

1401 than two jets are discarded). Going back to the three jet example, one has the possible combinations:

1402 jets 1+2 as tagged and jet 3 as untagged; jets 1+3 as tagged and jet 2 as untagged; and finally jets 2+3 as

1403 tagged and jet 1 as untagged, which yields a total event weight of

$$w_{tot} = \varepsilon_1 \varepsilon_2 (1 - \varepsilon_3) + \varepsilon_1 \varepsilon_3 (1 - \varepsilon_2) + \varepsilon_2 \varepsilon_3 (1 - \varepsilon_1) \quad (5.6)$$

1404 For some applications (e.g. in order to use variables like pTB<sub>1</sub>, the  $p_T$  of the harder  $b$ -tagged jet in

1405 an event, in MVA training), it is necessary to choose a combination of jets in an event as “tagged.”

1406 This combination is chosen randomly, with the probability for a given combination to be chosen

1407 being proportional to its truth-tag weight. In the three jet example, the probability of tagging jets

1408 I+2 is:

$$\frac{\varepsilon_1 \varepsilon_2 (1 - \varepsilon_3)}{w_{tot}} = \frac{\varepsilon_1 \varepsilon_2 (1 - \varepsilon_3)}{\varepsilon_1 \varepsilon_2 (1 - \varepsilon_3) + \varepsilon_1 \varepsilon_3 (1 - \varepsilon_2) + \varepsilon_2 \varepsilon_3 (1 - \varepsilon_1)} \quad (5.7)$$

1409 Though not used in the current analysis, functionality exists for generic truth-tagging require-  
1410 ments (i.e. an arbitrary number of tags on an arbitrary number of jets) through the logical combina-  
1411 toric extension and for so-called “pseudo-continuous tagging,” where a  $b$ -tag score is generated for  
1412 each jet in a given event. Since a random combination of jets is set by hand to pass the  $b$ -tagging cuts  
1413 regardless of its  $b$ -tag score, a new score must be generated if this information is to be used in further  
1414 analysis. Under current settings, jets that are tagged are assigned a random  $b$ -tag score that is sampled  
1415 from the MV2c10 cumulative distribution above the 70% efficiency working point cut. All other  
1416 jets in the event are assigned a random  $b$ -tag score below the 70% working point cut. Since these dis-  
1417 tributions are discrete, the scores are not truly continuous (cf. example distributions in Figure 5.6),  
hence the “pseudo-continuous” nomenclature.

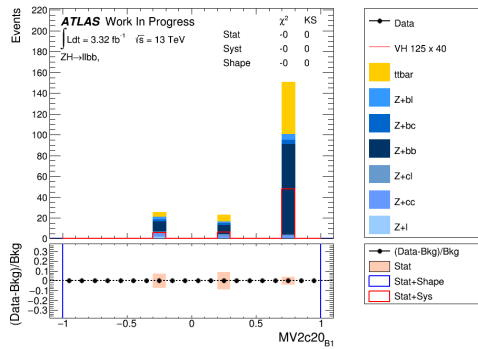


Figure 5.6: An example of a pseudo-continuous  $b$ -tagging distribution

1418

1419 A number of closure tests were performed on both the nominal and several systematics cases. In  
1420 the plots that follow, truth (solid) and direct (dashed) tagging distributions for  $m_{bb}$  and  $\Delta R(b_1, b_2)$

1421 in different  $p_T^V$  regimes for 2 lepton, 2 jet events. Agreement between the truth and direct tagging  
 1422 cases is generally very good, an example of which can be seen in Figure 5.7 for a signal  $\text{qqZIIH125}$   
 1423 sample, and the overall benefit of truth-tagging can be somewhat dramatically seen in the corre-  
 1424 sponding plots  $Z + \ell$  samples in Figure 5.8. At high  $p_T^V$  ( $p_T^V > 200$  GeV), however, in events with two  
 1425 real  $b$ -jets, there is a much greater likelihood that the  $b$ -jets will merge into a single jet, which render  
 1426 the naïve assumption that jets remain discrete invalid. While this does not appear to be a problem in  
 1427 most samples (cf.  $t\bar{t}$  in Figure 5.9), there is a mismodelling effect at low  $m_{bb}$  and low  $\Delta R(b_1, b_2)$  at  
 1428  $p_T^V > 200$  GeV for  $W/Z + bb$  samples where truth-tagging overestimates the number of events in  
 this merged regime, as can be seen in Figure 5.10

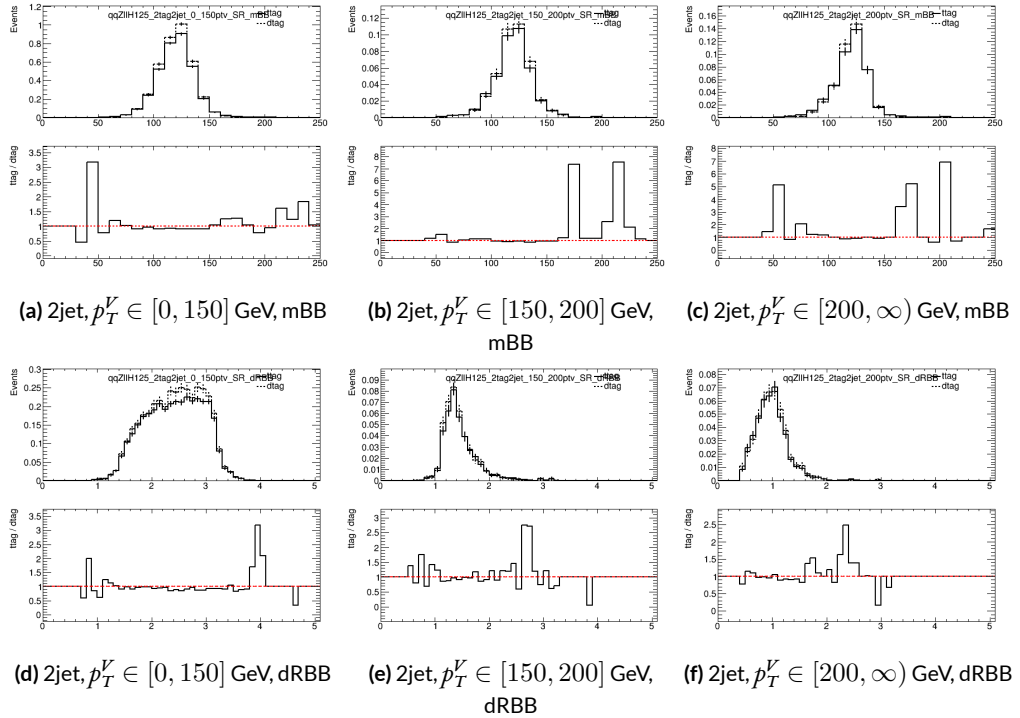
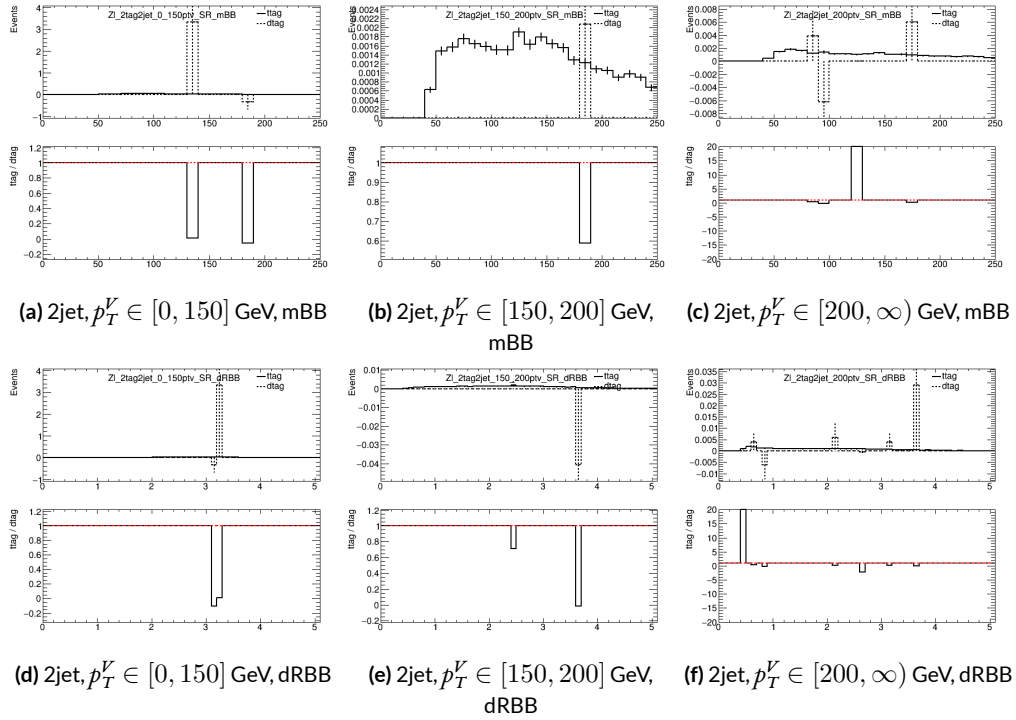
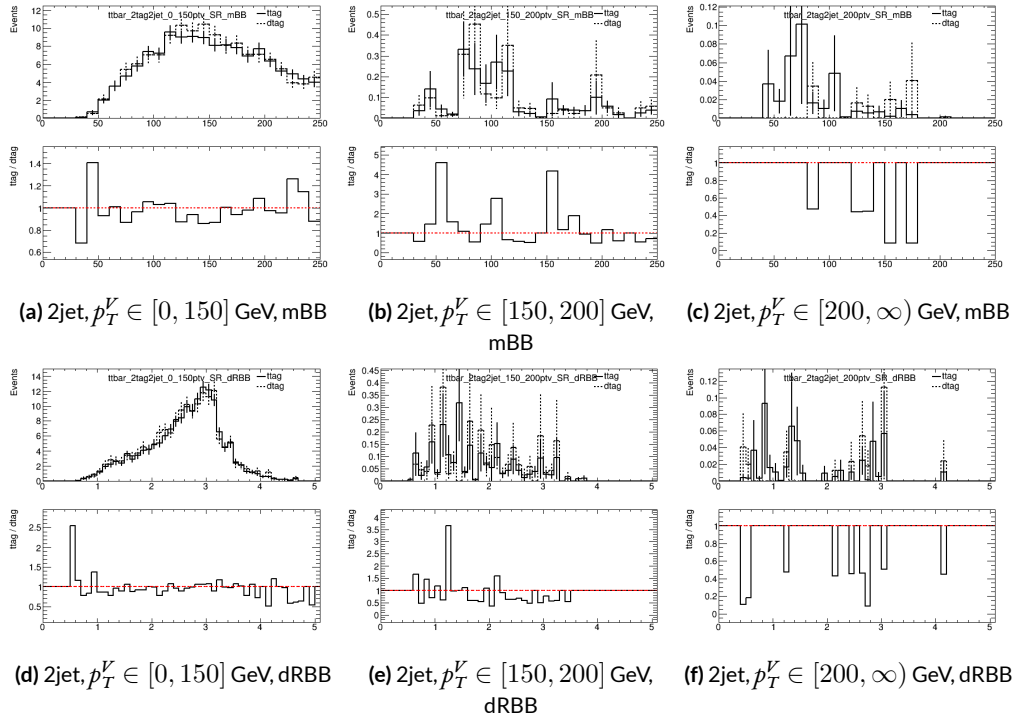


Figure 5.7: Truth-tagging closure tests for 2 lepton, 2 jet  $\text{qqZIIH125}$  samples in three different  $p_T^V$  regions.

1429



**Figure 5.8:** Truth-tagging closure tests for 2 lepton, 2 jet  $Z + \ell$  samples in three different  $p_T^V$  regions.



**Figure 5.9:** Truth-tagging closure tests for 2 lepton, 2 jet  $t\bar{t}$  samples in three different  $p_T^V$  regions.

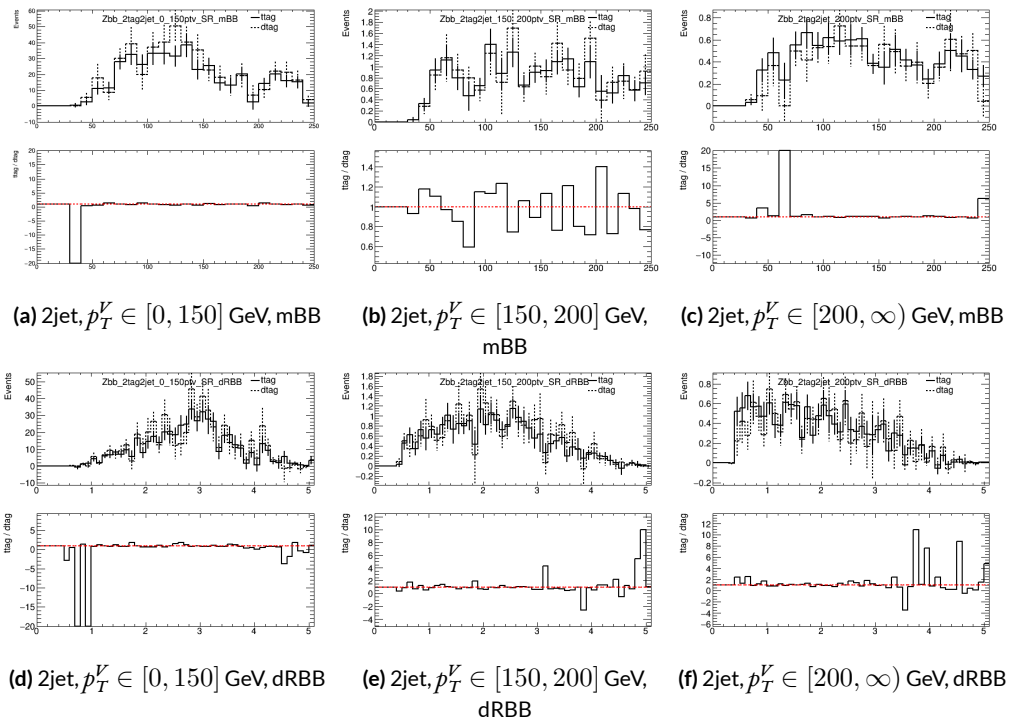


**Figure 5.10:** Truth-tagging closure tests for 2 lepton, 2 jet  $Z + bb$  samples in three different  $p_T^V$  regions.

1430 5.7 MISCELLANIA AND SYSTEMATICS SUMMARY

1431 A summary of all experimental systematics, taken from [65], may be found below. In addition to the  
1432 systematics discussed above, there are also two further systematics, on the total integrated luminosity  
1433 and on the event reweighting factor used to account for pileup, both included in Table 5.7.

1434 5.8 EVENT SELECTION AND ANALYSIS REGIONS

1435 With object and event reconstruction described, it is now time to address which events are actually  
1436 selected for use in analysis. This analysis focuses specifically on the 2-lepton channel of the fiducial  
1437 analysis, with the event selection and analysis region definitions being identical. Common to all  
1438 lepton channels in the fiducial analysis is the set of requirements on the jets in a given event. There  
1439 must be at least two central jets and exactly two signal jets that have been “*b*-tagged” according to the  
1440 MV2c10 algorithm [15], with at least one of these *b*-jets having  $p_T > 45$  GeV. For MVA training and  
1441 certain background samples, a process known as “truth-tagging” is applied instead of the standard  
1442 *b*-tagging to boost sample statistics and stabilize training/fits (cf. [65] Section 4.2 for details). After  
1443 event selection, the *muon-in-jet* and *PtReco* corrections, described in [31] 6.3.3-4, are applied to the  
1444 *b*-jets.

1445 In addition to the common selections, there are 2-lepton specific selections. All events are re-  
1446 quired to pass an un-prescaled single lepton trigger, a full list of which may be found in Tables 5 and  
1447 6 of [31] with the requirement that one of the two selected leptons in the event must have fired the  
1448 trigger. There must be 2 VH-loose leptons, and at least one of these must be a ZH-signal lepton (cf.

Systematic uncertainty	Short description	Reference
Luminosity	uncertainty on total integrated luminosity	Section 11.1 in Ref. [31]
Pileup Reweighting	uncertainty on pileup reweighting	Section 11.1 in Ref. [31]
	Electrons	
EL_EFF_Trigger_Total_1NPCOR_PLUS_UNCOR	trigger efficiency uncertainty	Section 11.2.2. in Ref. [31]
EL_EFF_Reco_Total_1NPCOR_PLUS_UNCOR	reconstruction efficiency uncertainty	Section 11.3.1. in Ref. [31]
EL_EFF_ID_Total_1NPCOR_PLUS_UNCOR	ID efficiency uncertainty	Section 11.3.1. in Ref. [31]
EL_EFF_Iso_Total_1NPCOR_PLUS_UNCOR	isolation efficiency uncertainty	Section 11.3.1. in Ref. [31]
EG_SCALE_ALL	energy scale uncertainty	Section 11.3.2. in Ref. [31]
EG_RESOLUTION_ALL	energy resolution uncertainty	Section 11.3.2. in Ref. [31]
	Muons	
MUON_EFF_TrigStatUncertainty	trigger efficiency uncertainty	Section 11.2.2. in Ref. [31]
MUON_EFF_TrigSystUncertainty	reconstruction and ID efficiency uncertainty for muons with $p_T > 15$ GeV	Section 11.4.1. in Ref. [31]
MUON_EFF_STAT	reconstruction and ID efficiency uncertainty for muons with $p_T < 15$ GeV	Section 11.4.1. in Ref. [31]
MUON_EFF_SYS	isolation efficiency uncertainty	Section 11.4.1. in [31]
MUON_EFF_STAT_LOWPT	track-to-vertex association efficiency uncertainty	Section 11.4.1. in Ref. [31]
MUON_EFF_SYST_LOWPT	momentum resolution uncertainty from inner detector	Section 11.4.2. in Ref. [31]
MUON_ISO_STAT	momentum resolution uncertainty from muon system	Section 11.4.2. in Ref. [31]
MUON_ISO_SYS	momentum scale uncertainty	Section 11.4.2. in Ref. [31]
MUON_TTVA_STAT	charge dependent momentum scale uncertainty	Section 11.4.2 in Ref. [31]
MUON_TTVA_SYS		
MUON_ID		
MUON_MS		
MUON_SCALE		
MUON_SAGITTA_RHO		
MUON_SAGITTA_RESBIAS		
	Jets	
JET_21NP_JET_EffectiveNP_1	energy scale uncertainty from the in situ analyses splits into 8 components	Section 11.5.1. in Ref. [31]
JET_21NP_JET_EffectiveNP_2	energy scale uncertainty from the in situ analyses splits into 8 components	Section 11.5.1. in Ref. [31]
JET_21NP_JET_EffectiveNP_3	energy scale uncertainty from the in situ analyses splits into 8 components	Section 11.5.1. in Ref. [31]
JET_21NP_JET_EffectiveNP_4	energy scale uncertainty from the in situ analyses splits into 8 components	Section 11.5.1. in Ref. [31]
JET_21NP_JET_EffectiveNP_5	energy scale uncertainty from the in situ analyses splits into 8 components	Section 11.5.1. in Ref. [31]
JET_21NP_JET_EffectiveNP_6	energy scale uncertainty from the in situ analyses splits into 8 components	Section 11.5.1. in Ref. [31]
JET_21NP_JET_EffectiveNP_7	energy scale uncertainty from the in situ analyses splits into 8 components	Section 11.5.1. in Ref. [31]
JET_21NP_JET_EffectiveNP_8restTerm	energy scale uncertainty from the in situ analyses splits into 8 components	Section 11.5.1. in Ref. [31]
JET_21NP_JET_EtaIntercalibration_Modeling	energy scale uncertainty on eta-intercalibration (modeling)	Section 11.5.1. in Ref. [31]
JET_21NP_JET_EtaIntercalibration_TotalStat	energy scale uncertainty on eta-intercalibrations (statistics/method)	Section 11.5.1. in Ref. [31]
JET_21NP_JET_EtaIntercalibration_NonClosure	energy scale uncertainty on eta-intercalibrations (non-closure)	Section 11.5.1. in Ref. [31]
JET_21NP_JET_Pileup_OffsetMu	energy scale uncertainty on pile-up (mu dependent)	Section 11.5.1. in Ref. [31]
JET_21NP_JET_Pileup_OffsetNPV	energy scale uncertainty on pile-up (NPV dependent)	Section 11.5.1. in Ref. [31]
JET_21NP_JET_Pileup_PtTerm	energy scale uncertainty on pile-up (pt term)	Section 11.5.1. in Ref. [31]
JET_21NP_JET_Pileup_RhoTopology	energy scale uncertainty on pile-up (density $\rho$ )	Section 11.5.1. in Ref. [31]
JET_21NP_JET_Flavor_Composition_Zjets	energy scale uncertainty on $Z+jets$ sample's flavour composition	Section 11.5.1. in Ref. [31]
JET_21NP_JET_Flavor_Composition_Wjets	energy scale uncertainty on $W+jets$ sample's flavour composition	Section 11.5.1. in Ref. [31]
JET_21NP_JET_Flavor_Composition_top	energy scale uncertainty on top sample's flavour composition	Section 11.5.1. in Ref. [31]
JET_21NP_JET_Flavor_Composition	energy scale uncertainty on $VV$ and $VH$ sample's flavour composition	Section 11.5.1. in Ref. [31]
JET_21NP_JET_Flavor_Response	energy scale uncertainty on samples' flavour response	Section 11.5.1. in Ref. [31]
JET_21NP_JET_BJES_Response	energy scale uncertainty on b-jets	Section 11.5.1. in Ref. [31]
JET_21NP_JET_PunchThrough_MC15	energy scale uncertainty for punch-through jets	Section 11.5.1. in Ref. [31]
JET_21NP_JET_SingleParticle_HighPt	energy scale uncertainty from the behaviour of high- $p_T$ jets	Section 11.5.1. in Ref. [31]
JET_JER_SINGLE_NP	energy resolution uncertainty	Section 11.5.1. in Ref. [31]
JET_JvtEfficiency	JVT efficiency uncertainty	Section 11.5.1. in Ref. [31]
FT_EFF_Eigen_B	$b$ -tagging efficiency uncertainties ("BTAG_MEDIUM"): 3 components for $b$ jets, 3 for $c$ jets and 5 for light jets	Section 11.7. in Ref. [31]
FT_EFF_Eigen_C		
FT_EFF_Eigen_L		
FT_EFF_Eigen_extrapolation	$b$ -tagging efficiency uncertainty on the extrapolation to high- $p_T$ jets	Section 11.7. in Ref. [31]
FT_EFF_Eigen_extrapolation_from_charm	$b$ -tagging efficiency uncertainty on tau jets	Section 11.7. in Ref. [31]
	MET	
METTrigStat	trigger efficiency uncertainty	Section 11.2.1. in Ref. [31]
METTrigTop/Z	track-based soft term related longitudinal resolution uncertainty	Section 11.6. in Ref. [31]
MET_SoftTrk_ResoPara	track-based soft term related transverse resolution uncertainty	Section 11.6. in Ref. [31]
MET_SoftTrk_ResoPerp	track-based soft term related longitudinal scale uncertainty	Section 11.6. in Ref. [31]
MET_SoftTrk_Scale	track MET scale uncertainty due to tracks in jets	Section 11.6. in Ref. [31]

**Table 5.7:** Summary of the experimental systematic uncertainties considered. Details on the individual systematic uncertainties can be found in the given Sections of Ref. [31].

<sup>1449</sup> Tables 5.3 and 5.4 for definitions). This lepton pair must have an invariant mass between 81 and 101  
<sup>1450</sup> GeV. In addition to the jet corrections described above, a kinematic fitter is applied to the leptons  
<sup>1451</sup> and two leading corrected jets in an event with three or fewer jets<sup>‡</sup> to take advantage of the fact that  
<sup>1452</sup> the 2-lepton final state is closed (cf. [20]); these objects are only used for MVA training/fit inputs.

<sup>1453</sup> In order to increase analysis sensitivity, the analysis is split into orthogonal regions based on the  
<sup>1454</sup> number of jets and the transverse momentum of the  $Z$  candidate (the vectoral sum of the lepton  
<sup>1455</sup> pair; this  $p_T$  is denoted  $p_T^V$ ): 2 and  $\geq 3$  jets;  $p_T^V$  in  $[75, 150), [150, \infty)$  GeV. In addition to the signal  
<sup>1456</sup> regions where the leptons are required to be the same flavor ( $e$  or  $\mu$ ), there are top  $e - \mu$  control  
<sup>1457</sup> regions used to constrain the top backgrounds.

<sup>1458</sup> All of these requirements are summarized in 5.8.

Category	Requirement
Trigger	un-prescaled, single lepton
Jets	$\geq 2$ central jets; 2 $b$ -tagged signal jets, harder jet with $p_T > 45$ GeV
Leptons	2 VH-loose leptons ( $\geq 1$ ZH-signal lepton); same (opp) flavor for SR (CR) $m_{\ell\ell} \in (81, 101)$ GeV
$p_T^V$ regions (GeV)	$[75, 150), [150, \infty)$

**Table 5.8:** Event selection requirements

<sup>1459</sup> It should be noted that the use of  $\geq 3$  jet events is a 2-lepton specific selection. These regions are  
<sup>1460</sup> exclusive 3 jet regions in the 0- and 1-lepton channels, but the fiducial 2-lepton analysis was found to  
<sup>1461</sup> see a  $\sim 4\%$  gain in sensitivity in studies by including  $\geq 4$  jet events [65].

---

<sup>‡</sup>The gain from using the kinematic fitter is found to be smeared out in events with higher jet multiplicities.

猛き者も遂には滅びぬ、  
偏に風の前の塵に同じ。

Heike monogatari

# 6

1462

1463

## Multivariate Analysis Configuration

1464 IN ORDER TO fully leverage the descriptive power of the 13 TeV dataset, this analysis makes use of a  
1465 multivariate (MVA) discriminant. Where traditionally event counts or single discriminating vari-  
1466 ables per region of phase space have been fed to fits, MVA discriminants seek to integrate additional  
1467 information not captured in the conventional phase space cuts plus dijet invariant mass distribu-

1468 tions. Formulating the MVA discriminant is an exercise in supervised learning to construct a binary  
1469 classifier, where one uses labeled “signal” and “background” MC events to optimize the parameters  
1470 of a statistical model—in this case a boosted decision tree (BDT) with some set of physically moti-  
1471 vated variables (or “factors”). The interested reader is directed to the standard references on machine  
1472 learning for further details. Sample and variable selection, including variables derived using the the  
1473 RestFrames and Lorentz Invariants concepts introduced in Sections 1.5–1.7, are discussed in Section  
1474 6.1; MVA training is treated in Section 6.2; and the data statistics only (no systematics) performance  
1475 of the three MVA discriminants is explored in Section 6.3.

## 1476 6.1 TRAINING SAMPLES AND VARIABLE SELECTION

1477 A subset of samples described in Chapter 3 is used for multivariate analysis training, with  $qqZH \rightarrow$   
1478  $\ell\ell b\bar{b}$  and  $ggZH \rightarrow \ell\ell b\bar{b}$  used as signal samples and  $Z+jets$ ,  $t\bar{t}$ , and  $VV$  used as background samples.  
1479 Truth-tagging (Section 5.6.2) is used on all samples in MVA training to improve training statistics  
1480 and stability. All figures quoted in this section scale distributions to a luminosity of  $36.1 \text{ fb}^{-1}$ .

### 1481 6.1.1 STANDARD VARIABLES

1482 The standard set of variables taken as a baseline is the same as used in the fiducial analysis. The vari-  
1483 ables fall into several main categories: energy/momenta scales of composite objects ( $m_{bb}$ ,  $m_{bbj}$ ,  
1484  $p_T^V$ ,  $m_{\ell\ell}$ ), angles ( $\Delta R(b_1, b_2)$ ,  $\Delta\phi(V, H)$ ,  $\Delta\eta(V, H)$ ), transverse momenta of the jets in the event  
1485 ( $p_T^{b_1}$ ,  $p_T^{b_2}$ ,  $p_T^{j_3}$ ), and  $E_T^{miss}$ . Input distributions for these variables in all the 2 ( $\geq 3$  jet) analysis signal  
1486 regions may be found in Figure 6.1 (6.2). The “kf” at the end of variable names denotes that these

are derived using 4-vectors that are the result of the kinematic fitter. The distributions in the figure

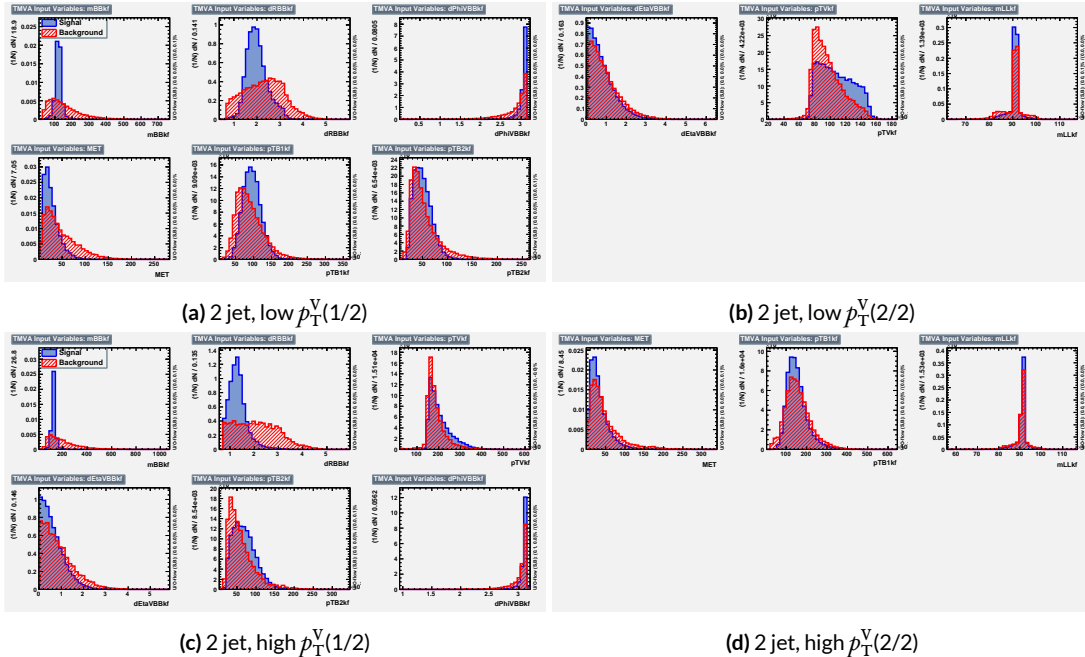


**Figure 6.1:** Input variables in 2 jet signal regions for the standard variable set. Signal distributions are in red, and background distributions are in blue.

1487

1488 are used as inputs for one of the two k-folded final discriminants, and the order of the distributions  
 1489 is the hyperparameter optimized order for feeding into the BDT; what precisely this means will be  
 1490 discussed in following sections. While variables in the analysis regions are generally similar, there are  
 1491 some notable exceptions.  $p_T^V$  and the correlated  $\Delta R(b_1, b_2)$  have different shapes, by construction  
 1492 for the former and by correlation for the latter, at low and high  $p_T^V$ . \* The  $\geq 3$  jet regions also have  
 1493 variables that are not applicable to the 2 jet regions; the inclusion of  $m_{BBJ}$  (the invariant mass of the  
 1494 two  $b$ -jets and leading untagged jet) in particular is of note and suggests a potential avenue forward

---

\*Recall that higher  $p_T^V$  means, in a balanced final state like  $ZH \rightarrow \ell\ell b\bar{b}$ , the  $b$ -jet pair will have higher  $p_T$  and hence be more collimated (lower  $\Delta R(b_1, b_2)$ ); this is not necessarily the case for background events, as the distributions show.

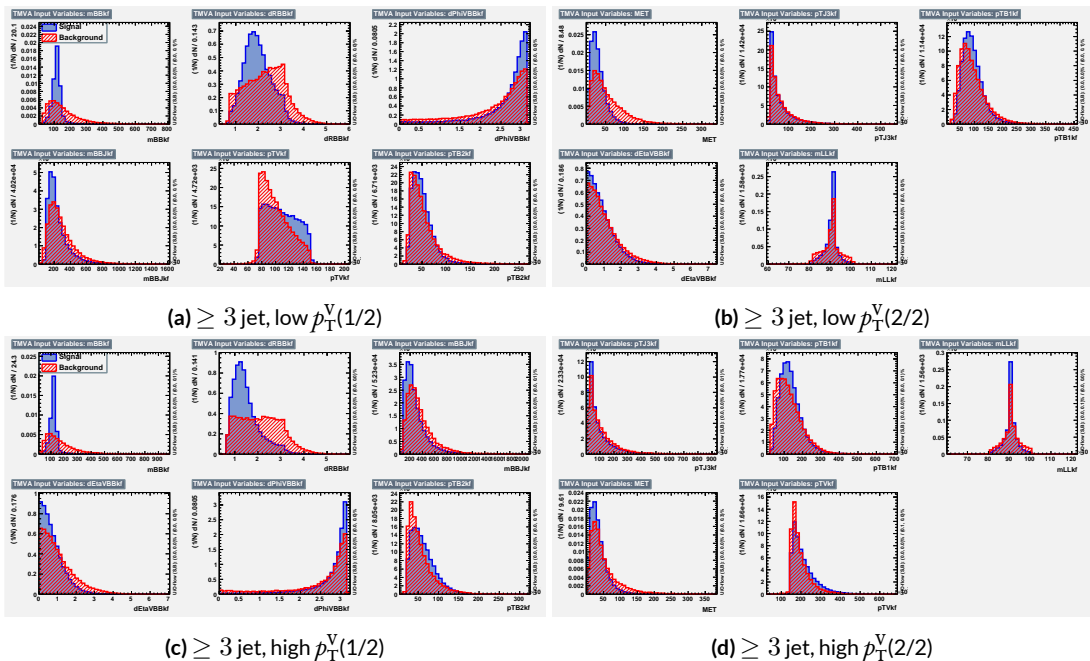


**Figure 6.2:** Input variables in  $\geq 3$  jet signal regions for the standard variable set. Signal distributions are in red, and background distributions are in blue.

1495 for refinements of the non-standard variables.

1496 Looking at the correlation matrices for the standard variables in Figure 6.3, it is easy to see that

there are large number of non-trivial correlations

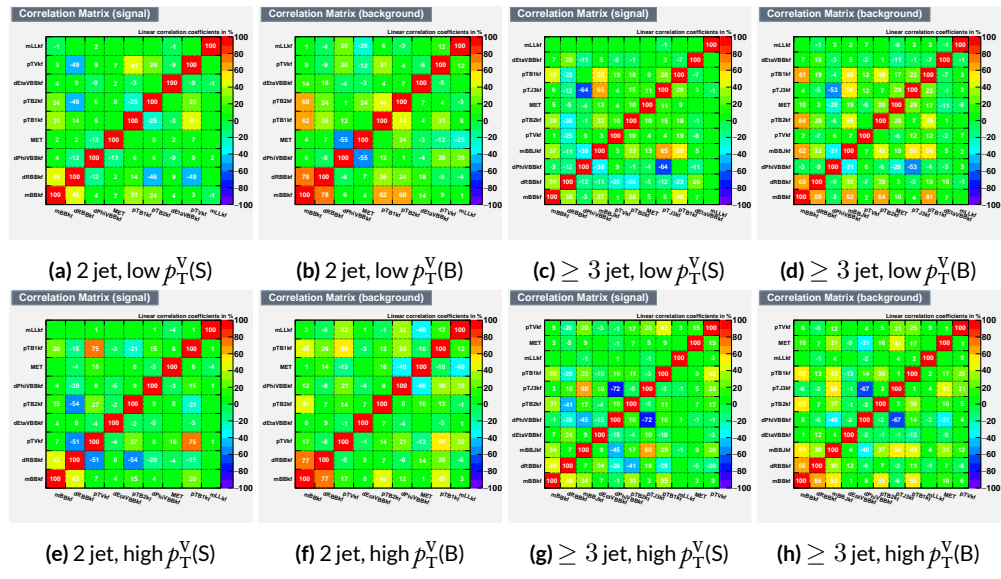


**Figure 6.3:** Signal and background variable correlations for the standard variable set.

1497

1498 6.1.2 LORENTZ INVARIANTS

1499 In choosing the set of variables used for a set of Lorentz Invariants based discriminants, we decided  
 1500 to use S. Hagebeck's set from [53] and related studies. Distributions of these variables in the same  
 arrangement as with the standard variables may be seen in Figures 6.4 and 6.5. One thing to note

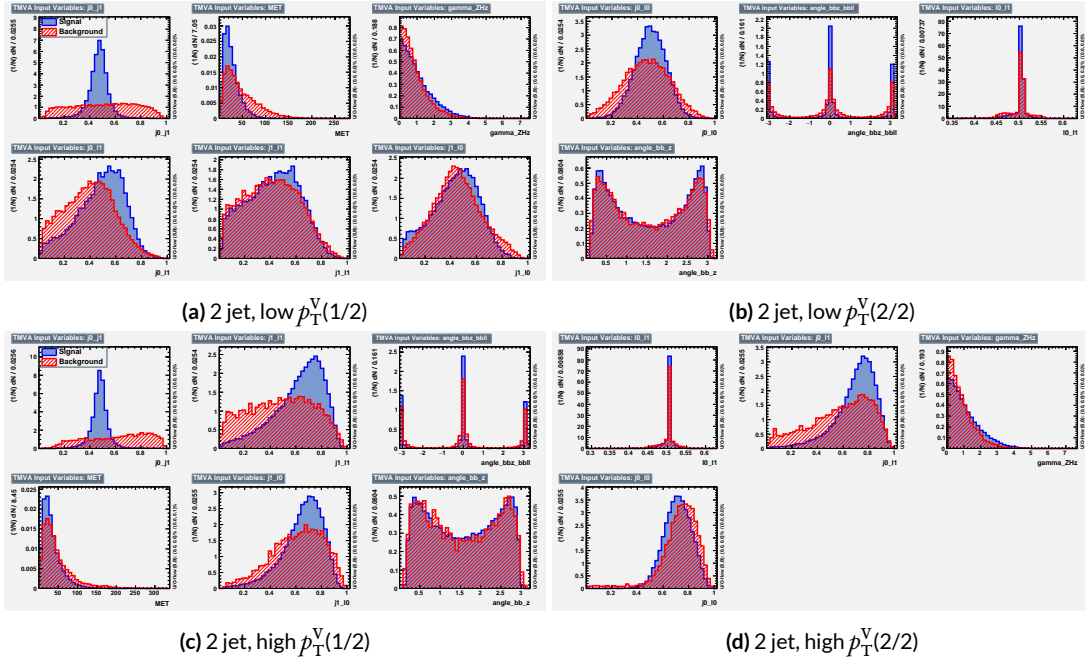
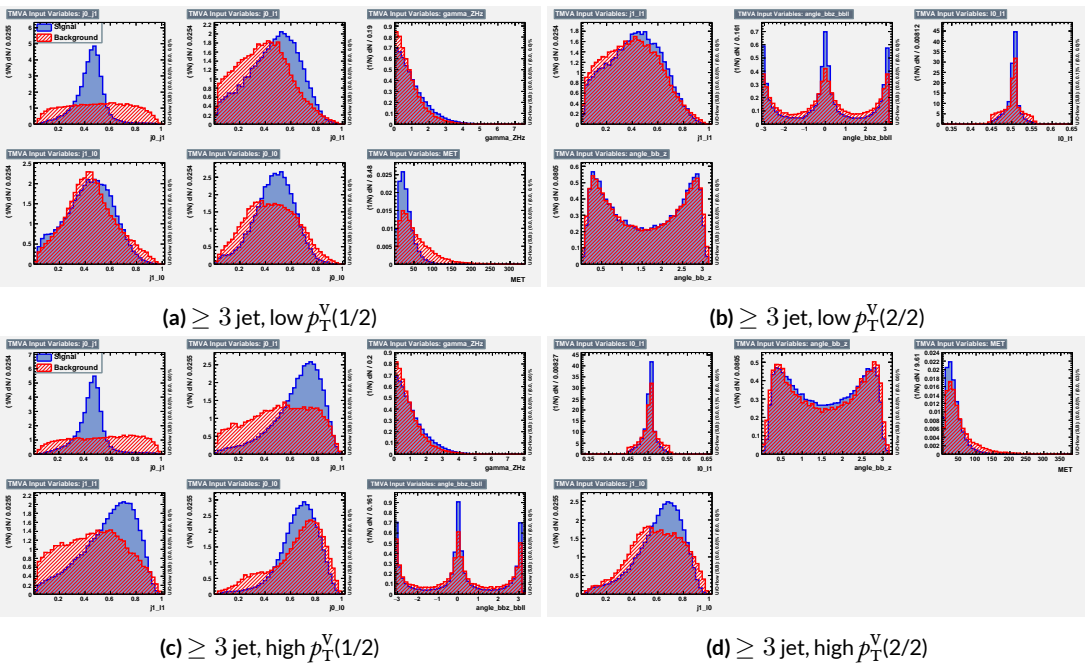


Figure 6.4: Input variables in 2 jet signal regions for the LI variable set. Signal distributions are in red, and background distributions are in blue.

1501

1502 about the variable set chosen here is that  $\vec{E}_T^{\text{miss}}$  has been added to the standard LI set. Since the LI  
 1503 construction assumes that this quantity is zero, there is no obvious way to include it. Nevertheless,  
 1504 as the correlation matrices for the LI variables show in Figure 6.6, there is actually very little correla-  
 1505 tion between  $\vec{E}_T^{\text{miss}}$  and the other variables (with this being slightly less the case for the background  
 1506 correlations, as to be expected since  $t\bar{t}$ , a principal background, is  $\vec{E}_T^{\text{miss}}$ -rich). Hence, if including



**Figure 6.5:** Input variables in  $\geq 3$  jet signal regions for the LI variable set. Signal distributions are in red, and background distributions are in blue.

1507  $\vec{E}_T^{\text{miss}}$  violates the spirit somewhat of the LI variables, it does not break terribly much with the aim of having a more orthogonal set.

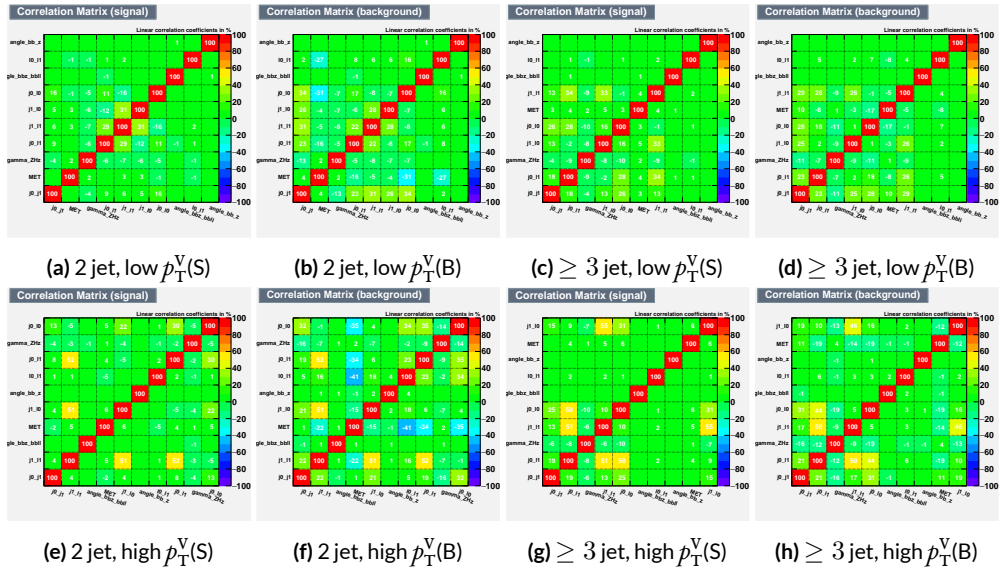


Figure 6.6: Signal and background variable correlations for the LI variable set.

1509 6.1.3 RESTFRAMES VARIABLES

1510 There is no precedent for using the RestFrames variables in the  $ZH \rightarrow \ell\ell b\bar{b}$  analysis, so a subset  
1511 of possible RF variables had to be selected as the basis of a discriminant. The masses and cosines of  
1512 boost angles from parent frames for the CM,  $Z$ , and  $H$  frames gives six variables, and it was decided  
1513 that it would be good to match the LI in terms of variable number and treatment (i.e. no special  
1514 treatment of the third jet), which leaves four more variables. In addition to the cosines, there are  
1515 also the  $\Delta\phi$  angles. Furthermore, there are the event-by-event scaled momentum ratios, both lon-  
1516 gitudinal and transverse. There is also both a  $\Delta\phi$  and an CM-scaled ratio for the  $\vec{E}_T^{\text{miss}}$ . All of these  
1517 variables were included in a ranking using slightly different training settings as the main hyperpa-  
1518 rameter optimization variable ranking described below. The goal of this study was not to develop a  
1519 discriminant, as the number of variables is too high, but rather to see which ones are generally use-  
1520 ful. Table 6.1 shows the results of this study. Percent gains (losses) at each step by adding the variable  
1521 with biggest gain (smallest loss) are shown in green (red). The final row shows an aggregate rank-  
1522 ing, calculated simply by adding up a variables ranks in all bins and ordering the variables smallest  
1523 to greatest. This simple aggregation does not take into account which regions are potentially more  
1524 sensitive and so where taken simply to give an idea of how variables generally performed. With this  
1525 in mind, the RF variables were chosen to be the masses  $M_{CM}$ ,  $M_H$ , and  $M_Z$ , the angles  $\cos CM$ ,  $\cosh$ ,  
1526  $\cos Z$ ,  $\cos \phi CMH$ , and the ratios  $R_{pt}$ ,  $R_{pz}$ , and  $R_{met}$ . Their distributions may be seen in Figures 6.7  
1527 and 6.8.

1528 Correlations for the chosen RF variables are shown in Figure 6.9. These correlations are much

Region	Variable Chain
2jet pTVbin1	Rpt (65.8%), Rpz (29.0%), cosZ (11.4%), MZ (-1.75%), dphiCMH (7.26%), cosCM (3.95%), cosH (0.142%), MCM (2.18%), dphiCMZ (-2.3%), dphiCMMet (-0.236%), dphiLABCM (0.404%), Rmet (-4.04%)
3jet pTVbin1	Rpt (50.8%), Rpz (15.6%), MZ (14.8%), cosZ (3.08%), MCM (3.79%), dphiCMH (3.24%), cosH (0.755%), dphiCMMet (1.04%), Rmet (-1.03%), cosCM (5.31%), dphiCMZ (-1.27%), dphiLABCM (-2.88%), pTJ3 (-1.27%)
2jet pTVbin2	Rpt (52.0%), Rpz (13.8%), cosZ (16.9%), cosH (6.49%), MCM (1.71%), cosCM (6.21%), Rmet (4.25%), dphiCMMet (-1.53%), dphiLABCM (-0.757%), dphiCMH (0.213%), MZ (-0.788%), dphiCMZ (-2.39%)
3jet pTVbin2	Rpt (31.5%), Rpz (21.6%), cosH (8.97%), cosZ (1.42%), cosCM (11.3%), dphiCMZ (-2.84%), MCM (8.17%), dphiCMH (-0.841%), dphiLABCM (-0.00318%), dphiCMMet (-2.6%), pTJ3 (-3.21%), MZ (-1.8%), Rmet (-6.29%)
Aggregate	Rpt (o,o,o,o), Rpz (i,i,i,i), cosZ (2,3,2,3), cosH (6,6,3,2), MCM (7,4,4,6), MZ (3,2,10,11), dphiCMH (4,5,9,7), cosCM (5,9,5,4), dphiCMMet (9,7,7,9), dphiCMZ (8,10,11,5), Rmet (11,8,6,12), dphiLABCM (10,11,8,8)

**Table 6.1:** Full RF variable ranking study summary. Green (red) percentages represent gains (losses) in a validation significance at each step.

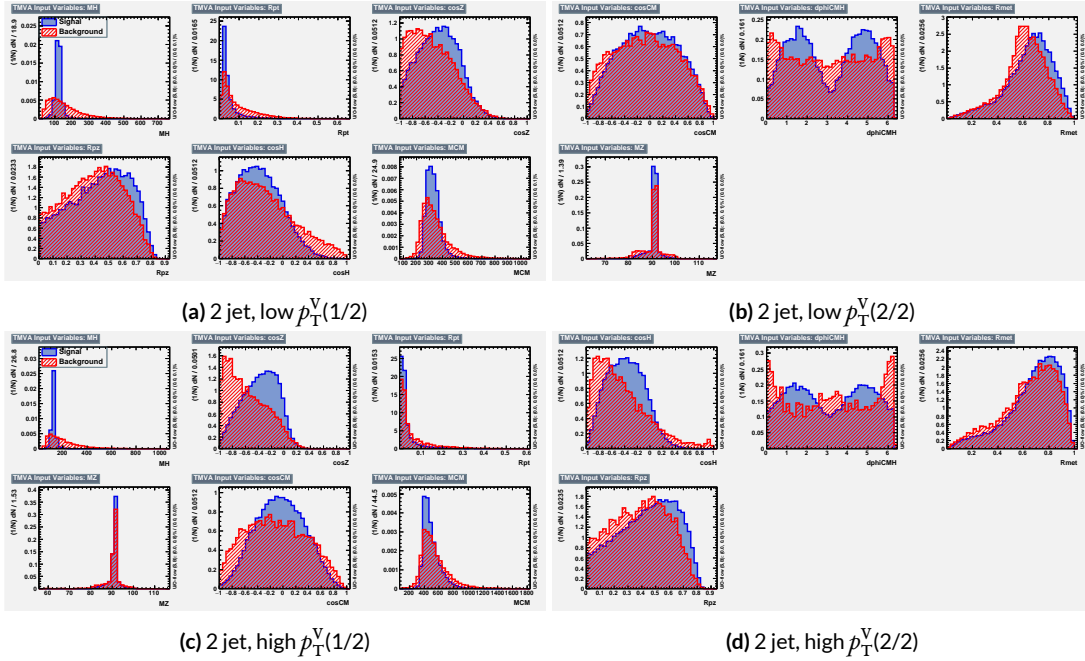


**Figure 6.7:** Input variables in 2 jet signal regions for the RF variable set. Signal distributions are in red, and background distributions are in blue.

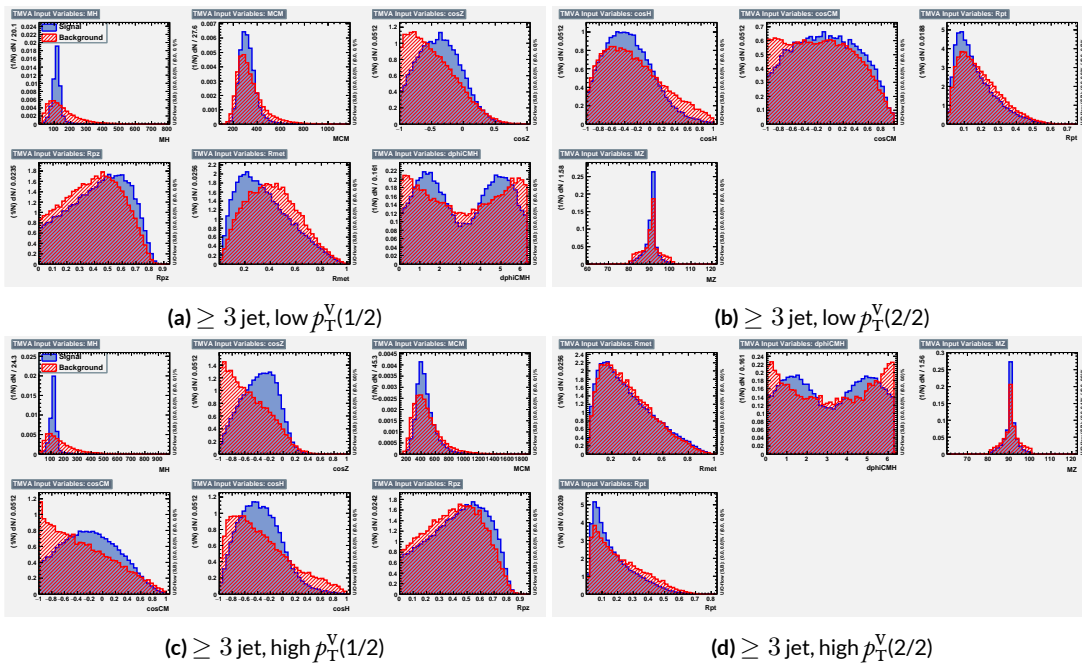


**Figure 6.8:** Input variables in  $\geq 3$  jet signal regions for the RF variable set. Signal distributions are in red, and background distributions are in blue.

1529 lower than for the standard case but still slightly higher than for the LI case. Notably, many strong  
 1530 correlations that exist for signal events do not exist in background events and vice versa, so what is  
 1531 lost in orthogonality may very well be recuperated in greater separation<sup>†</sup>. Given the generally better  
 1532 performance of the RF sets, as we shall see in following sections and chapters, this slight tradeoff is  
 1533 likely an aesthetic one, with the main benefits of a more orthogonal basis likely realized at this level  
 1534 of correlation.

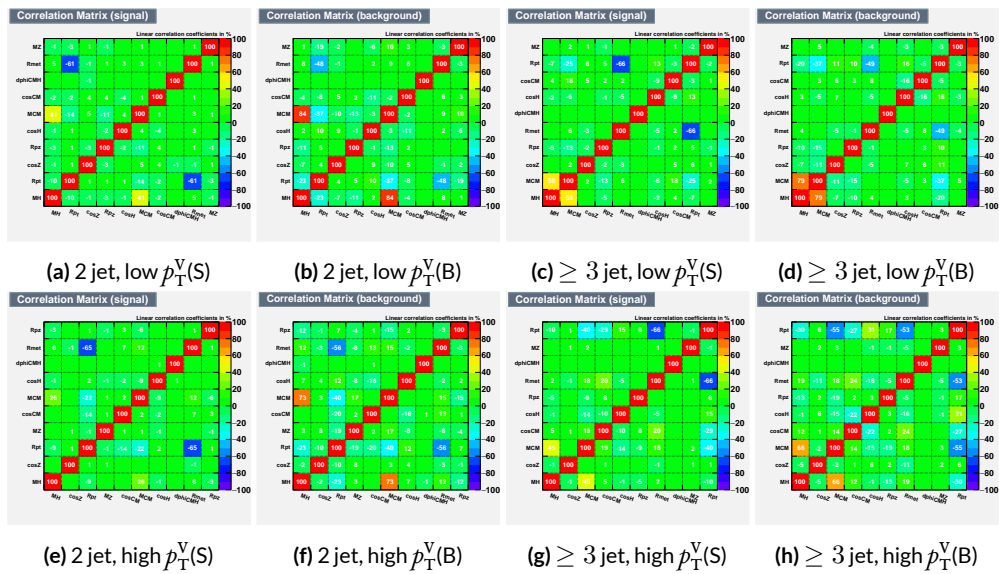


Figure 6.9: Signal and background variable correlations for the RF variable set.

1535 A summary of the variables used in the three cases is given in 6.2.

---

<sup>†</sup>It is very hard to say for certain whether this is the case for MVA discriminants, and such dedicated studies might make worthwhile future studies.

Variable Set	Variables
Standard	mBB, mLL, (mBBJ), pTV, pTB1, pTB2, (pTJ3), dRBB, dPhiVBB, dEtaVBB, MET 9(11) vars
Lorentz Invariants	j0_j1, j0_l1, l0_l1, j1_l1, j0_l0, j1_l0, gamma_ZHz, angle_bbz_bbll angle_bb_z, MET 10 vars
RestFrames	MH, MCM, MZ, cosH, cosCM, cosZ, Rpz, Rpt, dphiCMH, Rmet 10 vars

**Table 6.2:** Variables used in MVA training. Variables in parentheses are only used in the  $\geq 3$  jet regions.

## 1536 6.2 MVA TRAINING

1537 With variables chosen, the MVA discriminants must be trained and optimized. MVA training and  
 1538 hyperparameter optimization (in this case, just the order in which variables are fed into the MVA) is  
 1539 conducted using the “holdout” method. In this scheme, events are divided into three equal portions  
 1540 (in this case using `EventNumber%3`), with the first third (the “training” set) being used for the initial  
 1541 training, the second third (the “validation” set) being used for hyperparameter optimization, and  
 1542 the final third (the “testing” set) used to evaluate the performance of the final discriminants in each  
 1543 analysis region.

1544 The MVA discriminant used is a boosted decision tree (BDT). Training is done in TMVA using  
 1545 the training settings of the fiducial analysis [65]<sup>‡</sup>. For the purposes of hyperparameterization and  
 1546 testing, transformation D with  $z_s = z_b = 10$  is applied to the BDT distributions, and the cumula-  
 1547 tive sum of the significance  $S/\sqrt{S + B}$  in each bin is calculated for each pair of distributions.

1548 Transformation D is a histogram transformation, developed during the Run 1 SM  $VH(b\bar{b})$  search,

---

<sup>‡</sup>Namely, !H:!V:BoostType=AdaBoost:AdaBoostBeta=0.15:SeparationType=GiniIndex:-PruneMethod=NoPruning:NTrees=200:MaxDepth=4:nCuts=100:nEventsMin=5%

<sub>1549</sub> designed to reduce the number of bins in final BDT distributions and thereby mitigate the effect of  
<sub>1550</sub> statistical fluctuations in data while also maintaining sensitivity. Such an arbitrary transformation  
<sub>1551</sub> may be expressed as:

$$Z(I[k, l]) = Z(z_s, n_s(I[k, l]), N_s, z_b, n_b(I[k, l]), N_b) \quad (6.1)$$

<sub>1552</sub> where

- <sub>1553</sub> •  $I[k, l]$  is an interval of the histograms, containing the bins between bin  $k$  and bin  $l$ ;
- <sub>1554</sub> •  $N_s$  is the total number of signal events in the histogram;
- <sub>1555</sub> •  $N_b$  is the total number of background events in the histogram;
- <sub>1556</sub> •  $n_s(I[k, l])$  is the total number of signal events in the interval  $I[k, l]$ ;
- <sub>1557</sub> •  $n_b(I[k, l])$  is the total number of background events in the interval  $I[k, l]$ ;
- <sub>1558</sub> •  $z_s$  and  $z_b$  are parameters used to tune the algorithm.

<sub>1559</sub> Transformation D uses:

$$Z = z_s \frac{n_s}{N_s} + z_b \frac{n_b}{N_b} \quad (6.2)$$

<sub>1560</sub> Rebinning occurs as follow:

- <sub>1561</sub> 1. Begin with the highest valued bin in the original pair of distributions. Call this the “last” bin  
<sub>1562</sub> and use it as  $l$ , and have  $k$  be this bin as well.
- <sub>1563</sub> 2. Calculate  $Z(I[k, l])$
- <sub>1564</sub> 3. If  $Z \leq 1$ , set  $k \rightarrow k - 1$  and return to step 2. If not, rebin bins  $k-l$  into a single bin and name  
<sub>1565</sub>  $k - 1$  the new “last” bin  $l$ .
- <sub>1566</sub> 4. Continue until all bins have been iterated through; if  $Z \leq 1$  for any remaining  $n$  of the  
<sub>1567</sub> lowest-valued bins (as is often the case), simply rebin these as a single bin.

Variable ranking is done iteratively (greedily) in each analysis region. In each set, the validation significance of a BDT using an initial subset of variables is calculated ( $dRBB$  and  $mBB$  for the standard set;  $j0\_j1$  for the LI set; and  $MH$  for the RF set). Each of the remaining unranked variables are then added separately, one at a time, to the BDT. The variable yielding the highest validation significance is then added to the set list of ranked variables and removed from the list of unranked variables. This process is repeated until no variables remain. These rankings are shown in Figures 6.10–6.12. Rankings tend to be fairly stable.

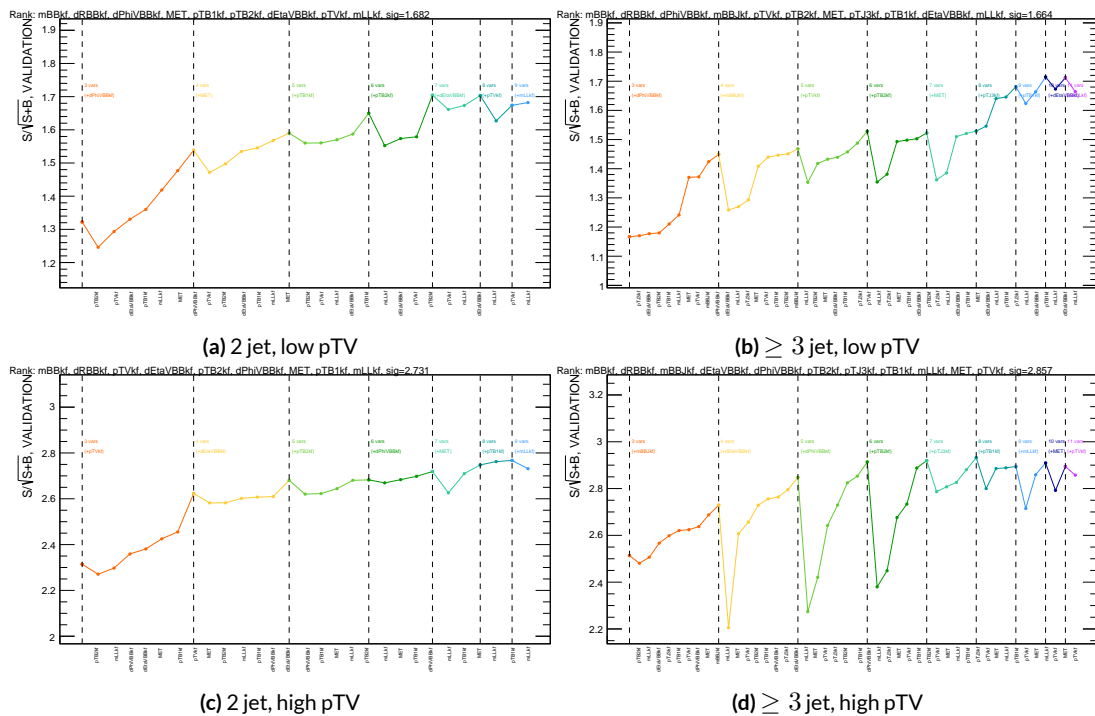


**Figure 6.10:** Rankings for the standard variable set.

Once variables have been ranked, the BDT may be used both to evaluate performance in a simplified analysis scenario in the absence of systematic uncertainties (described below in Section 6.3) and

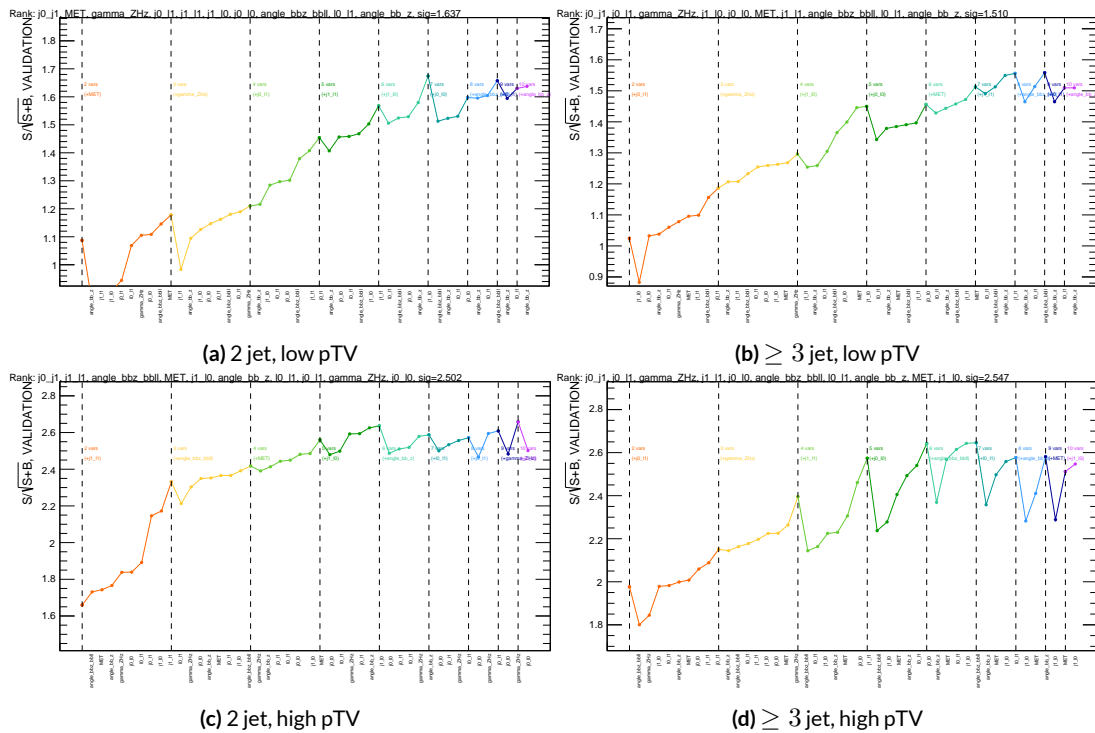
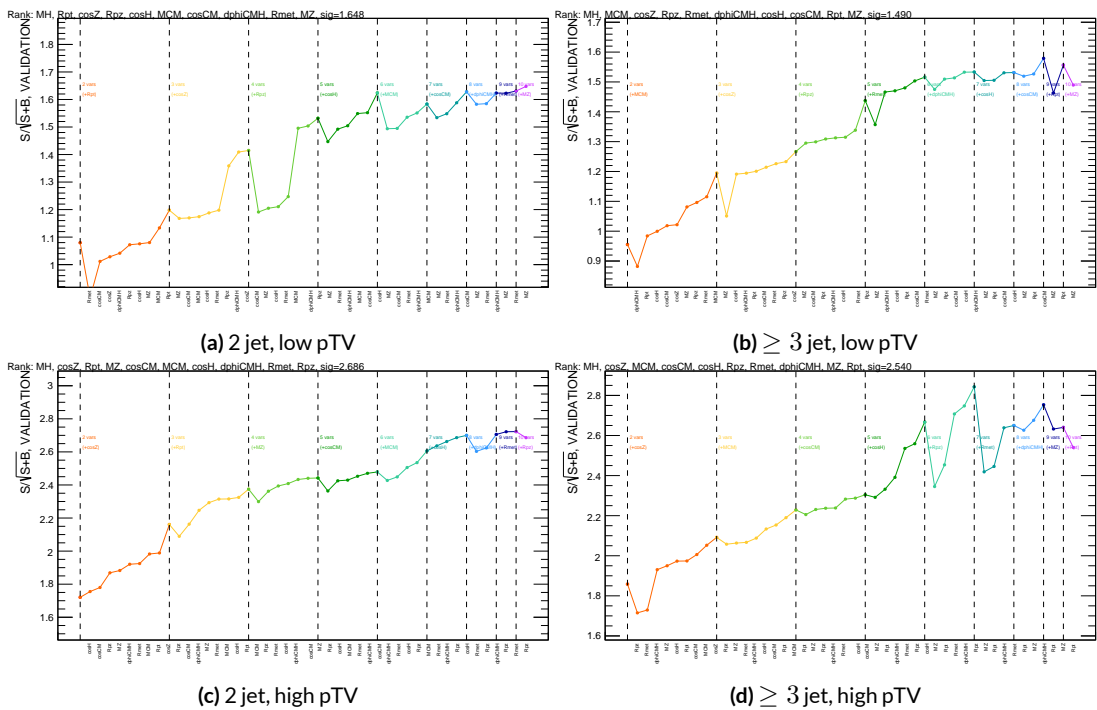


Figure 6.11: Rankings for the L1 variable set.



**Figure 6.12:** Rankings for the RF variable set.

1577 to create xml files for the production of fit inputs for an analysis including systematics. Following  
1578 the approach taken in the fiducial analysis, BDT discriminants using two “k-folds” are produced to  
1579 prevent overtraining, since the samples used for training are the same as those used to produce in-  
1580 puts for the full profile likelihood fit. In this scheme, a BDT trained on events with an even (odd)  
1581 `EventNumber` are used to evaluate events with an odd (even) `EventNumber`.

### 1582 6.3 STATISTICS ONLY BDT PERFORMANCE

1583 As described above, cumulative significances can be extracted from pairs of signal and background  
1584 BDT output distributions in a given region. In order to evaluate performance of variable sets in the  
1585 absence of systematic uncertainties, such pairs can be constructed by evaluating BDT score on the  
1586 testing set of events using the optimal variable rankings in each region. We show two versions of  
1587 each testing distribution for each variable set in each signal region in Figures 6.13–6.15. The training  
1588 distribution is always shown as points. The plots with block histograms with numbers of bins that  
1589 match (do not match) the training distribution do not (do) have transformation D applied. Trans-  
1590 formation D histograms are included to show the distributions actually used for significance evalu-  
1591 ation, while the untransformed histograms are included to illustrate that the level of overtraining is  
1592 not too terrible<sup>§</sup>. For better comparison of the distributions, all histograms have been scaled to have  
1593 the same normalization.

1594 As can be seen in the summary of cumulative significances for each of these analysis regions and  
1595 variable sets in Figure 6.16, the performance of each of the variable sets is quite similar. The standard

---

<sup>§</sup>The raw distributions include a K-S test statistic for signal (background) distributions.

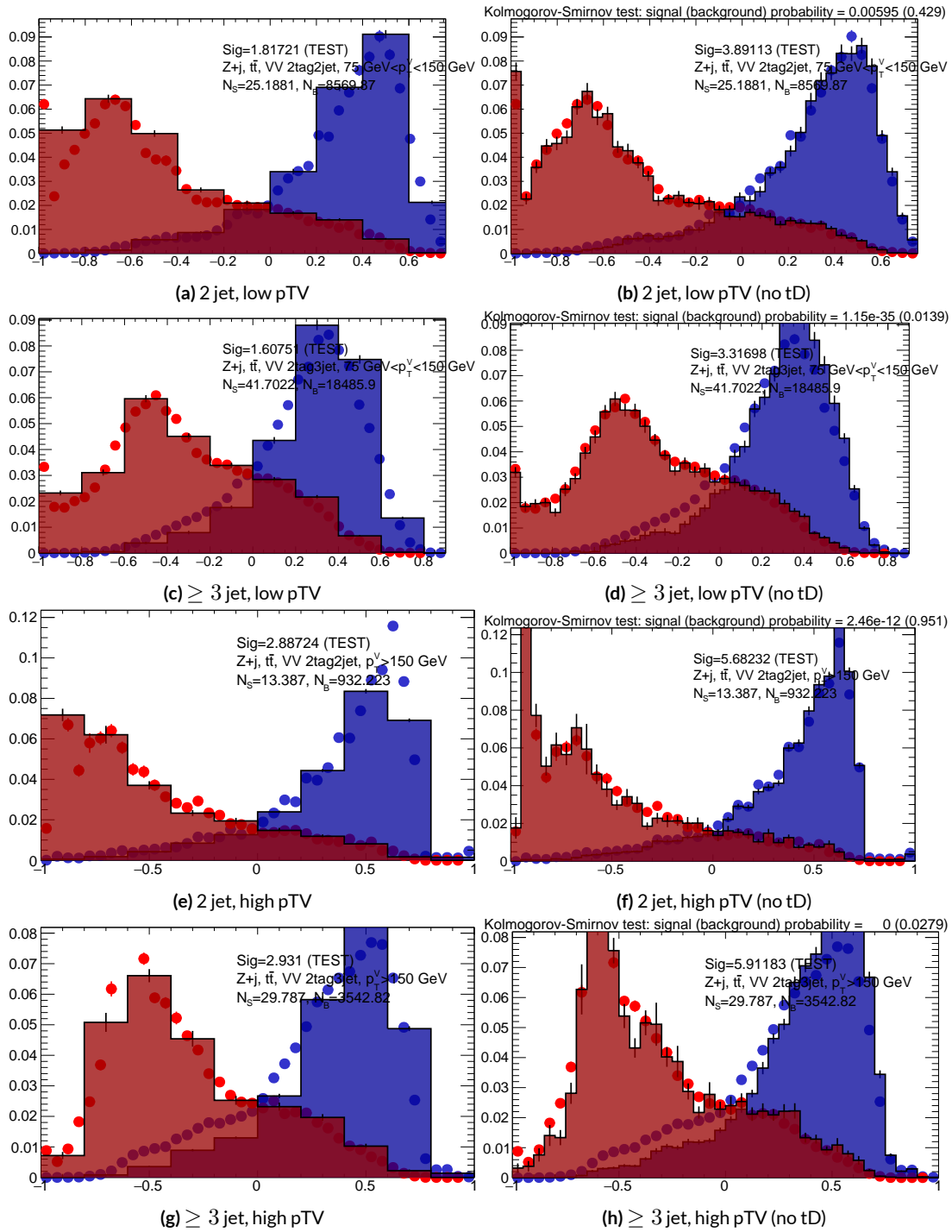


**Figure 6.13:** Training (points) and testing (block histogram) MVA distributions used for stat only testing for the standard variable set.

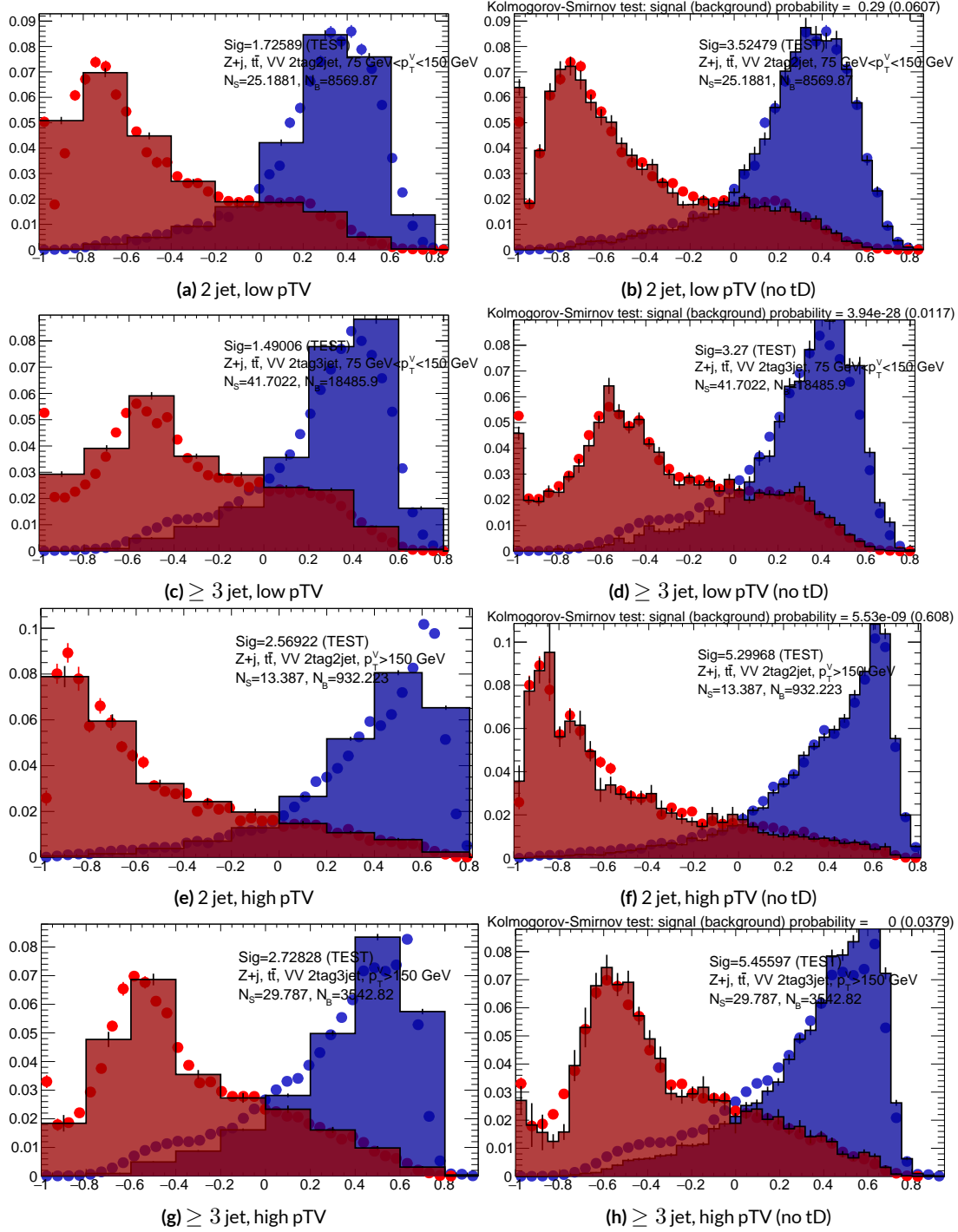


**Figure 6.14:** Training (points) and testing (block histogram) MVA distributions used for stat only testing for the LI variable set.

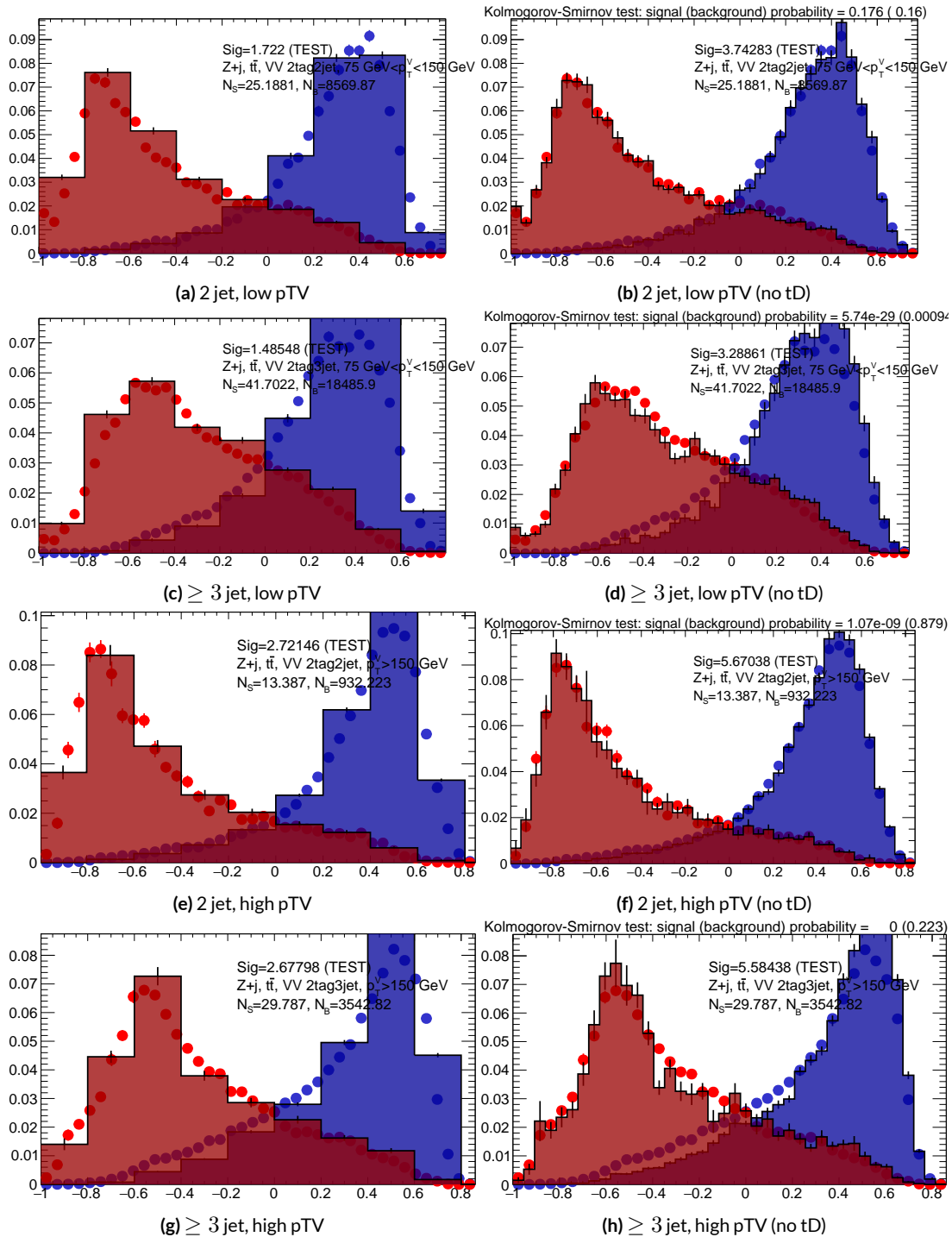


**Figure 6.15:** Training (points) and testing (block histogram) MVA distributions used for stat only testing for the RF variable set.

1596 set performs best, with the LI (RF) set having a cumulative significance that is 7.9% (6.9%) lower.  
 1597 This suggests that the LI and RF variables, in the  $ZH \rightarrow \ell\ell b\bar{b}$  closed final state, have no more in-  
 1598 trinsic descriptive power than the standard set. That these figures are all relatively high ( $\sim 4.5$ ) is  
 1599 due largely to the absence of systematics and possibly in part due to the fact that many of the most  
 1600 significant bins occur at high values of the BDT output, which, as can be seen in any of the testing  
 distributions, contain a small fraction of background events. An interesting feature to note in Fig-

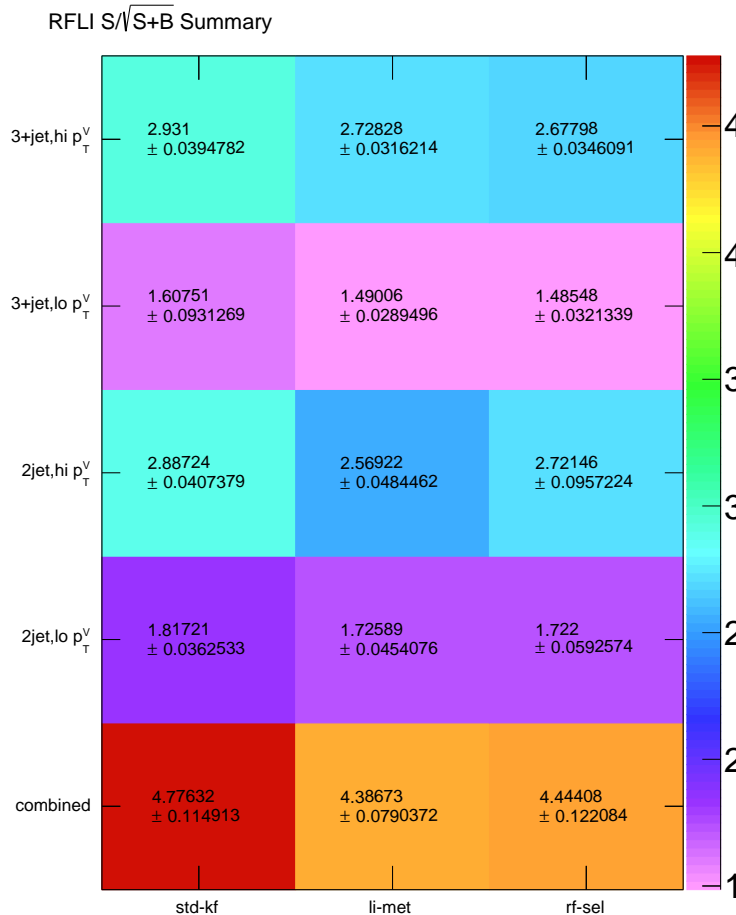


**Figure 6.16:** Results of testing significances sorted by analysis region and variable set.

1601

<sub>1602</sub> ure 6.16 is that while the standard set does perform better in all regions, the gap is larger in the  $\geq 3$   
<sub>1603</sub> jet regions, suggesting that further optimization in the  $\geq 3$  jet case could be useful. Moreover, as  
<sub>1604</sub> discussed at the end of Chapter 5, the choice of  $\geq 3$  jet and not exclusive 3 jet regions is a 2-lepton  
<sub>1605</sub> specific choice and may not be justified for the non-standard variable sets.

*Multivac picked you as most representative this year.*

*Not the smartest, or the strongest, or the luckiest, but*

*just the most representative. Now we don't question*

*Multivac, do we?*

Isaac Asimov, "Franchise"

1606

# 7

1607

## Statistical Fit Model and Validation

1608 THE ULTIMATE GOAL of an analysis like the search for SM  $VH(b\bar{b})$  decay is to say with as much  
1609 justified precision as possible with the ATLAS collision data whether or not the SM-like Higgs ob-  
1610 served in other decay modes also decays to  $b$ -quarks and, if so, whether this rate is consistent with  
1611 the SM prediction. In the limit of perfect modeling of both background processes and detector/reconstruction,

1612 the only free parameter is this production rate, referred to typically as a “signal strength,” denoted  $\mu$ ,  
1613 with  $\mu = 1$  corresponding to the SM prediction and  $\mu = 0$  corresponding to the SM with no  
1614 Higgs.

1615 To get a better sense of what this might look like, take a look at the example discriminant distri-  
1616 bution in Figure 7.1. The black points are data (with statistical error bars), and the colored block  
1617 histograms have size corresponding to the number of predicted events for each process in each bin of  
1618 the final BDT. In the limit of perfect understanding, a fit would correspond to a constant scale fac-  
1619 tor on the red, signal histogram, where one would choose a best fit  $\mu$  value, denoted  $\hat{\mu}$ , that would  
1620 minimize the sum in quadrature of differences between the number of observed data events and  
1621  $\mu s_i + b_i$ , where  $s_i$  and  $b_i$  are the predicted number of signal and background events in each bin.

1622 The only source of uncertainty would be due to data statistics, so for an infinitely large dataset with  
1623 perfect understanding,  $\mu$  could be fitted to arbitrary precision. This, of course, is not the case since  
1624 there is a finite amount of data and very many sources of systematic uncertainty, discussed in pre-  
1625 vious chapters. This chapter will first describe how systematic uncertainties are integrated into the  
1626 statistical fit of this analysis before describing two sets of cross checks on both a validation  $VZ$  fit and  
1627 on the fit for the  $VH$  fit of interest.

1628 7.1 THE FIT MODEL

1629 In order to derive the strength of the signal process  $ZH \rightarrow \ell\ell b\bar{b}$  and other quantities of interest  
1630 while taking into account systematic uncertainties or nuisance parameters (NP’s, collectively de-  
1631 noted  $\theta$ ), a binned likelihood function is constructed as the product over bins of Poisson distribu-

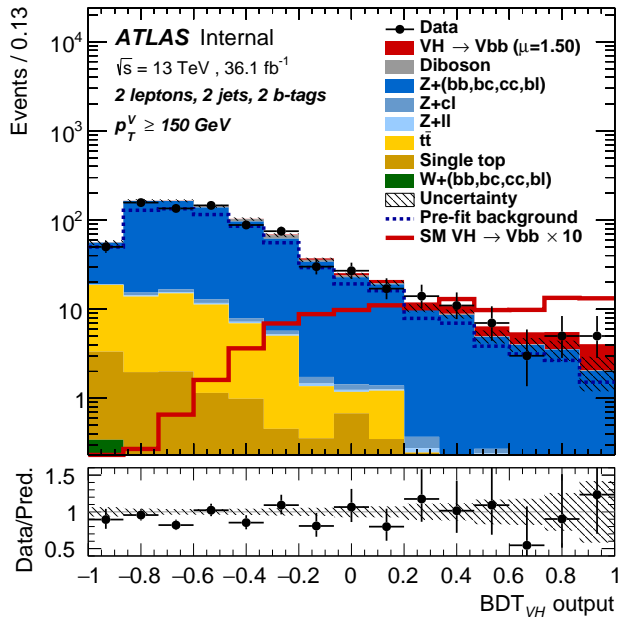


**Figure 7.1:** An example postfit distribution. The reason this looks different from postfit distributions later in this chapter is that this is a log plot.

1632 tions:

$$\mathcal{L}(\mu, \theta) = \text{Pois}(n | \mu S + B) \left[ \prod_{i \in \text{bins}} \frac{\mu s_i + b_i}{\mu S + B} \right] \prod_{j \in \text{NP's}} \mathcal{N}_{\theta_j}(\theta_j, \sigma_j^2 | 0, 1) \quad (7.1)$$

1633 where  $n$  is the total number of events observed,  $s_i$  and  $b_i$  are the number of expected signal and back-

1634 ground events in each bin, and  $S$  and  $B$  are the total expected signal and background events. The

1635 signal and background expectations generally are functions of the NP's  $\theta$ . NP's related to the nor-

1636 malization of signal and background processes fall into two categories. The first set is left to float

1637 freely like  $\mu$  while the second set are parametrized as log-normally distributed to prevent negative

1638 predicted values. All other NP's are parametrized with Gaussian priors. This results in a “penalty”

1639 on the NLL discussed below of  $(\hat{\alpha} - \mu_\alpha)^2 / \sigma_\alpha^2$ , for NP  $\alpha$ , normally parametrized with mean  $\mu_\alpha$

1640 (corresponding to the nominal prediction) and variance  $\sigma_\alpha^2$  (derived as discussed in Chapters 4 and

1641 5) for an MLE of  $\hat{\alpha}$ .

1642 One can maximize<sup>\*</sup> the likelihood in Equation 7.1 for a fixed value of  $\mu$  to derive estimators for  
1643 the NP's  $\theta$ ; values of  $\theta$  so derived are denoted  $\hat{\theta}_\mu$  to emphasize that these are likelihood maximizing  
1644 for a given  $\mu$ . The profile likelihood technique finds the likelihood function's maximum by compar-  
1645 ing the values of the likelihood over all possible values of  $\mu$  using these "profiles" and picking the  
1646 one with the greatest  $\mathcal{L}(\mu, \hat{\theta}_\mu)$  value; these values of  $\mu$  and  $\theta$  are denoted  $\hat{\mu}$  and  $\hat{\theta}$ . The profile like-  
1647 lihood can further be used to construct a test statistic<sup>†</sup>

$$q_\mu = -2 \left( \log \mathcal{L}(\mu, \hat{\theta}_\mu) - \log \mathcal{L}(\hat{\mu}, \hat{\theta}) \right) \quad (7.2)$$

1648 This statistic can be used to derive the usual significance ( $p$  value), by setting  $\mu = 0$  to find the com-  
1649 patability with the background-only hypothesis [45]. If there is insufficient evidence for the signal  
1650 hypothesis, the  $CL_s$  method can be used to set limits [18].

1651 In order to both validate the fit model and study the behavior of fits independent of a given dataset,  
1652 a so-called "Asimov"<sup>‡</sup> dataset can be constructed for a given fit model; this dataset has each bin equal  
1653 to its expectation value for assumed values of the NP's and a given  $\mu$  value (in this case,  $\mu = 1$ , the  
1654 SM prediction).

---

<sup>\*</sup>Maximization is mathematically identical to finding the minimum of the negative logarithm of the likelihood, which is numerically an easier problem.

<sup>†</sup>The factor of -2 is added so that this statistic gives, in the asymptotic limit of large  $N$ , a  $\chi^2$  distribution.

<sup>‡</sup>A reference to the short story quoted at the beginning of this chapter in which a computer picks a single voter to stand in for the views of the entire American electorate.

1655 7.2 FIT INPUTS

1656 Inputs to the binned likelihood are distributions of the BDT outputs described in Chapter 6 for the  
1657 signal regions and of  $m_{bb}$  for the top  $e - \mu$  control regions. These regions split events according  
1658 to their  $p_T^V$  and number of jets. All events are required to have two  $b$ -tagged jets, as well as pass the  
1659 other event selection requirements summarized in Table 5.8; the only difference between the signal  
1660 and control region selections is that the same flavor requirement (i.e. leptons both be electrons or  
1661 muons) is flipped so that events in the control region have exactly one electron and one muon. The  
1662 BDT outputs are binned using transformation D, while the  $m_{bb}$  distributions have 50 GeV bins,  
1663 with the exception of the 2 jet, high  $p_T^V$  region, where a single bin is used due to low statistics.

1664 Input distributions in MC are further divided according to their physics process. The signal pro-  
1665 cesses are divided based on both the identity of associated  $V$  and the number of leptons in the final  
1666 state;  $ZH \rightarrow \ell\ell b\bar{b}$  events are further separated into distributions for  $qq$  and  $gg$  initiated processes.  
1667  $V+jets$  events are split according to  $V$  identity and into the jet flavor bins described in Chapter 3.  
1668 Due to the effectiveness of the 2  $b$ -tag requirement suppressing the presence of both  $c$  and  $l$  jets,  
1669 truth-tagging is used to boost MC statistics in the  $cc$ ,  $cl$ , and  $ll$  distributions.<sup>§</sup> For top backgrounds,  
1670 single top production is split according to production mode ( $s$ ,  $t$ , and  $Wt$ ), with  $t\bar{t}$  as single category.  
1671 Diboson background distributions are also split according to the identity of the  $V$ 's ( $ZZ$ ,  $WZ$ , and  
1672  $WW$ ). Fit input segmentation is summarized in Table 7.1.

---

1673 <sup>§</sup>Since  $WW$  is not an important contribution to the already small total diboson background, no truth-  
tagging was applied here, in contrast to the fiducial analysis.

Category	Bins
# of Jets	2, 3+
$p_T^V$ Regions (GeV)	$[75, 150], [150, \infty)$
Sample	data, signal $[(W, qqZ, ggZ)] \times n_{lep}$ , $V+jets [(W, Z) \times (bb, bc, bl, cc, cl, ll)]$ , $t\bar{t}$ , diboson ( $ZZ, WW, WZ$ ), single top ( $s, t, Wt$ )

**Table 7.1:** Fit input segmentation.

### 1673 7.3 SYSTEMATIC UNCERTAINTIES REVIEW

1674 Tables 7.2 and 7.3 summarize modeling (Chapter 4) and experimental (Chapter 5) systematic uncer-  
 1675 tainties considered in this analysis, respectively. In addition to these, simulation statistics uncertain-  
 1676 ties (“MC stat errors”) are also included in the fit model. There is one distribution per systematic  
 1677 (one each for up and down) per sample per region. The  $\pm 1\sigma$  variation for a systematic is calculated  
 1678 as the difference in the integrals between the nominal and up/down varied distributions.

Process	Systematics
Signal	$H \rightarrow bb$ decay, QCD scale, PDF+ $\alpha_S$ scale, UE+PS (acc, $p_T^V$ , $m_{bb}$ , 3/2 jet ratio)
$Z+jets$	Acc, flavor composition, $p_T^V+m_{bb}$ shape
$t\bar{t}$	Acc, $p_T^V+m_{bb}$ shape
Single top	Acc, $p_T^V+m_{bb}$ shape
Diboson	Overall acc, UE+PS (acc, $p_T^V$ , $m_{bb}$ , 3/2 jet ratio), QCD scale (acc (2, 3 jet, jet veto), $p_T^V$ , $m_{bb}$ )

**Table 7.2:** Summary of modeling systematic uncertainties.

1679 The systematics distributions undergo processes known as “smoothing” and “pruning” before  
 1680 being combined into the final likelihood used in minimization.

1681 The difference between systematics varied distributions and nominal distributions approaches

Process	Systematics
Jets	21 NP scheme for JES, JER as single NP
$E_T^{\text{miss}}$	trigger efficiency, track-based soft terms, scale uncertainty due to jet tracks
Flavor Tagging	Eigen parameter scheme (CDI File: 2016-20_7-13TeV-MC15-CDI-2017-06-07_v2)
Electrons	trigger eff, reco/ID eff, isolation eff, energy scale/resoltuion
Muons	trigger eff, reco/ID eff, isolation eff, track to vertex association, momentum resolution/scale
Event	total luminosity, pileup reweighting

**Table 7.3:** Summary of experimental systematic uncertainties.

1682 some stable value in the limit of large simulation statistics, but if the fluctuations due to simulation  
 1683 statistics in a distribution are large compared to the actual physical effect (whether this is because  
 1684 the actual effect is small or if the actual distribution is derived from a small number of simulation  
 1685 events), then systematic uncertainty will be overestimated by, in effect, counting the MC stat error  
 1686 multiple times. Smoothing is designed to mitigate these effects by merging adjacent bins in some  
 1687 input distributions. Smoothing happens in two steps (the full details of smoothing algorithms may  
 1688 be found in [65] and in the `WSMaker` code):  
 1689     1. Merge bins iteratively where bin differences are smallest in input distributions until no local  
 1690         extrema remain (obviously, a single peak or valley is allowed to remain)  
 1691     2. Sequentially merge bins (highest to lowest, like transformation D) until the statistical uncer-  
 1692         tainty in a given bin is smaller than 5% of merged bin content  
 1693 Not all systematic uncertainties defined are included in the final fit. Systematics are subject “prun-  
 1694 ing” (individually in each region/sample: there are two histograms per systematic (up/down) per  
 1695 region per sample, so pruning just consists of removing the histograms from the set of distributions  
 1696 included in the likelihood) if they are do not have a significant impact, defined as follows:

- Normalization/acceptance systematics are pruned away if either:
  - The variation is less than 0.5%
  - Both up and down variations have the same sign
  
- Shape systematics pruned away if either:
  - Not one single bin has a deviation over 0.5% after the overall normalisation is removed
  - If only the up or the down variation is non-zero
  
- Shape+Normalisation systematics are pruned away if the associated sample is less than 2% of the total background and either:
  - If the predicted signal is < 2% of the total background in all bins and the shape and normalisation error are each < 0.5% of the total background
  - If instead at least one bin has a signal contribution > 2% of the total background, and only in each of these bins, the shape and normalisation error are each < 2% of the signal yield

## 7.4 THE VZ VALIDATION FIT

One of the primary validation cross-checks for the fiducial analysis was a  $VZ$  fit—that is, conducting the entire analysis but looking for  $Z \rightarrow b\bar{b}$  decays instead of the Higgs. The idea here is that the  $Z$  is very well understood and so “rediscovering”  $Z$  decay to  $b$ 's is taken as a benchmark of analysis reliability since the complexity of the fit model precludes the use of orthogonal control regions for validation as is done in other analyses (generally, if there is a good control region, one prefers to use it

1716 to constrain backgrounds and improve the fit model). To do this, a new MVA discriminant is made  
 1717 by keeping all hyperparameter configurations the same (e.g. variable ranking) but using diboson  
 1718 samples as signal. For the 2-lepton case, this means using  $ZZ \rightarrow \ell\ell b\bar{b}$  as the signal sample. This  
 1719 new MVA is used to make the inputs described in Section 7.2, and the fit is then run as for the  $VH$   
 1720 fit (again, with  $ZZ$  as signal).  $VH$  samples are considered background in these diboson fits.

1721 The  $VZ$  fit sensitivities for the standard, LI, and RF fits are summarized in Table 7.4. The ex-  
 1722 pected significances are all fairly comparable and about what was the case in the fiducial analysis.  
 1723 The observed significance for the standard set matches fairly well with the expected value on data,  
 1724 but the LI and RF observed significances are quite a bit lower.

	Standard	LI	RF
Expected (Asimov)	3.83	3.67	3.72
Expected (data)	3.00	2.95	3.11
Observed (data)	3.17	1.80	2.09

**Table 7.4:** Expected (for both data and Asimov) and observed  $VZ \rightarrow \ell\ell b\bar{b}$  sensitivities for the standard, LI, and RF variable sets.

1725 These values, however, are consistent with the observed signal strength values, which can be seen  
 1726 in Figure 7.2 (b), with both the LI and RF fits showing a deficit of signal events with respect to the  
 1727 SM expectation, though not by much more than one standard deviation (a possible explanation is  
 1728 explored in the following section). Just as in the  $VH$  fits, errors arising systematic uncertainties are  
 1729 lower in the fits to the observed dataset. That the effect is not noticeable in Asimov fits is not too  
 1730 surprising, since this analysis (and these variable configurations in particular), is not optimized for  
 1731  $VZ$ .

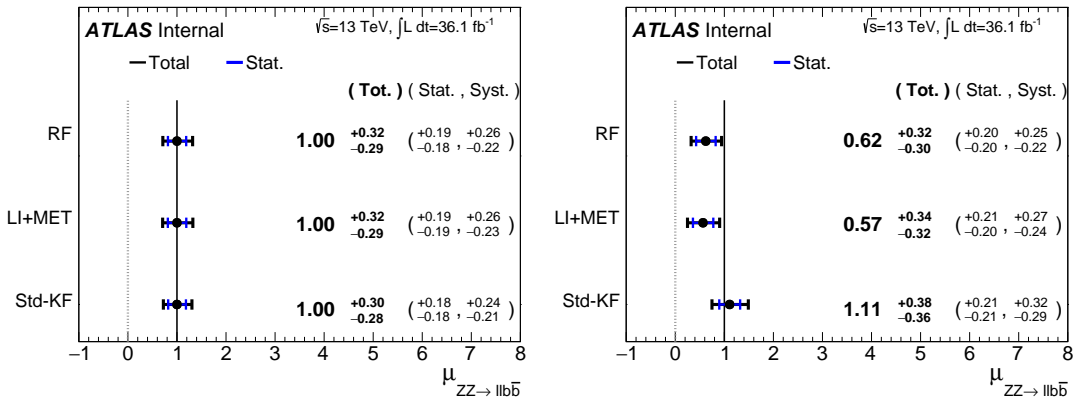


**Figure 7.2:**  $\mu$  summary plots for the standard, LI, and RF variable sets. The Asimov case (with  $\mu = 1$  by construction) is in (a), and  $\hat{\mu}$  best fit values and error summary are in (b).

#### 1732 7.4.I 2 AND $\geq 3$ JET FITS

1733 While the treatment of simply ignoring any additional jets in the event seems adequate for the  $VH$   
 1734 analysis (discussed below), the potential shortcoming of this treatment appears in the  $VZ$  analysis  
 1735 when the  $2$  and  $\geq 3$  jet cases are fit separately<sup>¶</sup>, as can be seen in Figure 7.3. Compared to the stan-  
 1736 dard fit, the LI and RF fits have lower  $\hat{\mu}_{\geq 3 \text{ jet}}$  values, consistent with the interpretation that the ad-  
 1737 ditional information from the third jet in the  $\geq 3$  jet regions for the standard case is important for  
 1738 characterizing events in these regions for  $VZ$  fits.

1739 A natural question to ask is why this would be an issue for the  $VZ$  but not the  $VH$  case. One  
 1740 potential answer is that at high transverse boosts, there is a greater probability for final state  
 1741 radiation in the hadronically decaying  $Z$ , so there are more events where the third jet should be in-  
 1742 cluded in the calculation of variables like  $m_{b\bar{b}}$  or for angles involving the  $b\bar{b}$  system (e.g.  $\cos\theta$  in the  
 1743 RF case). While the absolute scale at which the low and high  $p_T^V$  regions are separated remains the

<sup>¶</sup>standalone fits, with half the regions each, not 2 POI fits

<sup>1744</sup> same does not change from the  $VH$  to the  $VZ$  analysis, 150 GeV, the implicit cutoff on the transverse  
<sup>1745</sup> boost of the hadronically decaying boson does. For the Higgs, with a mass of 125 GeV, the  $p_T^V$  cutoff  
<sup>1746</sup> corresponds to  $\gamma \sim 1.56 - 6.74$ , but for the  $Z$ , with a mass of 91 GeV, this is  $\gamma \sim 1.93 - 9.21$ ,  
<sup>1747</sup> about 23–37% higher.

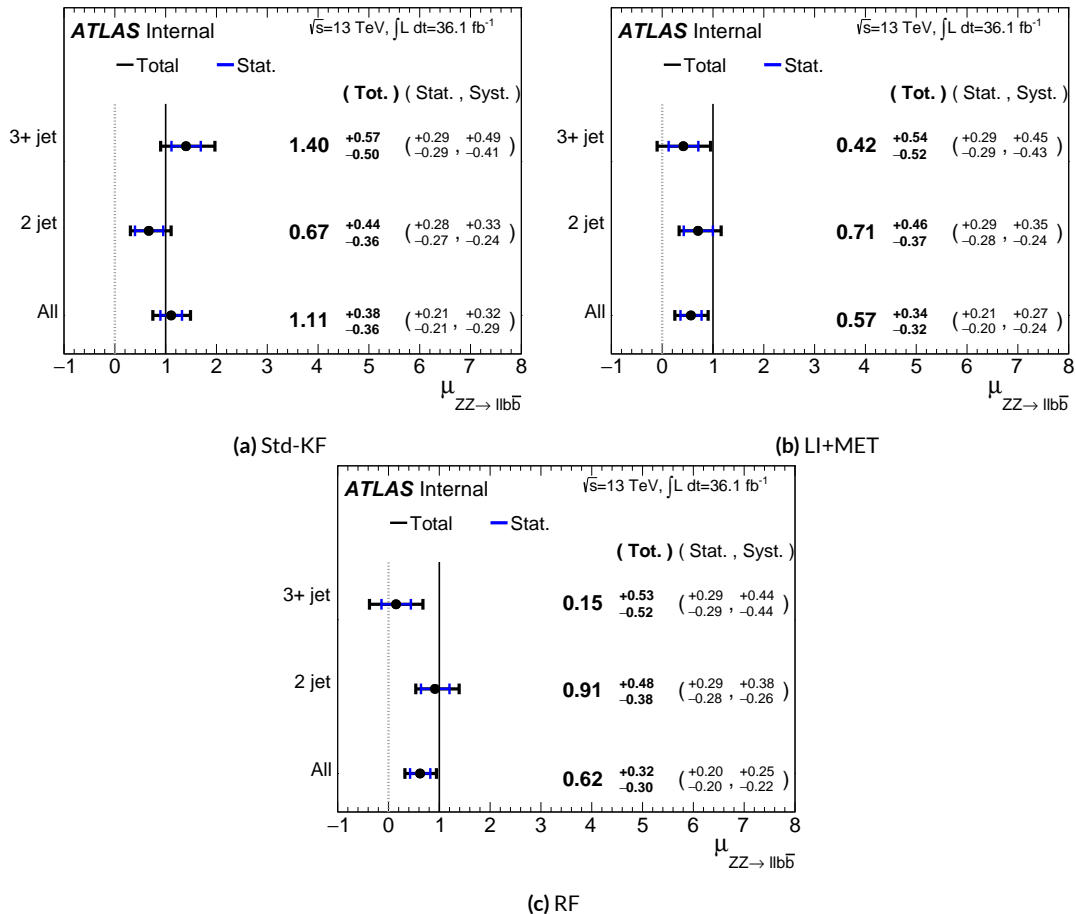


Figure 7.3:  $\hat{\mu}$  summary plots with standalone fits for the different  $n_{jet}$  regions for the standard, LI, and RF variable sets.

<sup>1748</sup> If either the LI or RF schemes were to be used in a mainstream analysis, these validation fits sug-  
<sup>1749</sup> gest that the third jet ought to be included in variable schemes (e.g. by adding the third jet to the

1750 Higgs in the high  $p_T^V$  case). On the issue of whether or not  $\geq 4$  jet events should be included, the  
1751 RF set shows very little sensitivity to this change (a 2 jet and 3 jet only fit moves  $\hat{\mu}$  to 0.64, while  
1752 doing so for the LI set moves it to 0.40), so this, like the addition of the third jet into the variable  
1753 sets, would have to be addressed individually. Nevertheless, this optimization is beyond the scope of  
1754 this thesis, which aims to preserve as much of the fiducial analysis as possible for as straightforward a  
1755 comparison as possible.

1756 For completeness, we include the full set of fit validation results for the  $VZ$  fit, explaining them in  
1757 turn.

## 1758 7.5 NUISANCE PARAMETER PULLS

1759 The first set of plots statistical fit experts will want to look at are the “pulls” and “pull comparisons.”  
1760 In these plots, the best fit (nominal) values and one standard deviation error bars are shown for ob-  
1761 served (Asimov) pull plots, with the green and yellow bands corresponding to  $\pm 1, 2\sigma$ , respectively.  
1762 These plots are divided by NP category for readability. <sup>¶</sup> In pull comparisons, these pulls are over-  
1763 layed and color-coded. Pull comparisons here have the following color code: black is the standard  
1764 variable set, red is the LI set, and blue is the RF set.

1765 A well-behaved fit has pulls close to nominal values (“closeness” should be interpreted in the  
1766 context of pull value divided by pull error). As can be seen in Figures 7.4–7.8, the fits for the three  
1767 different variable sets are fairly similar from a NP pull perspective, though the  $Z+{\rm jets}$   $m_{bb}$  and  $p_T^V$

---

¶Over 100 non-MC stat NP’s survive pruning in these 2-lepton only Run 2 fits; well over 500 survive in the Run 1+Run 2 combined fit.

1768 NP's and the jet energy resolution NP are heavily pulled (a handful of poorly behaved pulls is not  
 1769 uncommon, though typically warrants further investigation). As a general note, these pull plots cal-  
 1770 culate pulls using a simultaneous HESSE matrix inversion, which is fine for relatively small fits, but  
 1771 the more reliable MINOS result, which calculates the impact of each NP on its own, should be cross-  
 1772 checked for significant pulls\*\*. The ranking plots below do this.

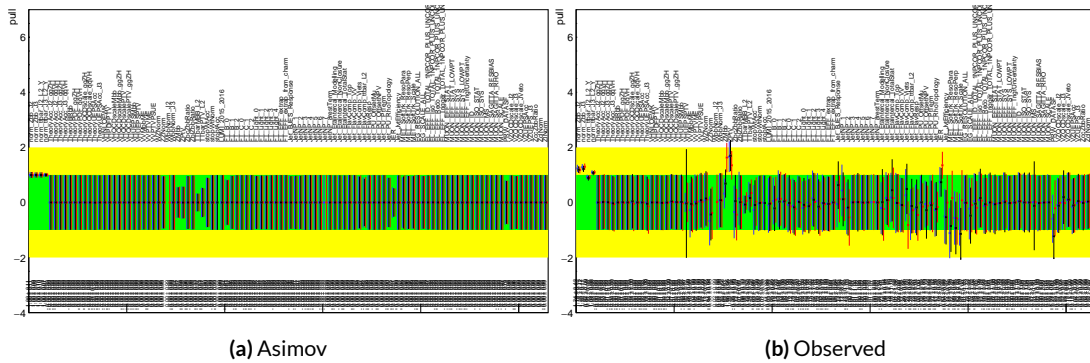


Figure 7.4: Pull comparison for all NP's but MC stats.

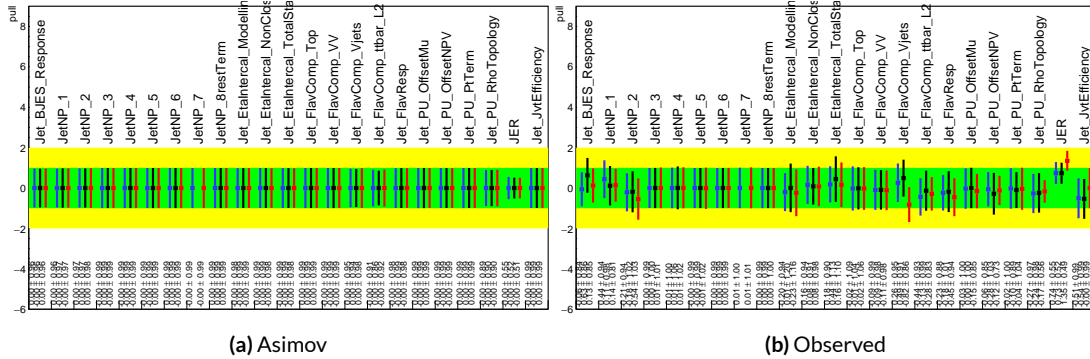


Figure 7.5: Pull comparison for jet NP's.

1773 Nuisance parameter correlation matrices (for correlations with magnitude at least 0.25) for all  
 1774 three variable set fits can be found in Figures 7.10–7.12. These are useful for seeing which NP's move

\*\*This becomes more of an issue for very large fits, like the full Run 1 + Run 2 combined fits in Chapter 9.

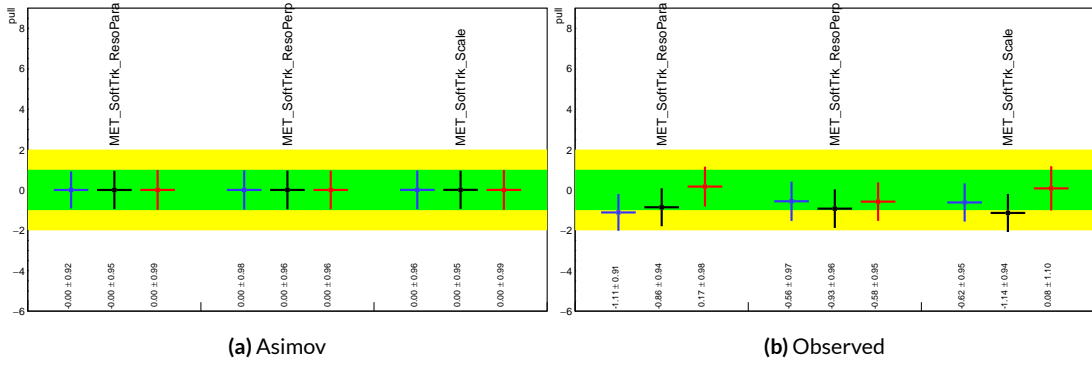


Figure 7.6: Pull comparison for MET NP's.

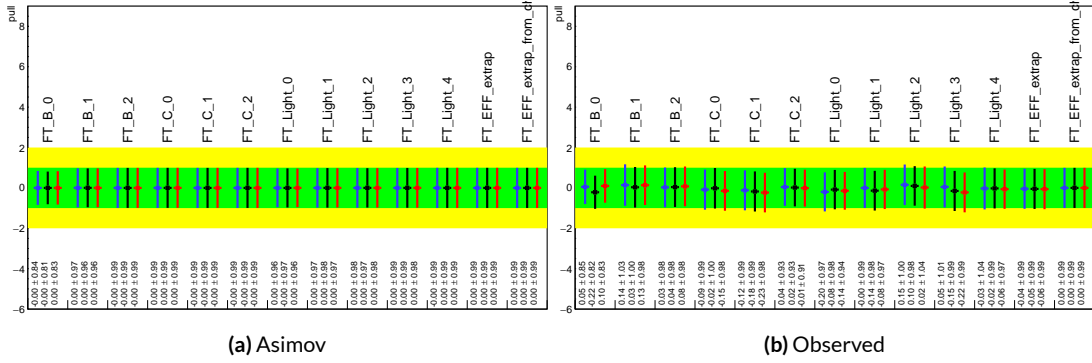


Figure 7.7: Pull comparison for Flavour Tagging NP's.

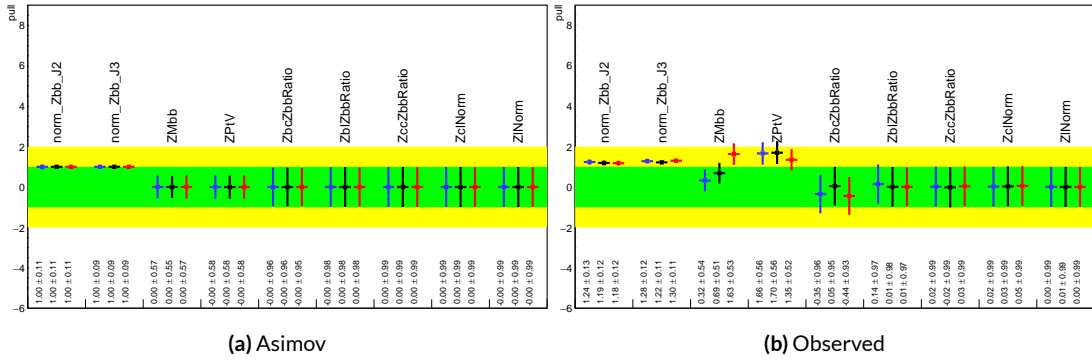
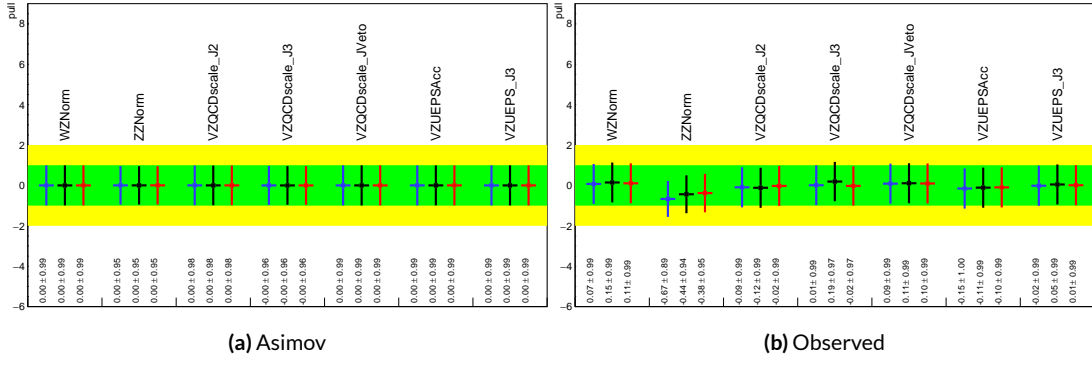


Figure 7.8: Pull comparison for  $Z$ +jets NP's.



**Figure 7.9:** Pull comparison for signal process modeling NP's.

together (if there is no physical argument for them to do so, this is a potential indicator that further

investigation is warranted).

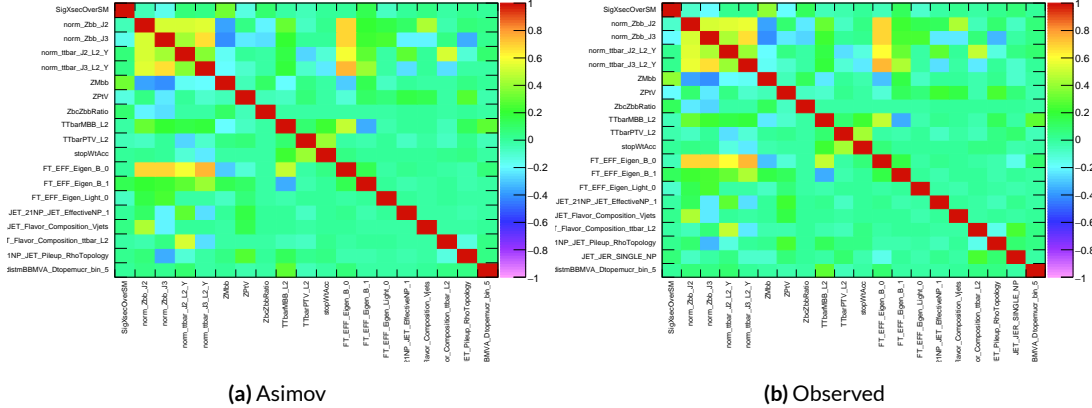


**Figure 7.10:** NP correlations for standard variable fits.

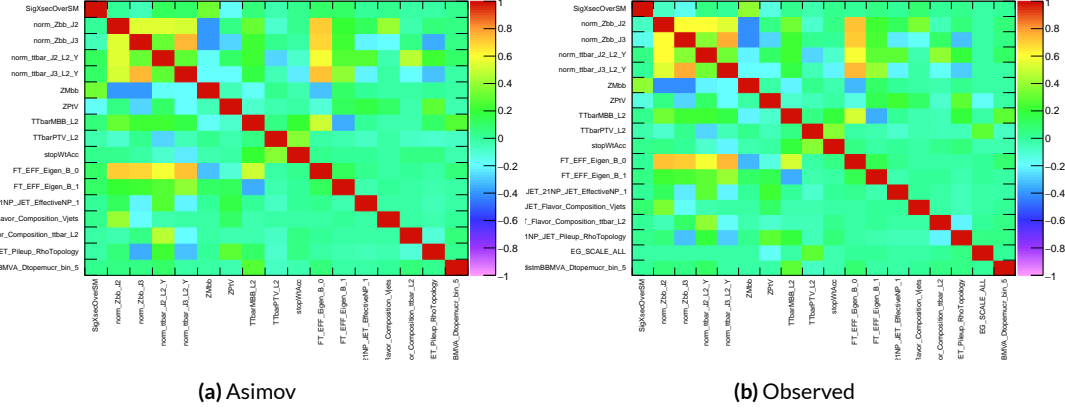


**Figure 7.11:** NP correlations for LI variable fits.

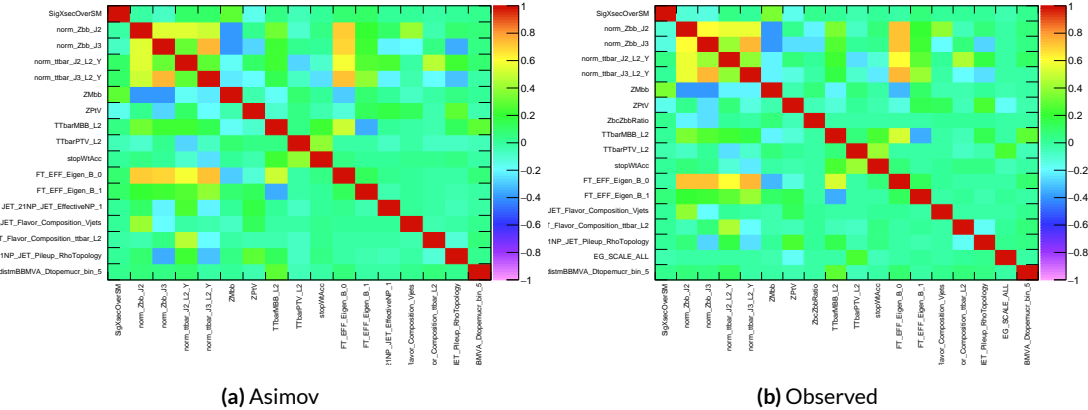


**Figure 7.12:** NP correlations for RF variable fits.

## 1777 7.5.1 NUISANCE PARAMETER RANKING PLOTS AND BREAKDOWNS

1778 The next set of fit results that is used to diagnose the quality of a fit is the impact of different nui-  
 1779 sance parameters on the total error on  $\mu$ , both individually and as categories. Figure 7.13 shows the  
 1780 top 25 nuisance parameters ranked by their postfit impact on  $\hat{\mu}$ ; these plots use the aforementioned,  
 1781 more reliable MINOS approach. This set of rankings is fairly similar, with  $Z+jets$  systematics being  
 1782 particularly prominent. The advantage of seeing individual nuisance parameter rankings, as op-  
 1783 posed to impacts of categories in aggregate, is that particularly pathological NP's are easier to see;  
 1784 in particular, jet energy resolution and  $Z+jets p_T^V$  systematic from the pull comparison plots show  
 up with high rankings. Yellow bands are pre-fit impact on  $\mu$ .

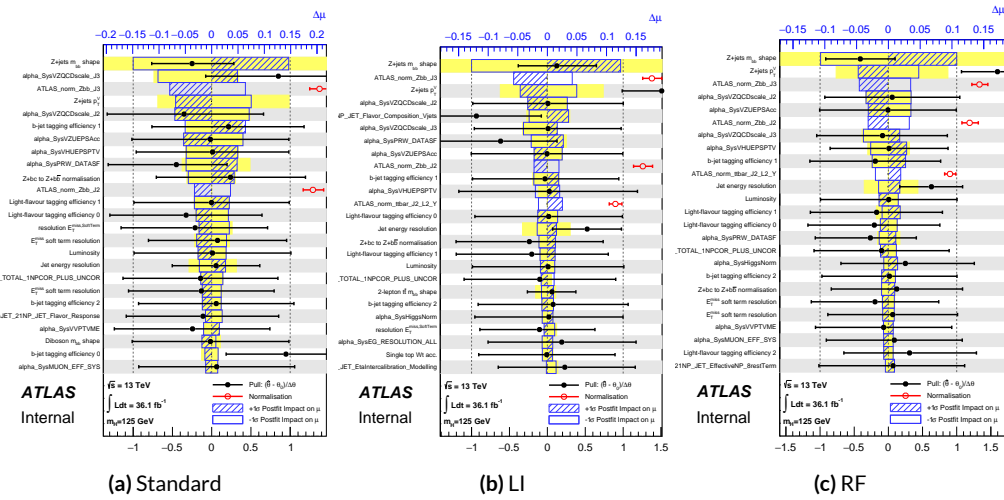


Figure 7.13: Plots for the top 25 nuisance parameters according to their postfit impact on  $\hat{\mu}$  for the standard (a), LI (b), and RF (c) variable sets.

1785  
 1786 This is consistent with the picture of NP's taken in aggregate categories in Tables 7.5 and 7.6,  
 1787 known as “breakdowns,” with  $Z+jets$  in particular featuring prominently. Of particular interest

<sup>1788</sup> is also the lower impact of MC stats in the observed fit.

	Std-KF	LI+MET	RF
Total	+0.305 / -0.277	+0.324 / -0.292	+0.319 / -0.288
DataStat	+0.183 / -0.179	+0.190 / -0.186	+0.188 / -0.184
FullSyst	+0.244 / -0.212	+0.262 / -0.226	+0.258 / -0.221
Floating normalizations	+0.092 / -0.084	+0.098 / -0.079	+0.094 / -0.076
All normalizations	+0.093 / -0.084	+0.098 / -0.079	+0.094 / -0.076
All but normalizations	+0.214 / -0.179	+0.229 / -0.188	+0.224 / -0.182
Jets, MET	+0.052 / -0.043	+0.041 / -0.034	+0.047 / -0.037
Jets	+0.034 / -0.029	+0.033 / -0.028	+0.032 / -0.026
MET	+0.035 / -0.027	+0.015 / -0.012	+0.020 / -0.016
BTag	+0.064 / -0.051	+0.063 / -0.031	+0.059 / -0.032
BTag b	+0.053 / -0.041	+0.061 / -0.028	+0.055 / -0.025
BTag c	+0.011 / -0.010	+0.006 / -0.005	+0.007 / -0.006
BTag light	+0.030 / -0.027	+0.016 / -0.013	+0.022 / -0.019
Leptons	+0.021 / -0.012	+0.022 / -0.014	+0.023 / -0.014
Luminosity	+0.039 / -0.022	+0.039 / -0.022	+0.040 / -0.022
Diboson	+0.049 / -0.028	+0.047 / -0.026	+0.047 / -0.026
Model Zjets	+0.106 / -0.105	+0.113 / -0.110	+0.102 / -0.099
Zjets flt. norm.	+0.039 / -0.053	+0.024 / -0.029	+0.021 / -0.031
Model Wjets	+0.000 / -0.000	+0.000 / -0.000	+0.000 / -0.000
Wjets flt. norm.	+0.000 / -0.000	+0.000 / -0.000	+0.000 / -0.000
Model ttbar	+0.015 / -0.013	+0.032 / -0.017	+0.030 / -0.016
Model Single Top	+0.004 / -0.003	+0.009 / -0.008	+0.005 / -0.004
Model Multi Jet	+0.000 / -0.000	+0.000 / -0.000	+0.000 / -0.000
Signal Systematics	+0.003 / -0.003	+0.003 / -0.003	+0.003 / -0.003
MC stat	+0.097 / -0.094	+0.108 / -0.103	+0.107 / -0.104

**Table 7.5:** Summary of impact of various nuisance parameter categories on the error on  $\mu$  for Asimov fits for the standard, LI, and RF variable sets.

	Std-KF	LI+MET	RF
$\hat{\mu}$	1.1079	0.5651	0.6218
Total	+0.381 / -0.360	+0.339 / -0.316	+0.322 / -0.299
DataStat	+0.214 / -0.211	+0.210 / -0.205	+0.201 / -0.197
FullSyst	+0.315 / -0.292	+0.267 / -0.241	+0.252 / -0.225
Floating normalizations	+0.120 / -0.122	+0.095 / -0.089	+0.082 / -0.079
All normalizations	+0.121 / -0.123	+0.095 / -0.090	+0.082 / -0.079
All but normalizations	+0.279 / -0.254	+0.228 / -0.200	+0.213 / -0.184
Jets, MET	+0.076 / -0.065	+0.045 / -0.043	+0.038 / -0.033
Jets	+0.047 / -0.040	+0.044 / -0.041	+0.027 / -0.024
MET	+0.055 / -0.046	+0.015 / -0.015	+0.012 / -0.010
BTag	+0.083 / -0.079	+0.041 / -0.031	+0.041 / -0.035
BTag b	+0.063 / -0.059	+0.032 / -0.022	+0.031 / -0.026
BTag c	+0.018 / -0.017	+0.008 / -0.007	+0.010 / -0.009
BTag light	+0.051 / -0.046	+0.024 / -0.021	+0.025 / -0.022
Leptons	+0.022 / -0.011	+0.015 / -0.008	+0.019 / -0.008
Luminosity	+0.044 / -0.022	+0.026 / -0.006	+0.027 / -0.008
Diboson	+0.049 / -0.026	+0.025 / -0.013	+0.027 / -0.017
Model Zjets	+0.156 / -0.162	+0.133 / -0.133	+0.115 / -0.117
Zjets flt. norm.	+0.061 / -0.089	+0.041 / -0.064	+0.028 / -0.056
Model Wjets	+0.000 / -0.001	+0.000 / -0.001	+0.000 / -0.001
Wjets flt. norm.	+0.000 / -0.001	+0.000 / -0.001	+0.000 / -0.001
Model ttbar	+0.015 / -0.024	+0.018 / -0.005	+0.017 / -0.009
Model Single Top	+0.005 / -0.003	+0.010 / -0.008	+0.007 / -0.004
Model Multi Jet	+0.000 / -0.001	+0.000 / -0.001	+0.000 / -0.001
Signal Systematics	+0.005 / -0.004	+0.009 / -0.006	+0.005 / -0.006
MC stat	+0.140 / -0.143	+0.132 / -0.131	+0.128 / -0.129

**Table 7.6:** Summary of impact of various nuisance parameter categories on the error on  $\hat{\mu}$  for observed fits for the standard, LI, and RF variable sets.

1789 7.6 POSTFIT DISTRIBUTIONS

1790 Finally, postfit distributions for the MVA discriminant ( $m_{bb}$ ) distribution in the signal (top  $e - \mu$   
1791 control) region for the standard, Lorentz Invariant, and RestFrames variable sets are shown. It is  
1792 generally considered good practice to check the actual postfit distributions of discriminating quan-  
1793 tities used to make sure there is good agreement. <sup>††</sup> It should be noted that agreement is not always  
1794 great when “eyeballing” a distribution, as fits are messy and  $V+hf$  modeling is notoriously hard.  
1795 This is particularly true in the  $VZ$  fit since normalizations for  $Z+hf$  in particular are derived using  
1796  $VH$  optimized sidebands. This is also why a lot of these plots are presented as log plots (which hide  
1797 disagreement better; the general argument goes that one has the ratio plots on the bottom and log  
1798 plots allow one to see rare backgrounds in plots).

---

<sup>††</sup>Sometimes distributions of input variables (MC histograms scaled by their postfit normalizations) are also used.

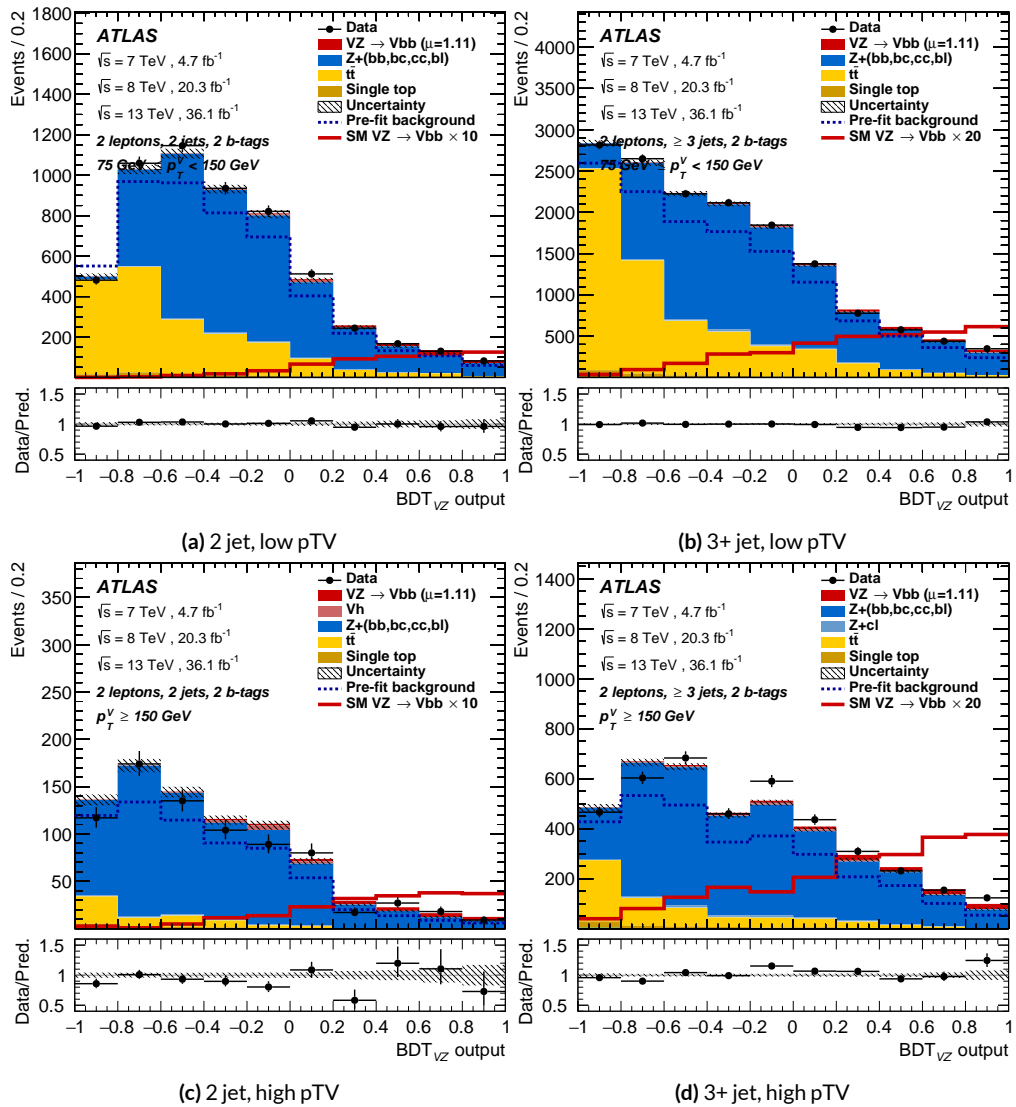


**Figure 7.14:** Postfit  $BDT_{VZ}$  plots in the signal region for the standard variable set.

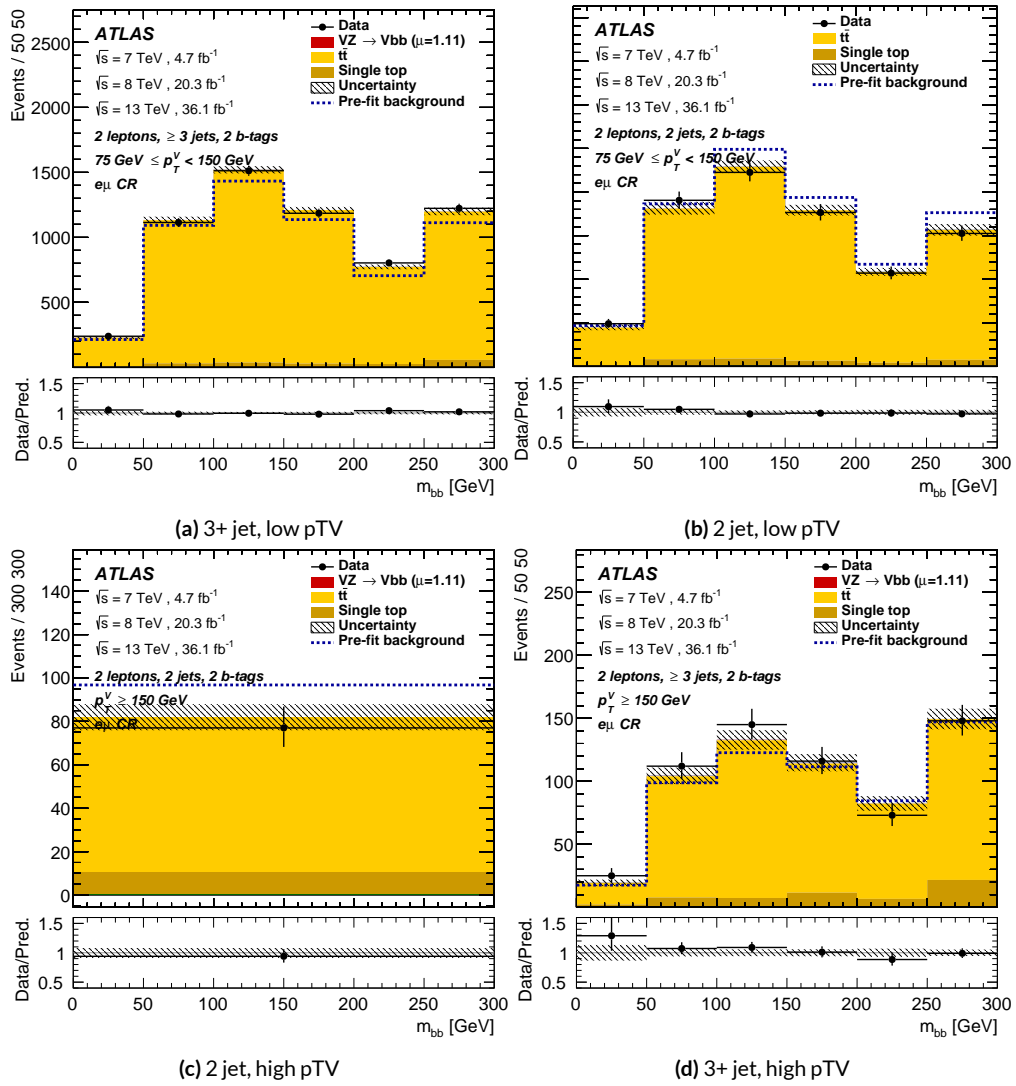


**Figure 7.15:** Postfit  $m_{bb}$  plots in the top  $e - \mu$  CR for the standard variable set.

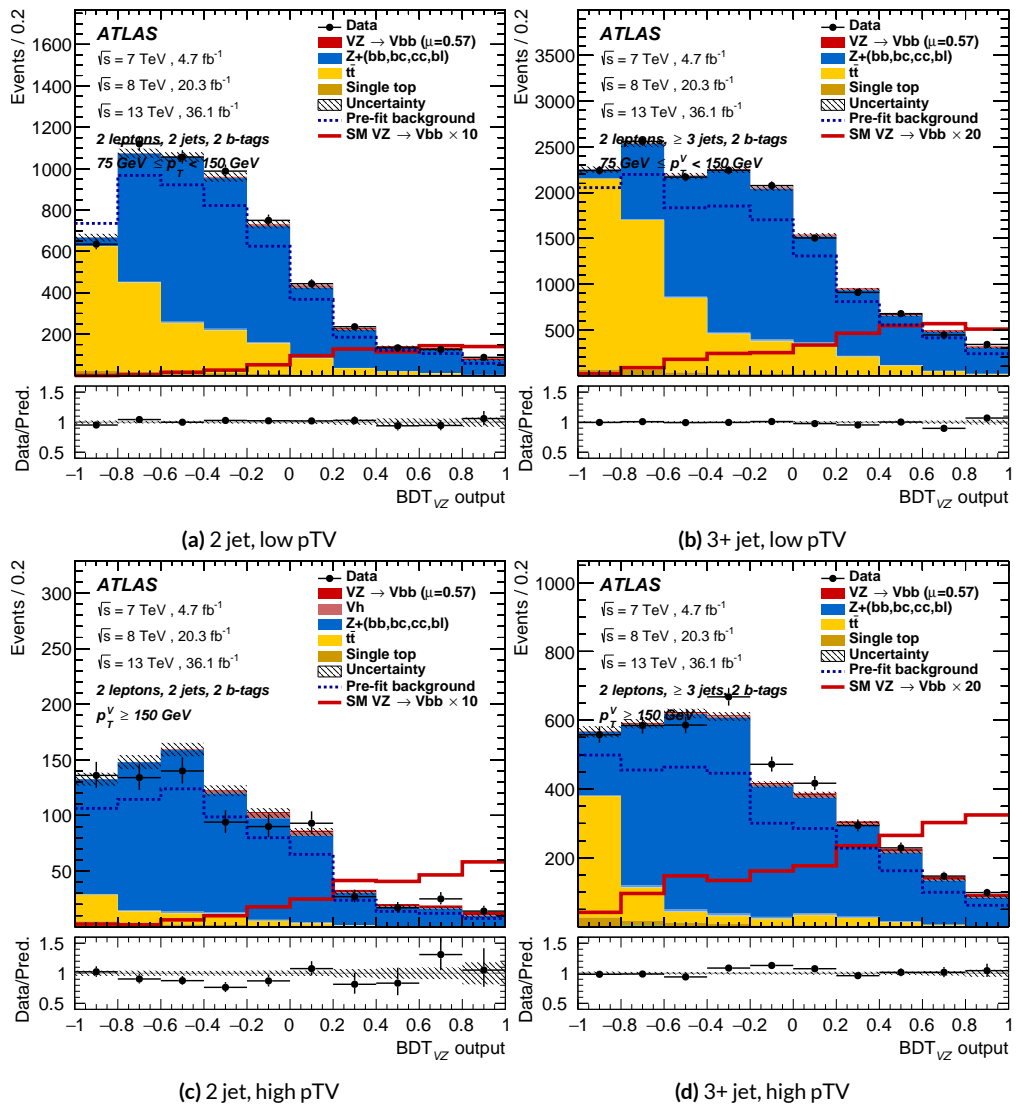


Figure 7.16: Postfit  $BDT_{VZ}$  plots in the signal region for the LI variable set.

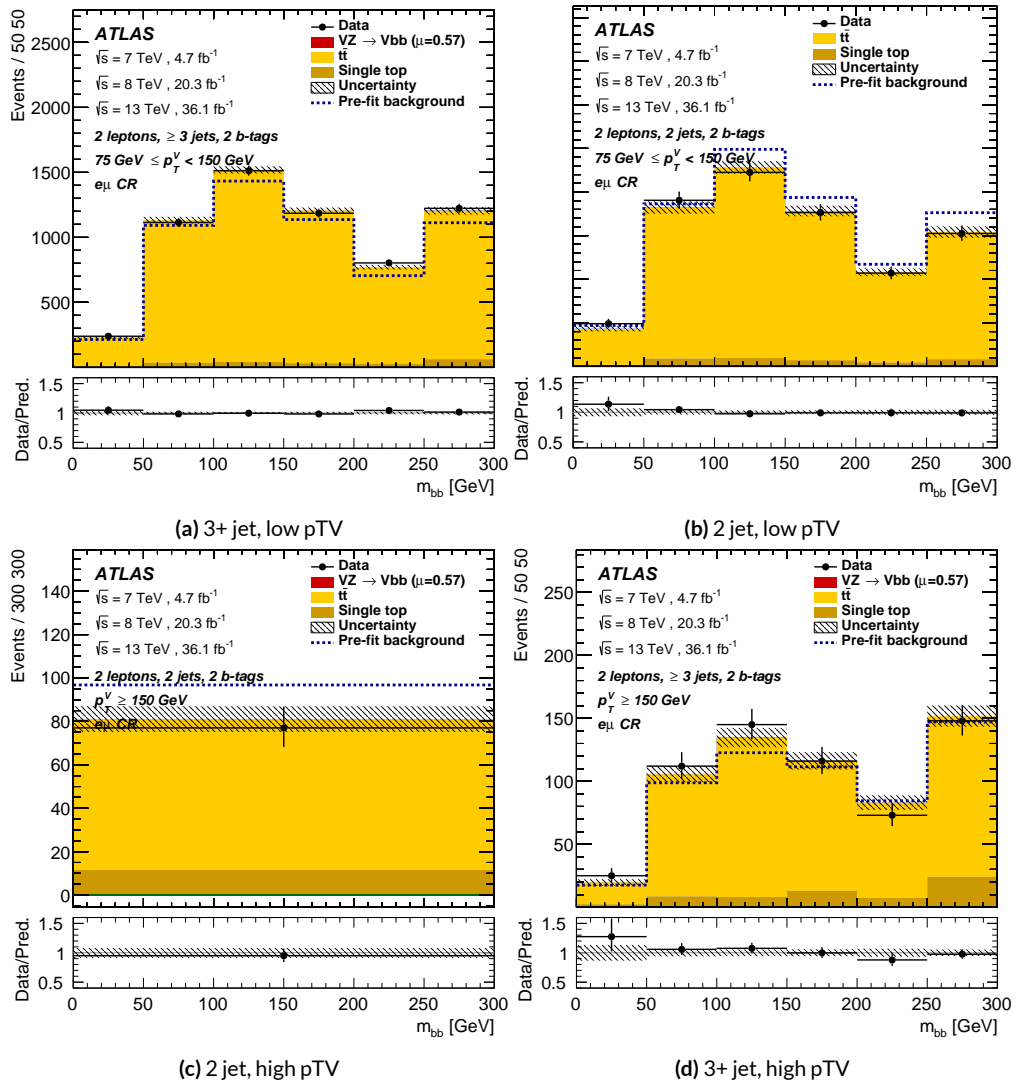
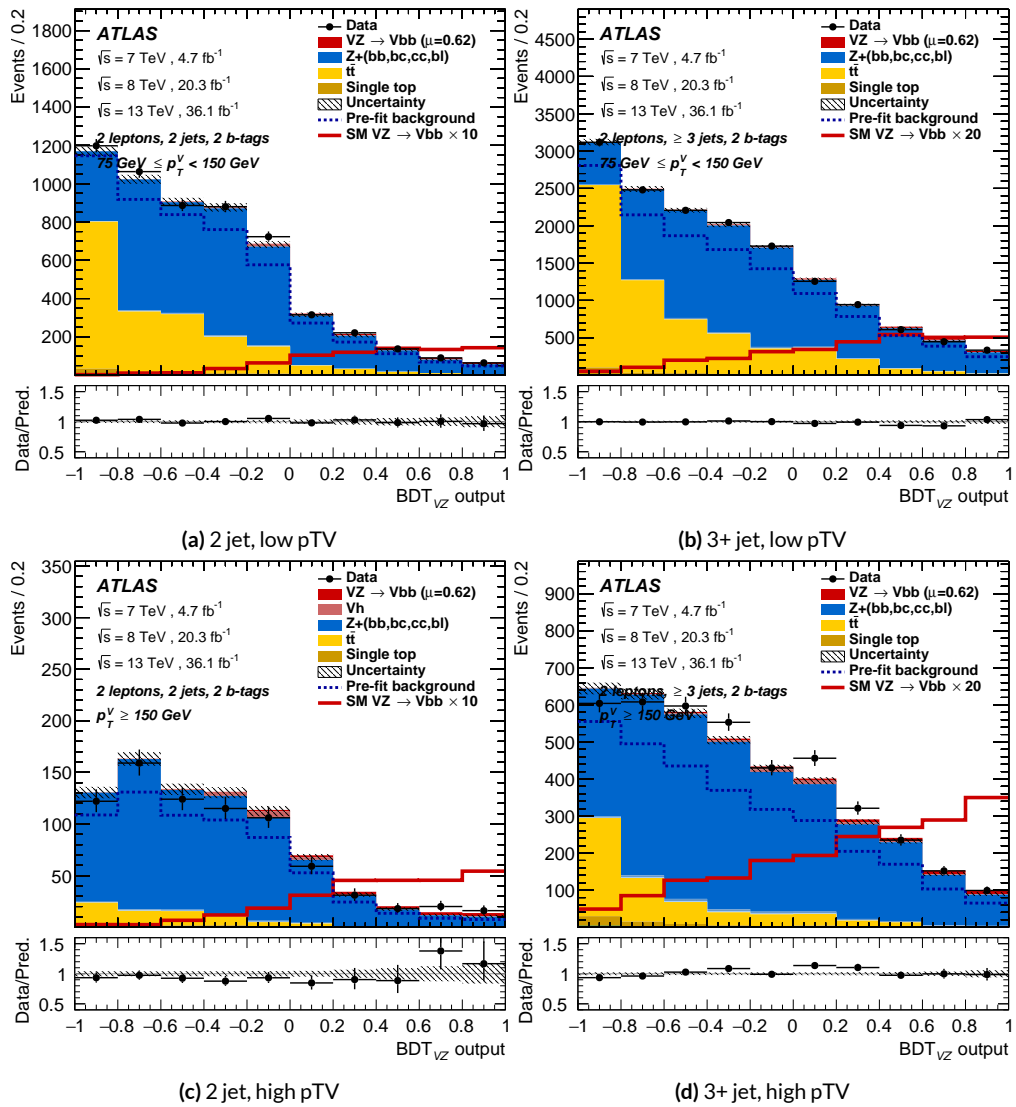
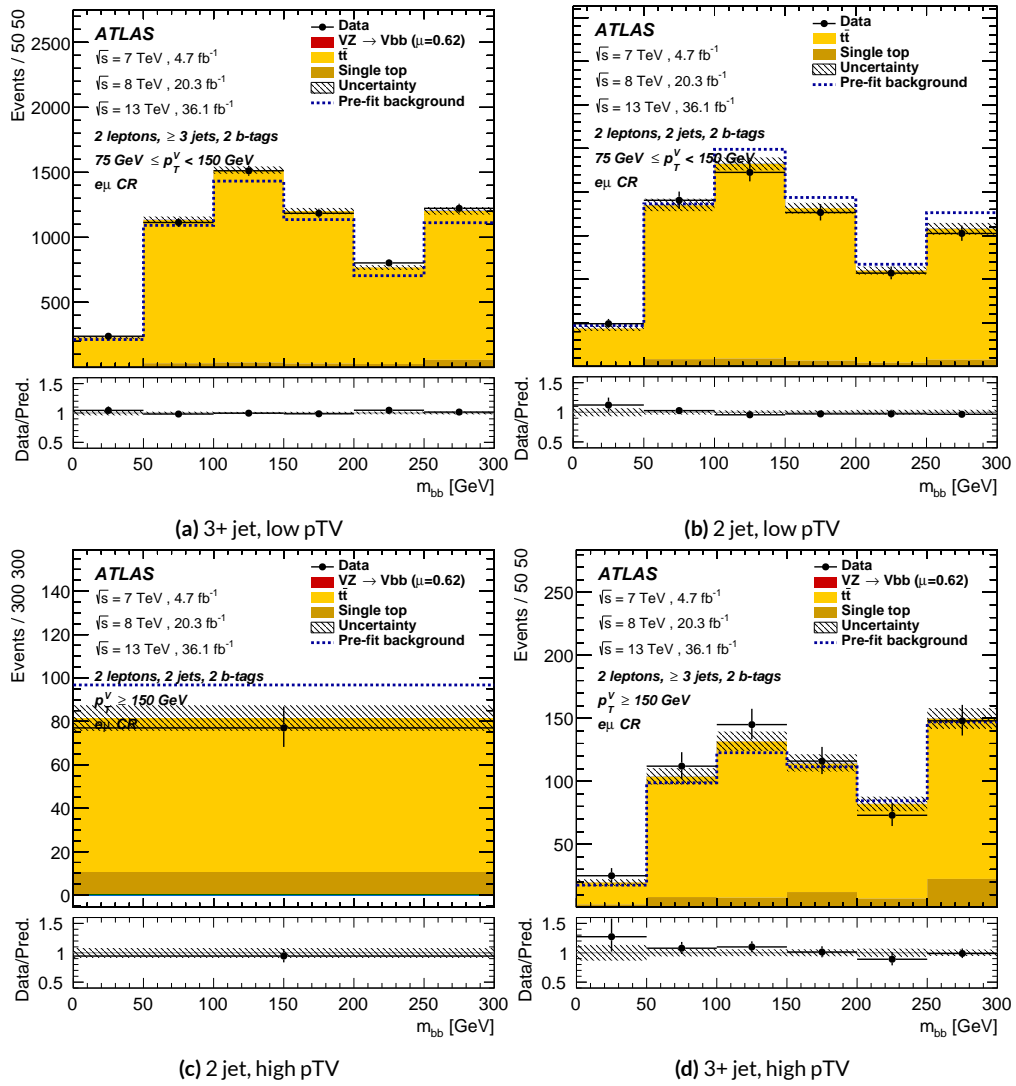


Figure 7.17: Postfit  $m_{bb}$  plots in the top  $e - \mu$  CR for the LI variable set.



**Figure 7.18:** Postfit  $BDT_{VZ}$  plots in the signal region for the RF variable set.



**Figure 7.19:** Postfit  $m_{bb}$  plots in the top  $e - \mu$  CR for the RF variable set.

1799 7.7 VH FIT MODEL VALIDATION

We now move onto the fit validation distributions and numbers for the  $VH$  fit of interest.

### 1801 7.7.1 NUISANCE PARAMETER PULLS

As can be seen in Figures 7.20–7.24, the fits for the three different variable sets are fairly similar from a NP pull perspective. Again, black is the standard variable set, red is the LI set, and blue is the RF set. The possible exception is the signal UE+PS  $p_T^V$  systematic, which looks very different for all three cases (underconstrained for the standard, but overconstrained for the novel variable cases), though this difference goes away in the ranking plot, meaning this is almost certainly an unphysical artifice of the faster HESSE inversion used to produce the pull comparison plots.

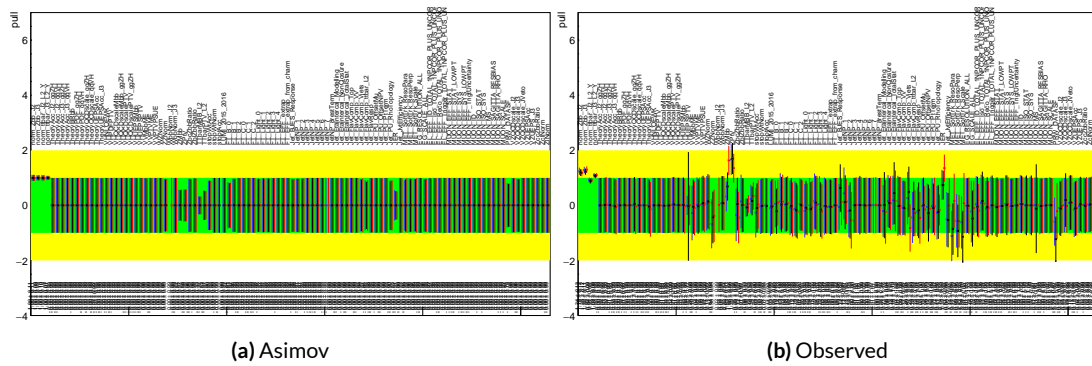


**Figure 7.20:** Pull comparison for all NP's but MC stats.

1808 Nuisance parameter correlation matrices (for correlations with magnitude at least 0.25) for all  
1809 three variable set fits can be found in Figures 7.26–7.28.

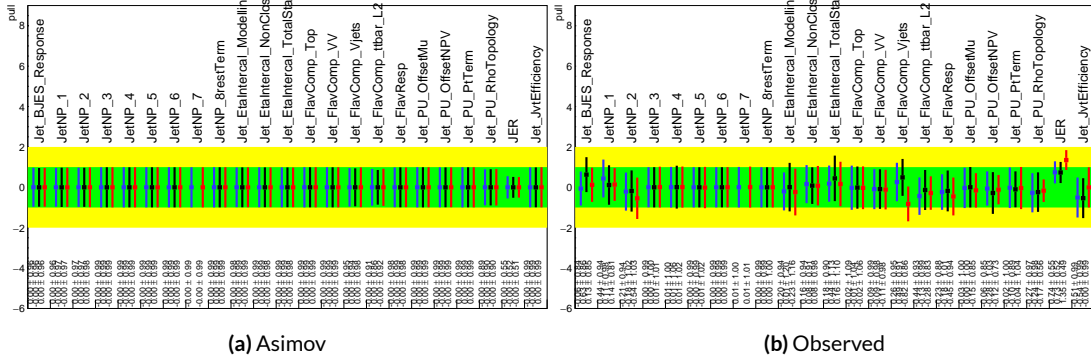


Figure 7.21: Pull comparison for jet NP's.

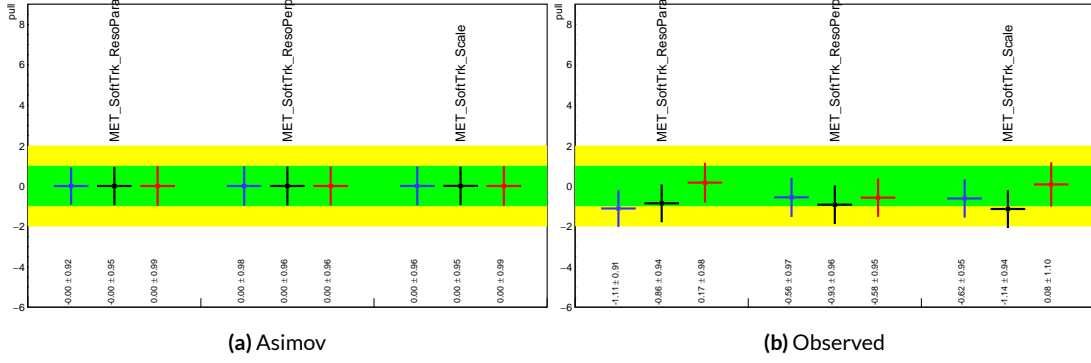


Figure 7.22: Pull comparison for MET NP's.

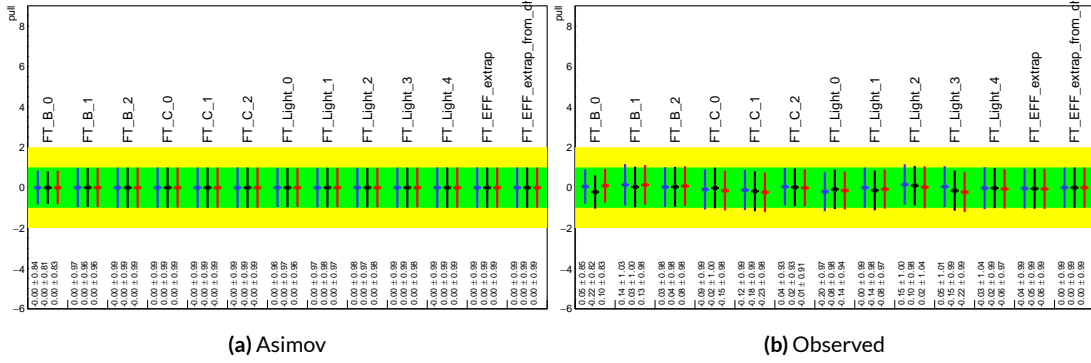


Figure 7.23: Pull comparison for Flavour Tagging NP's.

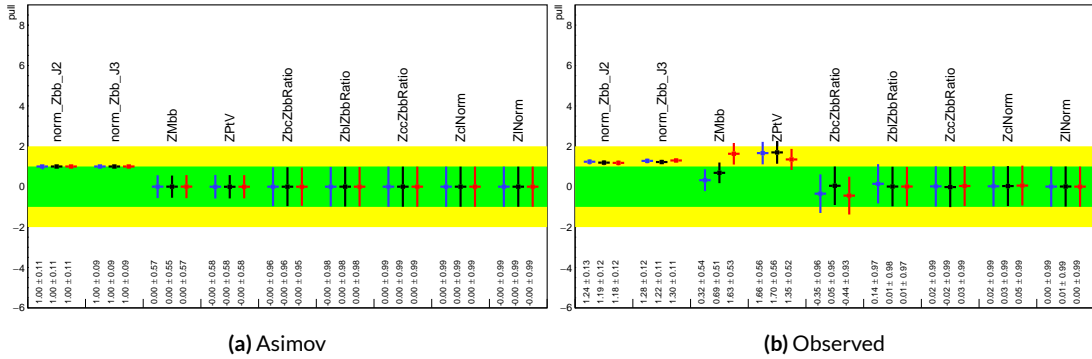


Figure 7.24: Pull comparison for  $Z + \text{jets}$  NP's.

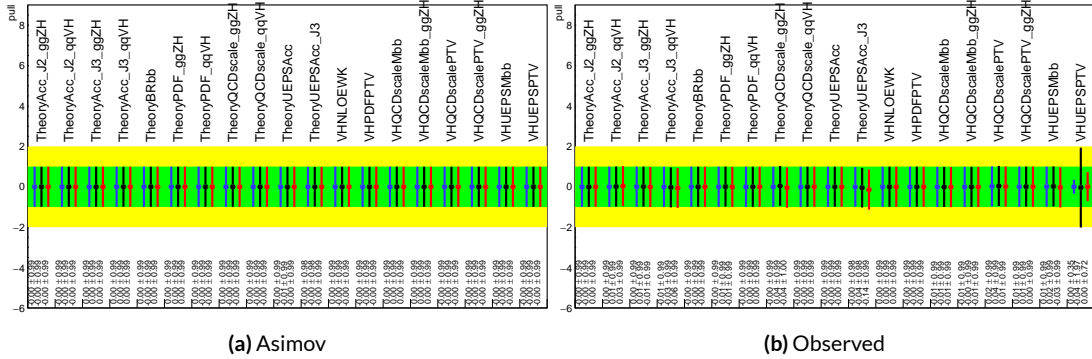


Figure 7.25: Pull comparison for signal process modeling NP's.

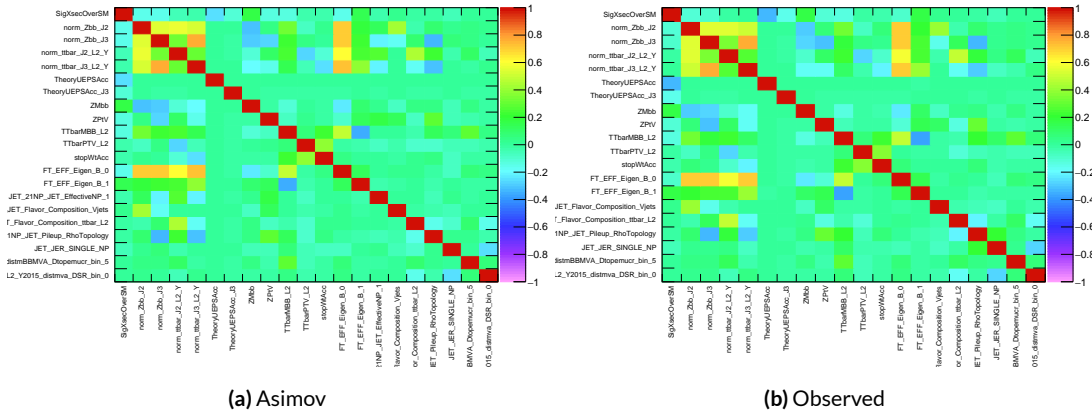


Figure 7.26: NP correlations for standard variable fits.

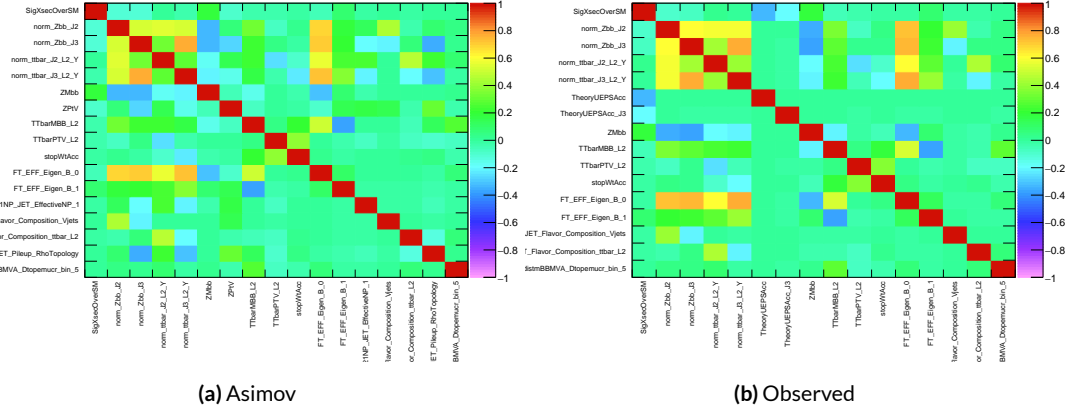


Figure 7.27: NP correlations for LI variable fits.

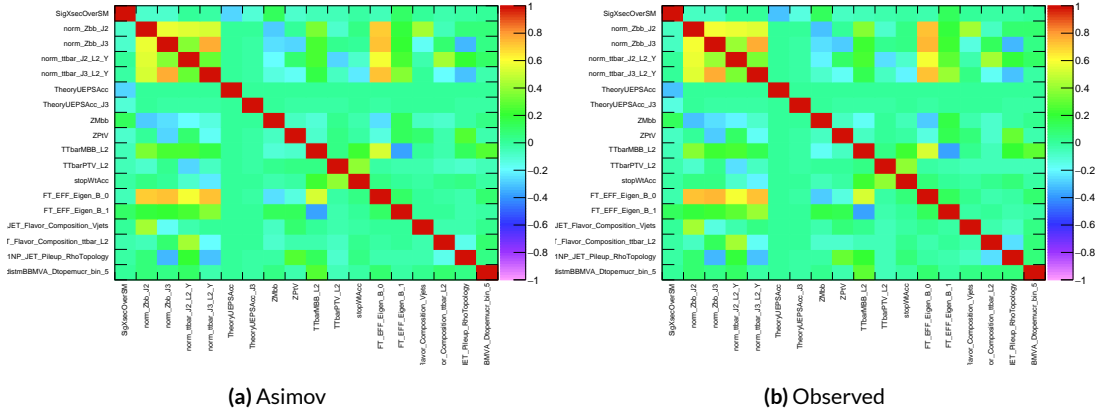
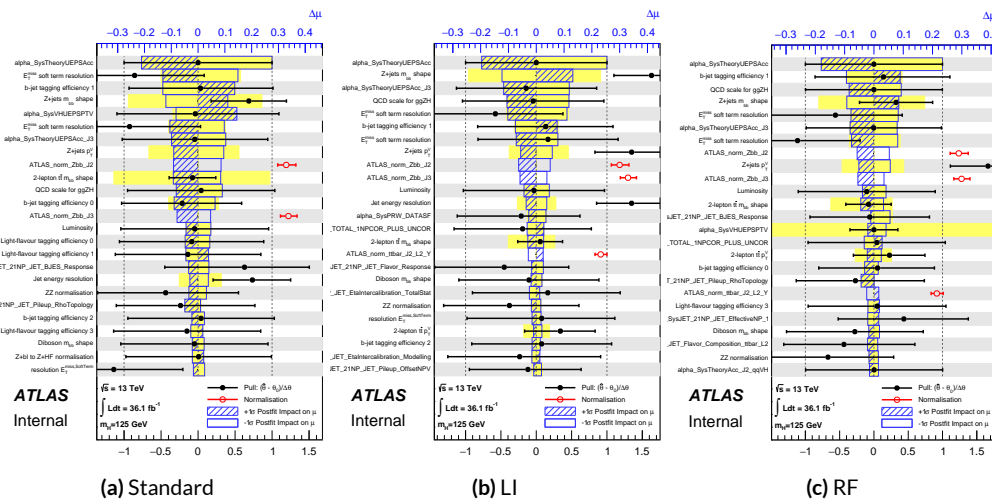


Figure 7.28: NP correlations for RF variable fits.

1810 7.7.2 FULL BREAKDOWN OF ERRORS

1811 A postfit ranking of nuisance parameters according to their impact on  $\hat{\mu}$  for the different variable  
 1812 sets may be found in Figure 7.29, with rankings being fairly similar. In particular, the signal UE+PS  
 1813  $p_T^V$  systematic is top-ranked for all three variable sets and also looks very similar, unlike in the pull  
 1814 comparison plot, reiterating the importance of evaluating individually the impact of highly ranked  
 1815 NP's. The  $Z+$ jets  $p_T^V$  is highly pulled in all three cases, though this is less severe for the non-standard  
 1816 set (it is off the scale for the standard variable ranking). The RF discriminant mitigates the effect of  
 1817 poorly modeled jet energy resolution better than the other sets.



**Figure 7.29:** Plots for the top 25 nuisance parameters according to their postfit impact on  $\hat{\mu}$  for the standard (a), LI (b), and RF (c) variable sets.

The Asimov (Table 7.7) and observed (Table 7.8) breakdowns both consistently suggest that the LI variable set does a better job of constraining systematic uncertainties than the standard set and that the RF set does better still. It is also not surprising that the gain is more substantial in the ob-

<sup>1821</sup> served fit than in the Asimov fits, as in the latter there are the “penalty” terms from pulls in addition  
<sup>1822</sup> to the overall broadening in the likelihood.

	Std-KF	LI+MET	RF
Total	+0.608 / -0.511	+0.632 / -0.539	+0.600 / -0.494
DataStat	+0.420 / -0.401	+0.453 / -0.434	+0.424 / -0.404
FullSyst	+0.440 / -0.318	+0.441 / -0.319	+0.425 / -0.284
Floating normalizations	+0.122 / -0.125	+0.110 / -0.111	+0.093 / -0.089
All normalizations	+0.128 / -0.129	+0.112 / -0.112	+0.099 / -0.092
All but normalizations	+0.403 / -0.274	+0.387 / -0.250	+0.382 / -0.227
Jets, MET	+0.180 / -0.097	+0.146 / -0.079	+0.122 / -0.083
Jets	+0.051 / -0.030	+0.044 / -0.035	+0.025 / -0.042
MET	+0.173 / -0.091	+0.140 / -0.074	+0.117 / -0.063
BTag	+0.138 / -0.136	+0.069 / -0.071	+0.076 / -0.078
BTag b	+0.125 / -0.125	+0.067 / -0.070	+0.073 / -0.075
BTag c	+0.018 / -0.016	+0.004 / -0.004	+0.005 / -0.005
BTag light	+0.057 / -0.051	+0.020 / -0.014	+0.009 / -0.018
Leptons	+0.013 / -0.012	+0.029 / -0.026	+0.012 / -0.023
Luminosity	+0.052 / -0.020	+0.050 / -0.016	+0.050 / -0.019
Diboson	+0.043 / -0.039	+0.035 / -0.031	+0.038 / -0.029
Model Zjets	+0.119 / -0.117	+0.124 / -0.127	+0.095 / -0.086
Zjets flt. norm.	+0.080 / -0.106	+0.052 / -0.092	+0.026 / -0.072
Model Wjets	+0.001 / -0.001	+0.001 / -0.001	+0.000 / -0.001
Wjets flt. norm.	+0.000 / -0.000	+0.000 / -0.000	+0.000 / -0.000
Model ttbar	+0.076 / -0.080	+0.025 / -0.035	+0.025 / -0.040
Model Single Top	+0.015 / -0.015	+0.002 / -0.004	+0.021 / -0.007
Model Multi Jet	+0.000 / -0.000	+0.000 / -0.000	+0.000 / -0.000
Signal Systematics	+0.262 / -0.087	+0.272 / -0.082	+0.290 / -0.088
MC stat	+0.149 / -0.136	+0.168 / -0.154	+0.153 / -0.136

**Table 7.7:** Expected error breakdowns for the standard, LI, and RF variable sets

	Std-KF	LI+MET	RF
$\hat{\mu}$	1.7458	1.6467	1.5019
Total	+0.811 / -0.662	+0.778 / -0.641	+0.731 / -0.612
DataStat	+0.502 / -0.484	+0.507 / -0.489	+0.500 / -0.481
FullSyst	+0.637 / -0.451	+0.591 / -0.415	+0.533 / -0.378
Floating normalizations	+0.153 / -0.143	+0.128 / -0.118	+0.110 / -0.109
All normalizations	+0.158 / -0.147	+0.130 / -0.119	+0.112 / -0.110
All but normalizations	+0.599 / -0.402	+0.544 / -0.354	+0.486 / -0.318
Jets, MET	+0.218 / -0.145	+0.198 / -0.113	+0.167 / -0.106
Jets	+0.071 / -0.059	+0.065 / -0.047	+0.036 / -0.051
MET	+0.209 / -0.130	+0.190 / -0.102	+0.152 / -0.077
BTAG	+0.162 / -0.166	+0.093 / -0.070	+0.115 / -0.099
BTAG b	+0.142 / -0.147	+0.090 / -0.066	+0.110 / -0.094
BTAG c	+0.022 / -0.021	+0.006 / -0.006	+0.007 / -0.007
BTAG light	+0.074 / -0.072	+0.025 / -0.022	+0.031 / -0.029
Leptons	+0.039 / -0.029	+0.035 / -0.031	+0.034 / -0.030
Luminosity	+0.079 / -0.039	+0.073 / -0.034	+0.069 / -0.032
Diboson	+0.047 / -0.043	+0.031 / -0.028	+0.029 / -0.028
Model Zjets	+0.164 / -0.152	+0.141 / -0.143	+0.101 / -0.105
Zjets flt. norm.	+0.070 / -0.109	+0.041 / -0.086	+0.033 / -0.083
Model Wjets	+0.001 / -0.001	+0.001 / -0.000	+0.001 / -0.001
Wjets flt. norm.	+0.000 / -0.000	+0.000 / -0.000	+0.000 / -0.000
Model ttbar	+0.067 / -0.102	+0.029 / -0.040	+0.040 / -0.048
Model Single Top	+0.015 / -0.020	+0.001 / -0.005	+0.004 / -0.006
Model Multi Jet	+0.000 / -0.000	+0.000 / -0.000	+0.000 / -0.000
Signal Systematics	+0.434 / -0.183	+0.418 / -0.190	+0.364 / -0.152
MC stat	+0.226 / -0.201	+0.221 / -0.200	+0.212 / -0.189

**Table 7.8:** Observed signal strengths, and error breakdowns for the standard, LI, and RF variable sets

1823 7.7.3 POSTFIT DISTRIBUTIONS AND S/B PLOTS

1824 Postfit distributions for the MVA discriminant ( $m_{bb}$ ) distribution in the signal (top  $e - \mu$  control)  
1825 region for the standard, Lorentz Invariant, and RestFrames variable sets are found in Figures 7.30–  
1826 7.35. Here, as in the  $VZ$  fit, agreement is reasonable. In a combined fit with all three channels,  $Z+hf$   
1827 normalizations in particular would be correlated across the 0- and 2-lepton channels, which might  
1828 help to better constrain this mismodeling (and perhaps as a result some of the  $Z+jets$  systematics as  
1829 well).

1830 One final type of plot presented as a result is the binned  $\log_{10} (S/B)$  in signal regions distribu-  
1831 tions may be found in Figure 7.36. For these plots, one fills a histogram with the  $\log_{10} (S/B)$  ratio in  
1832 each postfit distribution bin weighted by the total number of events. In this case, a log plot is help-  
1833 ful because the highest bins would be invisible on a linear plot. These distributions are allegedly use-  
1834 ful for seeing where most of one's sensitivity lies. Practically, it is problematic if the pull (from the  
1835 null hypothesis) is higher at lower  $S/B$  values, which may indicate a poorly optimized discriminant.

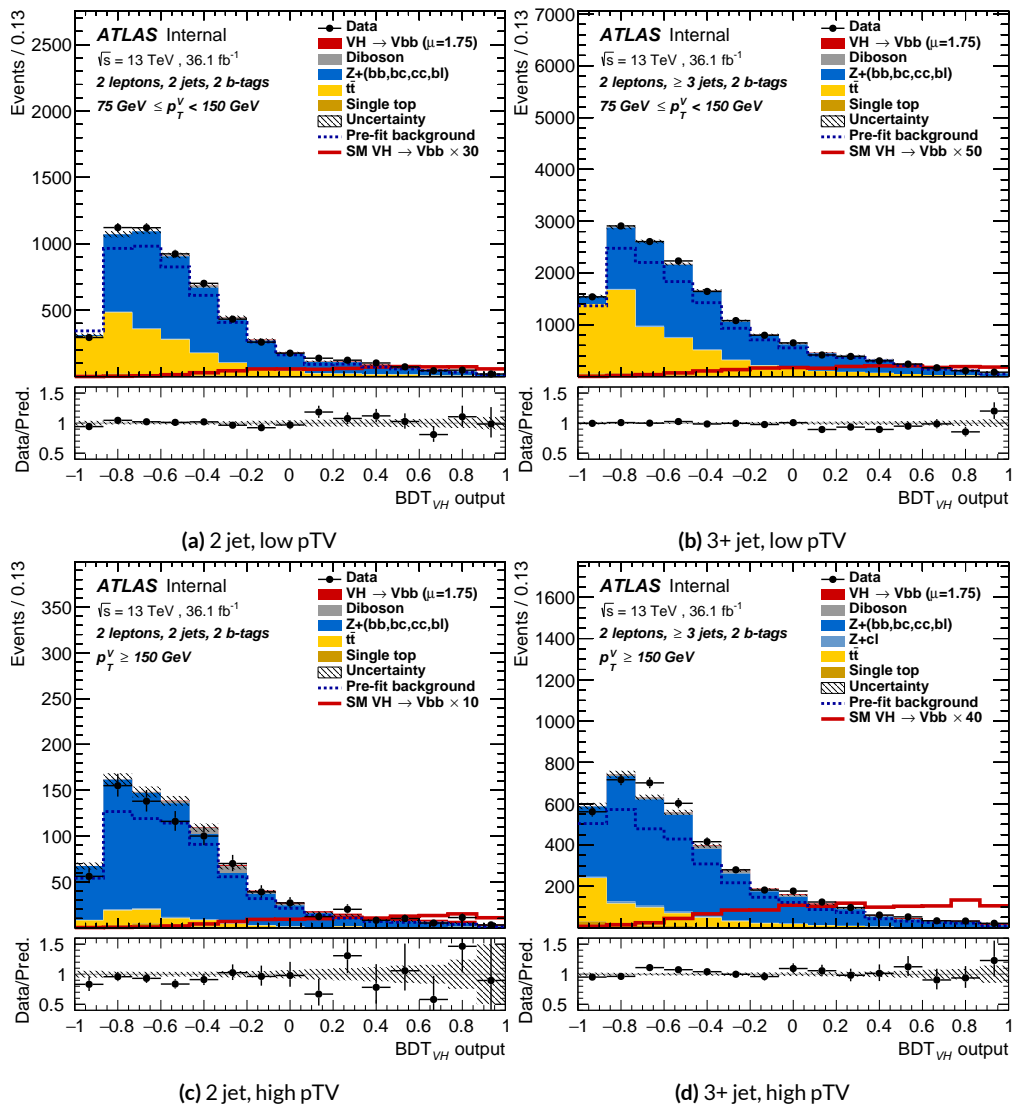


Figure 7.30: Postfit  $BDT_{VH}$  plots in the signal region for the standard variable set.

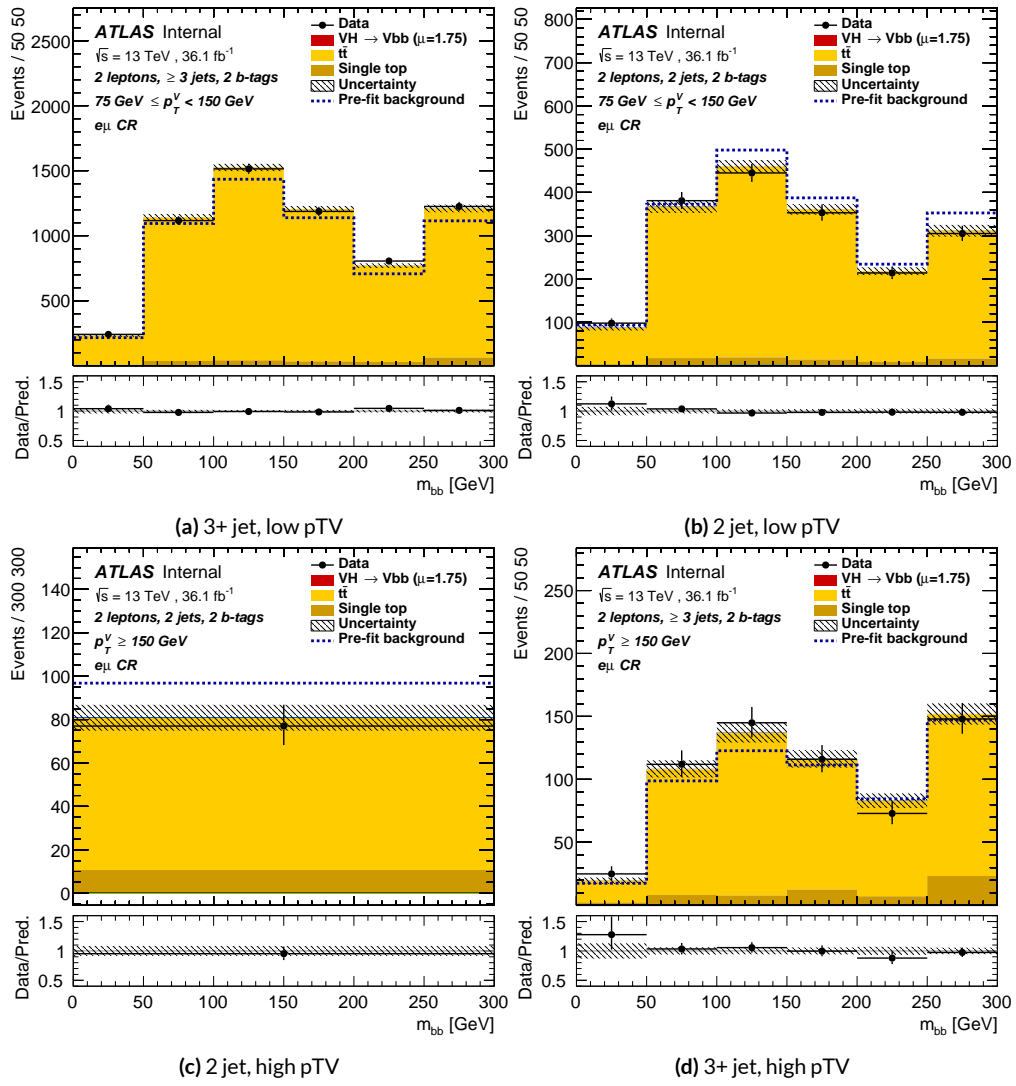


Figure 7.31: Postfit  $m_{bb}$  plots in the top  $e - \mu$  CR for the standard variable set.

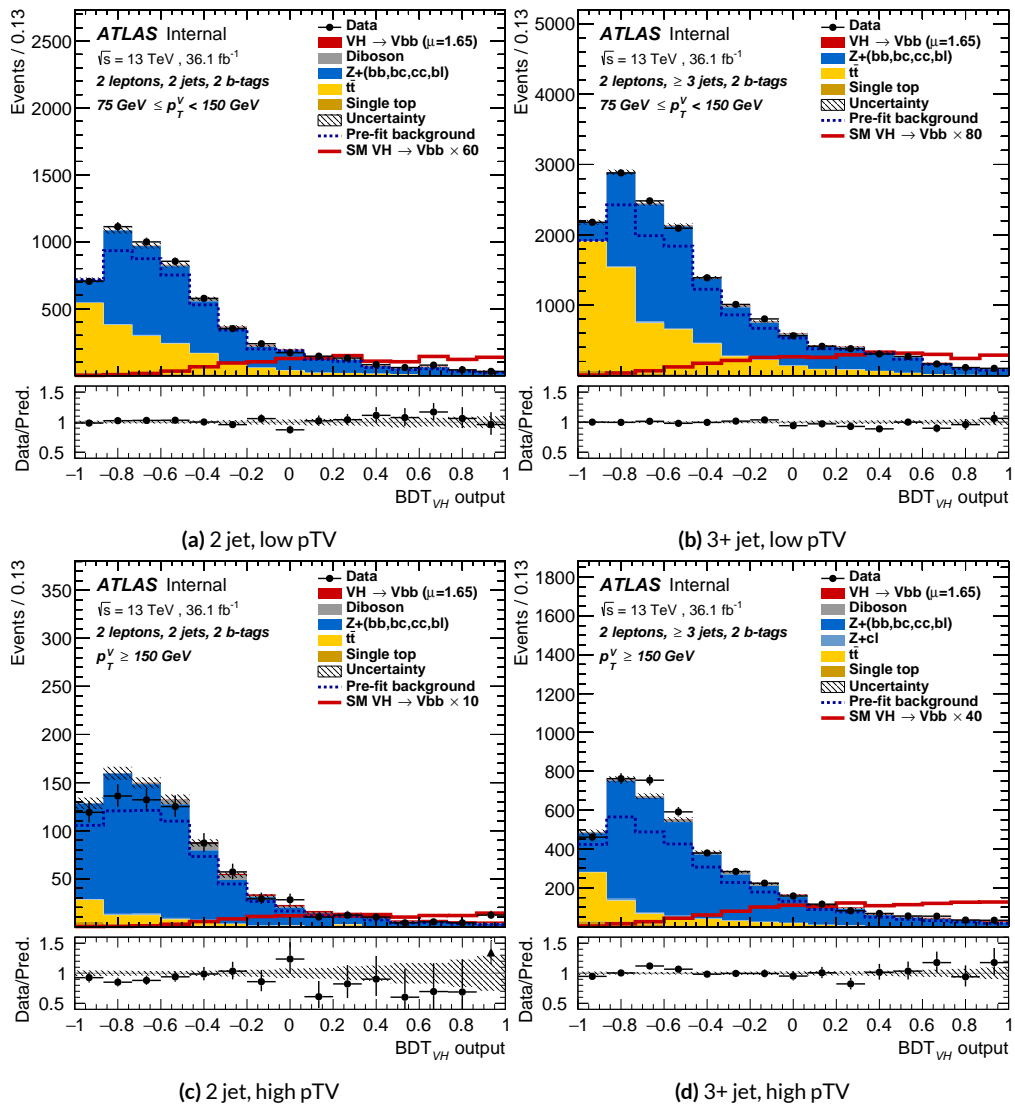


Figure 7.32: Postfit  $BDT_{VH}$  plots in the signal region for the LI variable set.

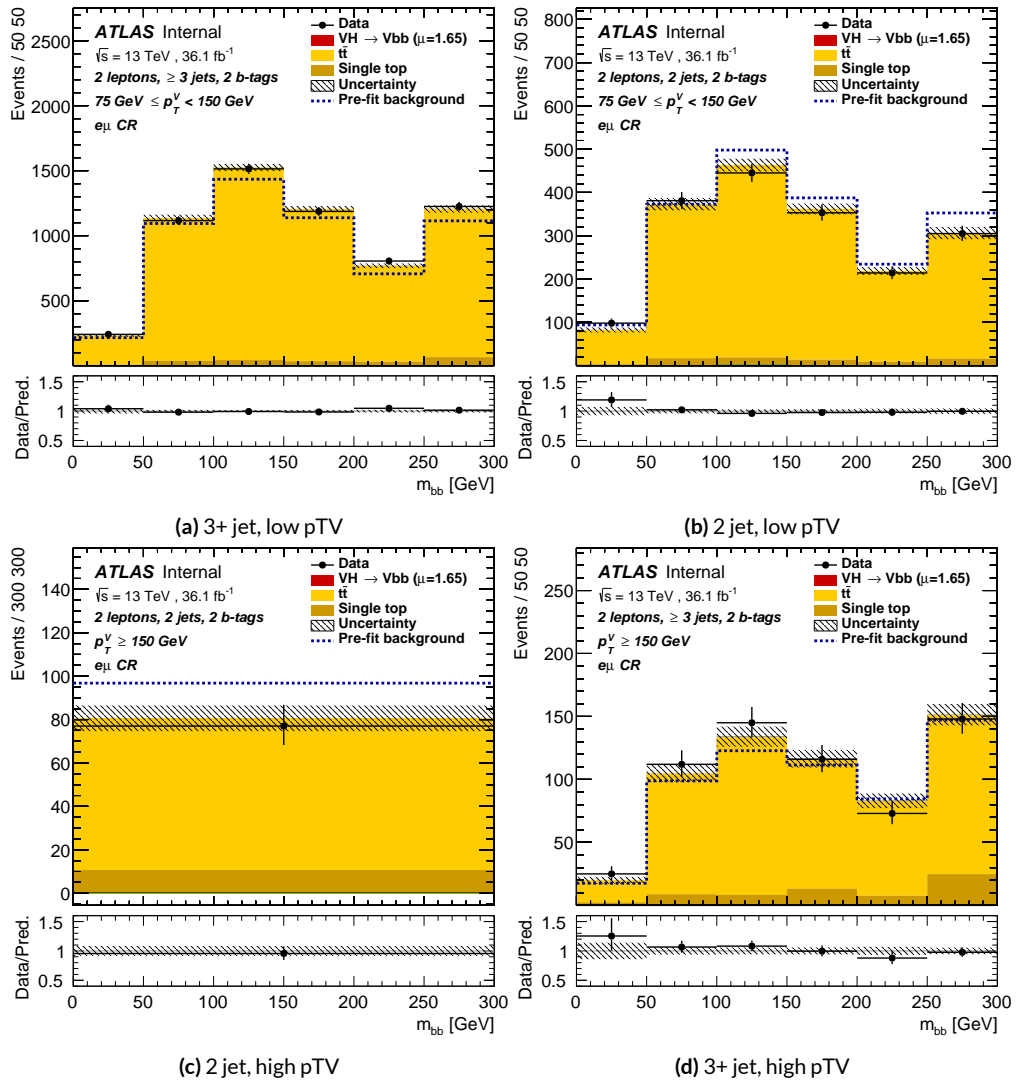


Figure 7.33: Postfit  $m_{bb}$  plots in the top  $e - \mu$  CR for the LI variable set.

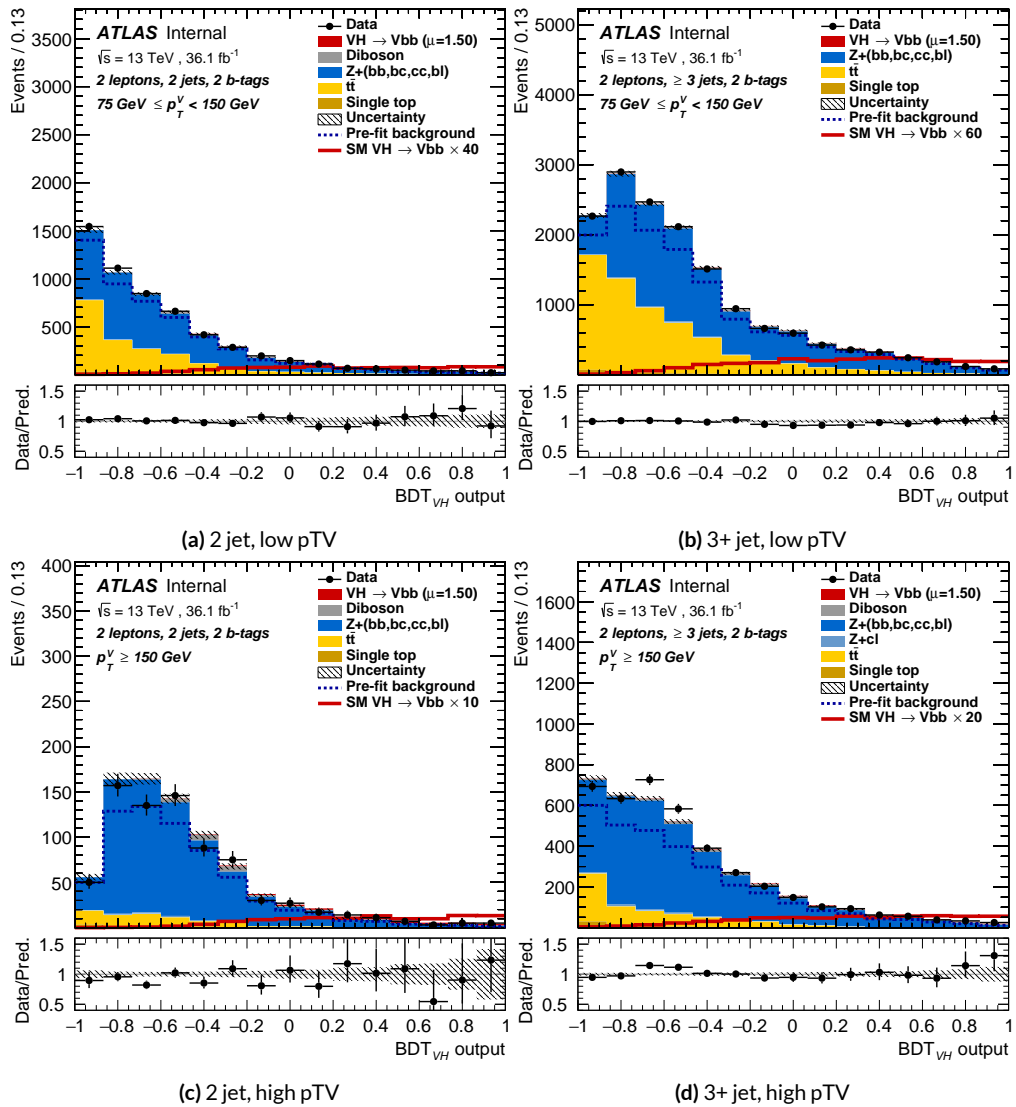
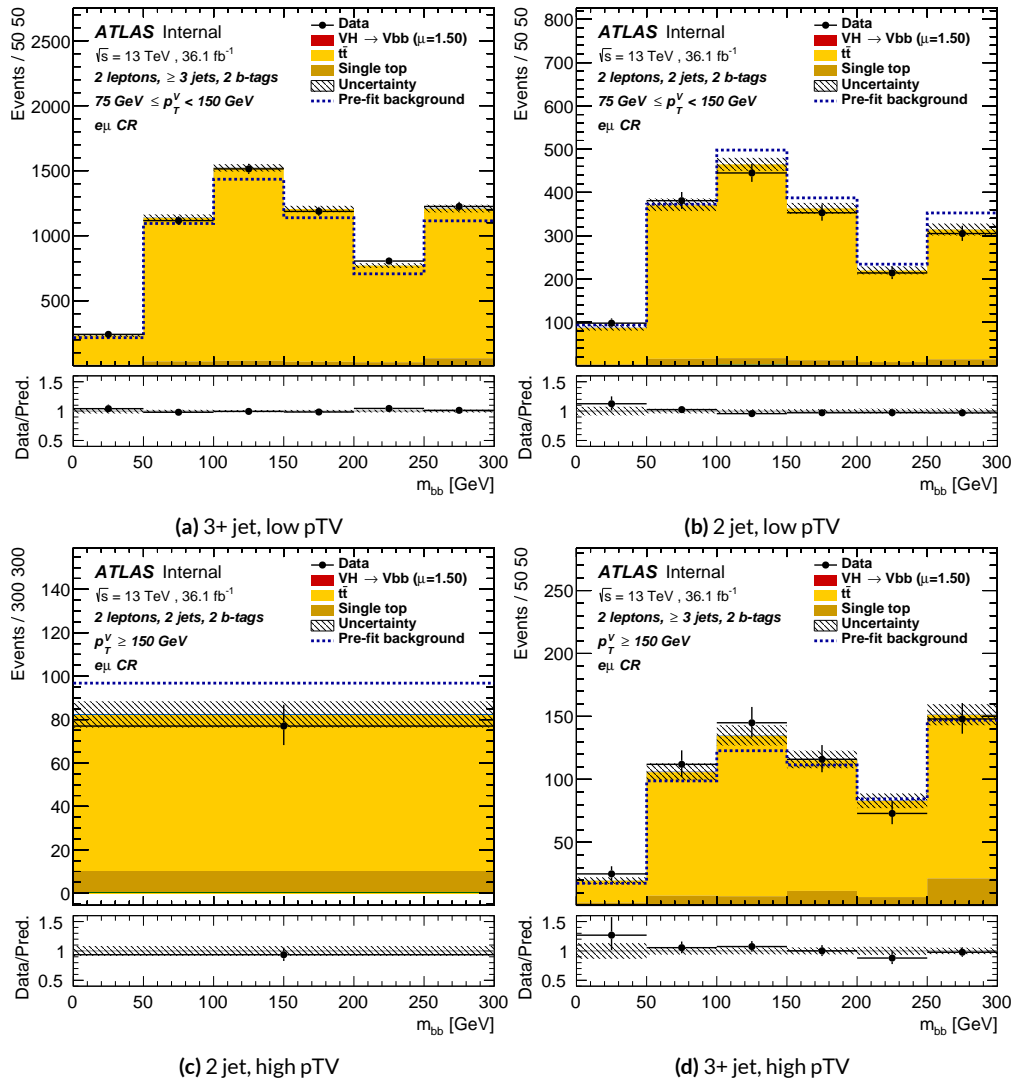
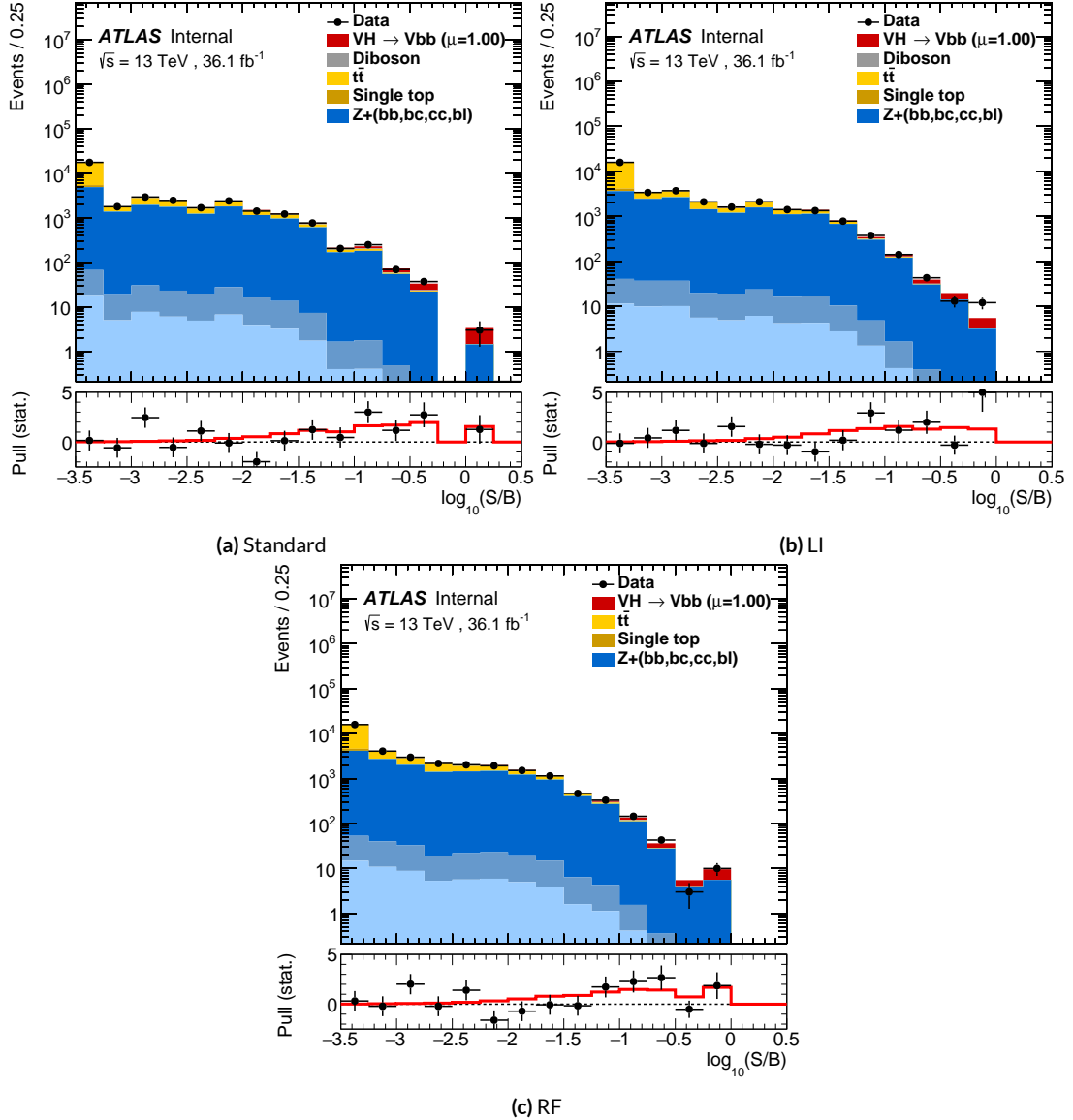


Figure 7.34: Postfit  $BDT_{VH}$  plots in the signal region for the RF variable set.



**Figure 7.35:** Postfit  $m_{bb}$  plots in the top  $e - \mu$  CR for the RF variable set.



**Figure 7.36:** Binned S/B plots for the standard (a), LI (b), and RF (c) variable sets. Signal is weighted to  $\mu = 1$  for comparison to the SM prediction.

*Kein Operationsplan reicht mit einiger Sicherheit  
über das erste Zusammentreffen mit der feindlichen  
Hauptmacht hinaus.*

Helmuth von Moltke

1836

# 8

1837

## Fit Results

1838 THE RESULTS IN THIS CHAPTER were first reported in [37] and describe how the three different fit  
1839 models detailed and validated Chapter 7, corresponding to the standard, RF, and LI variable sets  
1840 described in Chapter 6 perform on actual  $VH$  fits. In particular sensitivities, nuisance parameter  
1841 impacts, and signal strengths on expected fits to Asimov datasets and both expected and observed

1842 fits on the actual  $36.1 \text{ fb}^{-1}$  dataset are compared.

1843 Expected and observed sensitivities for the different variable sets may be found in Table 8.1. The  
1844 RF fits feature the highest expected sensitivities, outperforming the standard set by 3.5% and 3.4%  
1845 for fits to Asimov and observed datasets, respectively. The LI variable has a lower significance than  
1846 both for expected fits to both Asimov and data with a 6.7% (1.7%) significance than the standard set  
1847 for the Asimov (observed) dataset. While the fit using standard variables does have a higher observed  
1848 significance than both the LI and RF fits, by 2.8% and 8.6%, respectively, these numbers should be  
1849 viewed in the context of the best fit  $\hat{\mu}$  values, discussed below. That is, the standard set may yield the  
1850 highest sensitivity for this particular dataset, but this is not necessarily (and likely is not) the case for  
1851 any given dataset.

	Standard	LI	RF
Expected (Asimov)	2.06	1.92	2.13
Expected (data)	1.76	1.73	1.80
Observed (data)	2.87	2.79	2.62

**Table 8.1:** Expected (for both data and Asimov) and observed significances for the standard, LI, and RF variable sets.

1852 A summary of fitted signal strengths and errors for both the Asimov (a) and observed (b) datasets  
1853 are shown in Figure 8.1.\* A summary of error breakdowns is given in Tables 8.2 (Asimov) and 8.3  
1854 (observed) for total error, data statistics contributions, total systematic error contributions, and cat-  
1855 egories for which the total impact is  $\geq 0.1$  for the standard fit. As is to be expected for both the  
1856 Asimov and observed dataset fits, the contribution to the total error on  $\mu$  arising from data statistics

---

\*For reference, the standalone 2-lepton fit from the fiducial analysis is  $2.11^{+0.50}_{-0.48}(\text{stat.})^{+0.64}_{-0.47}(\text{syst.})$

<sup>1857</sup> is nearly identical, since each set of fits uses the same selections and data.<sup>†</sup>

	Std-KF	LI+MET	RF
Total	+0.608 / -0.511	+0.632 / -0.539	+0.600 / -0.494
DataStat	+0.420 / -0.401	+0.453 / -0.434	+0.424 / -0.404
FullSyst	+0.440 / -0.318	+0.441 / -0.319	+0.425 / -0.284
Signal Systematics	+0.262 / -0.087	+0.272 / -0.082	+0.290 / -0.088
MET	+0.173 / -0.091	+0.140 / -0.074	+0.117 / -0.063
Flavor Tagging	+0.138 / -0.136	+0.069 / -0.071	+0.076 / -0.078
Model Zjets	+0.119 / -0.117	+0.124 / -0.127	+0.095 / -0.086

**Table 8.2:** Summary of error impacts on total  $\mu$  error for principal categories in the Asimov standard, LI, and RF fits.

	Std-KF	LI+MET	RF
Total	+0.811 / -0.662	+0.778 / -0.641	+0.731 / -0.612
DataStat	+0.502 / -0.484	+0.507 / -0.489	+0.500 / -0.481
FullSyst	+0.637 / -0.451	+0.591 / -0.415	+0.533 / -0.378
Signal Systematics	+0.434 / -0.183	+0.418 / -0.190	+0.364 / -0.152
MET	+0.209 / -0.130	+0.190 / -0.102	+0.152 / -0.077
Flavor Tagging	+0.162 / -0.166	+0.093 / -0.070	+0.115 / -0.099
Model Zjets	+0.164 / -0.152	+0.141 / -0.143	+0.101 / -0.105

**Table 8.3:** Summary of error impacts on total  $\hat{\mu}$  error for principal categories in the observed standard, LI, and RF fits.

<sup>1858</sup> The contribution from systematic uncertainties, however, does vary considerably across the vari-  
<sup>1859</sup> able sets. The Asimov fits are a best case scenario in the sense that, by construction, all NP's are equal  
<sup>1860</sup> to their predicted values (and so no "penalty" is paid for pulls on Gaussian NP's). The systematics er-  
<sup>1861</sup> ror from the LI fit is slightly higher (subpercent) than that from the standard fit, and 4.6% higher er-  
<sup>1862</sup> ror overall due to differences in data stats. The RF Asimov fit, however, has a 6.5% lower total error

---

<sup>†</sup>Though not exactly identical. Since the BDT's are different for the different variable sets, the binning (as determined by transformation D) and bin contents in each set are generally different, leading to slightly different data statistics errors.

1863 from systematics than the standard Asimov fit (and a 2.2% lower error overall). Moreover, for both  
 1864 the LI and RF sets, errors are markedly smaller for the MET and Flavor Tagging categories, with the  
 1865 RF fit also featuring a smaller errors on  $Z$ +jets modeling; the only notable exception to this trend in  
 1866 Asimov fits are the signal systematics.

1867 These trends are more pronounced in the observed fits. As can be seen in Table 8.3, both the LI  
 1868 and RF fits have smaller errors from systematic uncertainties, both overall and in all principal cate-  
 1869 gories, with the LI and RF fits having 7.5% (3.7%) and 16% (8.8%) lower systematics (total) error on  
 1870  $\hat{\mu}$ , respectively.

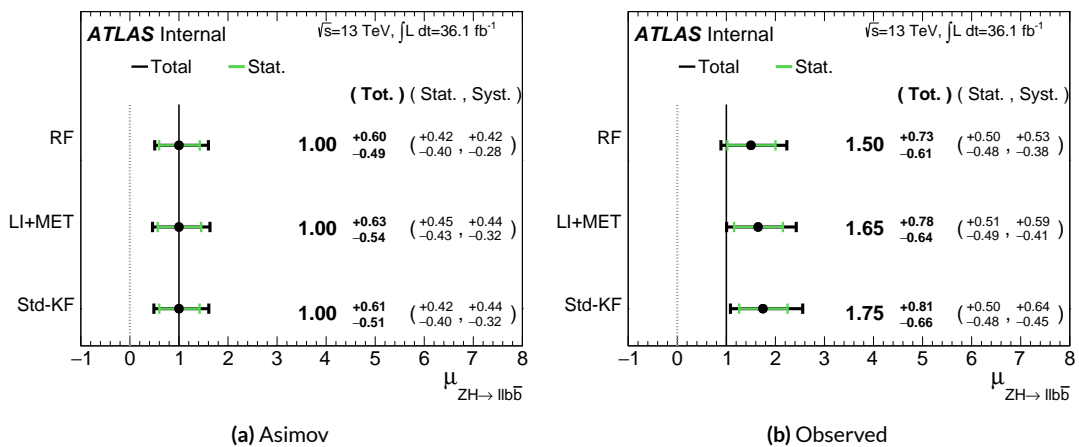


**Figure 8.1:**  $\mu$  summary plots for the standard, LI, and RF variable sets. The Asimov case (with  $\mu = 1$  by construction) is in (a), and  $\hat{\mu}$  best fit values and error summary are in (b).

1871 Studying the performance of the Lorentz Invariant and RestFrames variable sets at both a data  
 1872 statistics only context and with the full fit model in the  $ZH \rightarrow \ell\ell b\bar{b}$  channel of the  $VH(b\bar{b})$  anal-  
 1873 ysis suggests that these variables may offer a potential method for better constraining systematic un-  
 1874 certainties in  $VH(b\bar{b})$  searches as more orthogonal bases in describing the information in collision

1875 events.

1876 The marginally worse performance of the LI and RF variables (7.9% and 6.9%, respectively) with  
1877 respect to the standard variable at a stats only level illustrates that neither variable set has greater  
1878 intrinsic descriptive power in the absence of systematics in this closed final state. Hence, any gains  
1879 from either of these variable sets in a full fit come from improved treatment of systematic uncertain-  
1880 ties.

1881 With full systematics, the LI variable set narrows the sensitivity gap somewhat, with lower signif-  
1882 icances by 6.7% (1.7%) on expected fits to Asimov (data) and by 2.8% on observed significances. The  
1883 RF variable set outperforms the standard set in expected fits with 3.5% (3.4%) higher significance  
1884 on Asimov (data), but has an 8.6% lower observed significance, though the observed significances  
1885 should be viewed in the context of observed  $\hat{\mu}$  values.

1886 Moreover, the LI and RF variable sets generally perform better in the context of the error on  $\mu$ .  
1887 The LI fit is comparable to the standard set on Asimov data and has a 7.5% lower total systematics er-  
1888 ror on  $\hat{\mu}$  on observed data, while the RF fit is lower in both cases, with systematics error being 6.5%  
1889 (16%) lower on Asimov (observed) data.

1890 These figures of merit suggest that both the LI and RF variables are more orthogonal than the  
1891 standard variable set used in the fiducial analysis. Moreover, the RF variable set does seem to con-  
1892 sistently perform better than the LI set. Furthermore, both variable sets have straightforward exten-  
1893 sions to the other lepton channels in the  $VH(b\bar{b})$  analysis. The magnitude of any gain from the  
1894 more sophisticated treatment of  $E_T^{miss}$  in these extensions is beyond the scope of these studies, but  
1895 the performance in this closed final state do suggest that there is some value to be had in these non-

<sup>1896</sup> standard descriptions independent of these considerations.

*If I have seen further, it is by standing on ye shoulders of  
giants.*

Isaac Newton

# 9

1897

1898

## Measurement Combinations

1899 WHILE THE DISCUSSION thus far has focused on improvements looking towards future in just the  
1900  $ZH \rightarrow \ell\ell b\bar{b}$  channel, any actual result for SM  $VH(b\bar{b})$  combines all channels and all available  
1901 datasets. Using additional channels at a given center of mass energy is straightforward since the fit  
1902 model is designed with this combination in mind. Combining dataset results (known as “workspaces”)

1903 from different center of mass energies is not so simple an exercise since both the underlying physics  
1904 (and its associated modeling) and the treatment of key experimental considerations, like flavor tag-  
1905 ging, and their associated systematics change from dataset to dataset. A combined fit model must  
1906 take these considerations into account, and the formulation of the fit model combining the Run  
1907 1 ( $\sqrt{s} = 7$  TeV with  $4.7 \text{ fb}^{-1}$  of data, and  $\sqrt{s} = 8$  TeV with  $20.3 \text{ fb}^{-1}$  of data) and Run 2 ( $\sqrt{s} = 13$   
1908 TeV with  $36.1 \text{ fb}^{-1}$ ) SM  $VH(b\bar{b})$  results is the topic of Section 9.1. Its results, as reported in [42], are  
1909 given in 9.2.

## 1910 9.1 THE COMBINED FIT MODEL

1911 It is clear the signal strength parameter of interest should be fully correlated among the different  
1912 datasets. Some signal modeling systematics were left unchanged from Run 1 through Run 2 and/or  
1913 were designed to be explicitly correlated. Beyond these two special cases, it is not immediately clear  
1914 what level of correlation should be imposed. The general methodology for settling upon a correla-  
1915 tion scheme is as follows:

- 1916 1. Identify which NP categories have significant impacts on  $\mu$
- 1917 2. Of these NP's, identify which have one-to-one correspondences or established correlation  
1918 schemes among  $\sqrt{s}$  values
- 1919 3. Test whether correlation has a sizeable impact on expected fit quantities

1920 The only two sizeable experimental NP categories are jet energy scale (JES) and flavor tagging sys-  
1921 tematics. Correlation schemes of varying degrees of completeness exist for these categories, so ex-  
1922 plicit NP correlations can be tested for these two categories. As these studies were conducted before

1923 unblinding, “sizeable impact” was judged by comparing fit results (sensitivities, pull comparisons,  
1924 and breakdowns) on combined workspaces using the unblinded and public  $\mu = 0.51$  result for  
1925 Run 1 and Asimov data for the Run 2 result. These are treated in Sections 9.1.1 and 9.1.2. Modeling  
1926 systematics require a slightly different treatment, and are explored in 9.1.3.

1927 As noted in Chapter 7 when looking at pull comparison plots for combined workspaces, the error  
1928 bars in these plots are calculated using a simultaneous HESSE matrix inversion, which can fail to give  
1929 sensible values for high dimensional models (the combined workspaces have well over 500 NP’s).  
1930 This is not true of the nuisance parameter ranking plots, which use a MINOS based approach to test  
1931 the effect of each NP individually. This is much slower but much more rigorous, which is why only  
1932 ranking plots appear outside of supporting material and pull comparisons are considered “diagno-  
1933 tic” plots.

### 1934 9.1.1 JET ENERGY SCALE SYSTEMATICS

1935 Fortunately for the case of jet energy scale systematics, the JetEtMiss group provides two recom-  
1936 mended “strong” and “weak” correlation schemes between Run 1 and Run 2. These were used as  
1937 a point of departure for the JES combination correlation scheme. However, the JES NP’s in both  
1938 the Run 1 and Run 2 workspaces are a reduced set of NP’s, with some 56 (75) NP’s reduced to 6 (8)  
1939 for Run 1 (2). In order to restore the full set of JES NP’s, the effective NP’s in each workspace are un-  
1940 folded using maps detailing the linear combinations of unfolded NP’s that form the effective NP’s.

1941

The linear combinations used to unfold the effective JES NP's were calculated as follows:

$$NP_{i,eff} = \frac{\sum_j A_{ij} |NP_{j,unf}| NP_{j,unf}}{\sqrt{\sum_j A_{ij}^2 |NP_{j,unf}|^2}} \quad (9.i)$$

where  $eff$  and  $unf$  are for effective and unfolded NP's, respectively, the  $A_{ij}$ 's are scalar coefficients.

<sup>1943</sup> taken from raw maps, and  $|NP_{j,unf}|$  are the amplitudes of the unfolded NP's. The raw  $A_{ij}$  and scaled  
<sup>1944</sup> maps for Run 1 and Run 2 may be found in Figure 9.1

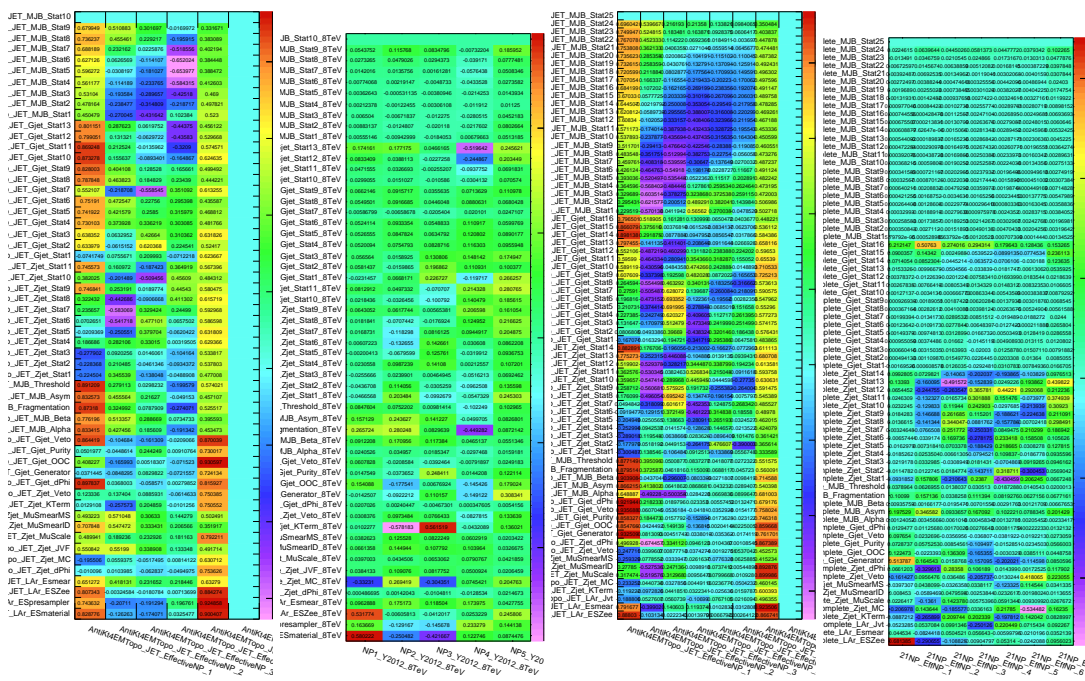


**Figure 9.1:** The raw and scaled coefficients for unfolding Run 1 (a and b) and Run 2 (c and d), respectively.

1915

Unfolding was found to have very little effect on both expected sensitivities and errors, as can be seen from Figure 1.

1046

seen in Tables 9.1–9.4.

	R <sub>1</sub> Unfold	R <sub>1</sub> Eff	R <sub>2</sub> Unfold	R <sub>2</sub> Eff	Comb Unfold	Comb Eff
Exp. Sig.	2.604	2.606	3.014	3.014	4.005	3.998
Obs. Sig.	1.369	1.374	3.53	3.53	3.581	3.571
Exp. Limit	0.755 <sup>+0.296</sup> <sub>-0.211</sub>	0.755 <sup>+0.296</sup> <sub>-0.211</sub>	0.732 <sup>+0.287</sup> <sub>-0.205</sub>	0.732 <sup>+0.287</sup> <sub>-0.205</sub>	0.512 <sup>+0.201</sup> <sub>-0.143</sub>	0.51 <sup>+0.2</sup> <sub>-0.143</sub>
Obs. Limit	1.21	1.21	1.94	1.94	1.36	1.37

**Table 9.1:** Expected and observed sensitivities for Run 1, Run 2, and combined workspaces with effective and unfolded JES NP's.

	R <sub>1</sub> Unfold	R <sub>1</sub> Eff
$ \Delta\hat{\mu} $	0.0018	
$\hat{\mu}$	0.5064	0.5082
Total	+0.400 / -0.373	+0.401 / -0.373
DataStat	+0.312 / -0.301	+0.312 / -0.301
FullSyst	+0.250 / -0.220	+0.251 / -0.220
Jets	+0.060 / -0.051	+0.060 / -0.052
BTag	+0.094 / -0.079	+0.095 / -0.079

**Table 9.2:** Error on signal strength breakdowns for Run 1 workspaces with effective and unfolded JES NP's.

	R <sub>2</sub> Unfold	R <sub>2</sub> Eff
$ \Delta\hat{\mu} $	0.0	
$\hat{\mu}$	1.2051	1.2052
Total	+0.421 / -0.366	+0.421 / -0.366
DataStat	+0.239 / -0.234	+0.239 / -0.234
FullSyst	+0.346 / -0.282	+0.346 / -0.282
Jets	+0.066 / -0.047	+0.066 / -0.047
BTag	+0.119 / -0.106	+0.119 / -0.106

**Table 9.3:** Error on signal strength breakdowns for Run 2 workspaces with effective and unfolded JES NP's.

	Comb Unfold	Comb Eff
$ \Delta\hat{\mu} $	0.0006	
$\hat{\mu}$	0.8992	0.8985
Total	+0.278 / -0.261	+0.278 / -0.261
DataStat	+0.185 / -0.181	+0.185 / -0.181
FullSyst	+0.208 / -0.187	+0.208 / -0.188
Jets	+0.040 / -0.044	+0.041 / -0.036
BTag	+0.076 / -0.076	+0.077 / -0.076

**Table 9.4:** Error on signal strength breakdowns for combined workspaces with effective and unfolded JES NP's.

1947 It was also found that fit sensitivities and breakdowns were similarly indifferent to the use of ei-

ther the strong or weak JES correlation schemes, as shown in Tables 9.5 and 9.6.

	JES Weak Unfold	JES Weak Eff	JES Strong Unfold	JES Strong Eff
Exp. Sig.	3.57	3.57	3.59	3.59
Exp. Limit	0.493 <sup>+0.193</sup> <sub>-0.138</sub>	0.494 <sup>+0.193</sup> <sub>-0.138</sub>	0.493 <sup>+0.193</sup> <sub>-0.138</sub>	0.493 <sup>+0.193</sup> <sub>-0.138</sub>

**Table 9.5:** Expected sensitivities for both effective and unfolded combined workspaces using the strong and weak JES correlation schemes.

	Comb Unfold	Comb Eff	Strong Unfold	Strong Eff
$\Delta\hat{\mu}$	0.0009		0.0025	
Total	+0.269 -0.254	+0.27 -0.255	+0.27 -0.255	+0.27 -0.255
DataStat	+0.181 -0.177	+0.181 -0.177	+0.181 -0.177	+0.181 -0.178
FullSyst	+0.199 -0.183	+0.2 -0.183	+0.2 -0.183	+0.201 -0.183
Jets	+0.0387 -0.032	+0.041 -0.0337	+0.0425 -0.0329	+0.0432 -0.0338
BTag	+0.0975 -0.0933	+0.098 -0.0936	+0.0979 -0.0935	+0.098 -0.0936

**Table 9.6:** Error on signal strength breakdowns for both effective and unfolded combined workspaces using the strong and weak JES correlation schemes.

1949 Comparisons of top ranked nuisance parameters in Figures 9.2–9.4 and for the complete JES pull

1950 comparisons in Figures 9.5–9.8 also show very little difference with respect to correlation scheme  
 1951 (except obviously for the number of JES NP's). Constrained pulls in pull comparisons should once  
 again be taken as a shortcoming of HESSE and not the fit model.

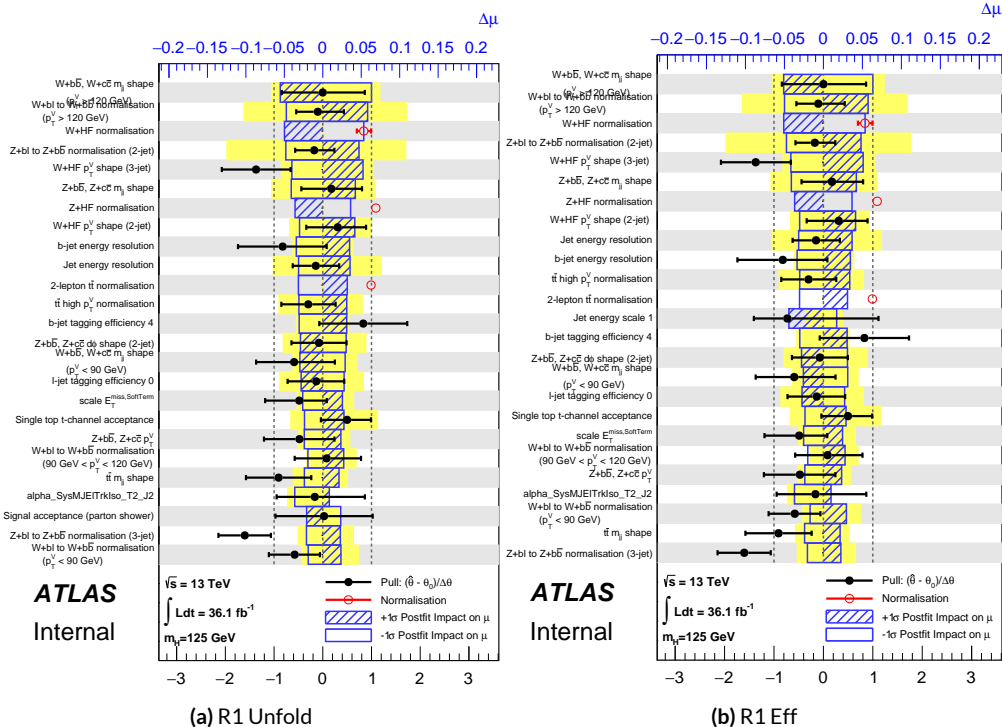


Figure 9.2: Ranks for the effective and unfolded JES NP Run1 combined workspaces.

1952  
 1953 As a result of these studies, the weak JES correlation scheme with uncorrelated effective JES NP's  
 1954 (i.e. just the  $b$ -jet energy scale NP) has been chosen as the treatment of JES in the Run 1 + Run 2  
 1955 combined fit.

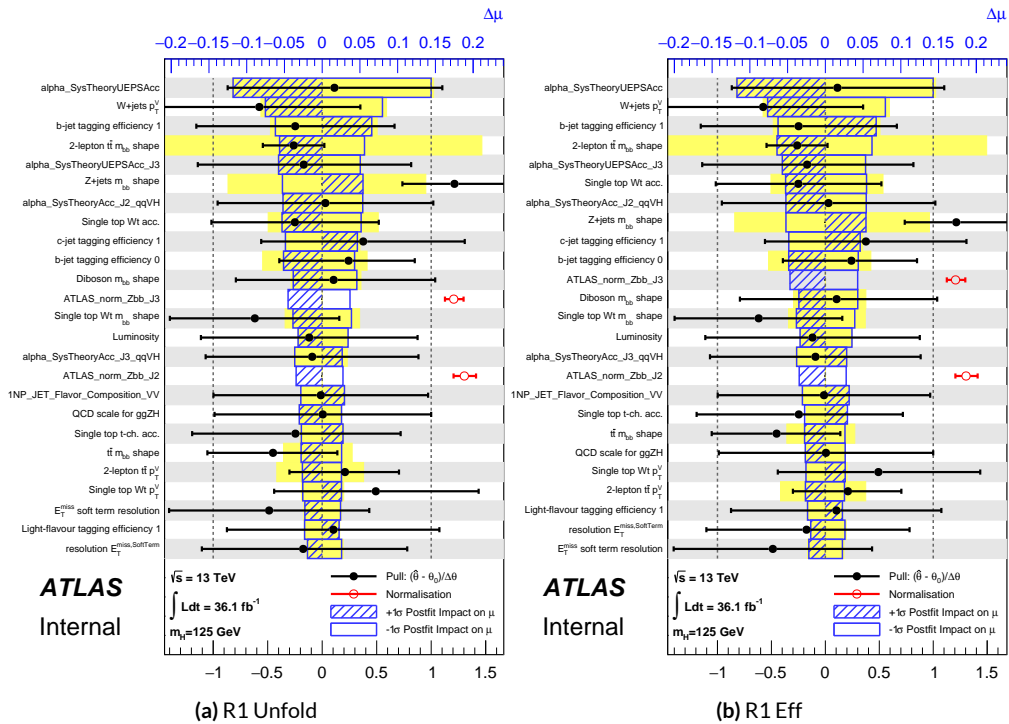


Figure 9.3: Ranks for the effective and unfolded JES NP Run2 combined workspaces.

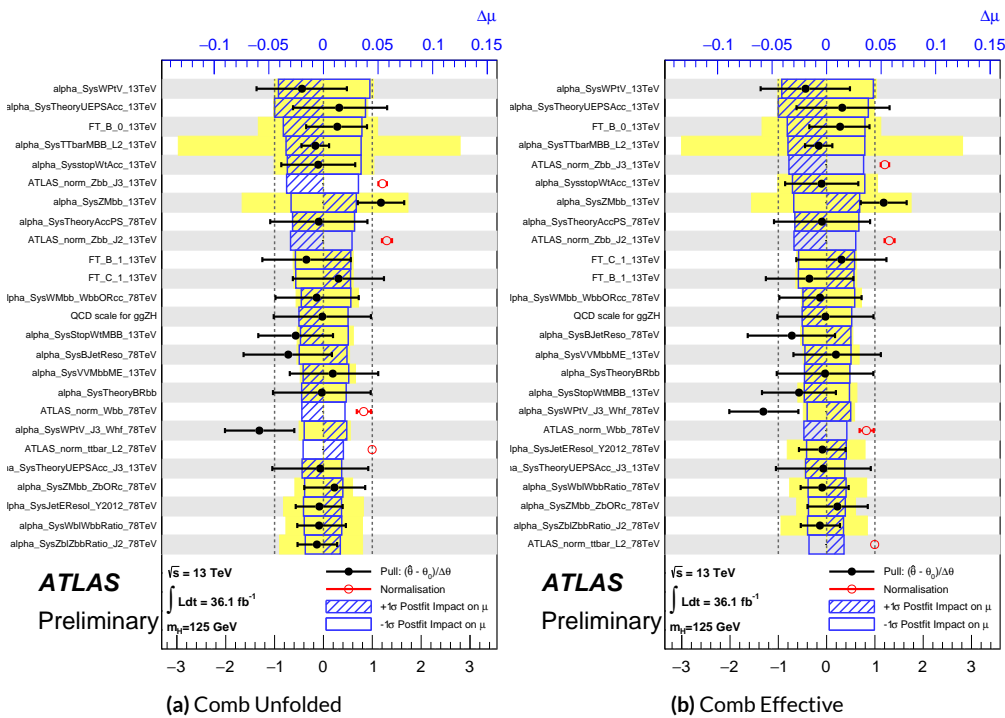


Figure 9.4: Ranks for the effective and unfolded JES NP Run1+Run2 combined workspaces.

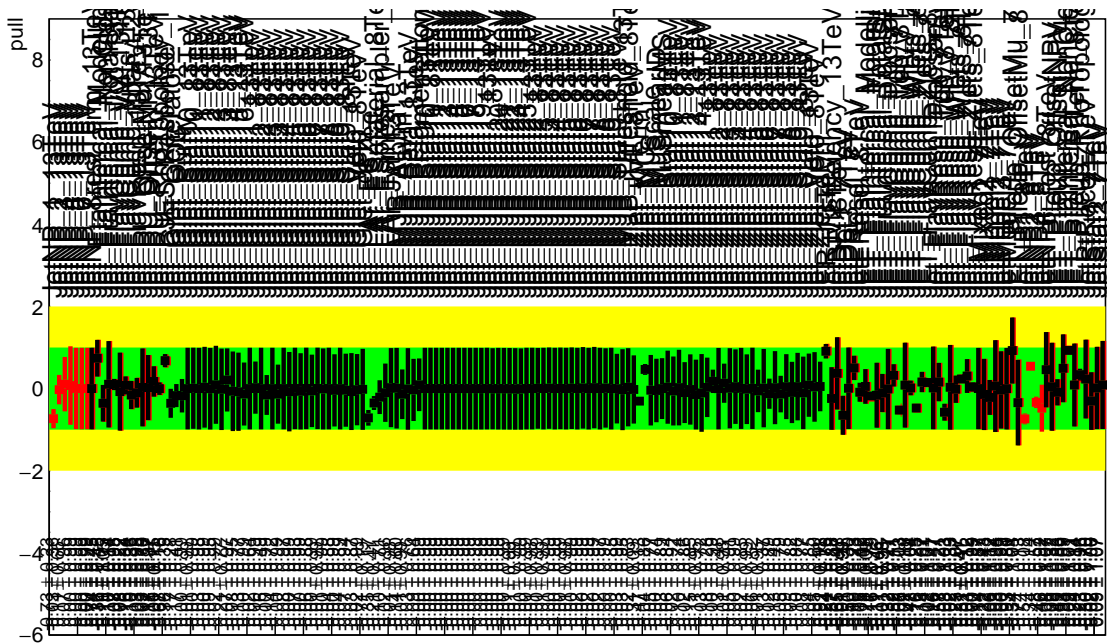


Figure 9.5: Pull Comparisons: jesu---Jet Comb Unfold, Comb Eff, Strong Unfold, Strong Eff

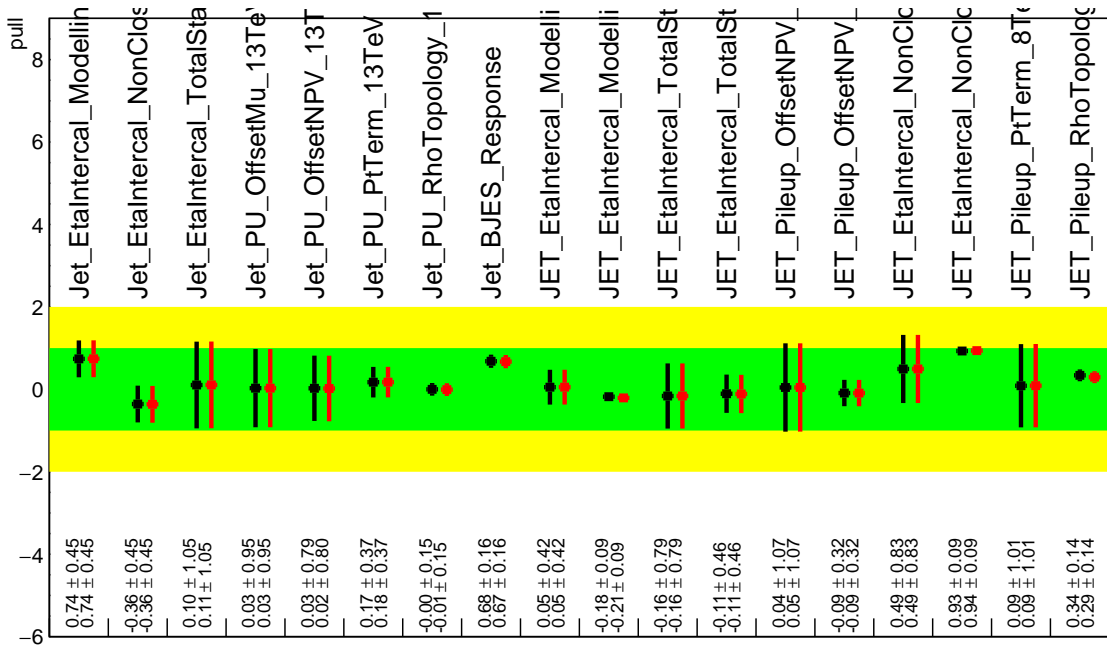


Figure 9.6: Pull Comparisons: jesu---JetMatched Comb Unfold, Comb Eff, Strong Unfold, Strong Eff

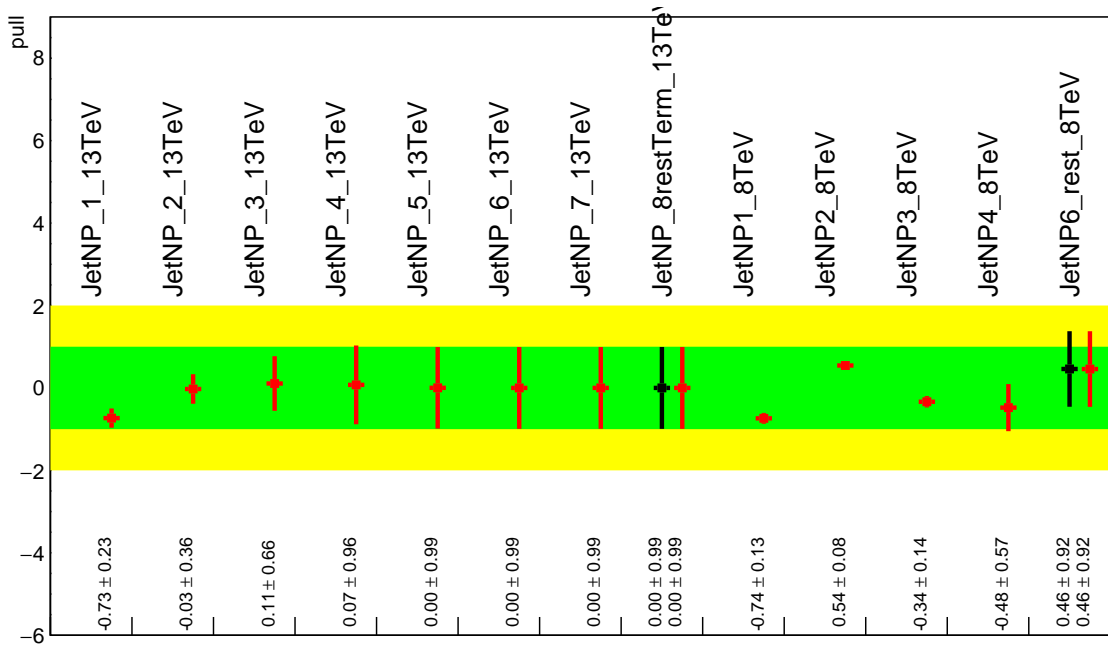


Figure 9.7: Pull Comparisons: jesu---JetEff Comb Unfold, **Comb Eff**, Strong Unfold, **Strong Eff**

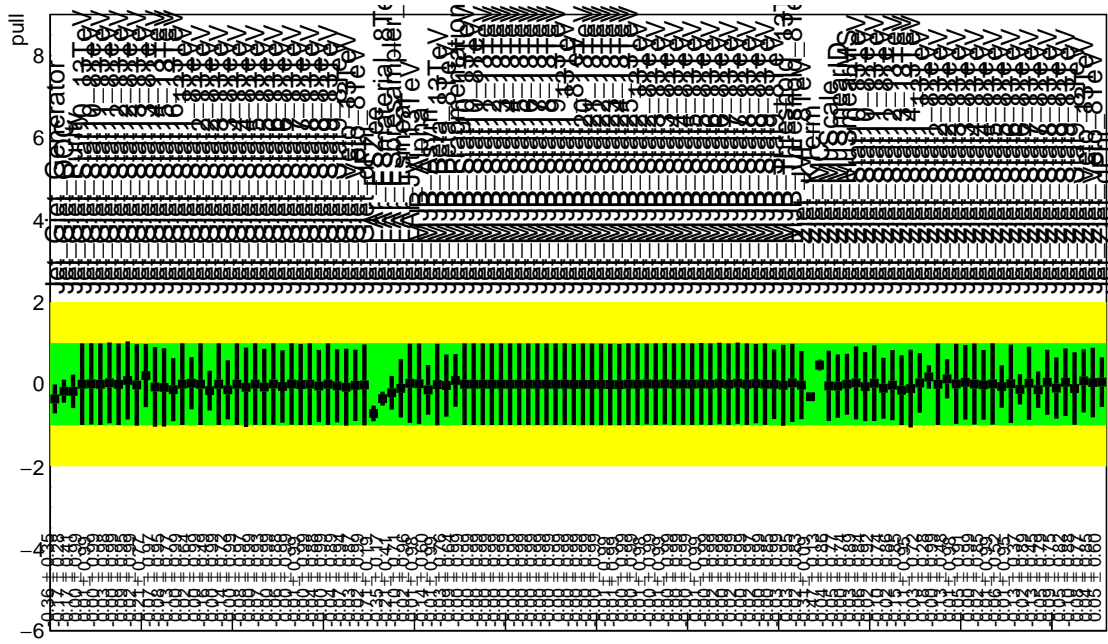


Figure 9.8: Pull Comparisons: jesu---JetUnfold Comb Unfold, **Comb Eff**, Strong Unfold, **Strong Eff**

1956 9.1.2 FLAVOR TAGGING

1957 Unfortunately, the ATLAS Flavor Tagging group did not provide any recommendations for corre-  
1958 lating Run 1 and Run 2 NP's, though given the high ranking of these NP's in the Run 2, result, per-  
1959 forming at least some studies was deemed crucial. Nevertheless, great improvements and changes to  
1960 the treatment of flavor tagging between Run 1 and Run 2 does weaken the argument for any strong  
1961 flavor tagging correlation scheme.

1962 Given that  $c$ -tagging changed significantly between Run 1 and Run 2 and that light tagging NP's  
1963 are very lowly ranked, these sets of NP's are left uncorrelated. Moreover, the change in the physical  
1964 meaning of the effective  $b$ -tagging NP's means a full correlation of such NP's (insomuch as they exist  
1965 in each result) is one of limited utility. Hence, it was decided to leave flavor tagging NP's uncorre-  
1966 lated. However, since the meaning of the leading  $b$ -tagging NP's is approximately constant across  
1967 years and since Run 2  $b$ -tagging NP's are very highly ranked in both the Run 2 only and combined  
1968 fits, tests correlating these NP's were conducted, the results of which can be seen below. It should be  
1969 noted that the leading B NP at 8 TeV, `SysBTagB0Effic_Y2012_8TeV`, has an opposite effect on  $t\bar{t}$   
1970 normalization than the 7 and 13 TeV NP's, and so must be flipped using a similar strategy as for JES  
1971 unfolding. Initial studies of flavor tagging correlations did not flip this NP, and so results for this  
1972 scheme (labeled "Bo 8TeV Not Flipped") have also been included for comparison.

1973 It is clear from these results that correlating the leading effective Eigen NP associated with  $b$ 's can  
1974 have a noticeable effect on final fit results and that the 8 TeV Bo NP is the most important compo-  
1975 nent of a combined Bo NP. It is also not so surprising that the 8 TeV result should drive the com-

	Comb Eff	BTag Bo	Bo 8TeV Not Flipped
Exp. Sig.	3.998	4.127	3.921
Obs. Sig.	3.571	3.859	3.418
Exp. Limit	0.51 <sup>+0.2</sup> <sub>-0.143</sub>	0.5 <sup>+0.196</sup> <sub>-0.14</sub>	0.517 <sup>+0.202</sup> <sub>-0.144</sub>
Obs. Limit	1.37	1.41	1.35

**Table 9.7:** Expected and observed sensitivities for a combination featuring the weak JES scheme, combination with the weak JES scheme + leading  $b$  NP's correlated, and the  $b$  correlation with the 8 TeV NP with sign unflipped.

	Comb Eff	BTag Bo	Bo 8TeV Not Flipped
$ \Delta\hat{\mu} $	—	0.0446	0.0268
$\hat{\mu}$	0.8985	0.9431	0.8717
Total	+0.278 / -0.261	+0.275 / -0.256	+0.282 / -0.263
DataStat	+0.185 / -0.181	+0.180 / -0.177	+0.189 / -0.186
FullSyst	+0.208 / -0.188	+0.207 / -0.186	+0.209 / -0.186
BTag	+0.077 / -0.076	+0.071 / -0.068	+0.079 / -0.075
BTag b	+0.062 / -0.059	+0.055 / -0.049	+0.064 / -0.060

**Table 9.8:** Breakdowns of the impact of different NP sets on total error on  $\hat{m}_{ll}$  for a combination featuring the weak JES scheme and a combination with the weak JES scheme + leading  $b$  NP's correlated.

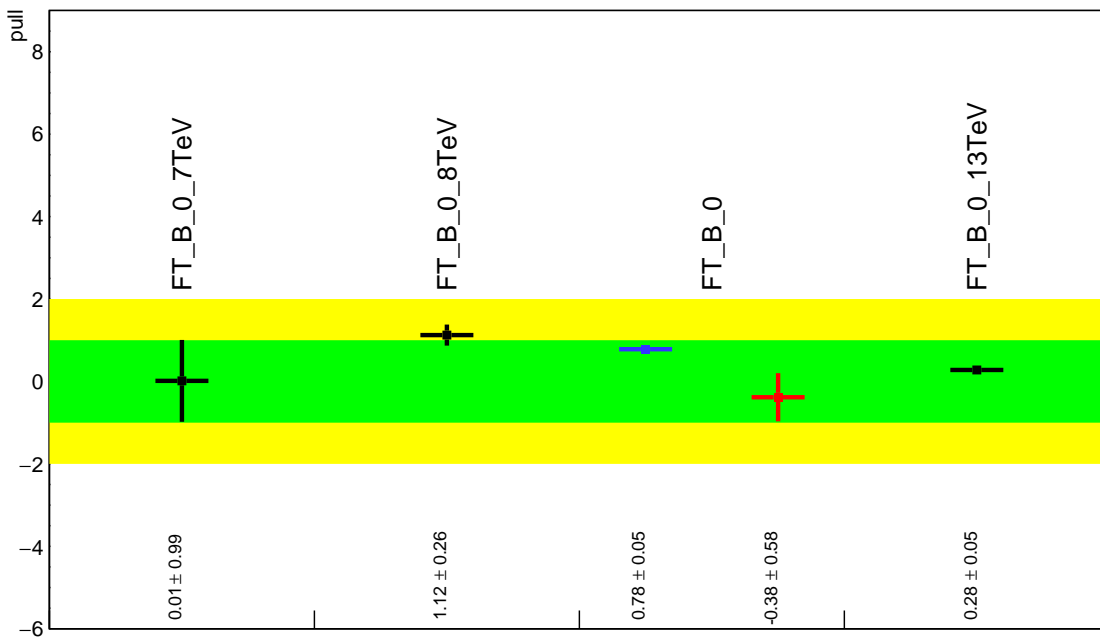


Figure 9.9: Pull Comparisons: btag-b---BTagBO Comb Eff, BTag BO

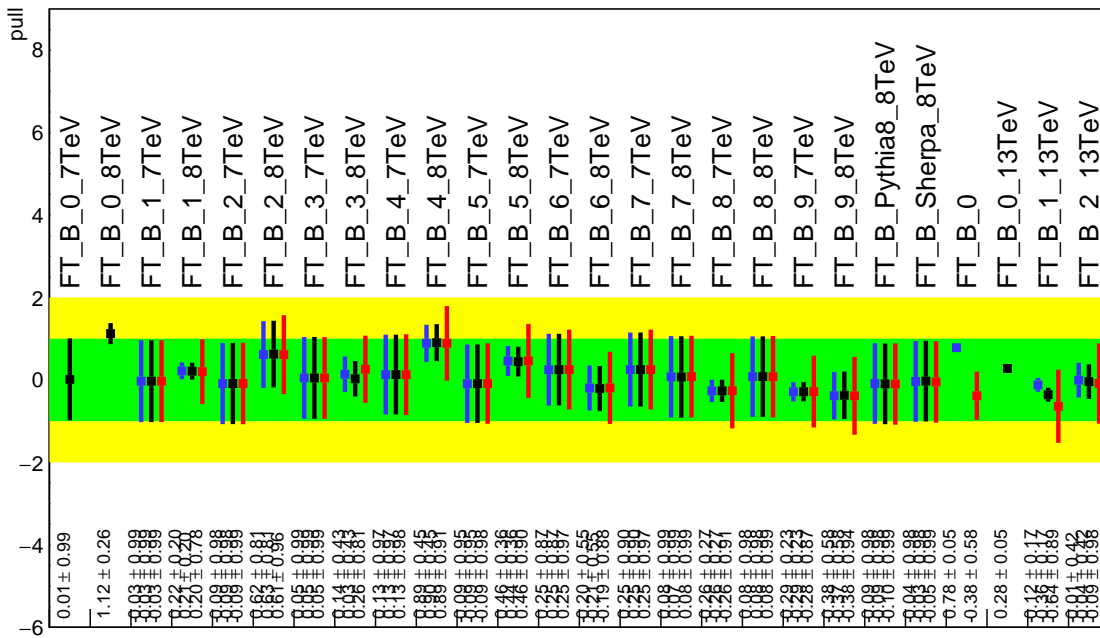
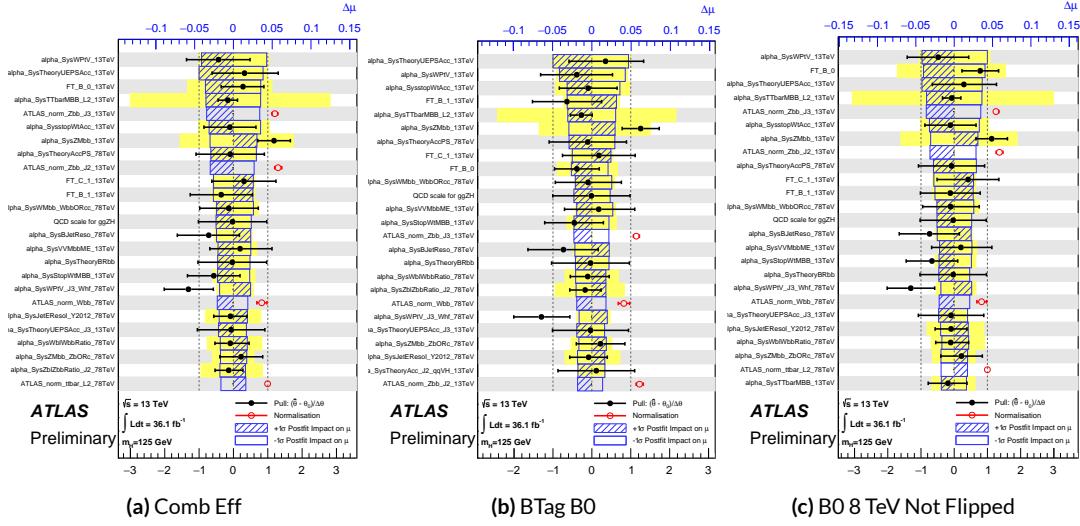


Figure 9.10: Pull Comparisons: btag-b---BTagB Comb Eff, BTag BO



**Figure 9.11:** NP rankings for a combination featuring the weak JES scheme and a combination with the weak JES scheme + leading  $b$  NP's correlated.

1976 bined nuisance parameter since it is the only result to make use of both pseudocontinuous tagging-  
 1977 based and  $b$ -tag regions into the final fit, implicitly yielding much more information about  $b$ 's. The  
 1978  $13\text{ TeV}$  fit has neither of these regions. What is less clear is whether there are sufficient grounds for  
 1979 implementing this correlation (i.e. does the correspondence of these NP's across years warrant a full  
 1980 correlation). While there are no current plans to do so, this matter warrants careful scrutiny if Run 1  
 1981 is to be combined with future results.

### 1982 9.1.3 MODELING SYSTEMATICS

1983 Another principal systematic category is modeling uncertainties. The effect of correlating groups  
 1984 of systematics was estimated using the same strategy employed by the ATLAS/CMS SM  $VH(b\bar{b})$   
 1985 combination for Run 1. This extrapolation can be used to estimate the impact of correlations on  
 1986 the estimated signal strength, the total error on the signal strength, and the  $\chi^2$  of the result. The

<sup>1987</sup> impact of such correlations is no more than a few percent effect, as the following tables demonstrate,  
<sup>1988</sup> beginning with the category with the greatest shift, W+jets modeling, in Table 9.9.

	$ \Delta\mu $	$\sigma$	$ \Delta\sigma $	$\chi^2$
$\rho=-1$	0.0024	0.2448	0.011 (4.3%)	0.95
$\rho=-0.6$	0.0015	0.2493	0.00654 (2.55%)	0.9804
$\rho=-0.3$	0.0008	0.2526	0.00325 (1.27%)	1.0045
$\rho=0$	—	0.2558	—	1.0298
$\rho=0.3$	0.0008	0.259	0.0032 (1.25%)	1.0564
$\rho=0.6$	0.0017	0.2622	0.00636 (2.49%)	1.0844
$\rho=1$	0.0029	0.2664	0.0105 (4.11%)	1.1242

**Table 9.9:** Run 1 + Run 2 W+jets modeling correlation projections

#### <sup>1989</sup> 9.1.4 FINAL CORRELATION SCHEME

<sup>1990</sup> The final Run 1 + Run 2 correlation scheme is shown in Table 9.10. As detailed above, neither JES  
<sup>1991</sup> nor modeling systematics had any demonstrable effect on combined fit results. Hence, only signal  
<sup>1992</sup> NP's and the  $b$ -jet energy scale are correlated (the weak JES scheme without unfolding). While the  
<sup>1993</sup> effect of flavor tagging correlations is less clear, the result physical arguments for correlation are less  
<sup>1994</sup> strong; the size of effect was discovered rather late in the analysis process; and no nuisance parameter  
<sup>1995</sup> unfolding maps exist for flavor tagging as they do for JES, so it was decided to leave these uncorre-  
<sup>1996</sup> lated as well.

7 TeV NP	8 TeV NP	13 TeV NP
	ATLAS_BR_bb	SysTheoryBRbb
	SysTheoryQCDscale_ggZH	SysTheoryQCDscale_ggZH
	SysTheoryQCDscale_qqVH	SysTheoryQCDscale_qqVH
—	SysTheoryPDF_ggZH_8TeV	SysTheoryPDF_ggZH
—	SysTheoryPDF_qqVH_8TeV	SysTheoryPDF_qqVH
—	SysTheoryVHPt_8TeV	SysVHNLOEWK
SysJetFlavB_7TeV	SysJetFlavB_8TeV	SysJET_21NP_JET_BJES_Response

**Table 9.10:** A summary of correlated nuisance parameters among the 7, 8, and 13 TeV datasets.

1997 **9.2 COMBINED FIT RESULTS**

1998 **9.2.1 COMBINED FIT MODEL VALIDATION**

1999 Before moving onto the final results, we present the rest of the validation for the Run 1 + Run 2  
2000 combined fits, beginning with impacts of ranked individual nuisance parameters in Figure 9.12 and  
2001 for all nuisance parameter categories in Table 9.11. Both of these sets of results point to the most im-  
2002 portant nuisance parameters being signal systematics,  $b$ -tagging, and  $V$ +jets modeling systematics,  
2003 with Run 2 NP's generally being higher ranked. That some NP's are strongly pulled is not unusual  
2004 as the fit model has so many NP's;  $V$ +jets modeling in particular has been historically difficult.

2005 In addition to looking at the behaviors of nuisance parameters to gauge fit model performance  
2006 and stability, fits are conducted using multiple parameters of interest. Typical divisions are Run 1  
2007 vs. Run 2, lepton channels, and  $WH$  vs  $ZH$ . As mentioned in Chapter 7, the profile likelihood test  
2008 statistic given in Equation 7.2 is, in the limit of large sample statistics, a  $\chi^2$  distribution with degrees  
2009 of freedom equal to the number of parameters of interest plus number of nuisance parameters.  
2010 Thus, changing the number of interest parameters and leaving the rest of the fit model unchanged

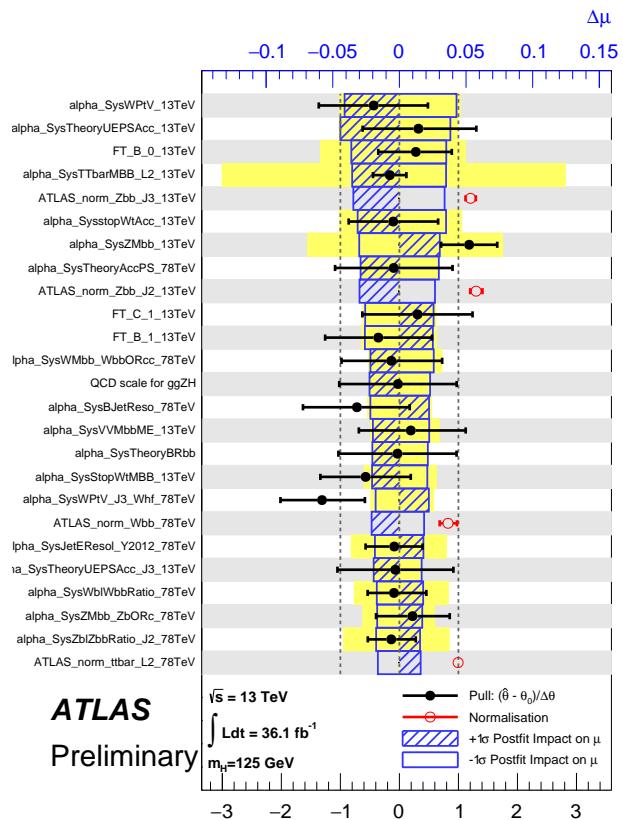


Figure 9.12: Ranked nuisance parameters for the Run1+Run2 combination.

Total	+0.278 / -0.261
DataStat	+0.185 / -0.181
FullSyst	+0.208 / -0.188
Floating normalizations	+0.055 / -0.056
All normalizations	+0.068 / -0.069
All but normalizations	+0.192 / -0.172
Jets, MET	+0.046 / -0.040
Jets	+0.041 / -0.036
MET	+0.023 / -0.018
BTag	+0.077 / -0.076
BTag b	+0.062 / -0.059
BTag c	+0.033 / -0.032
BTag light	+0.028 / -0.028
Leptons	+0.008 / -0.008
Luminosity	+0.026 / -0.014
Diboson	+0.030 / -0.027
Model Zjets	+0.049 / -0.050
Zjets flt. norm.	+0.032 / -0.040
Model Wjets	+0.082 / -0.083
Wjets flt. norm.	+0.031 / -0.027
Model ttbar	+0.047 / -0.046
ttbar flt. norm.	+0.025 / -0.026
Model Single Top	+0.047 / -0.045
Model Multi Jet	+0.027 / -0.038
Signal Systematics	+0.098 / -0.052
MC stat	+0.080 / -0.084

**Table 9.11:** Summary of the impact of different nuisance parameter categories on the total error on  $\hat{\mu}$  for the combined Run1+Run2 fit.

2011 means that the difference between the nominal fit and a fit with more parameters of interest ought  
 2012 to also be distributed as a  $\chi^2$  distribution with degrees of freedom equivalent to the number of extra  
 2013 parameters of interest. This difference can then be interpreted as a compatibility between the two  
 2014 results using the standard tables for this distribution, giving another gauge of fit performance. These  
 2015 are shown in Table 9.12.

Fit	Compatibility
Leptons (3 POI)	1.49%
$WH/ZH$ (2 POI)	34.2%
Run 1/Run 2 (2 POI)	20.8%
Run 1/Run 2 $\times$ Leptons (6 POI)	7.10%
Run 1/Run 2 $\times$ $WH/ZH$ (4 POI)	34.6%

**Table 9.12:** Summary of multiple POI compatabilities. The well-known Run 1 7 TeV 0-lepton deficit is responsible for the low compatibility with the 6 and 3 POI fits.

2016 The low compatabilities associated with treating the lepton channels as separate parameters of  
 2017 interest are a symptom of the low signal strengths associated with the Run 1 0-lepton channel, in par-  
 2018 ticular the 7 TeV result. Given the relatively small amount of data associated with the 7 TeV result,  
 2019 this should not be a cause for alarm. Signal strength summary plots for the fits treating Run 1 and  
 2020 Run 2 separately are shown in Figures 9.13-9.15, where the effect of the Run 1 parameters can be seen  
 2021 graphically.

### 2022 9.2.2 FINAL RESULTS

2023 The combined results yields an observed (expected) significance of 3.57 (4.00) and an observed (ex-  
 2024 pected) limit of 1.37 ( $0.510^{+0.200}_{-0.143}$ ), with a signal strength of  $\hat{\mu} = 0.898^{+0.278}_{-0.261}$ .

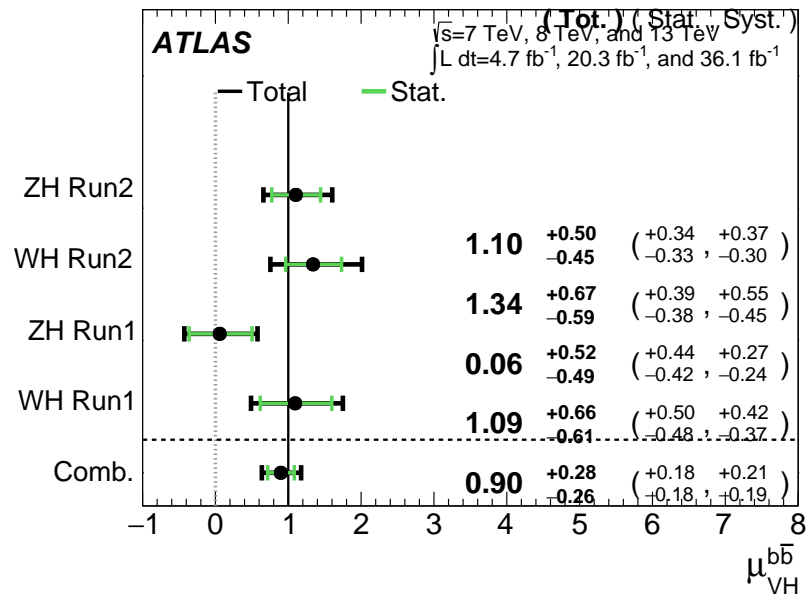


Figure 9.13:  $\hat{\mu}$  summary plot for a four parameter of interest fit.

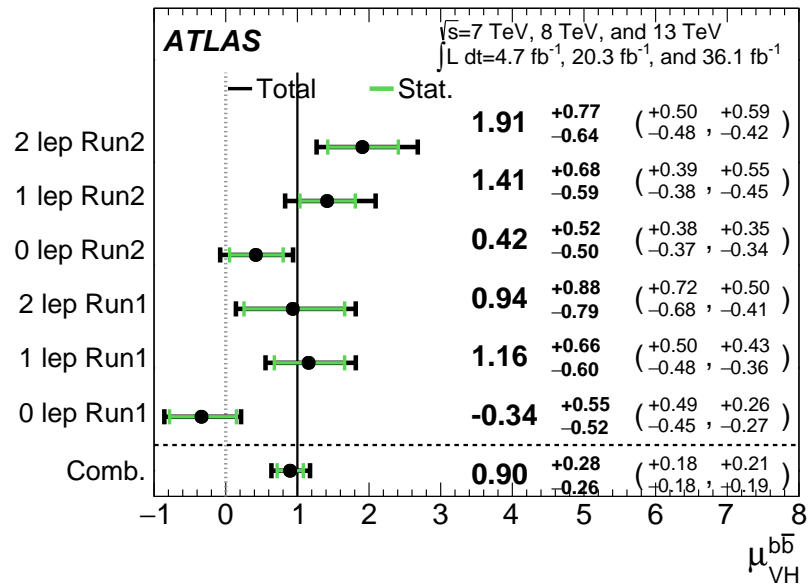
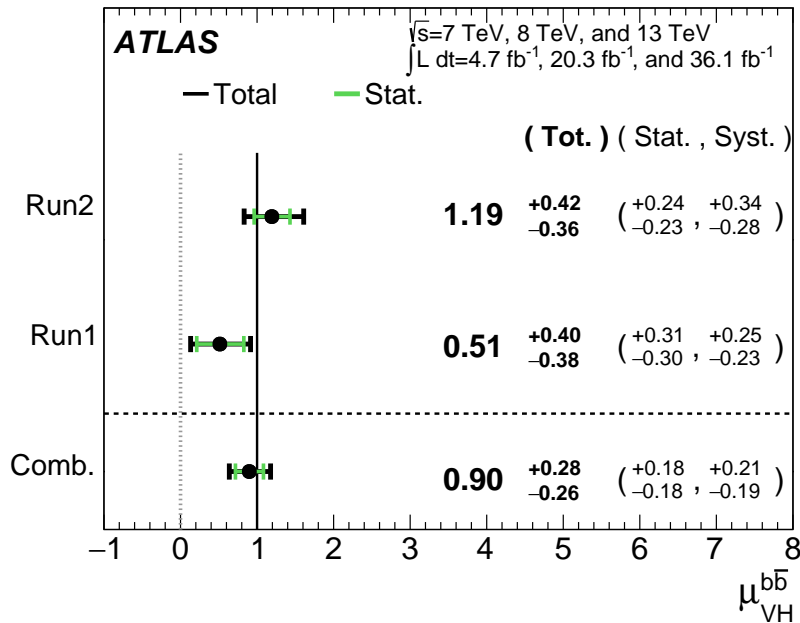


Figure 9.14:  $\hat{\mu}$  summary plot for a six parameter of interest fit.



**Figure 9.15:**  $\hat{\mu}$  summary plot for a two parameter of interest (Run 1 and Run 2) values.

2025      The two and three parameter of interest fit signal strength summary plots, as well as a summary  
 2026      of the historical values of the 7, 8, and 13 TeV results may be found in Figures 9.16-9.18. The main  
 2027      results for Run 1, Run 2, and the combination may be found in Table 9.13. These results were collec-  
 2028      tively noted as the first ever experimental evidence for SM  $VH(b\bar{b})$  in [42].

Dataset	$\hat{\mu}$	Total Error in $\hat{\mu}$	Obs. (Exp.) Significance
Run 1	0.51	+0.40 / -0.37	1.4 (2.6)
Run 2	1.20	+0.42 / -0.36	3.54 (3.03)
Combined	0.90	+0.28 / -0.26	3.57 (4.00)

**Table 9.13:** A summary of main results for the Run 1, Run 2, and combined fits.

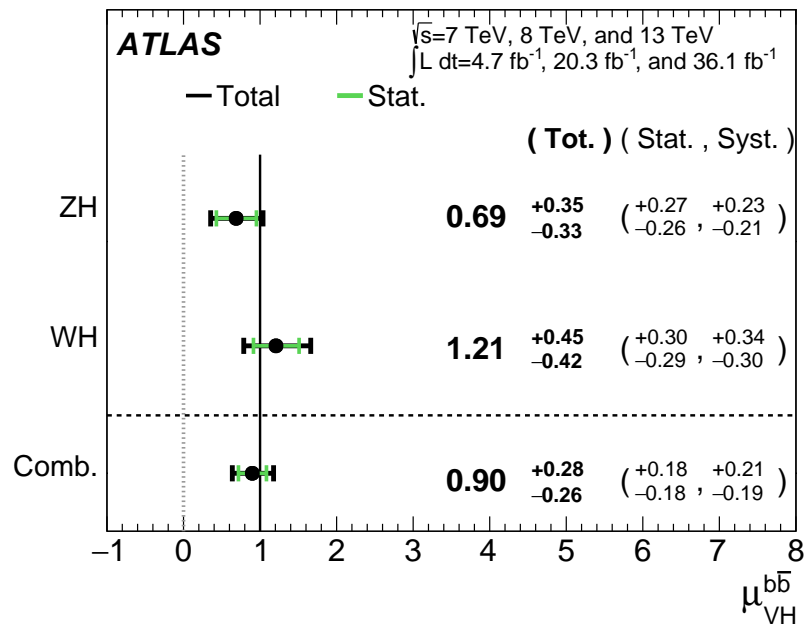


Figure 9.16:  $\hat{\mu}$  summary plot for a two parameter of interest fit.

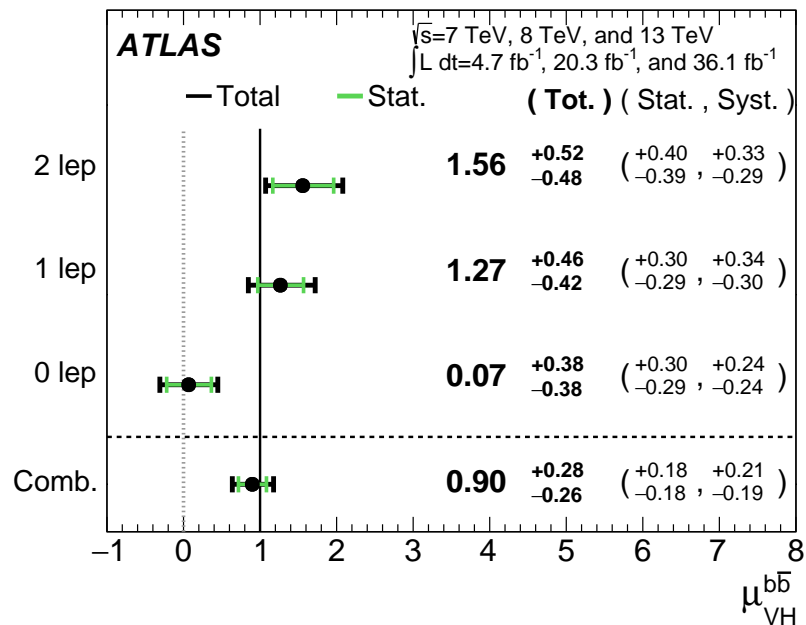


Figure 9.17:  $\hat{\mu}$  summary plot for a three parameter of interest fit.

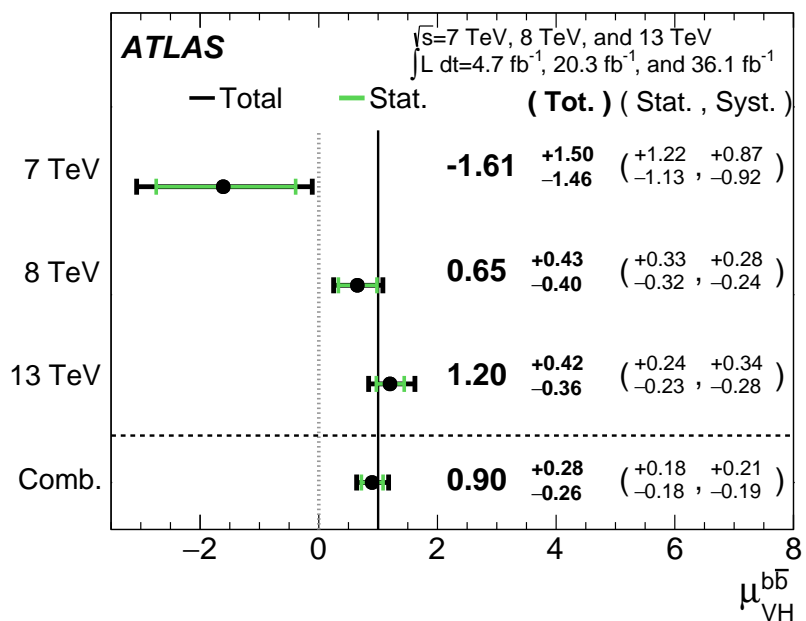


Figure 9.18:  $\hat{\mu}$  summary plot for different  $\sqrt{s}$  values.

*Vanitas vanitatum, omnis vanitas*

Ecclesiastes 1:2

# 10

2029

2030

## Closing Thoughts

2031 SINCE BOTH THE LHC and ATLAS are performing very well, it is only a matter of time before the  
2032 evidence for SM  $VH(b\bar{b})$  passes the 5 Gaussian standard deviation threshold necessary for discovery.  
2033 Official discovery may come less than a year after reports of first evidence and may not even require  
2034 a combination with the Run 1 result, depending on the latter two years of ATLAS Run 2 data (2017

2035 and 2018).

2036 It is entirely natural to ask, then, how essential the techniques and results described in this thesis  
2037 will prove to be moving forward. Neither the LI/RF multivariate techniques nor combination with  
2038 Run 1 datasets and their accompanying low signal strength values are necessary for discovery, and  
2039 the latter may not even be essential to timely<sup>\*</sup> discovery of SM  $VH(b\bar{b})$ . Nevertheless, both sets of  
2040 results hold great potential as key parts of a concerted ensemble of efforts towards precision Higgs  
2041 physics.

2042 With the perhaps final major center of mass energy increase at the energy frontier ever complete,  
2043 analyses must rely on increased integrated luminosity. Hence, it is becoming increasingly likely that  
2044 any new fundamental physics at colliders will require the use of results of systematics limited analy-  
2045 ses. This is the regime where the techniques described in this thesis will be most useful.

2046 As the LHC and its experiments undergo successive stages of upgrades and operate in evermore  
2047 extreme environments, the statistical fit models used to describe LHC data will continue to evolve in  
2048 complexity and diverge from their predecessors. The techniques described in Chapter 9 will become  
2049 increasingly more vital to producing the best physics results possible. The improvement in precision  
2050 from  $\hat{\mu}_{VH} = 1.20^{+0.24}_{-0.23}(\text{stat.})^{+0.34}_{-0.28}(\text{syst.})$  to  $\hat{\mu}_{VH} = 0.90^{+0.18}_{-0.18}(\text{stat.})^{+0.21}_{-0.19}(\text{syst.})$  is just the begin-  
2051 ning.

2052 The best methods for reduction of systematic uncertainties will naturally depend in part on the  
2053 state of the art for both fundamental physics process and detector modeling, but techniques that  
2054 can reduce systematic uncertainties independent of fit model, dataset, and physics process provide

---

\*i.e. before or coincident with CMS

2055 a promising avenue forward. The improvements in systematic uncertainties using the Lorentz In-  
 2056 variant and RestFrames variable techniques in the  $ZH \rightarrow \ell\ell b\bar{b}$  analysis, summarized in Table 10.1,  
 2057 show that a smarter and more orthogonal decomposition of information in a collision event pro-  
 2058 vides benefits independent of any clever treatment of  $\vec{E}_T^{\text{miss}}$  (which both schemes also provide). Both  
 2059 techniques are readily extendible to other analysis channels, with the RestFrames concept demon-  
 2060 strating stronger performance and greater flexibility to nearly completely generic final states.

	Standard	LI	RF
$\hat{\mu}$	$1.75^{+0.50, 0.64}_{-0.48, 0.45})$	$1.65^{+0.51, 0.59}_{-0.49, 0.41}$	$1.50^{+0.50, 0.53}_{-0.48, 0.36}$
Asi. $\Delta err(\mu)$	—	< 1%, +4.6%	-6.5%, -2.2%
Obs. $\Delta err(\hat{\mu})$	—	-7.5%, -3.7%	-16%, -8.8%
Stat only sig.	4.78	4.39 (-7.9%)	4.44 (-6.9%)
Exp. (Asi.) sig.	2.06	1.92 (-6.7%)	2.13 (+3.5%)
Exp. (data) sig.	1.76	1.73 (-1.7%)	1.80 (+3.4%)
Obs. (data) sig.	2.87	2.79 (-2.8%)	2.62 (-8.6%)

**Table 10.1:** Summary of performance figures for the standard, LI, and RF variable sets. Uncertainties on  $\hat{\mu}$  are quoted stat., syst. In the case of the latter two, % differences are given where relevant. Differences in errors on  $\mu$  are on full systematics and total error, respectively.

2061 Critical work remains to be done refining and extending the treatment of both the LI and RF

2062 techniques in  $VH(b\bar{b})$  analyses and their fit models, and completely independent techniques, like

2063 the use of multiple event interpretations addressed in Appendix B promise further improvements

2064 still.

2065 No one can say for certain what the future of the energy frontier of experimental particle physics

2066 may hold, but more nuanced treatments of the information in collision events born of meaningful

2067 physical insight are sure to light the way.

*If it's stupid but it works, it isn't stupid.*

Conventional Wisdom

A

2068

## 2069 Micromegas Trigger Processor Simulation

2070 IN ORDER TO PRESERVE key physics functionality by maintaining the ability to trigger on low  $p_T$   
2071 muons, the Phase I Upgrade to ATLAS includes a New Small Wheel (NSW) that will supply muon  
2072 track segments to the Level 1 trigger. These NSW trigger segments will combine segments from the  
2073 sTGC and Micromegas (MM) trigger processors (TP). This note will focus in particular on the al-

2074 gorithm for the MMTP, described in detail with initial studies in [41]. The goal of this note is to de-  
2075 scribe the MMTP algorithm performance under a variety of algorithm settings with both nominal  
2076 and misaligned chamber positions, as well as addressing a number of performance issues.

2077 This note is organized as follows: the algorithm and its outputs are briefly described in Section  
2078 A.1; Monte Carlo samples used are in Section B.1; nominal algorithm performance and certain quan-  
2079 tities of interest are described in Section A.3; algorithm performance under misalignment, misalign-  
2080 ment corrections, and corrected performance are shown in Section A.9; and conclusions are pre-  
2081 sented in Section A.24.

## 2082 A.1 ALGORITHM OVERVIEW

2083 The MMTP algorithm is shown schematically in Figure A.1, taken from [41], where a more detailed  
2084 description may be found. The algorithm begins by reading in hits, which are converted to slopes.  
2085 These slopes are calculated under the assumption that the hit originates from the IP; slopes calcu-  
2086 lated under this assumption are denoted by a superscript  $g$  for global in order to distinguish them  
2087 from local slopes calculated using only hits in the wedge. In the algorithm simulation, events are  
2088 screened at truth level to make sure they pass certain requirements. The track's truth-level coor-  
2089 dinates must place it with the wedge since some generated tracks do not reach the wedge. These  
2090 hits are stored in a buffer two bunch crossings (BCs) in time deep that separates the wedge into so-  
2091 called "slope-roads." If any given slope-road has sufficient hits to pass what is known as a coinci-  
2092 dence threshold, a fit proceeds. A coincidence threshold is a requirement for an event expressed as  
2093  $aX+bUV$ , which means that an slope-road must have at least  $a$  hits in horizontal (X) planes and at

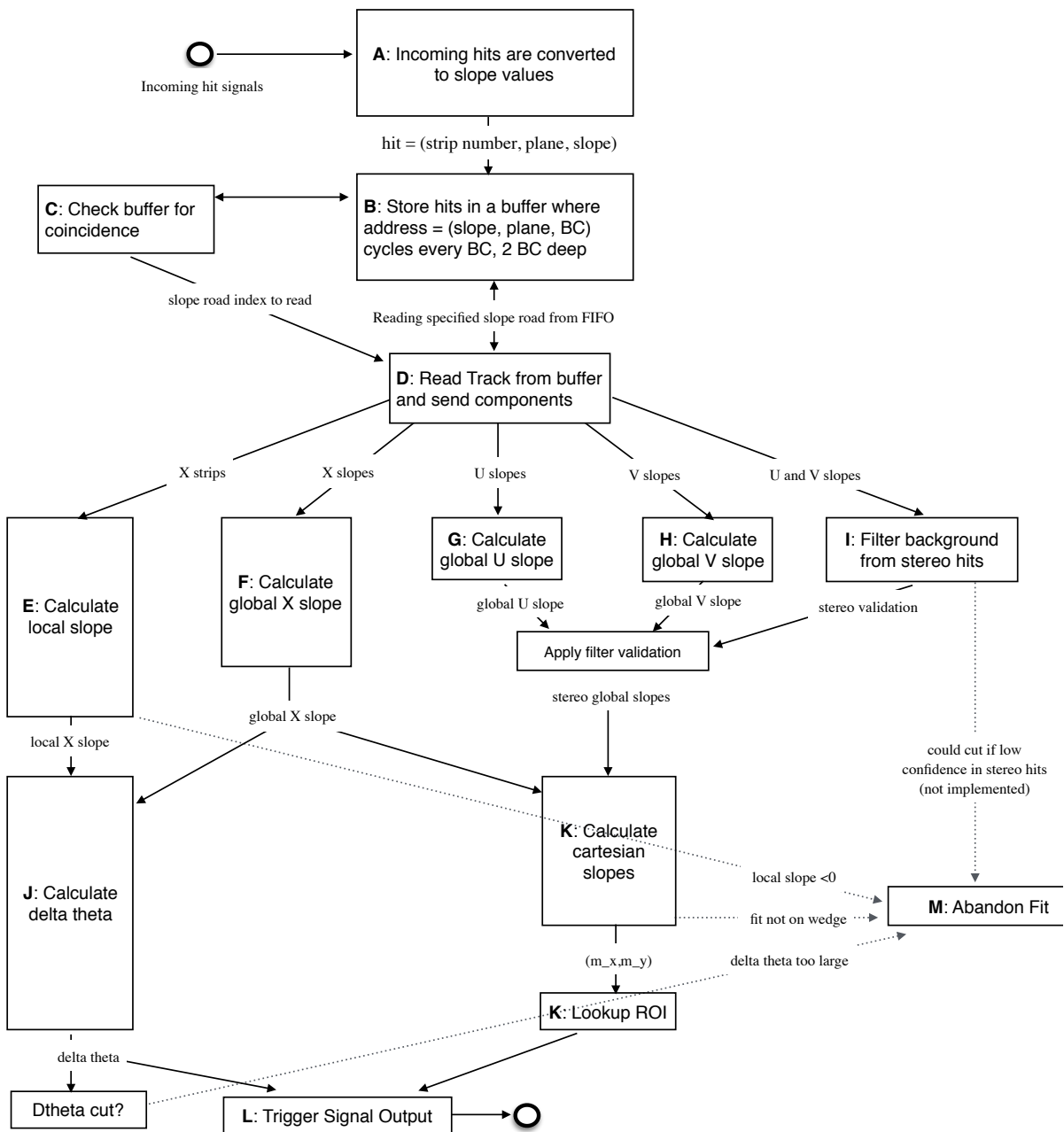


Figure A.1: A flow chart describing the algorithm steps, taken from [41].

2094 least  $b$  hits in stereo (U or V (corresponding to positive and negative stereo rotations)) planes. For  
 2095 coincidence thresholds with a  $2X$  hit requirement there is the extra requirement that, in the case of  
 2096 only  $2X$  hits, one be on each quadruplet in order to ensure an adequate lever arm for the  $\Delta\theta$  calcu-  
 2097 lation. Note that less stringent (lower hit) coincidence thresholds are inclusive; i.e. a slope-road pass-  
 2098 ing a  $4X+4UV$  cut automatically passes  $2X+1UV$ . The coincidence threshold, size of the slope-roads  
 2099 (denoted  $b$ ), and the number of slope-roads into which each horizontal and stereo hits get written  
 2100 centered upon their nominal value are configurable parameters of the algorithm.

2101 An individual hit's slope is calculated as shown in Equation A.1, where  $y_{base}$  is the local  $y$  coordi-  
 2102 nate (orthogonal to the beamline and direction of the horizontal strips) of a station's base,  $w_{str}$  is the  
 2103 strip pitch,  $n_{str}$  is the hit's strip number, and  $z_{plane}$  is the location of the hit's plane along the beam-  
 2104 line.

$$M_{hit} = \frac{y}{z} = \frac{y_{base}}{z_{plane}} + \frac{w_{str}}{z_{plane}} \times n_{str} \quad (\text{A.1})$$

2105 In the fit, individual hit slopes in a slope-road are used to calculate global slopes associated with each  
 2106 plane type, which are averages (e.g.  $M_X^{\ell}$  for the average slope of horizontal planes). These in turn are  
 2107 used to calculate the three composite slopes: slopes associated with the horizontal ( $m_x$ ) and vertical  
 2108 coordinates ( $m_y$ ) and the local slope of hits in the horizontal planes ( $M_X^l$ ), all of which are shown in  
 2109 Equation A.4. Note that the expression for  $M_X^l$  differs but is equivalent to the expression given in  
 2110 [41]. This is due to a procedural change in the algorithm. The local X slope is expressed in [41] as:

$$M_X^{local} = A_k \sum_i y_i z_i - B_k \sum_i y_i, \quad B_k = \frac{1}{n} \sum_i z_i A_k = \bar{z} A_k \quad (\text{A.2})$$

2111 Procedurally, this entails doing the sums over  $y_i$  and  $y_i z_i$ , multiplying the sums by  $A_k$ ,  $B_k$ , and then  
 2112 subtracting both of these numbers,  $\mathcal{O}(10^3)$ , to get local slopes,  $\mathcal{O}(10^{-1})$ , while requiring preci-  
 2113 sion on these numbers on the order of  $\mathcal{O}(10^{-3})$ . This requires precision in the sums  $\mathcal{O}(10^{-7})$ ,  
 2114 and with 32 bit fixed point numbers, there are deviations with respect to the floating point calcula-  
 2115 tions at the level of  $\mathcal{O}(10^{-5})$ , which is enough to introduce a significant bias in the  $\Delta\theta$  calculation.

2116 In order to prevent these errors, we do the subtraction first

$$M_X^{local} = A_k \sum_i y_i z_i - B_k \sum_i y_i = A_k \sum_i (y_i z_i - y_i \bar{z}) = B_k \sum_i y_i \left( \frac{z_i}{\bar{z}} - 1 \right) \quad (\text{A.3})$$

2117 Thus, we change the order of operations and store  $1/\bar{z}$  instead of  $A_k$  in addition to  $B_k$ . We also  
 2118 change the units of  $y_i$  and  $z_i$  in the calculation by dividing the millimeter lengths by 8192.\* With  
 2119 these changes, a 32 bit fixed point based algorithm has essentially identical performance to that of an  
 2120 algorithm based on the usual C++ 32 floating point numbers. Future work includes converting the  
 2121 32 bit fixed point arithmetic to 16 bit where possible in the algorithm. While introducing 16 bit num-  
 2122 bers uniformly might seem preferable, since simple 16-bit operations in the firmware can be done in  
 2123 a single clock tick, and a larger number of bits increases the algorithm latency, some numbers in the  
 2124 algorithm will require a larger number of bits, in particular in the local slope calculation, which is  
 2125 the single calculation in the algorithm requiring the largest numeric range.

2126 In Equation A.4,  $\theta_{st}$  is the stereo angle of 1.5 degrees; the sums are over relevant planes;  $\bar{z}$  is the  
 2127 average position in  $z$  of the horizontal planes; and  $y_i$  and  $z_i$  in the local slope expression refer to the  $y$

---

\*Chosen since it is a perfect power of 2 and of order the length scale of  $z$  in millimeters

2128 and  $z$  coordinates of hits in X planes.

$$m_x = \frac{1}{2} \cot \theta_{st} (\mathcal{M}_U^g - \mathcal{M}_V^g), \quad m_y = \mathcal{M}_X^g, \quad \mathcal{M}_X^l = \frac{\bar{z}}{\sum_i z_i^2 - 1/n (\sum_i z_i)^2} \sum_i y_i \left( \frac{z_i}{\bar{z}} - 1 \right) \quad (\text{A.4})$$

2129 From these composite slopes, the familiar expressions for the fit quantities  $\theta$  (the zenith),  $\phi$  (the az-  
2130 imuth<sup>†</sup>), and  $\Delta\theta$  (the difference in  $\theta$  between the direction of the segment extrapolated back to the  
2131 interaction point and its direction when entering the detector region; the following is an approxima-  
2132 tion) may be calculated, as noted in [41]:

$$\theta = \arctan \left( \sqrt{m_x^2 + m_y^2} \right), \quad \phi = \arctan \left( \frac{m_x}{m_y} \right), \quad \Delta\theta = \frac{\mathcal{M}_X^l - \mathcal{M}_X^g}{1 + \mathcal{M}_X^l \mathcal{M}_X^g} \quad (\text{A.5})$$

2133 Looking at Equations A.4 and A.5, the dependence of fit quantities on input hit information be-  
2134 comes clear.  $\Delta\theta$  relies exclusively on information from the horizontal (X) planes. Both  $\theta$  and  $\phi$  rely  
2135 on both horizontal and stereo slope information. However, the sum in quadrature of  $m_x$  and  $m_y$  in  
2136 the arctangent for  $\theta$  means that  $\theta$  is less sensitive to errors in stereo hit information than  $\phi$ . Given  
2137 that  $\theta_{st}$  is small,  $\cot \theta_{st}$  is large ( $\sim 38$ ), so  $m_x$  multiplies small differences in  $\mathcal{M}_U$  and  $\mathcal{M}_V$ , where  $m_y$   
2138 is simply an average over slopes. This means that while errors in horizontal hit information will af-  
2139 fect all three fit quantities, comparable errors in stereo hits will have a proportionately larger effect  
2140 on  $\theta$  and particularly on  $\phi$ . The  $\Delta\theta$  cut after step J in Figure A.1 has been implemented, requiring  
2141 all fits to have  $|\Delta\theta| < 16$  mrad. This requirement ensures good quality fits but also slightly reduces

---

<sup>†</sup>Defined with respect to the center ( $y$ ) axis and *not* the axis of the strips ( $x$ ) as is sometimes typical, so a hit along the center of the wedge has  $\phi = 0$

2142 algorithm efficiency.

## 2143 A.2 MONTE CARLO SAMPLES

2144 The Monte Carlo (MC) samples used for these studies were generated in Athena release 20.1.0.2 us-  
2145 ing simulation layout ATLAS-R2-2015-01-01-00 with muon GeoModel override version MuonSpectrometer-  
2146 R.07.00-NSW and modifications to have two modules per multiplet and xxuvuvxx geometry with a  
2147 stereo angle of 1.5 degrees. Muons of a single  $p_T$  were generated around the nominal IP with a smear-  
2148 ing of 50 mm along the beam line and 0.015 mm orthogonal to it; these muons were pointed toward  
2149 a single, large sector of the NSW. Each event consists of one muon fired towards the single NSW  
2150 wedge separated by effectively infinite time from other events.

## 2151 A.3 NOMINAL PERFORMANCE

2152 In order to evaluate algorithm performance, a number of quantities are evaluated, including the fit  
2153 quantities  $\theta$ ,  $\phi$ , and  $\Delta\theta$  as well as algorithm efficiency. Unless otherwise stated, that algorithm is  
2154 run with a 4X+4UV coincidence threshold, slope-road size of 0.0009, an X tolerance of two slope-  
2155 roads (i.e. hits in horizontal planes are written into the two slope-roads closest to the hits' value),  
2156 a UV tolerance of four slope-roads<sup>†</sup>, and a charge threshold requirement on hits of 1 (measured in  
2157 units of electron charge) for a sample of 30 000 events with a muon  $p_T$  of 100 GeV. Samples were  
2158 also generated for  $p_T$  values of 10 GeV, 20 GeV, 30 GeV, 50 GeV, and 200 GeV, which were used in

---

2159 <sup>†</sup>The larger tolerance on stereo hits takes into account the particulars of the  $m_x$  calculation mentioned in  
Section A.1.

2159 some of the following studies.

#### 2160 A.4 FIT QUANTITIES

2161 In order to evaluate the performance of the algorithm’s fit quantities  $\theta$ ,  $\phi$ , and  $\Delta\theta$ , fit values are com-  
2162 pared to truth-level MC values. The residual of the three fit quantities,  $\theta_{fit} - \theta_{tru}$ ,  $\phi_{fit} - \phi_{tru}$ , and  
2163  $\Delta\theta_{fit} - \Delta\theta_{tru}$ , are recorded for every fitted track. The distributions of these quantities, in particular  
2164 their biases and standard deviations, are then used to evaluate performance. In most cases, follow-  
2165 ing [41], the mean and standard deviation of a  $3\sigma$  Gaussian fit are quoted, as they capture the main  
2166 features of the algorithm and generally behave like the raw mean and rms. Nevertheless, discussion  
2167 of the raw quantities will be included when their behavior deviates markedly from that of the  $3\sigma$  fit  
2168 quantities.

2169 The truth-level quantities used in residual distribution are taken from information in the MC.

2170 These come directly from the MC for  $\theta$ ,  $\phi$ , and  $\Delta\theta$ . These quantities, along with the geometry of  
2171 the (large) wedge, are then in turn used to calculate truth-level values for any intermediate quantities  
2172 used in the algorithm.  $m_{x,tru}$ , for instance, is given by  $\tan \theta_{tru} \sin \phi_{tru}$ .

2173 Residual distributions for fit quantities under the previously described default settings of the al-  
2174 gorithm are shown in Figure A.2. Both the  $\theta_{fit} - \theta_{tru}$  and  $\Delta\theta_{fit} - \Delta\theta_{tru}$  distributions feature a  
2175 mostly Gaussian shape with more pronounced tails. The mean bias for these distributions is negligi-  
2176 ble at under one tenth of a milliradian, and the fitted (raw) rms values are 0.349 (0.614) mrad for  $\theta$   
2177 and 1.03 (2.55) mrad for  $\Delta\theta$ . The case of the  $\phi_{fit} - \phi_{tru}$  distribution is less straightforward, with both  
2178 the shape and bias arising from the xxuvuvxx geometry and relatively large extent of one of the two

<sup>2179</sup>  $\eta$ -stations, as explained in Appendix B of [38]. The fitted (raw) rms for the  $\phi$  distribution is 8.67  
<sup>2180</sup> (16.6) mrad.

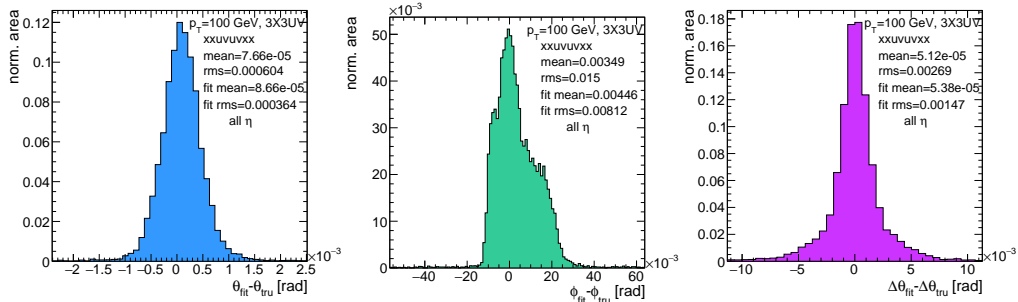


**Figure A.2:** Nominal residual plots;  $\theta, \phi, \Delta\theta$  for  $p_T = 100 \text{ GeV}$  muons

<sup>2181</sup> Both increasing muon  $p_T$  and increasing muon  $\eta$  for a fixed  $p_T$  imply increasing muon energy. As  
<sup>2182</sup> muons become more energetic, two effects compete in affecting the quality of fit. On the one hand,  
<sup>2183</sup> higher energy muons are deflected less by the ATLAS magnetic field, which should tend to improve  
<sup>2184</sup> the quality of the fit, since the fitted  $\theta$  (upon which  $\Delta\theta$  also relies) and  $\phi$  values are calculated under  
<sup>2185</sup> the infinite momentum muon (straight track) assumption. However, as muon energy increases, the  
<sup>2186</sup> likelihood that the muon will create additional secondaries increases, which creates extra hits that  
<sup>2187</sup> degrade the quality of the fit. While the geometry of the multiplet is such that there is very good res-  
<sup>2188</sup> olution in the direction orthogonal to the horizontal strip direction, the shallow stereo angle of 1.5  
<sup>2189</sup> degrees means that early hits caused by secondaries can have an outsize impact on  $m_x$ .  $\Delta\theta$ , which  
<sup>2190</sup> does not rely upon stereo information should feel the effect of secondaries the least and benefit from  
<sup>2191</sup> straighter tracks the most and hence benefit from higher muon energies;  $\phi$ , relying upon stereo in-  
<sup>2192</sup> formation the most, would be most susceptible to secondaries and benefit the least from straighter

2193 tracks and hence least likely to benefit from higher muon energy;  $\theta$  relies upon both horizontal and  
 2194 vertical slope information, though small errors are less likely to seriously affect the calculation, so the  
 2195 two effects are most likely to be in conflict for this fit quantity.

2196 The interplay of these effects on the residual standard deviations can be seen in their dependen-  
 2197 cies on  $\eta$  (Figure A.3; note that the final point in each of these plots is the rms of the distribution  
 2198 overall  $\eta$ ) and  $p_T$  (Figure A.4). For  $p_T = 100$  GeV muons,  $\Delta\theta$  performance increases with  $\eta$  (en-  
 2199 ergy), and  $\phi$  performance decreases, as expected;<sup>§</sup> for  $\theta$ , the two effects appear to compete, with per-  
 2200 formance first increasing with  $\eta$  until the effects of secondaries begins to dominate. Integrated over  
 2201 all  $\eta$ , the effects are less clearly delineated. Both  $\Delta\theta$  and  $\theta$  performance increases with increasing  $p_T$ ,  
 2202 suggesting straighter tracks with increasing energy are the dominant effect for these quantities, while  
 2203  $\phi$  performance appears to improve and then deteriorate (the slight improvement at high  $p_T$  is due to  
 2204 the addition of the  $\Delta\theta$  cut into the algorithm, which filters out very poor quality fits).

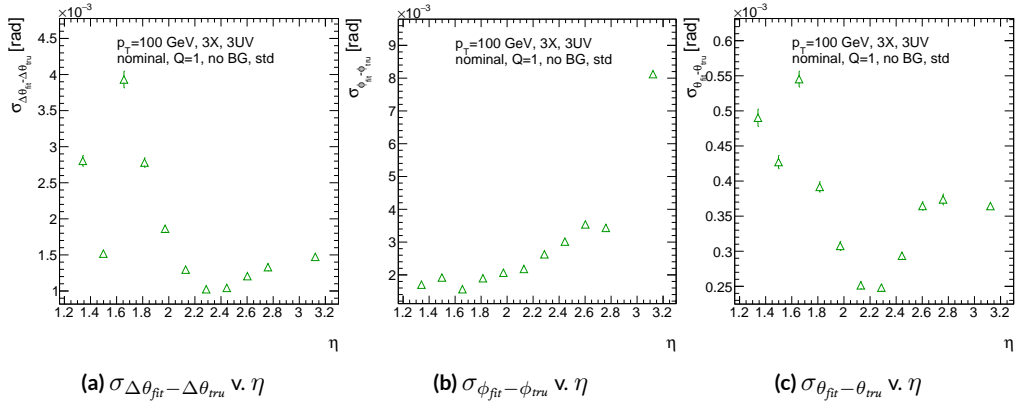


**Figure A.3:** The rms distributions of  $\Delta\theta$ ,  $\phi$ , and  $\theta$  as a function of  $\eta$  for  $p_T = 100$  GeV; the final point in each plot is the rms obtained from a fit to the full distribution including all  $\eta$  bins.

---

<sup>§</sup>The much worse overall performance for  $\phi$  is due to the  $\eta$  dependent bias and other effects

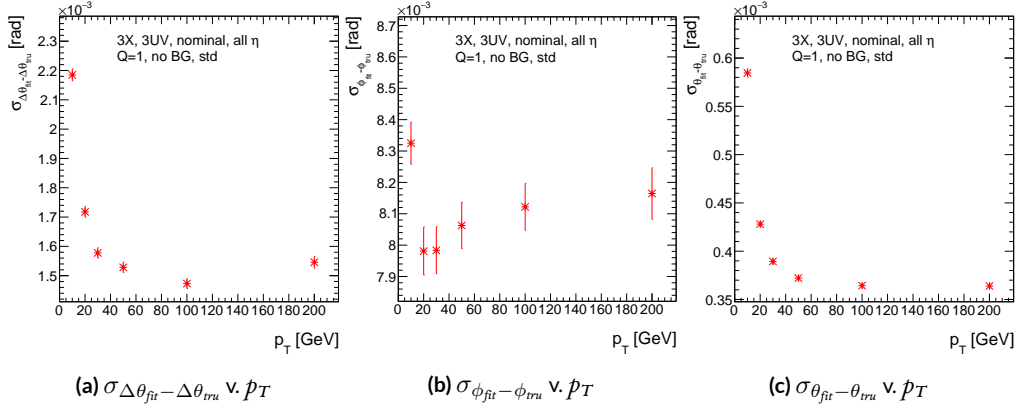


**Figure A.4:** The rms distributions of  $\Delta\theta$ ,  $\phi$ , and  $\theta$  as a function of  $p_T$ .

2205 The rms of the three benchmark quantities as a function of algorithm set (i.e. slope-road) coinci-  
 2206 dence threshold are shown in Figure A.5 using Gaussian fits and in Figure A.6 for the raw quantities.  
 2207 The fitted  $\sigma$ 's for  $\theta$  and  $\phi$  are fairly stable across coincidence threshold.  $\Delta\theta$ , on the other hand, per-  
 2208 forms better particularly for the most stringent coincidence threshold; this is a result of the fact that  
 2209 additional information for more hits greatly improves the quality of the local slope fit calculation.  
 2210 The raw rms is a different story. Naïvely, one would expect the performance to get better with more  
 2211 stringent coincidence threshold, but this is not the case in Figure A.6. As the coincidence thresh-  
 2212 old gets more stringent, fewer and fewer tracks are allowed to be fit. When moving from 2X hits to  
 2213 3X hits, the tracks that get vetoed populate the tails of the distribution outside the  $3\sigma$  fit range but  
 2214 are not in the very extremes of the distribution. While tracks with 2X hits are of lower quality than  
 2215 those with 3 and 4 X hits, tracks with the very worst fit values pass even the most stringent coinci-  
 2216 dence threshold requirements (e.g. as a result of many hits arising from a shower of secondaries).  
 2217 This is best illustrated when comparing the 2X+1UV  $\Delta\theta$  residual distribution with the 4X+4UV

distribution in Figure A.7. As both the overlayed normalized curves and ratio distribution show,  
 while the most central regions are fairly similar, the  $\omega X + 1$  UV distribution is much more prominent  
 in the tails but not the extreme tails, which means that, though the overall  $\omega X + 1$  UV raw rms goes  
 down, the overall quality of algorithm fits is worse.

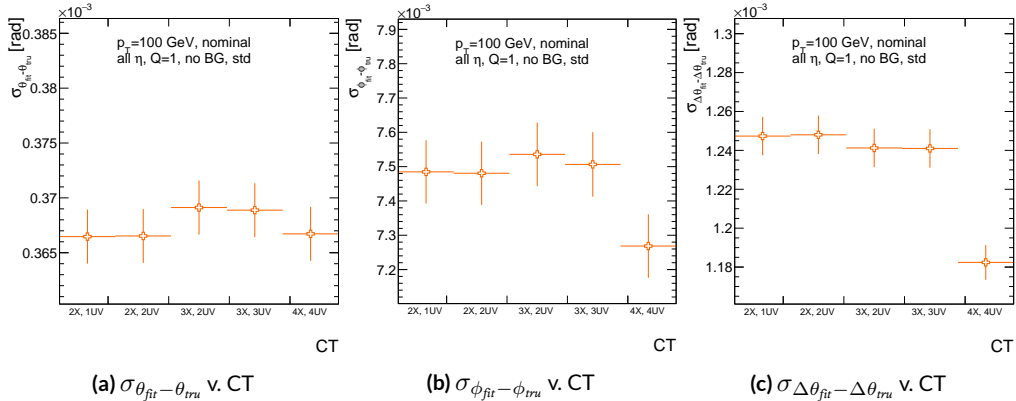


**Figure A.5:** The fitted rms of residual distributions for  $\theta$ ,  $\phi$ , and  $\Delta\theta$  as a function of coincidence threshold for  $p_T = 100$  GeV.

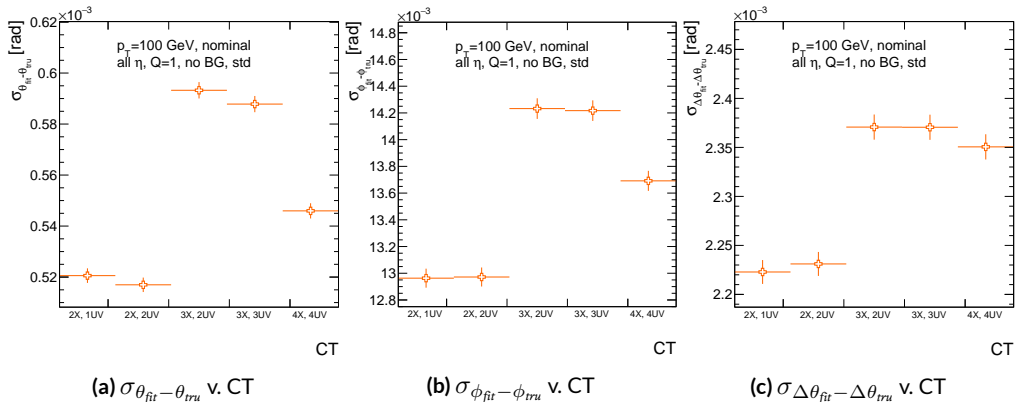


**Figure A.6:** The raw rms of residual distributions for  $\theta$ ,  $\phi$ , and  $\Delta\theta$  as a function of coincidence threshold for  $p_T = 100$  GeV.

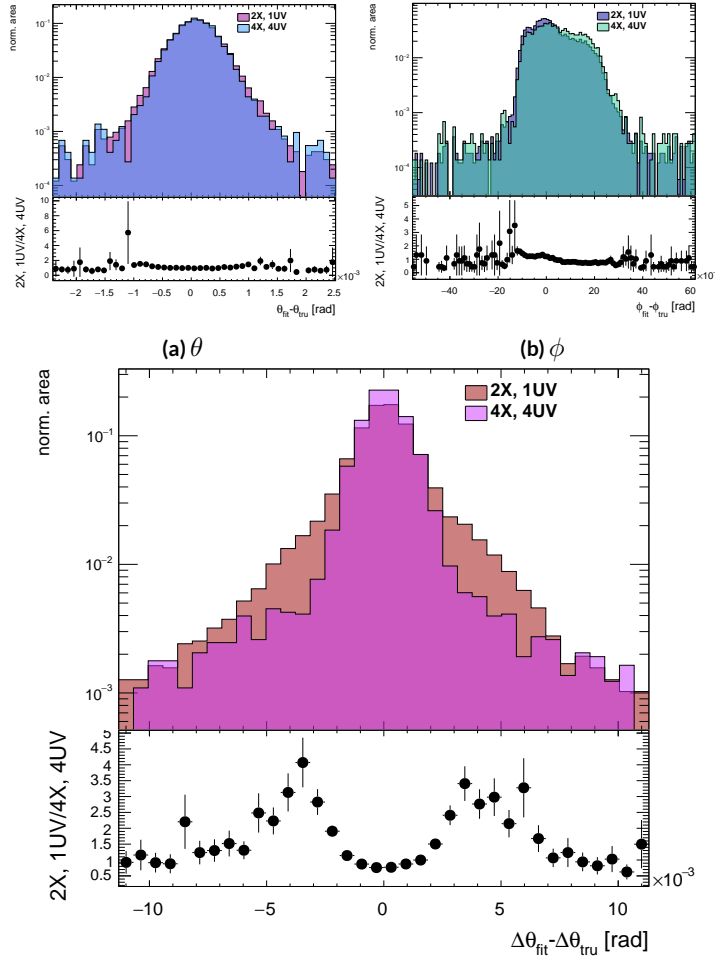


**Figure A.7:** Nominal  $\Delta\theta$  residual distribution for  $p_T = 100$  GeV muons with coincidence thresholds 2X+1UV and 4X+4UV normalized to the same area and plotted together (top) as well as the ratio of the 2X+1UV distribution and the 4X+4UV per bin.

2222 A.5 EFFICIENCIES

2223 Two general efficiencies have been formulated to study the performance of the MMTP algorithm.  
 2224 The first, denoted  $\varepsilon_{alg}$ , is the fraction of tracks that pass some (slope-road) coincidence threshold  
 2225 configuration that are successfully fit. An event that passes a slope-road coincidence but does not fit  
 2226 fails because some of the hits included are of sufficiently poor quality to throw off the fit. This effi-  
 2227 ciency answers the question of how often the algorithm performs fits when technically possible, giv-  
 2228 ing a measure of overall algorithm performance for a given configuration. For example,  $\varepsilon = 95\%$  for  
 2229  $3X+2UV$  means that 95% of tracks that produce at least  $3X$  hits and  $2UV$  hits in at least one slope-  
 2230 road will be successfully fitted 95% of the time. The performance of this efficiency as a function of  
 2231 coincidence threshold,  $\eta$  (with the final point once again being the efficiency integrated over all  $\eta$ ),  
 2232 and  $p_T$  is shown in Figure A.8.  $\varepsilon_{alg}$  is fairly constant in  $\eta$  and decreases with increased  $p_T$ , which can  
 2233 be attributed to the increased likelihood of secondaries introducing lower quality hits that cause the  
 2234 fit to fail.

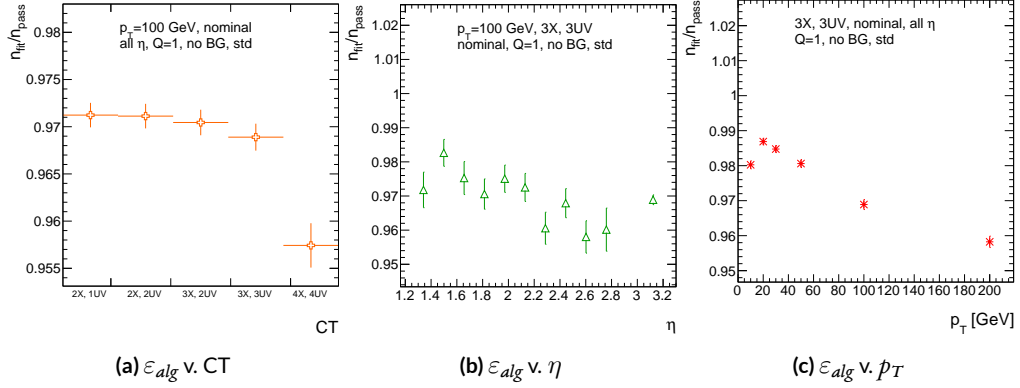
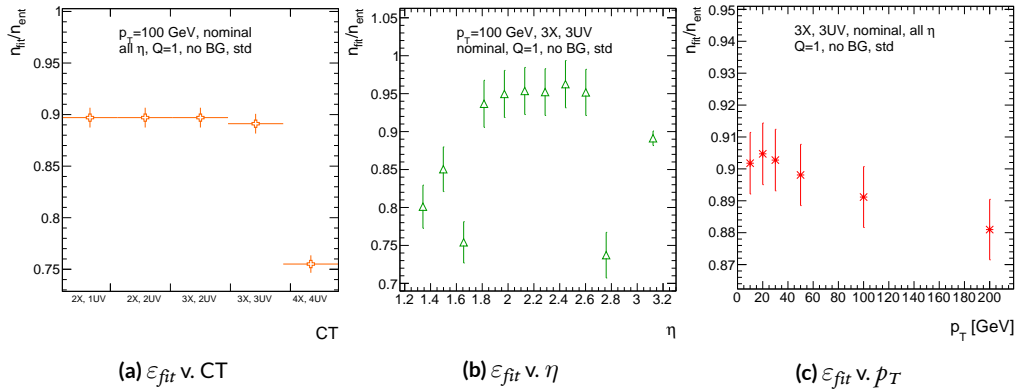


Figure A.8:  $\varepsilon_{alg}$  and as a function of coincidence threshold,  $\eta$  (final point is  $\varepsilon_{alg}$  integrated over all  $\eta$ ), and  $p_T$ .

2235 The second efficiency type, denoted  $\varepsilon_{fit}$ , is the fraction of tracks that enter the wedge whose fits  
 2236 (if any) satisfy a given coincidence threshold. This efficiency can be used to help establish an optimal  
 2237 coincidence threshold setting in the algorithm, balancing the improved overall fit quality of higher  
 2238 thresholds with the greater number of fits for lower thresholds. Hence, an  $\varepsilon_{fit}$  of 95% at 3X+2UV  
 2239 means that 95% of tracks entering the wedge are fit and that these fits include at least 3X and 2UV  
 2240 hits.  $\varepsilon_{fit}$  as a function of coincidence threshold is shown in Figure A.9 (a), which shows that the ma-  
 2241 jority of fits having at most 3X+3UV hits. That there is a marked drop to 4X+4UV is not surpris-  
 2242 ing, as there is a substantial population outside the 4X+4UV bin in Figure A.10. The behavior of  
 2243  $\varepsilon_{fit}$  with  $\eta$  in Figure A.9 (b) (with the final point once again being the efficiency integrated over all  
 2244  $\eta$ ) is much more varied, with geometric effects of detector acceptance coming into play. The per-  
 2245 formance of  $\varepsilon_{fit}$  as a function of  $p_T$ , shown in Figure A.9 (c), is similar to that of  $\varepsilon_{alg}$  coincidence  
 2246 threshold, again consistent with the effects of secondaries at higher energies.



**Figure A.9:**  $\varepsilon_{fit}$  and as a function of coincidence threshold,  $\eta$  (final point is  $\varepsilon_{fit}$  integrated over all  $\eta$ ), and  $p_T$ .

2247 In order to better understand efficiency behavior with coincidence threshold, the distribution of

2248 highest slope-road coincidence thresholds in events is shown in Figure A.10, with the o,o bin con-  
 2249 taining events that did not meet requirements for the minimum  $2X+1UV$  coincidence threshold for  
 2250 a fit to occur. That the efficiency is lower at higher coincidence threshold suggests that most of the  
 2251 fits that fail have high hit multiplicity (i.e. a similar number fails in each of the coincidence thresh-  
 2252 old bins in Figure A.8 (a)), which is consistent with the interpretation that the primary source of fit  
 2253 failures is bad hits originating from secondaries created by higher energy muons.

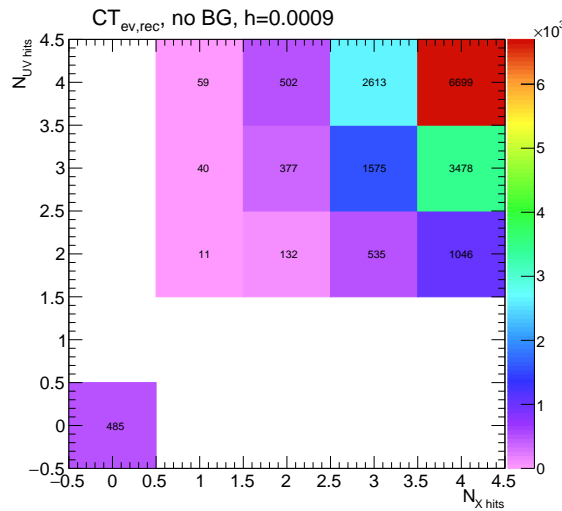


**Figure A.10:** The distribution of highest slope-road coincidence thresholds in events; the 0,0 bin is the number of events passing selection requirements that fail to form the minimum  $2X+1UV$  coincidence threshold necessary for a fit.

2254 A.6 INCOHERENT BACKGROUND

2255 The default slope-road size and tolerances associated with horizontal and stereo hits used in the  
2256 above studies were configured to optimize algorithm performance, similar to studies in [41]. In or-  
2257 der to evaluate algorithm performance under conditions with more limited resources, as might be  
2258 expected at run-time, additional studies were conducted with the slope-road size and hit tolerances  
2259 set equivalent to the sensitive area of a single VMM chip<sup>¶</sup> both with and without generation of inco-  
2260 herent background.

2261 Incoherent background is generated based on the assumption that the intensity only varies as a  
2262 function of the distance from a point to the beamline,  $r$ . The number of hits per unit area per unit  
2263 time as a function of  $r$  is given in Equation A.6 and taken from [41].

$$I = I_0 (r/r_0)^{-2.125} \quad (\text{A.6})$$

2264 where  $r_0 = 1000$  mm and  $I_0 = 0.141$  kHz/mm<sup>2</sup>

2265 Background generation happens per event as follows:

- 2266 1. Determine the total number of hits to be generated in this event according to a Poisson distri-  
2267 bution
- 2268 2. Assign a time to hits uniformly in  $[t_{\text{start}} - t_{\text{VMM}}, t_{\text{end}}]$  where start and end are for the event  
2269 clock and  $t_{\text{VMM}}$  is the VMM chip deadtime (100 ns)
- 2270 3. Assign a plane to hits uniformly
- 2271 4. Assign a  $\phi$  value to hits uniformly

---

<sup>¶</sup>One VMM is assumed to cover 64 MM strips at 0.445 mm each.

2272 5. Assign an  $r$  to hits according to Equation A.6

2273 6. Calculate hit information according to these values.

2274 The expectation value for the Poisson distribution is determined by integrating Equation A.6

2275 over the surface area of the wedge to get the total hit rate for the wedge,  $\Gamma$ , and then multiplying this

2276 by the length of the time window over which hits may be generated. With  $H = 982$  mm,  $b_1 =$

2277 3665 mm, and  $\theta_w = 33\pi/180$ , we find<sup>||</sup>:

$$\Gamma = 2I_0 r_0^{2.125} \int_0^{\theta_w/2} d\phi \int_{H \sec \phi}^{(H+b_1) \sec \phi} r dr r^{-2.125} = 98.6657 \text{ MHz} \quad (\text{A.7})$$

2278 In this case, we have taken the nominal values of the MM sector geometry for  $H$  (wedge base),  $b_1$

2279 (the wedge height), and  $\theta_w$  (the wedge opening angle).

2280 The effects of incoherent background and larger slope road size are summarized in Figure A.11 for

2281 efficiencies and in Figure A.13 and Table A.1 for residual of fit quantities.

2282 Figure A.11 show the effect of both wider slope-roads and the introduction of background on ef-

2283 ficiencies. The introduction of wider slope-roads increases the chance that an early errant hit (either

2284 from secondaries/ionization or background) will be introduced into the fit, and the presence of in-

2285 coherent background greatly increases the number of such errant hits. Both wider slope-roads and

2286 background drive down the number of fits (numerator) in both efficiencies, and background can

2287 artificially inflate the denominator of  $\varepsilon_{alg}$ , a reco-level, slope-road coincidence threshold. The shape

2288 of the  $\varepsilon_{fit}$  versus coincidence threshold distributions remains fairly constant with each complicat-

---

<sup>||</sup>Using Mathematica and the extra factor of  $r$  from the volume element

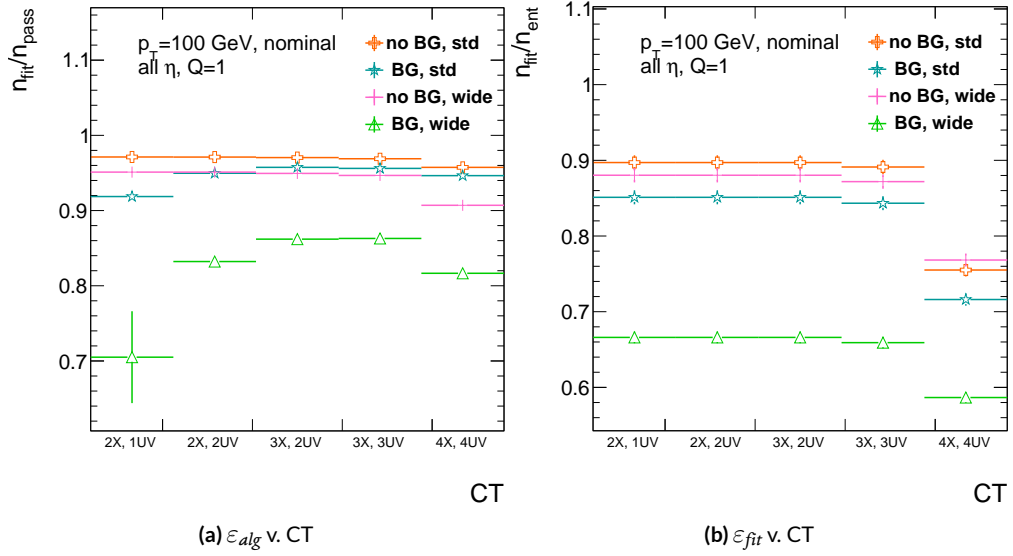


**Figure A.11:** The algorithm and total efficiencies as a function of coincidence threshold for different background settings and slope-road sizes (standard and wide (one slope road as 1 VMM chip)).

ing factor (standard, wider slope-roads, background, both wider slope-roads and background), suggesting many muons will simply not be fit with any number of hits;  $\varepsilon_{fit}$  does not take into account the coincidence threshold of tracks that are not fit, so the effect appears uniform across coincidence threshold. The effects seen for  $\varepsilon_{alg}$ , which are not uniform across coincidence threshold can be better understood when examining the distribution of event highest coincidence thresholds, shown for wide slope-roads both without and with background in Figure A.12. Take, for example the  $2X+1UV$  case. The  $2X+1UV$  bin in particular has a marked increase when background is introduced. No new, good tracks are introduced between the no background and background cases, so the increase is entirely due to bad, background hits; hence, these events do not (and should not) fit, causing the particularly pronounced drop in this bin between these two cases in Figure A.11.

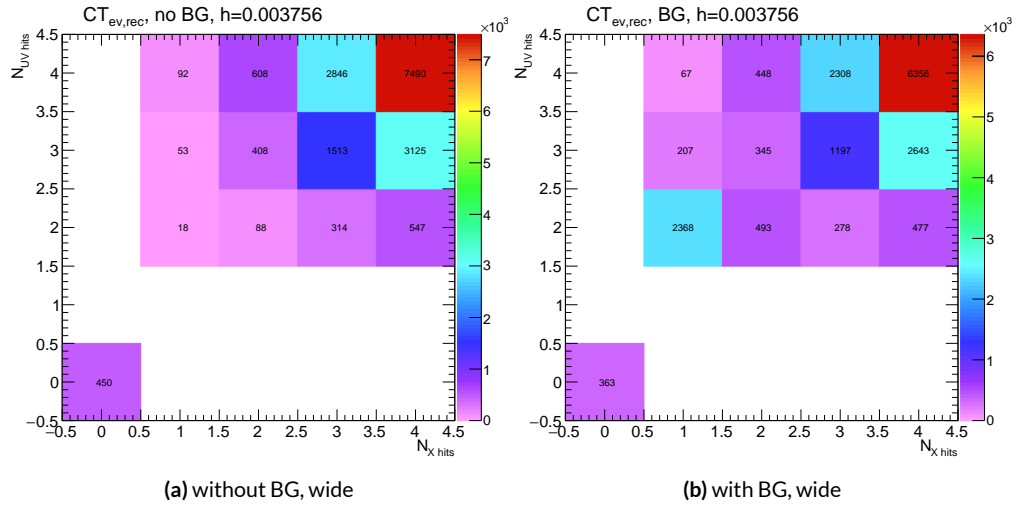


**Figure A.12:** The distribution of highest slope-road coincidence thresholds in events for the algorithm with wide slope-roads (width of 1 VMM) both without (a) and with (b) incoherent background; the 0,0 bin is the number of events passing selection requirements that fail to form the minimum  $2X+1UV$  coincidence threshold necessary for a fit.

The effect of increasing slope-road size and incoherent background on fit quantity residual rms values as a function of  $p_T$  is shown in Figure A.13. As the figure shows, the fitted rms values are fairly robust against increased slope-road size and background. This does not hold for all of the raw rms values, however, as shown in Table A.1. Just as with the efficiencies, the introduction of background has a larger effect than that of increased slope-road size, which does not seem to have an overly large impact on any of the fit quantities on its own. While  $\Delta\theta$  remains robust to both increased slope-road size and background (likely due to the  $\Delta\theta$  cut of 16 mrad built into the algorithm),  $\theta$  shows some degradation in performance, and the  $\phi$  residual raw rms shows a very large increase upon the introduction of background. Nevertheless, the contrasting behavior of the fitted and raw rms values suggests that tracks that drive up the raw rms values already had very poor fit quality even before the introduction of background, so the impact on fit quantities should remain fairly limited.

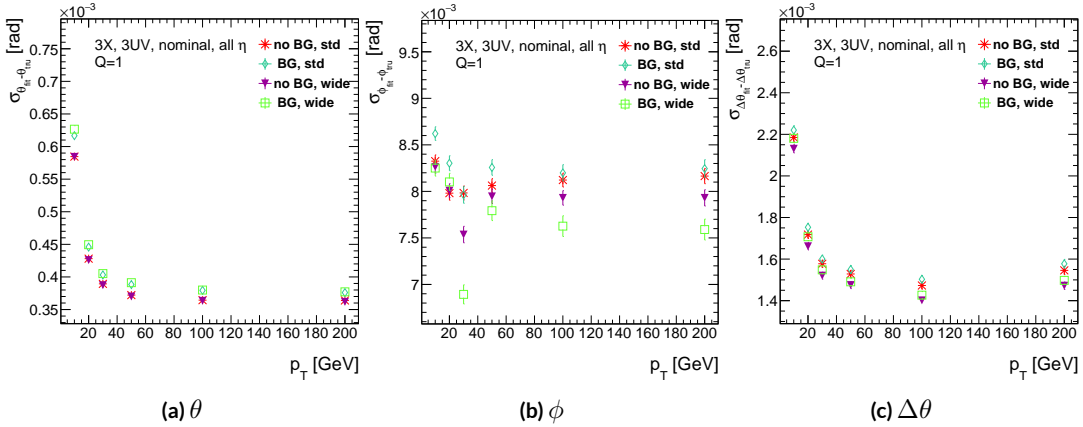


**Figure A.13:** The three fit quantity residual rms values as a function of  $p_T$  for different background settings and slope-road sizes (standard and wide (one slope road as 1 VMM chip)).

	No BG, std	No BG, wide	BG, std	BG, wide
$\theta$	0.364 (0.604)	0.363 (0.542)	0.379 (0.886)	0.380 (1.07)
$\phi$	8.12 (15.0)	7.93 (13.2)	8.20 (24.6)	7.63 (24.8)
$\Delta\theta$	1.47 (2.69)	1.40 (2.66)	1.50 (2.89)	1.43 (2.90)

**Table A.1:** The fitted (absolute)  $\sigma$  of fit quantity residuals in mrad under different algorithm settings.

2310 As Table A.1 shows, rms values appear to be robust to an increase in slope-road size. Neverthe-  
2311 less, though the fitted  $\sigma$  residual values are also fairly robust to the introduction of background, the  
2312 raw rms values are not. While the raw  $\Delta\theta$  rms stays stable, both  $\theta$  and  $\phi$  suffer noticeable degra-  
2313 dation, which suggests that the introduction of background has a detrimental effect on horizontal  
2314 slope residual (i.e. on stereo strips in particular). This level of degradation is likely acceptable for  $\theta$ ,  
2315 though further steps may need to be taken to address  $\phi$ .

### 2316 A.7 BCID

2317 A fitted track's BCID is determined by the most common BCID associated with its hits. Concerns  
2318 were raised that this might cause incorrect BCID association for fitted tracks. In order to address  
2319 this, the rate of successful BCID association for fitted tracks was recorded. Figure A.14 shows the  
2320 dependence of this success rate as a function of  $p_T$  and coincidence threshold in the different back-  
2321 ground and resource conditions used in the previous section. The successful BCID identification  
2322 rate is always over 99.5%, demonstrating that this issue is not a concern with the state-of-the-art de-  
2323 tector simulation.

### 2324 A.8 CHARGE THRESHOLD

2325 The MMTP uses the first hits registered passing a charge threshold requirement given in units of  
2326 electron charge. In principle, it would be beneficial to be able to use any hits that are registered re-  
2327 gardless of deposited charge, but in the high rate environment envisioned for the NSW, this require-  
2328 ment might need to be raised. Nominal algorithm settings have this charge threshold requirement

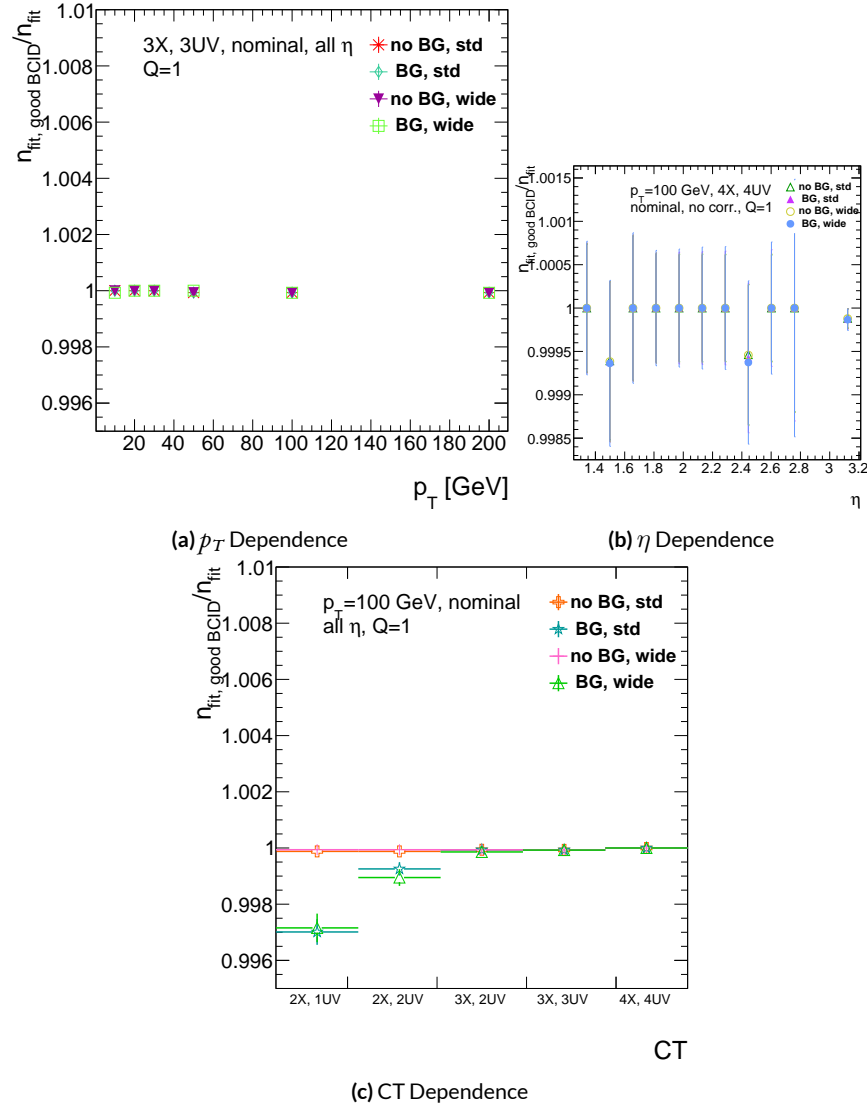


**Figure A.14:** The rate of good BCID association based majority hit BCID as a function of  $p_T$  and coincidence threshold.

2329 set to 1, and studies were conducted on algorithm performance for charge threshold values of 0, 1,  
 2330 and 2. Efficiencies as a function of coincidence threshold for different charge thresholds are shown  
 2331 in Figure A.15. Increasing the charge threshold lowers both efficiencies, particularly at high coinci-  
 2332 dence threshold, which suggests that energetic muons with secondaries create both very many hits  
 2333 and hits with higher charge. While the shapes of the fit quantity distributions as a function of  $p_T$  in  
 2334 Figure A.16 are fairly constant across charge threshold, performance is not.  $\theta$  and  $\Delta\theta$  show some im-  
 2335 provement with higher charge threshold, particularly at low  $p_T$ , suggesting that resolution improves  
 2336 in the vertical direction, but  $\phi$  shows degradation at higher charge threshold, which is a symptom  
 2337 of more highly charged particles experiencing greater bending in the ATLAS magnetic field in the  $\phi$   
 2338 direction.

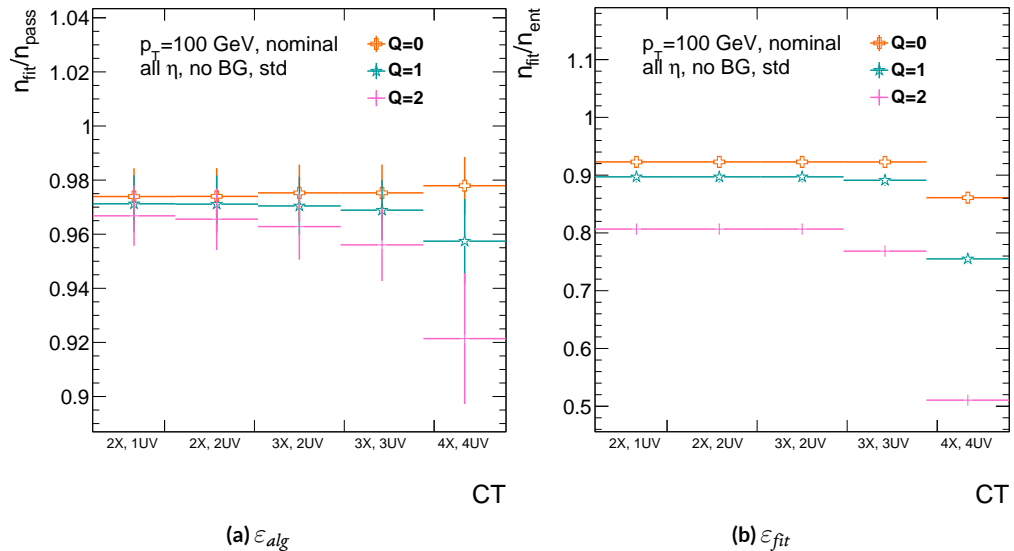


**Figure A.15:** The efficiencies as a function of coincidence threshold for charge thresholds of 0, 1, and 2.

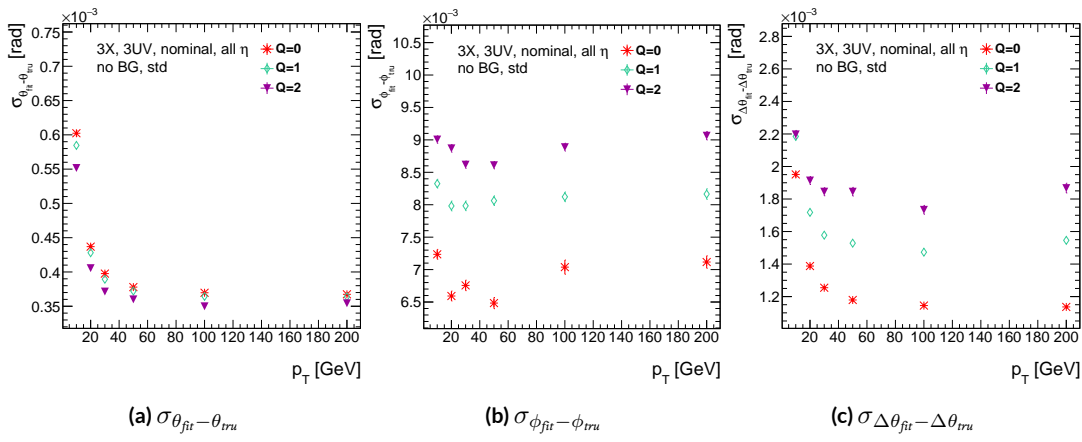


**Figure A.16:** The fit quantity residual rms values as a function of  $p_T$  for charge thresholds of 0, 1, and 2.

2339 A.9 MISALIGNMENTS AND CORRECTIONS

2340 The performance of the trigger algorithm under misalignment has been studied for each of the six  
2341 alignment quantities (three translations and three rotations all along the principal axes) described  
2342 in [?] and [?], whose convention we will follow here. For the simulated wedge studied here the  
2343 local coordinates described in [?] are taken to be centered at the center of the base of the wedge<sup>\*\*</sup>,  
2344 the local  $t$  axis corresponds to the axis of the beam line, the local  $z$  axis corresponds to the direction  
2345 orthogonal to both the beam line and the horizontal strips, and the local  $s$  axis completes the right-  
2346 handed coordinate system. The rotation angles  $\alpha$ ,  $\beta$ , and  $\gamma$  correspond to rotations around the local  
2347  $t$ ,  $z$ , and  $s$  axes, respectively. Note that the local  $s$ ,  $z$ , and  $-t$ , axes correspond to the usual global  $x$ ,  $y$ ,  
2348 and  $z$  axes. Misalignments were studied in twenty evenly spaced increments from nominal positions  
2349 to misalignments of 1.5 mrad for the rotations (-1.5 mrad to +1.5 mrad for the  $\gamma$  case), and of 5 mm  
2350 (a roughly corresponding linear shift) for the translations. In all cases, the front quadruplet is mis-  
2351 aligned while the rear quadruplet remains in its nominal position. While only the front quadruplet  
2352 of a single wedge is misaligned, the framework for misalignment presented below could be used to  
2353 study generic local and global misalignments. The six misalignments are schematically represented  
2354 in Figure A.17.

2355 Chamber misalignments manifest themselves as altered strips in algorithm input. In order to sim-  
2356 ulate the effects of misalignment, the change in the local  $y$  coordinate—the distance from the bot-

---

<sup>\*\*</sup>Not, as is sometimes the case, the centroid position for simplicity's sake, as the agreed upon geometry of the detector changed several times while studies were in progress; any transformation in a centroid-origin coordinate system can of course be formed by a combination of the six transformations examined.

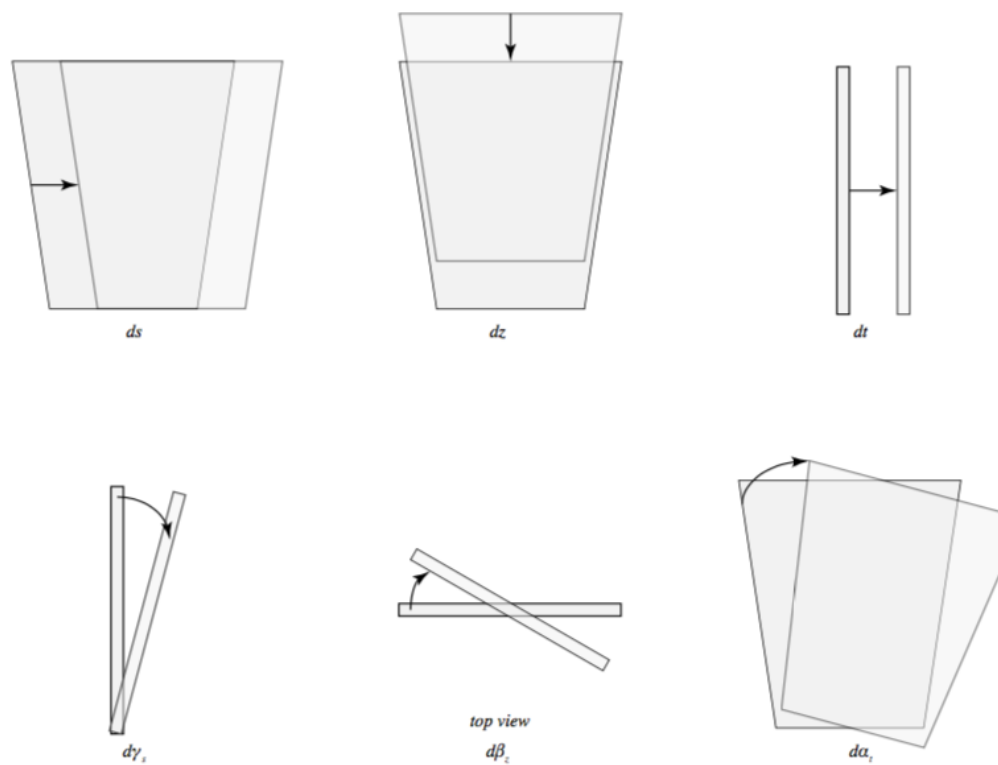


**Figure A.17:** The different misalignment cases as defined in the AMDB manual.

2357 tom wedge center in the direction perpendicular to both the beamline and the strip direction—is  
 2358 calculated for a track coming straight from the interaction point defined by the truth-level  $\theta$  and  $\phi$   
 2359 angles for generic misalignment. This displacement in  $y$  is then added to input hit information and  
 2360 the algorithm is then run normally.

2361 To understand how this displacement is calculated, some notation first needs to be described.

**Table A.2:** A summary of notation used in this section: note that non-AMDB notation is used in this section.

Symbol	Definition
$s_x, s_y, s_z, \vec{s}$	Position of the muon hit in ATLAS global coordinates; the infinite momentum muon track
$\hat{n}$	Vector normal to the plane; taken to be $\hat{z}$ (the beamline) in the nominal case
$\vec{\mathcal{O}}_{IP}^{g,l}$	Position of the interaction point in ATLAS global ( $g$ ) or wedge local ( $l$ ) coordinates
$\vec{\mathcal{O}}_{base}^{g,l}$	Position of the plane base in ATLAS global ( $g$ ) or wedge local ( $l$ ) coordinates; $(0, y_{base}, z_{pl})$ ( $(0, 0, 0)$ ) for the nominal case in global (local) coordinates
$\vec{\zeta}$	$\vec{s} - \vec{\mathcal{O}}_{base}$
primed quant.	quantities after misalignment

2362 Generically speaking, a hit is the intersection of a line (the muon track) with a plane (the individual plane in the multiplet). We assume the muon moves in a straight line defined by the origin and  
 2363 the truth-level  $\theta_{pos}$  and  $\phi_{pos}$  (i.e. the infinite momentum limit) and that the MM plane is rigid and  
 2364 defined by a point, which we take to be the center of the bottom edge of the plane, and a normal  
 2365 vector, which we take to be the  $z$  axis in the nominal case.

2366 The coordinate axes  $x, y, z$  axes used here correspond to the usual AMDB  $s, z, -t$  axes. Since the  
 2367 direction does not really matter when studying misalignment or corrections thereof, the major dif-

<sup>2369</sup> ference is the choice of origin.

<sup>2370</sup> The muon track we denote<sup>††</sup>  $\vec{s}$ , the bottom point of the plane  $\vec{\mathcal{O}}_{base}$ , and the normal vector  $\hat{n}$ .

<sup>2371</sup> The muon track will always be given as (the wedge gets moved, not the muon):

$$\vec{s} = \mathcal{O}_{IP} + k\hat{s} \quad (\text{A.8})$$

$$\hat{s} = \sin \theta_{pos} \sin \phi_{pos} \hat{x} + \sin \theta_{pos} \cos \phi_{pos} \hat{y} + \cos \theta_{pos} \hat{z} \quad (\text{A.9})$$

$$\vec{s} = k\hat{s} = \frac{z_{pl}}{\cos \theta_{pos}} \hat{s} = z_{pl} (\tan \theta \sin \phi \hat{x} + \tan \theta \cos \phi \hat{y} + 1) \quad (\text{A.10})$$

<sup>2372</sup> where  $k \in \mathbb{R}$ , along with the unit vector  $\hat{s}$ , defines the point where the track intersects the wedge.

<sup>2373</sup> Rotations are done before translations, according to the order prescribed in the AMDB guide for

<sup>2374</sup> chamber alignment, so the axes the principal axes of the plane are rotated according to the following

<sup>2375</sup> matrix (where  $s$ ,  $c$ , and  $t$  are the obvious trigonometric substitutions)

$$\begin{aligned} & \begin{pmatrix} 1 & 0 & 0 \\ 0 & c\gamma & -s\gamma \\ 0 & s\gamma & c\gamma \end{pmatrix} \begin{pmatrix} c\beta & 0 & s\beta \\ 0 & 1 & 0 \\ -s\beta & 0 & c\beta \end{pmatrix} \begin{pmatrix} c\alpha & -s\alpha & 0 \\ s\alpha & c\alpha & 0 \\ 0 & 0 & 1 \end{pmatrix} = \begin{pmatrix} 1 & 0 & 0 \\ 0 & c\gamma & -s\gamma \\ 0 & s\gamma & c\gamma \end{pmatrix} \begin{pmatrix} c\alpha c\beta & -s\alpha c\beta & s\beta \\ s\alpha & c\alpha & 0 \\ -c\alpha s\beta & s\alpha s\beta & c\beta \end{pmatrix} \\ & = \boxed{\begin{pmatrix} c\alpha c\beta & -s\alpha c\beta & s\beta \\ s\alpha c\gamma + c\alpha s\beta s\gamma & c\alpha c\gamma - s\alpha s\beta s\gamma & -c\beta s\gamma \\ s\alpha s\gamma - c\alpha s\beta c\gamma & c\alpha s\gamma + s\alpha s\beta c\gamma & c\beta c\gamma \end{pmatrix}} = \mathcal{A} \end{aligned} \quad (\text{A.11})$$

---

<sup>††</sup>Recall  $\phi_{pos}$  is defined with respect to the  $y$  axis instead of the  $x$  axis, as might otherwise be typical.

2376     The thing that matters is what the new strip hit is—i.e. what the new  $y$  value is since this, along  
 2377     with a plane number, is all that is fed into the algorithm. To find this, we must solve for the new  
 2378     point of intersection with the rotated plane and then apply the effects of translations. The path con-  
 2379     necting the base of the wedge with the intersection of the muon track will always be orthogonal to  
 2380     the normal vector of the plane. Our quantities after misalignment, denoted by primed quantities,  
 2381     will look like

$$\mathcal{O}_{base} \rightarrow \mathcal{O}_{base} + ds\hat{x} + dz\hat{y} + dt\hat{z} = \mathcal{O}'_{base}, \hat{n} \rightarrow A\hat{n} = A\hat{z} = \hat{z}', \vec{s} \rightarrow k'\hat{s} + \mathcal{O}_{IP} = \vec{s}' \quad (\text{A.12})$$

2382     so, moving to explicit, global coordinates in the last line so we can do the computation (relying on  
 2383     the fact that any vector in the wedge, namely  $\vec{\zeta} = \vec{s} - \mathcal{O}$  the local coordinates of the interaction  
 2384     point, is necessarily orthogonal to  $\hat{n}$ ):

$$0 = \hat{n} \cdot (\vec{\mathcal{O}}_{base} - \vec{s}) \rightarrow 0 = A\hat{z}' \cdot (\vec{\mathcal{O}}'_{base} - (k'\hat{s} + \vec{\mathcal{O}}_{IP})) \quad (\text{A.13})$$

$$\rightarrow k' = \frac{s\beta\mathcal{O}'_{base-IP,x} - c\beta s\gamma\mathcal{O}'_{base-IP,y} + c\beta c\gamma\mathcal{O}'_{base-IP,z}}{\hat{s} \cdot \hat{z}'} \quad (\text{A.14})$$

$$= \frac{s\beta ds - c\beta s\gamma(y_{base} + dz) + c\beta c\gamma(z_{pl} + dt)}{s\beta s\theta s\phi - c\beta s\gamma s\theta c\phi + c\beta c\gamma c\theta} \quad (\text{A.15})$$

2385     To find our new  $y$  coordinate, we need to evaluate  $s'_y = \hat{y}' \cdot k'\vec{s}$  to find the final correction of:

$$\Delta y = \vec{\zeta}' \cdot \hat{y}' - \vec{\zeta} \cdot \hat{y} = (k'\hat{s} - \vec{\mathcal{O}}'_{base}) \cdot \hat{y}' - (s_y - y_{base}) \quad (\text{A.16})$$

<sup>2386</sup> The correction will be plane dependent since (denoting the stereo angle  $\omega$ ):

$$\hat{y}_x = \hat{y} \rightarrow \hat{y}'_x = -s\alpha c\beta \hat{x} + (c\alpha c\gamma - s\alpha s\beta s\gamma) \hat{y} + (c\alpha s\gamma + s\alpha s\beta c\gamma) \hat{z} \quad (\text{A.17})$$

<sup>2387</sup> and

$$\begin{aligned} \hat{y}_{U,V} = & \pm s\omega \hat{x}' + c\omega \hat{y}'_{U,V} = [\pm c\alpha c\beta s\omega - s\alpha c\beta c\omega] \hat{x} + [\pm (s\alpha c\gamma + c\alpha s\beta s\gamma) s\omega \\ & + (c\alpha c\gamma - s\alpha s\beta s\gamma) c\omega] \hat{y} + [\pm (s\alpha s\gamma - c\alpha s\beta c\gamma) s\omega + (c\alpha s\gamma + s\alpha s\beta c\gamma) c\omega] \hat{z} \end{aligned} \quad (\text{A.18})$$

## <sup>2388</sup> A.10 INDIVIDUAL CASES

<sup>2389</sup> Currently we only study the cases where one misalignment parameter is not zero. We examine these  
<sup>2390</sup> in detail below, calculating the most pertinent quantities in the misalignment calculation,  $k'/k$  and  
<sup>2391</sup> the new horizontal and stereo  $y$  axes. Before setting out, we simplify the expressions for the trans-  
<sup>2392</sup> formed  $\hat{y}'$ 's, removing any terms with the product of two sines of misalignment angles, which will be  
<sup>2393</sup> zero.<sup>††</sup>

$$\hat{y}'_x = -s\alpha c\beta \hat{x} + c\alpha c\gamma \hat{y} + c\alpha s\gamma \hat{z} \quad (\text{A.19})$$

<sup>2394</sup>

$$\hat{y}'_{U,V} = [\pm c\alpha c\beta s\omega - s\alpha c\beta c\omega] \hat{x} + [\pm s\alpha c\gamma s\omega + c\alpha c\gamma c\omega] \hat{y} + [\mp c\alpha s\beta c\gamma s\omega + c\alpha s\gamma c\omega] \hat{z} \quad (\text{A.20})$$

---

<sup>††</sup>If only one misalignment parameter is non-zero, then two or more sines will contain at least one term will contain  $\sin 0 = 0$ .

<sup>2395</sup> If the translations are zero,

$$k' = \frac{-c\beta s\gamma y_{base} + c\beta c\gamma z_{pl}}{s\beta s\theta s\phi - c\beta s\gamma s\theta c\phi + c\beta c\gamma c\theta}, \quad k'/k = \frac{-c\beta s\gamma y_{base}/z_{pl} + c\beta c\gamma}{s\beta t\theta s\phi - c\beta s\gamma t\theta c\phi + c\beta c\gamma} \quad (\text{A.21})$$

<sup>2396</sup> A.II  $ds \neq 0$

<sup>2397</sup>  $k'/k = 1$  (the point of intersection does not move closer or further from the IP), and only the stereo planes are affected. Note that only relevant term in Equation A.16, for the stereo strip  $\hat{y}$  for  $\vec{\mathcal{O}}'_{base} =$   
<sup>2398</sup>  $ds\hat{x}$  is:

$$\pm \sin \omega ds \approx \pm 0.0261 ds \quad (\text{A.22})$$

<sup>2400</sup> meaning that a displacement in  $x$  of 17 mm, more than three times the range of misalignments studied, would be necessary for a shift in the stereo planes corresponding to one strip width.

<sup>2402</sup> A.12  $dz \neq 0$

<sup>2403</sup>  $k'/k = 1$  (the point of intersection does not move closer or further from the IP). This case is the trivial one (cf. Equation A.16 with  $\vec{\mathcal{O}}'_{base} = dz\hat{y}$ ).  $y$  just gets moved in the opposite direction as the wedge. Correction is an additive constant.

<sup>2406</sup> A.13  $dt \neq 0$

<sup>2407</sup>  $k'/k = (z_{pl} + dt) / z_{pl}$ .  $y$  gets modified by a simple scale factor. Correct by storing changing definitions of plane positions in algorithm to match the misaligned values.

<sup>2409</sup> A.14  $\alpha \neq 0$

<sup>2410</sup>  $k'/k = 1$  and

$$\hat{y}'_x = -s\alpha\hat{x} + c\alpha\hat{y} \quad (\text{A.23})$$

$$\hat{y}'_{U,V} = [\pm c\alpha s\omega - s\alpha c\omega] \hat{x} + [\pm s\alpha s\omega + c\omega] \hat{y} \quad (\text{A.24})$$

<sup>2411</sup> A.15  $\beta \neq 0$

<sup>2412</sup> We have  $k'/k = (1 + \tan \beta \tan \theta \sin \phi)^{-1}$ , and

$$\hat{y}'_x = \hat{y} \quad (\text{A.25})$$

$$\hat{y}'_{U,V} = \hat{y} \pm (c\beta\hat{x} - s\beta\hat{z}) s\omega \quad (\text{A.26})$$

<sup>2413</sup> A.16  $\gamma \neq 0$

$$k'/k = \frac{1 - \tan \gamma \frac{y_{base}}{z_{pl}}}{1 - \tan \gamma \tan \theta \cos \phi} \quad (\text{A.27})$$

$$\hat{y}'_x = c\gamma\hat{y} + s\gamma\hat{z} \quad (\text{A.28})$$

$$\hat{y}'_{U,V} = \pm s\omega\hat{x} + c\omega\hat{y} - s\gamma c\omega\hat{z} \quad (\text{A.29})$$

<sup>2414</sup> In order to evaluate algorithm performance under misalignment and corrections for misalign-

<sup>2415</sup> ment, the absolute means and relative resolutions of the fit quantities  $\theta$ ,  $\phi$ , and  $\Delta\theta$  are measured as

2416 a function of misalignment. In the following, results will only be shown for which the effects of mis-  
2417 alignment are significant. “Significant,” for misalignments of 1 mm (0.3 mrad) for translations (ro-  
2418 tations) means more than a 5% degradation in rms and/or bias shifts in  $\theta$ ,  $\phi$ , and  $\Delta\theta$  of 0.01 mrad, 1  
2419 mrad, and 0.1 mrad, respectively.

2420 While corrections are typically done on a case-by-base basis, they fall under two general cate-  
2421 gories, analytic and simulation based. Analytic corrections rely upon specific knowledge of the mis-  
2422 alignment, with each case being handled separately; as such, the additional resources required, both  
2423 extra constants and operations, if any, vary accordingly. Simulation based corrections are all done in  
2424 the same manner. The algorithm is run over a training MC sample (same setup but with  $p_T = 200$   
2425 GeV instead of the normal 100 GeV sample so as not to overtrain the corrections), and the mean bi-  
2426 ases for  $\theta$ ,  $\phi$ , and  $\Delta\theta$  are saved for different, equally spaced regions in the  $\eta - \phi$  plane over the wedge  
2427 based on the fitted  $\theta$  and  $\phi$  values. Currently, these values are saved for 10  $\eta$  and 10  $\phi$  bins (100  $\eta, \phi$   
2428 bins total), with the number of bins in each direction being a configurable parameter. When the al-  
2429 gorithm runs with simulation based correction, this table of constant corrections is saved in a LUT  
2430 before runtime, and corrections are added to final fit quantities based on the (uncorrected)  $\theta$  and  
2431  $\phi$  fit values. With the settings mentioned, this is 300 extra constants ( $10\eta\text{-bins} \times 10\phi\text{-bins} \times 3$  fit  
2432 quantities) and two extra operations (a lookup and addition for each quantity done in parallel). The  
2433 simulation correction can, in principle, also be applied to the algorithm in nominal conditions with  
2434 non-trivial improvements, as detailed below in Section A.17. Depending on the misalignment case in  
2435 question, different approaches work better. A summary of correction methods, including resources  
2436 necessary for the individual analytic cases, is shown in Table A.3.

	$\Delta_s$	$\Delta z$	$\Delta t$	$\gamma_s$	$\beta_z$	$\alpha_t$
Analytic Resources	yes+ 11c/2op	yes+ oc/oop	yes+ oc/oop	yes 56c/1op	no —	yes 400c/2n <sub>X</sub> op, 32c/12n <sub>X</sub> op
Simulation	yes+	no	no	no	yes+	yes+

**Table A.3:** A summary of corrections with additional constants/operations (written as  $n_{const}c/n_{ops}op$ ;  $n_X$  is the number of X hits in a fit) necessary for analytic corrections. Yes means a correction exists but might not entirely remove misalignment effects, while yes+ means a quality of correction is only limited by knowledge of misalignment and memory

2437 A.17 SIMULATION CORRECTION OF THE ALGORITHM UNDER NOMINAL CONDITIONS

2438 In addition to using simulation based correction to counter the effects of several classes of misalign-  
 2439 ment, the correction can be applied at to the algorithm under nominal conditions. The main effect  
 2440 of this correction is to mitigate the effects of the bias in stereo strips. As such, the correction has a  
 2441 larger effect on quantities that rely on the aggregate slope  $m_y$ , as can be seen in Figure A.18, im-  
 2442 proving  $\sigma_{\theta_{fit} - \theta_{tru}}$  resolution by about 25%, and reducing  $\sigma_{\phi_{fit} - \phi_{tru}}$  by over 50% and restoring a largely  
 2443 Gaussian shape. The slight, apparent degradation in  $\Delta\theta$  is due to a more mild version of the effect  
 2444 seen in Figure A.7.

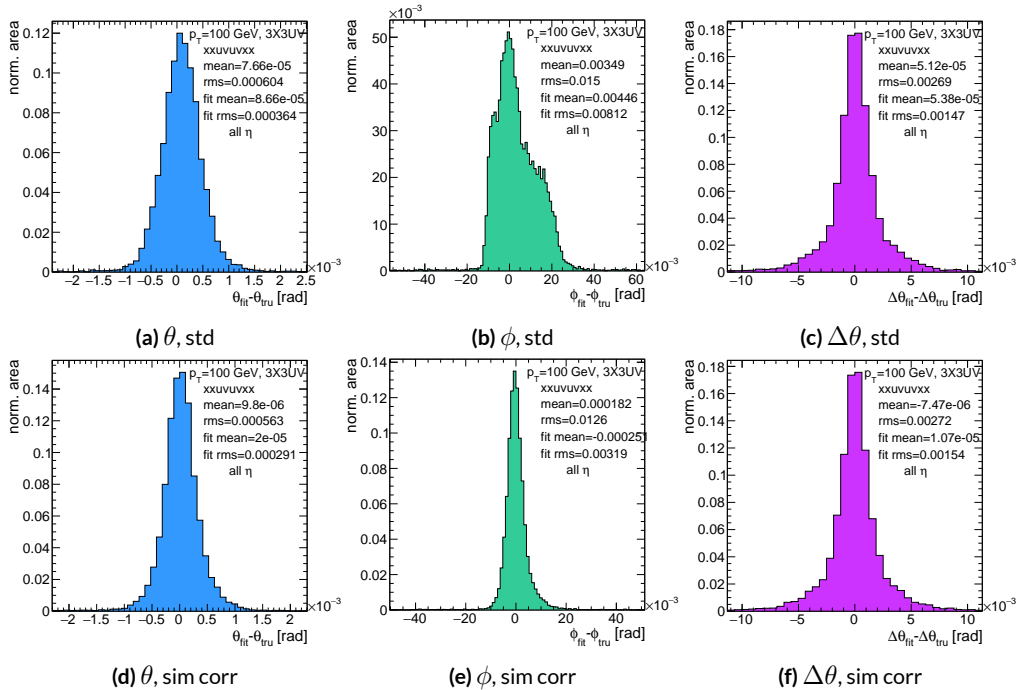


**Figure A.18:** Nominal residual plots for both uncorrected and simulation corrected cases;  $\theta$ ,  $\phi$ ,  $\Delta\theta$  for  $p_T = 100$  GeV muons

2445 As can be seen in Figure A.19, the simulation based correction also removes the  $\eta$  dependence to  
 2446 fit quantity resolution distributions, as expected. One consequence of this is that simulation-based  
 2447 corrections applied to the misalignment cases below will restore performance to the “sim” and not  
 2448 the “std” distributions of Figure A.18. Hence, when making comparisons between simulation cor-  
 2449 rected curves and the nominal performance point, simulation-corrected distributions of benchmark  
 quantities versus misalignment will often look generally better.

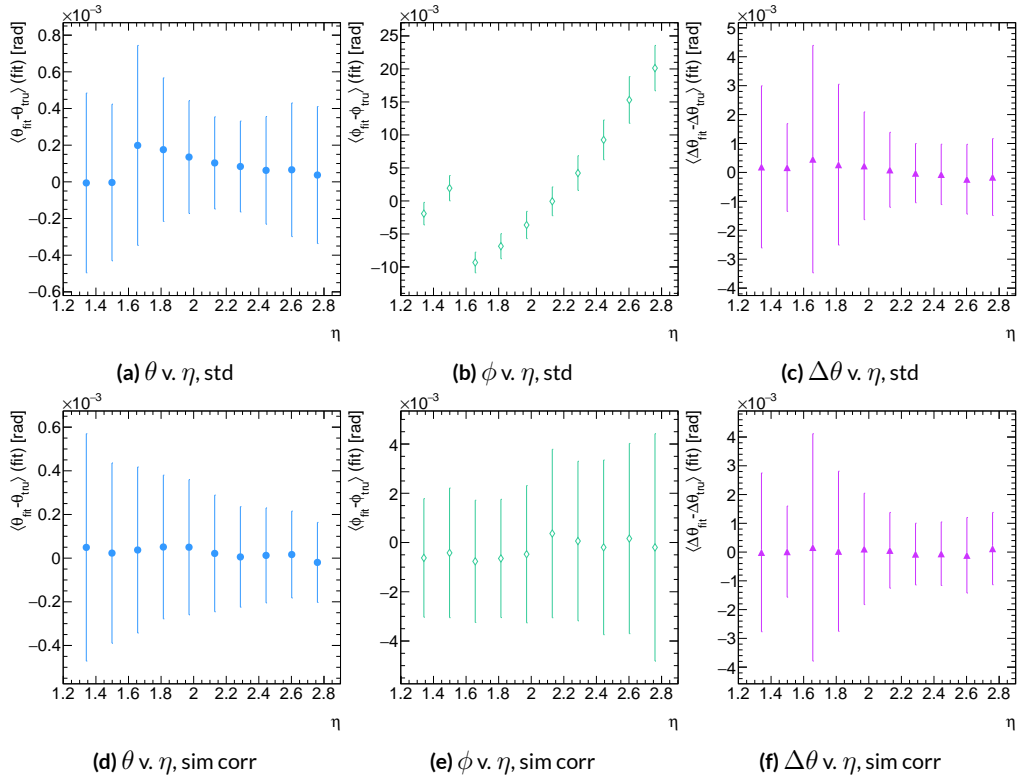


**Figure A.19:** Nominal residual plots as a function of  $\eta$  with points as means and error bars as rms values in each  $\eta$  bin for the angles  $\theta, \phi, \Delta\theta$  for  $p_T = 100$  GeV muons in the uncorrected and simulation corrected cases.

2450

2451 That the improvements from a simulation-based correction improve performance of the algo-

2452 rithm in nominal conditions most for the quantities that depend most on stereo information ( $\phi$  and  
 2453  $\theta$ ) and remove the  $\eta$  dependence of fit quantity resolutions suggests that there could, in principle, be  
 2454 analytic corrections that could be applied to the nominal algorithm. One possible solution is to in-  
 2455 troduce an additional set of constants, having the  $y_{base}$  depend on the strip number, similar to the  $\gamma_s$   
 2456 correction for  $z_{plane}$  described in Section A.21, which would add a lookup per hit and  $8 \times n_{bins,y}$  extra  
 2457 constants that would be optimized as the  $\gamma_s$  correction was.

$$M_{hit} = \frac{\gamma}{z} = \frac{y_{base}}{z_{plane}} (n_{str}) + \frac{w_{str}}{z_{plane}} n_{str} \quad (\text{A.30})$$

2458 The simulation correction residual rms values suggest a limit on the quality of such correction  
 2459 and could perhaps be implemented generically on their own regardless of misalignment for rms val-  
 2460 ues on fit quantities of 0.291 mrad for  $\theta$ , 3.19 mrad for  $\phi$ , and 1.54 for  $\Delta\theta$ , which represent a 20%  
 2461 improvement for  $\theta$ , a 62% improvement for  $\phi$ , and a slight degradation in  $\Delta\theta$  of 4.7%, again owing  
 2462 to an effect similar to the one in A.7.

2463 A.18 TRANSLATION MISALIGNMENTS ALONG THE HORIZONTAL STRIP DIRECTION ( $\Delta s$ )

2464 A translation in  $s$  (i.e. along the direction of a horizontal strip) only affects the stereo strips, and,  
2465 since the stereo angle is small, a very large misalignment is necessary for effects to be noticeable (a  
2466 misalignment of roughly 17 mm corresponds to one strip's misalignment in the stereo planes). The  
2467 only quantity to show any meaningful deviation with misalignments with translations in  $s$  is the  $\phi$   
2468 residual bias (a change of 0.4 mrad at  $\Delta s = 1$  mm), as can be seen in the uncorrected curve of Figure  
2469 A.20.

2470 A translation in  $s$  induces a constant shift in the calculated horizontal slope,  $m_x$  in Equation A.4.  
2471 This constant shift should only depend on which stereo planes included in a fit are misaligned and  
2472 how misaligned they are. Hence, the correction to  $m_x$ , for a sum over misaligned stereo planes  $i$ ,  
2473 with their individual misalignments in  $s$  and plane positions in  $z$  is:

$$\Delta m_x = \frac{1}{N_{\text{stereo}}} \sum_{i, \text{misal stereo}} \frac{\Delta s_i}{z_{i, \text{plane}}} \quad (\text{A.31})$$

2474 Given prior knowledge of misalignment, these corrections to  $m_x$  can be performed ahead of time  
2475 and saved in a lookup table (LUT), similar to the LUT used for constants in the X local slope ( $M_x^l$ )  
2476 calculation. The added overhead of this analytic correction is hence eleven constants in memory, a  
2477 lookup, and one addition. The correction perfectly corrects the effects of misalignment, as can be  
2478 seen in Figure A.20. The simulation based correction described above can also be used to correct  
2479 for  $\Delta s$  misalignments, with the results of that correction also shown in Figure A.20. The apparent

2480 discrepancy between the simulated and analytic correction is a natural consequence of the fact that  
 2481 the simulation correction, as previously mentioned, restores the  $\phi$  residual distribution to an overall  
 2482 more Gaussian shape.

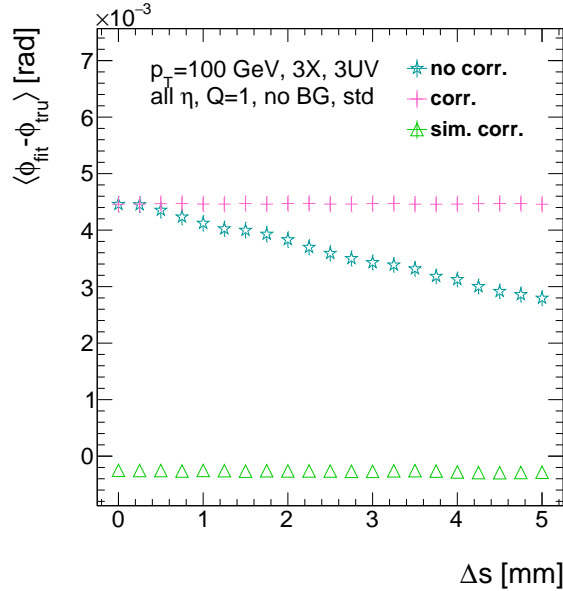


**Figure A.20:** The mean of the  $\phi$  residual as a function of misalignment for the uncorrected case and the analytic and simulation correction cases.

2483 A.19 TRANSLATION MISALIGNMENTS ORTHOGONAL TO THE BEAMLINE AND HORIZON-  
2484 TAL STRIP DIRECTION ( $\Delta z$ )

2485 A translation in AMDB  $z$ , the direction orthogonal to both the beamline and the horizontal strip  
2486 direction, corresponds to a translation in the  $y$  of Equation A.1, affecting all slope calculations. This  
2487 has a large impact on the  $\theta$  residual bias and both the bias and rms of  $\Delta\theta$  residual, as can be seen in  
2488 Figures A.21 (a)–(c). The marked degradation and non-linear behavior in performance at very high  
2489 levels of misalignments is a result of low statistics; there are fewer fits at high level of misalignments  
2490 since for  $\Delta z \gtrsim 3$  mm, most fits will fail the  $\Delta\theta$  cut. The  $\theta$  bias shifts by about 0.075 mrad at  $\Delta z =$   
2491 1 mm, and  $\Delta\theta$  shifts by about 5 mrad for the same level of misalignment. While the fitted rms of the  
2492  $\Delta\theta$  residual remains fairly stable for  $\Delta z < 1$  mm or so, between  $\Delta z = 2$  mm and  $\Delta z = 3$  mm, the  
2493 rms increases by 15% before the  $\Delta\theta$  cut issue mentioned above intervenes.

2494 Fortunately, these misalignments are straightforward to correct with knowledge of the misalign-  
2495 ment. The only modification necessary for this correction is to change the definitions of  $y_{base}$  in  
2496 Equation A.1 for the individual hit slope addressing. This is done before runtime and adds no over-  
2497 head to the algorithm, and the correction quality is only limited by knowledge of the misalignment.  
2498 The results of this correction are also shown in Figures A.21 (a)–(c) and restore nominal perfor-  
2499 mance.

---

Since  $\Delta\theta = \frac{M_x^l - M_x^e}{1 + M_x^l M_x^e}$  and  $M_x^l = B_k \sum y_i (z/\bar{z} - 1)$ , a shift  $\Delta y$  translates (with typical slope values of  $\sim 0.3$ ) to  $5B_k (z_1 + z_2)/\bar{z}$  (with  $B_k$  in units of inverse mm); set equal to 16 mrad ( $\Delta\theta$  is centered at zero), this corresponds to  $\Delta y = 2.7$  mm

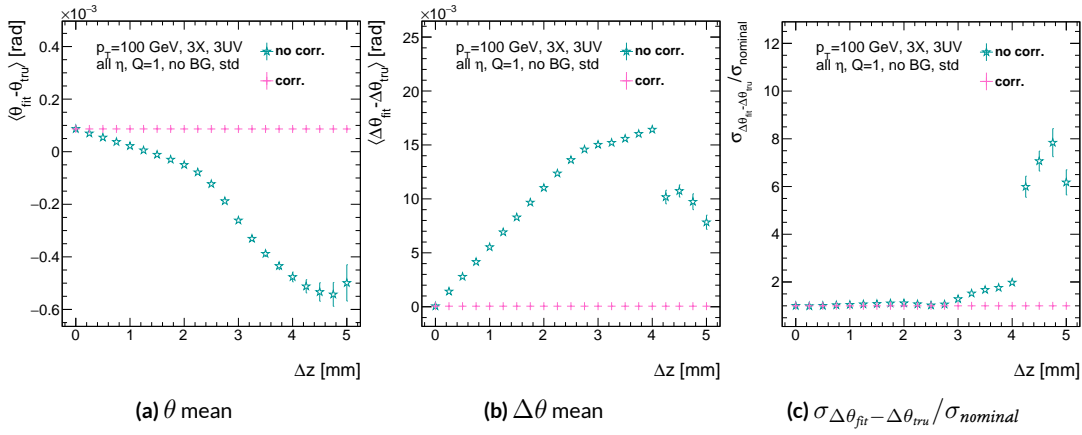


**Figure A.21:** The affected quantities of  $\Delta z$  misalignments:  $\theta$  bias,  $\Delta\theta$  bias, and  $\sigma_{\Delta\theta_{\text{fit}} - \Delta\theta_{\text{tru}}} / \sigma_{\text{nominal}}$  for both the misaligned and corrected cases.

2500 A.20 TRANSLATION MISALIGNMENTS PARALLEL TO THE BEAMLINE ( $\Delta t$ )

2501 The effects of misalignment due to translations in  $t$  are very similar to those due to translations in  
 2502  $z$  without the complication of the  $\Delta\theta$  cut, affecting the  $z$  instead of the  $y$  coordinate that enters  
 2503 into hit slope calculations. Again,  $\theta$  bias,  $\Delta\theta$  bias, and  $\sigma_{\Delta\theta_{fit}-\Delta\theta_{true}}$  are the primarily affected quan-  
 2504 tities. For  $\Delta t = 1$  mm,  $\theta$  bias shifts by about 0.02 mrad,  $\Delta\theta$  bias shifts by just under 2 mrad, and  
 2505  $\sigma_{\Delta\theta_{fit}-\Delta\theta_{true}}$  degrades by about 20%. The correction for this misalignment once again costs no over-  
 2506 head and consists of changing stored constants in the algorithm, in this case the positions along the  
 2507 beamline of the misaligned planes, with results similarly limited by knowledge of the misalignment.

2508 The slight improvement with correction to  $\Delta\theta$  rms is due to the real effect of a larger lever arm.

2509 Both the misaligned and corrected distributions of affected quantities of interest are shown in Fig-  
 ure A.22.

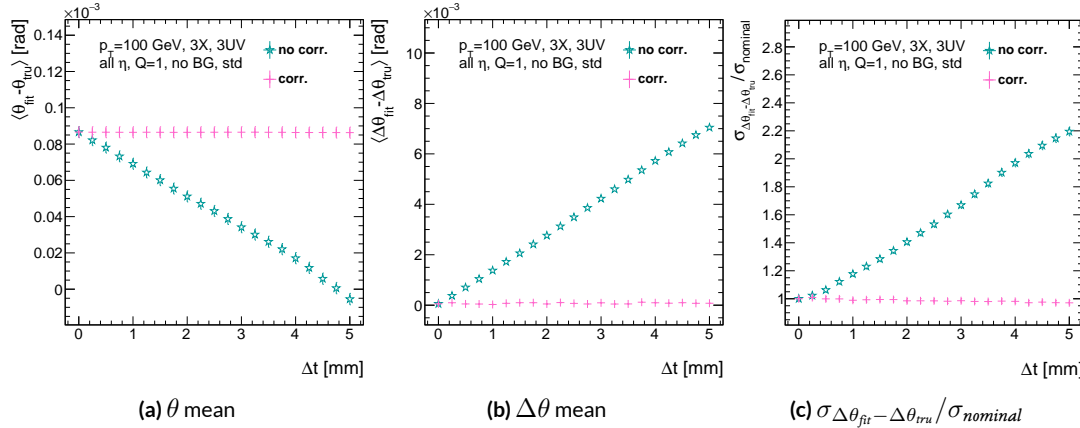


Figure A.22: The affected quantities of  $\Delta t$  misalignments:  $\theta$  bias,  $\Delta\theta$  bias, and  $\sigma_{\Delta\theta_{fit}-\Delta\theta_{true}} / \sigma_{nominal}$  for both the misaligned and corrected cases.

2511 A.21 CHAMBER TILTS TOWARDS AND AWAY FROM THE IP ( $\gamma_s$  ROTATION)

2512 Chamber misalignment due to rotations around the  $s$  axis act effectively like a translation in  $t$  that  
2513 depends on strip number. These rotations tilt misaligned chambers away from (towards) the IP for  
2514 positive (negative) values of  $\gamma_s$ . Since, unlike for the other two rotation cases that will be studied,  
2515 positive and negative rotation values are not symmetric, this misalignment is studied for both posi-  
2516 tive and negative  $\gamma_s$  values. The divergent effect at the tails is a result of a large population of fits not  
2517 having fit quantities within the cores, and so not appearing in the fit rms. Once again, affected quan-  
2518 tities of interest  $\theta$  bias,  $\Delta\theta$  bias, and  $\sigma_{\Delta\theta_{fit}-\Delta\theta_{tru}}$ . The effects of misalignment can be seen in Figures  
2519 A.23 (a)–(c). The relationship between biases and  $\gamma_s$  is roughly linear with  $\Delta\gamma_s = 0.3$  mrad (the an-  
2520 gular scale corresponding to linear shifts of  $\sim 1$  mm) corresponding to 0.005 mrad (0.12 mrad) for  $\theta$   
2521 ( $\Delta\theta$ ). For  $\sigma_{\Delta\theta_{fit}-\Delta\theta_{tru}}$ , degradation is not symmetric. For negative (positive)  $\gamma_s$ , with the quadruplet  
2522 tilted towards (away from) the IP, slope-roads are artificially expanded (shrunk), decreasing (increas-  
2523 ing) the granularity of the trigger, explaining the asymmetry in Figure A.23 (c), with the degradation  
2524 being a 10% (25%) effect for  $\gamma_s$  of  $+(-)0.3$  mrad.

2525 Corrections are less simple in this case. In principle, corrections of the same accuracy of the trans-  
2526 lations could be calculated per strip, but the overhead of one correction per strip (many thousands  
2527 of constants) is prohibitive. Instead, each plane was divided into eight equal segments with a  $t$  value  
2528 ( $z$  in the slope calculation) assigned to strips in each region to correct for the misalignment. This  
2529 amounts to 56 extra constants and a 2D instead of a 1D LUT for  $z$  positions while the algorithm  
2530 runs. The corrected distributions can also be seen in Figures A.23 (a)–(c). The corrections, while not

as effective as for the simple translation cases, are still very effective with the quoted misalignment values for bias shifts down to 0.001 mrad (0.25 mrad) for  $\theta$  ( $\Delta\theta$ ) and no more than a 2% degradation in  $\sigma_{\Delta\theta_{fit}-\Delta\theta_{true}}$  for  $|\gamma_s| = 0.3$  mrad.

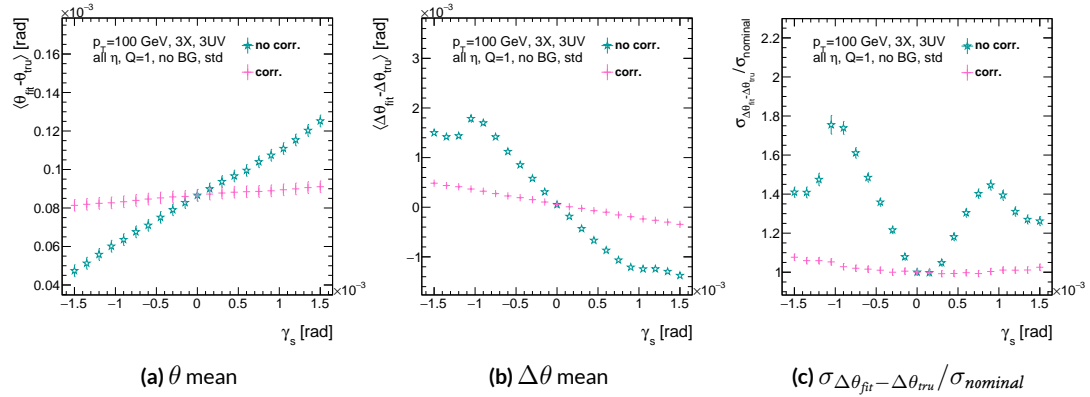


**Figure A.23:** The noticeable effects of rotations in the  $s$  axis and the behavior of these quantities ( $\theta$  and  $\Delta\theta$  bias shifts and  $\sigma_{\Delta\theta_{fit}-\Delta\theta_{true}}/\sigma_{nominal}$ ) with and without misalignment correction.

2534 A.22 ROTATION MISALIGNMENTS AROUND THE WEDGE VERTICAL AXIS ( $\beta_z$ )

2535 While misalignments coming from rotations around the  $z$  axis (the direction orthogonal to both  
 2536 the beamline and the horizontal strip direction) foreshorten the strips as seen from the IP and add  
 2537 a deviation in  $t$ , the long lever arm largely washes out any effects of this misalignment. Only the  
 2538  $\sigma_{\Delta\theta_{fit}-\Delta\theta_{tru}}$  is noticeably affected, though only at severe misalignments, with only about a 1% degra-  
 2539 dation in performance at  $\beta_z = 0.3$  mrad (corresponding to a linear shift of  $\sim 1$  mm). A simulation  
 2540 based correction works well to cancel out the effects of this misalignment, and the  $\sigma_{\Delta\theta_{fit}-\Delta\theta_{tru}}$  as a  
 2541 function of misalignment with and without corrections are shown in Figure A.24. The apparent  
 2542 2% effect in the simulation corrected curve is a result of a more mild version of the effect shown in  
 2543 Figure A.7.

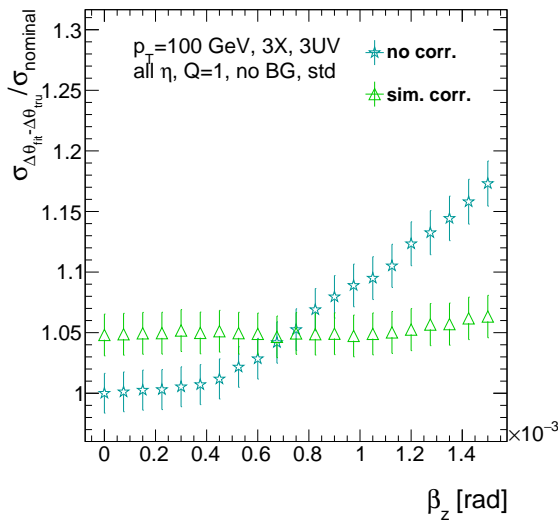
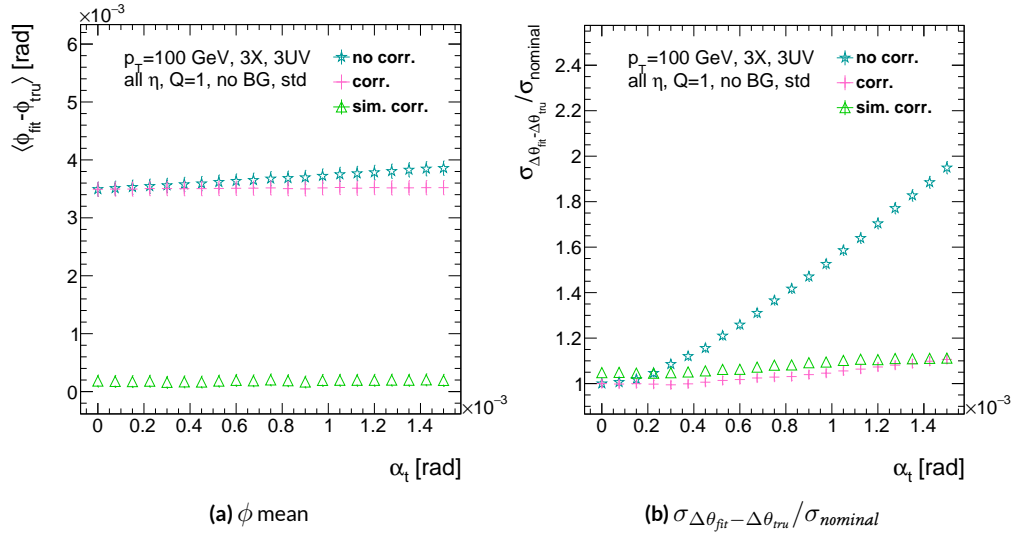


Figure A.24: The effects of rotations in the  $z$  axis on  $\sigma_{\Delta\theta_{fit}-\Delta\theta_{tru}} / \sigma_{nominal}$  a function of  $\beta_z$  both with and without misalignment corrections.

2544 A.23 ROTATION MISALIGNMENTS AROUND THE AXIS PARALLEL TO THE BEAMLINE ( $\alpha_t$ )

2545 Misalignments arising from rotations around the  $t$  axis (parallel to the beamline at the center of  
2546 the base of the wedge) are essentially rotations in the  $\phi$  direction. The quantities of interest most  
2547 affected are the  $\phi$  bias and  $\sigma_{\Delta\theta_{fit}-\Delta\theta_{tru}}$ , as shown in Figures A.25 (a) and (b), respectively, and cor-  
2548 respond to a shift in  $\phi$  bias of 0.2 mrad and a 10% degradation in  $\sigma_{\Delta\theta_{fit}-\Delta\theta_{tru}}$  for  $\alpha_t = 0.3$  mrad  
2549 (corresponding to a linear shift of  $\sim 1$  mm). The raw instead of fitted mean  $\phi$  biases is used in Fig-  
2550 ure A.25 (a) to better illustrate the effect of misalignment.

2551 Since the effect of misalignment is dependent on horizontal (along the strip direction,  $\hat{s}$ ) in addi-  
2552 tion to vertical information, corrections cannot be applied before a fit takes place. The  $\phi$  bias shift is  
2553 uniform over the entire wedge, so a constant additive correction to  $\phi$  based on the level of misalign-  
2554 ment can be applied to all fits depending on how many misaligned stereo planes enter in the fit.  $\Delta\theta$   
2555 is less straightforward, but corrections to the  $y$  and  $z$  information used in the local slope calculation  
2556 in Equation A.4 can be applied once  $\theta_{fit}$  and  $\phi_{fit}$  are known. These corrections are calculated ahead  
2557 of time in bins of uniform  $\eta$  and  $\phi$  as with the simulation corrections using the same framework  
2558 as the misalignment calculation. The results of both types of correction can be seen in Figure A.22.  
2559 The apparent discrepancy between the simulation and analytic corrections in the  $\phi$  bias happens for  
2560 the same reason as in the  $\Delta s$  misalignment correction cases, as simulation correction restores a more  
2561 Gaussian shape to the  $\phi$  residual distribution opposed to the uncorrected nominal case, as discussed  
2562 in Section A.17.



**Figure A.25:** The effects of rotation misalignments around the  $t$  axis for  $\phi$  bias and  $\sigma_{\Delta\theta_{fit} - \Delta\theta_{true}} / \sigma_{nominal}$  as a function of misalignment. The uncorrected and both the analytic and simulation correction cases are shown.

2563 A.24 CONCLUSION

2564 The algorithm for Micromegas detectors in the NSW Trigger Processor performs well in a variety of  
2565 conditions and has proven robust to a number of effects to deliver measurements on muon tracks  
2566 of the three angles  $\theta$ ,  $\phi$ ,  $\Delta\theta$ . Under nominal conditions, the rms values for the residuals of these  
2567 quantities are 0.364 mrad for  $\theta$ , 8.12 mrad for  $\phi$ , and 1.47 mrad for  $\Delta\theta$ . Algorithm performance was  
2568 found to be largely independent of the charge threshold setting, and a hit majority BCID associa-  
2569 tion was found to provide proper timing information over 99.7% even in the most relaxed settings  
2570 (2X+1UV coincidence threshold requirement+wide slope-road+background). The introduction of  
2571 wide slope-roads to better mimic potentially limited algorithm resources at run time and the intro-  
2572 duction of incoherent background was found to have a manageable effect on fit quantity residual  
2573 rms values and on total algorithm efficiency for sufficiently stringent coincidence threshold. The ef-  
2574 ffects of the three translation and three rotation misalignments specified by AMDB convention were  
2575 studied, and correction methods for each of the six cases was developed. Simulation-based correc-  
2576 tions were found to improve nominal algorithm performance to residual rms value of 0.291 mrad for  
2577  $\theta$ , 3.19 mrad for  $\phi$ , and 1.54 for  $\Delta\theta$ , which represent improvements of 20%, 62%, and -4.7%, respec-  
2578 tively. Misalignment corrections were found to restore nominal performance for all but the rotation  
2579 around the  $s$  axis, and a summary of tolerances may be found in Table A.4.

	No Correction	Correction
$\Delta s$	4 mm ( $\phi$ bias)	> 5 mm
$\Delta z$	0.25 mm ( $\Delta\theta$ )	> 5 mm
$\Delta t$	0.25 mm ( $\Delta\theta$ )	> 5 mm
$\gamma_s$	0.15 mrad ( $\Delta\theta$ bias)	0.75 mrad
$\beta_z$	0.9 mrad ( $\Delta\theta$ rms)	> 1.5 mrad
$\alpha_t$	0.375 mrad ( $\Delta\theta$ rms)	> 1.5 mrad

**Table A.4:** A summary of levels of misalignment corresponding to a 10% degradation in any residual rms or, for biases shifts of 0.01 mrad for  $\theta$ , 1 mrad for  $\phi$ , and 0.25 mrad for  $\Delta\theta$  for both the uncorrected and corrected cases; > 5 mm and > 1.5 mrad mean that such a degradation does not occur for the range of misalignment studied. Most affected quantity in parentheses.

*Tod-Not-Brot*

Old German Proverb

2580

# B

2581

## Telescoping Jets

2582 ANOTHER APPROACH TO IMPROVING  $ZH \rightarrow \ell\ell b\bar{b}$  is the use of telescoping jets [36], which har-  
2583 nesses the power of multiple event interpretations. The use of multiple event interpretations was  
2584 originally developed with non-deterministic jet algorithms like the Q-jets (“quantum” jets) algo-  
2585 rithm [69]. When a traditional or “classical” algorithm, such as the Cambridge-Aachen[81] and

259

2586 anti- $k_t$ [63] algorithms, is applied to an event, it produces one set of jets for that event, i.e. a single  
2587 interpretation of that event. With multiple event interpretations, each event is instead given an en-  
2588 semble of interpretations. In the case of Q-jets, this ensemble is created through a non-deterministic  
2589 clustering process for an anti- $k_t$  jet algorithm. With telescoping jets, multiple jet cone radii (the char-  
2590 acteristic size parameter,  $R$ ) around a set of points in the pseudorapidity-azimuth ( $\eta - \phi$ ) plane are  
2591 used to generate a series of jet collections. Instead of an event passing or not-passing a given set of  
2592 cuts, a fraction (called the cut-weight,  $z$ ) of interpretations will pass these cuts. This cut-weight al-  
2593 lows for enhanced background suppression and increased significance of observed quantities for a  
2594 given data set, as detailed in Ref. [47]. The telescoping jets algorithm provides the benefits of mul-  
2595 tiple event interpretations without the significant computational overhead of a non-deterministic  
2596 algorithm like the Q-jets algorithm, and its multiple cone sizes are particularly suited to studying  
2597 processes like associated production, which suffers from a pronounced low tail in the dijet invariant  
2598 mass distribution due to final state radiation (FSR) “leaking” outside the relatively narrow jets used  
2599 for object reconstruction.

## 2600 B.I MONTE CARLO SIMULATION

2601 The MC simulated samples used in this study are the same as in Ref. [? ]. The signal sample used  
2602 is generated in PYTHIA8 [77] with the CTEQ6L1 parton distributions functions (PDFs) and AU2  
2603 tune[55, 2, 3] for the  $ZH$  process with  $m_H = 125$  GeV (henceforth,  $ZH125$ ). The primary back-  
2604 ground processes examined in this study were  $Z$ +jets with massive  $b$  and  $c$  quarks. These samples  
2605 are generated with version 1.4.1 of the SHERPA generator [76].

2606 B.2 JET RECONSTRUCTION AND CALIBRATION

2607 In order to construct telescoping jets, jet axes must first be found around which to “telescope.” In  
2608 the reconstructed-level analysis, the anti- $k_t$  algorithm with  $R = 0.4$  is used to reconstruct jets from  
2609 topological clusters in the calorimeters. The four vectors of these anti- $k_t$  algorithm with  $R = 0.4$   
2610 jets are calibrated to match truth information obtained from simulation and validated in data. To  
2611 take into account the effect of pile-up interactions, jet energies are corrected using a jet-area based  
2612 technique [32], and each jet with  $p_T < 50$  GeV and  $|\eta| < 2.4$  is subject to a requirement that at least  
2613 50% of the scalar sum of the  $p_T$  of tracks matched to this jet be composed of tracks also associated  
2614 with the primary vertex. Jet energies are also calibrated using  $p_T$  and  $\eta$ -dependent correction factors  
2615 [11]. Furthermore, at least two jets must have  $|\eta| < 2.5$  in order to be  $b$ -tagged. The MV1 algorithm  
2616 [4? ? ? ?] is used for  $b$ -tagging. Once jets are reconstructed and  $b$ -tag weights have been calculated,  
2617 the two hardest,  $b$ -tagged jets are used as the telescoping jet axes. Additional details can be found in  
2618 Ref. [12].

2619 After the telescoping jet axes have been established, telescoping jets are constructed using topo-  
2620 logical clusters in the calorimeters at a variety of jet cone sizes. Including the original anti- $k_t$  jets  
2621 used for the  $R = 0.4$  case, twelve total sets of jets of cone sizes ranging from  $R = 0.4\text{--}1.5$  are  
2622 constructed, with each successive size having a radius 0.1 larger than the preceding set. For each jet  
2623 axis, telescoping jets consist of any topological cluster lying within  $R$  of the axis. In the event of over-  
2624 lap, clusters are assigned to the closer jet axis. If a given cluster is equidistant from the two jet axes,  
2625 the cluster is assigned to whichever jet axis is associated with the anti- $k_t$  jet with higher  $p_T$ . Calibra-

tion for the telescoping jets is conducted using corrections for anti- $k_t$  calorimeter topological cluster jets; the  $R = 0.4$  corrections are used for telescoping  $R = 0.5$ , and the  $R = 0.6$  corrections are used for telescoping  $R \geq 0.6$  (cf. Sec. B.4). The telescoping cone jets ( $R \geq 0.5$ ) at reconstructed level are trimmed using Cambridge-Aachen jets with  $R = 0.3$  and  $f_{cut} = 0.05$  with respect to the untrimmed jet  $p_T$  [48]. Since these jets are trimmed, the active area correction is not applied. In the event a  $Z$  candidate electron falls within  $R$  of the axis of a telescoping jet, its 4-momentum is subtracted from that of the jet vectorially.

A similar process is used to construct telescoping jets in the truth-level analysis below. Instead of the two hardest  $b$ -tagged anti- $k_t$  with  $R = 0.4$  jets reconstructed with calorimeter topological clusters, the two hardest truth  $b$ -jets in an event are used. Instead of making a cut on  $b$ -tagging weight to  $b$ -tag, truth jets are examined to see whether a  $b$ -hadron with  $p_T > 5$  GeV is contained within  $\Delta R < 0.4$  of the jet axis; the presence of a  $b$ -hadron is used to  $b$ -tag truth-level jets. These two jets again provide the jets for the  $R = 0.4$  case and the axes around which telescoping takes place. Stable truth particles, not including muons and neutrinos, are used in place of calorimeter topological clusters.  $Z$  candidate electron-telescoping jet overlap removal is performed at truth level, too. Missing  $E_T$  is calculated using the vector sum of the four momenta of stable truth-level neutrinos. Since there are no pileup particles stored at truth level, truth-level telescoping jets are not trimmed.

### 2643 B.3 EVENT RECONSTRUCTION AND SELECTION

Events are selected on the basis of a combination of leptonic, jet, and missing  $E_T$  requirements, which are outlined in Table B.1. Leptons are categorized by three sets of increasingly stringent qual-

2646   ity requirements, which include lower limits on  $E_T$ , upper limits on  $|\eta|$ , impact-parameter require-  
2647   ments, and track-based isolation criteria. The requirements differ for electrons [5] and muons [1].  
2648   Events are selected with a combination of single lepton, dielectron, and dimuon requirements. Each  
2649   event must contain at least one lepton passing medium requirements and at least one other lepton  
2650   passing loose requirements. These leptons are used to create a dilepton invariant mass cut to ensure  
2651   the presence of a  $Z$  boson and suppress multijet backgrounds.

2652   Event selection requirements are also imposed on the anti- $k_t$  with  $R = 0.4$  jets. There must be at  
2653   least two  $b$ -tagged jets in a given event. The  $p_T$  of the harder  $b$ -tagged jet must be at least 45 GeV, and  
2654   the second  $b$ -tagged jet must have  $p_T$  of at least 20 GeV. There are further topological cuts on the  
2655   separation of the two jets  $\Delta R(b, \bar{b})$ , the distance between the two jets in the  $(\eta, \phi)$  plane, according  
2656   to the transverse momentum of the  $Z$  boson,  $p_T^Z$ . These are shown in Table B.2.

2657   The truth-level analysis has the same missing  $E_T$ , jet  $p_T$ ,  $m_{ll}$ , and additional topological selection  
2658   criteria, but the use of truth-level information simplifies the other requirements. Instead of lepton  
2659   quality requirements,  $Z$  boson candidate leptons' statuses and MC record barcodes are checked to  
2660   ensure the leptons are stable.

2661   In the jet calibration validation, the reconstructed level analysis lepton and  $m_{ll}$  requirements are  
2662   imposed, but neither the missing  $E_T$  nor the jet selection requirements are applied so as not to bias  
2663   the validation.

**Table B.1:** A summary of basic event selection requirements. Truth-level  $b$ -tagging is done with truth-level information.

Requirement	Reconstructed	Truth	Validation
Leptons	1 medium + 1 loose lepton	2 produced by $Z$ boson	1 medium + 1 loose lepton
$b$ -jet	2 $b$ -tags	2 $b$ -jets	—
$p_T$ jet 1 (jet 2)		$> 45 \text{ GeV} (> 20) \text{ GeV}$	—
Missing $E_T$		$E_T^{\text{miss}} < 60 \text{ GeV}$	—
$Z$ boson		$83 < m_{ll} < 99 \text{ GeV}$	

**Table B.2:** Topological requirements of the event selection.

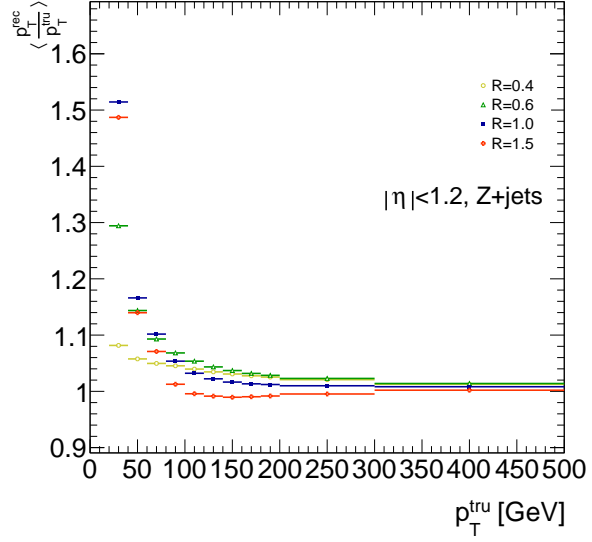
$p_T^Z [\text{GeV}]$	$\Delta R(b, b)$
0–90	0.7–3.4
90–120	0.7–3.0
120–160	0.7–2.3
160–200	0.7–1.8
$> 200$	$< 1.4$

2664    B.4    VALIDATION OF JET CALIBRATION

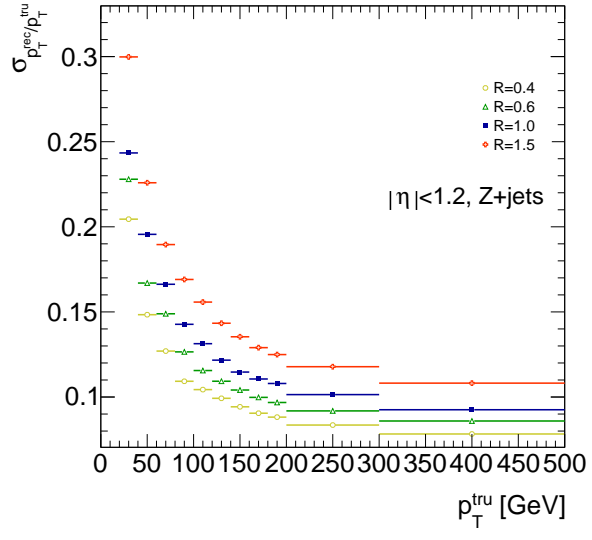
2665    In order to validate the jet energy scale and resolution of jets constructed with this telescoping-jets  
2666    algorithm, values of  $p_T^{rec}/p_T^{tru}$  are studied for each value of  $R$  for the  $Z+jets$  MC sample. In a given  
2667    event, all jets, not just the two hardest  $b$ -tagged jets, are telescoped. These jets are constructed in the  
2668    same way as in the reconstructed and truth-level analyses; reconstructed-level jets are made from  
2669    calorimeter topological clusters within  $R$  of the anti- $k_t$  with  $R = 0.4$  jet axes and then trimmed,  
2670    and truth-level jets are made from stable truth particles within  $R$  of the anti- $k_t$  with  $R = 0.4$  jet  
2671    axes. The reconstructed and truth-level telescoping jet ensembles are matched according to the sep-  
2672    aration in the  $(\eta, \phi)$  plane of their corresponding anti- $k_t$  with  $R = 0.4$  jets used as seeds. Only jets  
2673    with  $|\eta| < 1.2$  are examined here, and the results of studies on the  $ZH125$ ,  $ZZ$ , and  $t\bar{t}$  samples, as  
2674    well as over other  $|\eta|$  ranges, are outlined in [36]. Any reconstructed jets not within  $\Delta R = 0.3$  of a  
2675    truth jet are discarded. In the event that multiple reconstructed jets are the same distance away from  
2676    a given truth jet, the reconstructed jet with the highest  $p_T$  gets matched. Matching is retained for all  
2677     $R$  values (i.e. telescoping seeds are matched, and telescoping jets are assumed to match if the anti- $k_t$   
2678    jets from which their seeds are derived match).

2679       Once anti- $k_t$  with  $R = 0.4$  reconstructed and truth jets are matched, response functions are cre-  
2680       ated by generating a series of distributions of  $p_T^{rec}/p_T^{tru}$  in 20 GeV bins of  $p_T^{tru}$  from 20–200 GeV, one  
2681       bin for 200–300 GeV, and one bin for 300–500 GeV for each  $R$ , with bins chosen for purposes of  
2682       statistics. Ensembles with  $p_T^{tru} < 20$  GeV are ignored since no calibration exists for jets with trans-  
2683       verse momentum below this value. The values of  $\langle p_T^{rec}/p_T^{tru} \rangle$  in each  $p_T^{tru}$  bin are calculated by doing

2684 a two sigma gaussian fit on the distribution of  $p_T^{rec}/p_T^{tru}$  in that bin and taking the mean of that fit,  
2685 and the error on the mean is taken from the error of this parameter in the fit. The resolutions are the  
2686 values of the square root of the variance on this fit. As the total response distributions in Figure B.1  
2687 show, performance is best for low  $R$  values and high values of  $p_T^{tru}$ . Figure B.1 shows the  $R = 0.4$   
2688 ( $anti k_t$ ) case to show a baseline for performance,  $R = 0.6$  to show the deviations with “correct”  
2689 calibrations, and  $R = 1.0, 1.5$  to show how big those deviations get with larger  $R$  jets. The resolu-  
2690 tions,  $\sigma_{p_T^{rec}/p_T^{tru}}$ , as a function of  $p_T^{tru}$  are shown in Figure B.1(b). For  $p_T^{tru} > 60$  GeV, response is fairly  
2691 consistent over various  $R$  values. Resolution, as might naively be expected, is worse for increasingly  
2692 larger values of  $R$ . For  $p_T^{tru} < 60$  GeV, resolution degrades, and response degrades in particular for  
2693 increasing  $R$ ; this is likely a result from residual pileup effects.



(a)



(b)

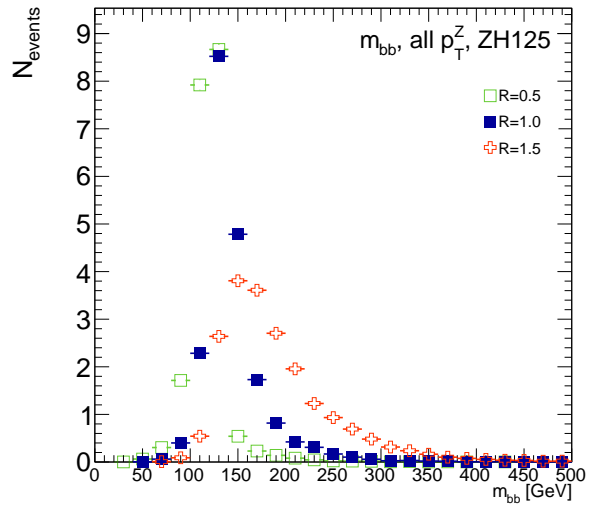
**Figure B.1:** The mean and resolution of  $p_T^{rec}/p_T^{tru}$  for the background  $Z+jets$  sample for  $|\eta| < 1.2$  and for  $R = 0.4, 0.6, 1.0$ , and  $1.5$  in  $20\text{ GeV}$  bins of  $p_T^{tru}$  for  $20\text{--}200\text{ GeV}$ , one bin for  $200\text{--}300\text{ GeV}$ , and one bin for  $300\text{--}500\text{ GeV}$ , with bins chosen for purposes of statistics.

2694 B.5 TRUTH-LEVEL ANALYSIS

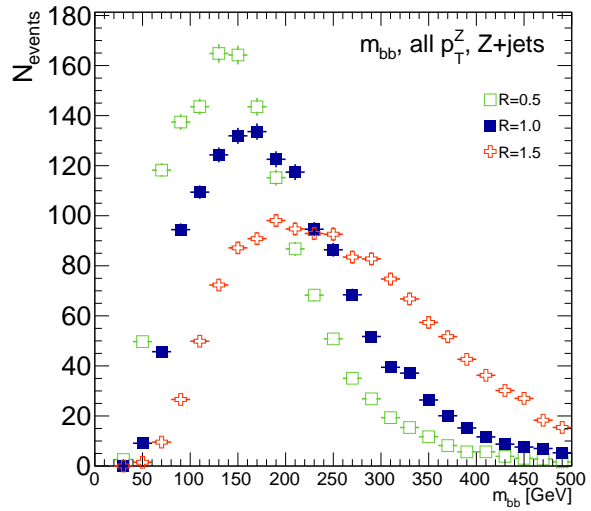
2695 To understand the limits and sources of any potential improvements, a truth-level analysis was con-  
2696 ducted on MC samples with a  $ZH_{125}$  signal sample and a  $Z+jets$  background sample. Distributions  
2697 for the dijet invariant mass,  $m_{bb}$ , were made for each telescoping radius. Both signal and background  
2698 samples develop more pronounced tails in the high  $m_{bb}$  region as  $R$  increases, as shown in Figure  
2699 B.2.  $N_{events}$  is normalized to expected values in data.

2700 One way to take advantage of this information is to make a cut on  $m_{bb}$  for two different radii.  
2701 This is graphically depicted in Figure B.3 for the optimized combination of  $m_{bb,R=0.9}$  (telescoping  
2702 cone jets constructed as outlined in Sec. B.2) vs.  $m_{bb,R=0.4}$  (anti- $k_t$  jets). At truth-level, the majority  
2703 of events in the signal  $ZH_{125}$  sample are concentrated in relatively narrow region of parameter space,  
2704 where this is certainly not the case for the more diffuse  $Z+jets$  background sample.

2705 Another way to take advantage of multiple event interpretations is to make use of an event's cut-  
2706 weight, denoted  $z$  and defined as the fraction of interpretations in a given event that pass a certain set  
2707 of cuts (in this note, a cut on  $m_{bb}$ ). The distribution of cut-weights for a sample of events is denoted  
2708  $\rho(z)$ . To enhance the significance of a cut-based analysis, events can be weighted by the cut-weight  
2709 or any function  $t(z)$  of the cut-weight. Weighting events by  $t(z)$  modifies the usual  $S/\delta B$  formula  
2710 used to calculate significances. In this note,  $\delta B$  is based on Poissonian statistics and is taken as  $0.5 +$   
2711  $\sqrt{0.25 + N_B}$ , where  $N_B$  is the number of background events.



(a)



(b)

**Figure B.2:** The  $m_{bb}$  distribution for the telescoping jets with  $R = 0.5, 1.0$ , and  $1.5$  truth-level jets is shown for the signal and background samples in (a) and (b), respectively.

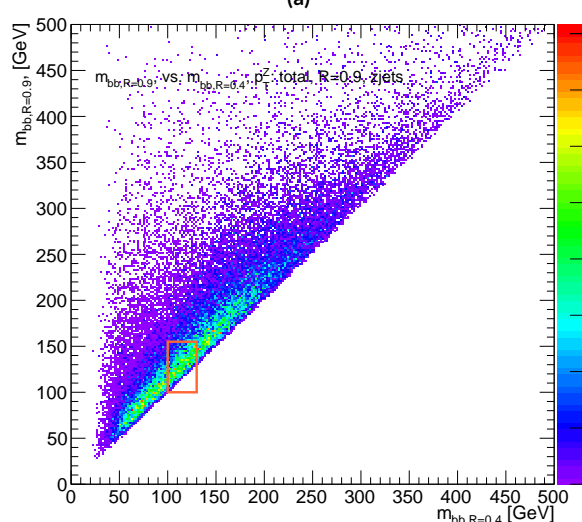
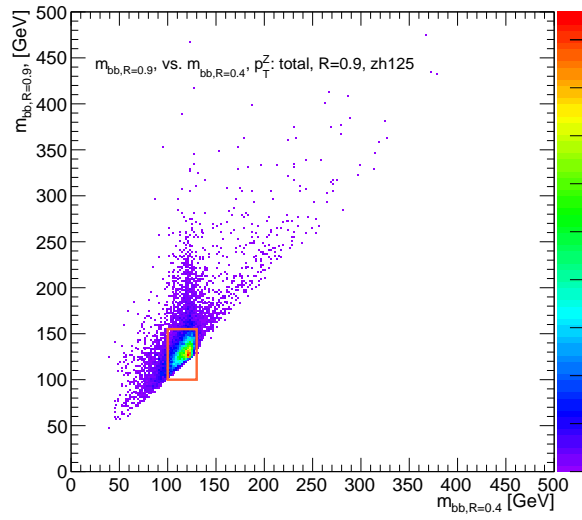


**Figure B.3:** The 2D distribution of  $m_{bb,R=0.9}$  vs.  $m_{bb,R=0.4}$  is shown for signal and background truth-level samples in (a) and (b), respectively. The region chosen for the double  $m_{bb}$  cut is outlined in orange.

2712 B.6 ERRORS ON TELESCOPING SIGNIFICANCES

2713 Significances of measurements are quoted in units of expected background fluctuations, schemati-  
2714 cally,  $S/\delta B$ . For counting experiments with high numbers of events, we can use Gaussian statistics  
2715 and express this as  $S/\sqrt{B}$ , which we here denote as  $\mathcal{S}$ . However, with lower statistics, it becomes  
2716 more appropriate to use Poissonian statistics, and

$$\mathcal{S}_{gaus} = \frac{S}{\sqrt{B}} \rightarrow \mathcal{S}_{pois} = \frac{S}{0.5 + \sqrt{0.25 + B}} \quad (\text{B.1})$$

2717 where  $0.5 + \sqrt{0.25 + B}$  is the characteristic upward fluctuation expected in a Poissonian data set  
2718 using the Pearson chi-square test[79].

2719 B.7 COUNTING

2720 The significance is given as above, where  $S = N_S$  and  $B = N_B$ . That is, the signal and background  
2721 are just the number of events in signal and background that pass some cuts. The error for the Guas-  
2722 sian case is the standard:

$$\Delta \mathcal{S}_{gaus} = \frac{1}{\sqrt{B}} \Delta S \oplus \frac{S}{2B^{3/2}} \Delta B \quad (\text{B.2})$$

2723 The error for the Poissonian case is:

$$\Delta \mathcal{S}_{pois} = \frac{1}{0.5 + \sqrt{0.25 + B}} \Delta S \oplus \frac{S}{2(0.5 + \sqrt{0.25 + B})^2 \sqrt{0.25 + B}} \Delta B \quad (\text{B.3})$$

<sup>2724</sup> where  $\oplus$  denotes addition in quadrature, and  $\Delta S(B)$  is the error on signal (background).

## <sup>2725</sup> B.8 MULTIPLE EVENT INTERPRETATIONS

<sup>2726</sup> Using multiple event interpretations changes the formulae used in with simple counting. That is,  $S$

<sup>2727</sup> is not necessarily merely  $N_S$ , the number of events passing some signal cuts, and similarly for  $B$  and

<sup>2728</sup>  $N_B$ . Using an event weighting by some function of the cut-weight,  $z$ , denoted  $t(z)$ ,  $S = N_S \langle t \rangle_{\rho_S}$

<sup>2729</sup> and  $B = N_B \langle t^2 \rangle_{\rho_B}$ . So

$$\mathcal{S}_{t,gaus} = \frac{N_S \langle t \rangle_{\rho_S}}{\sqrt{N_B \langle t^2 \rangle_{\rho_B}}} \rightarrow \mathcal{S}_{t,pois} = \frac{N_S \langle t \rangle_{\rho_S}}{0.5 + \sqrt{0.25 + N_B \langle t^2 \rangle_{\rho_B}}} = \frac{N_S \int_0^1 dz t(z) \rho_S(z)}{0.5 + \sqrt{0.25 + N_B \int_0^1 dz t^2(z) \rho_B(z)}} \quad (\text{B.4})$$

For histograms, everything is done bin-wise. The notation used below is as follows:  $\rho_i$  is the value of  $\rho(z)$  at bin  $i$  (where the bins run from 0 to  $n_{tel}$ , where  $n_{tel}$  is the total number of telescoping radii).  $t_i = t_i(\rho_{S,i}, \rho_{B,i}, i/n_{tel})$  is the value of  $t(z)$  at bin  $i$ , which can depend, in principle, on  $\rho_{S,i}$ ,  $\rho_{B,i}$ , and  $i/n_{tel}$  (the last of which is  $z$  in bin  $i$ ). Explicitly,

$$N = \sum_{i=0}^{n_{tel}} \rho_i, \quad \int_0^1 dz t(z) \rho_S(z) = \sum_{i=0}^{n_{tel}} t_i \rho_{S,i}, \quad \int_0^1 dz t^2(z) \rho_B(z) = \sum_{i=0}^{n_{tel}} t_i^2 \rho_{B,i}$$

<sup>2730</sup> For the calculations that follow, let  $\xi = \sum_{i=0}^{n_{tel}} t_i \rho_{S,i}$ ,  $\psi = 0.5 + \sqrt{0.25 + N_B \sum_{i=0}^{n_{tel}} t_i^2 \rho_{B,i}}$ ,  
<sup>2731</sup>  $\partial_S = \frac{\partial}{\partial \rho_{S,i}}$  (and similarly for  $B$ ), so  $\mathcal{S}_t = N_S \xi / \psi$

<sup>2732</sup> Some partial derivatives:

$$\begin{aligned}
 \partial_S N_S &= 1, & \partial_{B,i} N_B &= 1 \\
 \partial_S \xi &= t_i + (\partial_S t_i) \rho_{S,i}, & \partial_B \xi &= (\partial_B t_i) \rho_{B,i} \\
 \partial_S \psi &= \frac{N_B t_i (\partial_S t_i) \rho_{B,i}}{\sqrt{0.25 + N_B \sum_{i=0}^{n_{tel}} t_i^2 \rho_{B,i}}}, & \partial_B \psi &= \frac{\sum_{i=0}^{n_{tel}} t_i^2 \rho_{B,i} + N_B (t_i^2 + 2t_i (\partial_B t_i) \rho_{B,i})}{2\sqrt{0.25 + N_B \sum_{i=0}^{n_{tel}} t_i^2 \rho_{B,i}}} \\
 \partial_S \mathcal{S}_t &= \frac{\xi}{\psi} + \frac{N_S}{\psi} \partial_S \xi - \frac{N_S \xi}{\psi^2} \partial_S \psi, & \partial_B \mathcal{S}_t &= N_S \left( \frac{1}{\psi} \partial_B \xi - \frac{\xi}{\psi^2} \partial_B \psi \right)
 \end{aligned}$$

<sup>2733</sup> Thus,

$$\Delta \mathcal{S}_{t,i} = \left[ \frac{\xi}{\psi} + \frac{N_S}{\psi} \partial_S \xi - \frac{N_S \xi}{\psi^2} \partial_S \psi \right] \Delta \rho_{S,i} \oplus N_S \left[ \frac{1}{\psi} \partial_B \xi - \frac{\xi}{\psi^2} \partial_B \psi \right] \Delta \rho_{B,i} \quad (\text{B.5})$$

<sup>2734</sup> and the total error is given by the sum in quadrature over all bins  $i$  of  $\Delta \mathcal{S}_{t,i}$ .

<sup>2735</sup> B.9  $t(z) = z$

<sup>2736</sup> With  $t(z) = z$ ,  $t_i = i/n_{tel}$ , so  $\partial_S t_i = \partial_B t_i = 0$ . So:

$$\begin{aligned}
 \partial_S \psi &= \partial_B \xi = 0 \\
 \partial_S \xi &= \frac{i}{n_{tel}} \\
 \partial_B \psi &= \frac{\sum_i i^2 \rho_{B,i} + N_B t^2}{n_{tel} \sqrt{n_{tel}^2 + N_B \sum_i i^2 \rho_{B,i}}}
 \end{aligned}$$

<sup>2737</sup> so  $\Delta\mathcal{S}_{z,i}$  reduces to

$$\Delta\mathcal{S}_{t,i} = \left[ \frac{\xi + N_S t_i}{\psi} \right] \Delta\rho_{S,i} \oplus \left[ \frac{N_S \xi}{\psi^2} \partial_B \psi \right] \Delta\rho_{B,i} \quad (\text{B.6})$$

<sup>2738</sup> B.10  $t(z) = \rho_S(z) / \rho_B(z)$

<sup>2739</sup> With the likelihood optimized\*  $t^*(z) = \rho_S(z) / \rho_B(z)$ ,  $t_i = \rho_{S,i} / \rho_{B,i}$ , so  $\partial_S t_i = 1 / \rho_{B,i}$  and  $\partial_B t_i =$

<sup>2740</sup>  $-\rho_{S,i} / \rho_{B,i}^2$ . So:

$$\begin{aligned} \partial_S \xi &= 2 \frac{\rho_{S,i}}{\rho_{B,i}} = 2t_i \\ \partial_B \xi &= -\frac{\rho_{S,i}}{\rho_{B,i}} = -t_i \\ \partial_S \psi &= \frac{N_B t_i}{\sqrt{0.25 + N_B \sum_i \rho_{S,i}^2 / \rho_{B,i}}} \\ \partial_B \psi &= \frac{\sum_i \rho_{S,i}^2 / \rho_{B,i} - N_B (\rho_{S,i} / \rho_{B,i})^2}{\sqrt{1 + 4N_B \sum_i \rho_{S,i}^2 / \rho_{B,i}}} \end{aligned}$$

<sup>2741</sup> simplifying somewhat the terms in the per bin error in Equation B.6.

<sup>2742</sup> The new significance figure using multiple event interpretations becomes, with  $\rho_S$  and  $\rho_B$  denot-  
<sup>2743</sup> ing the cut-weight distributions in signal and background, respectively

$$\frac{S}{\delta B} = \frac{N_S \langle t \rangle_{\rho_S}}{0.5 + \sqrt{0.25 + N_B \langle t^2 \rangle_{\rho_B}}} \quad (\text{B.7})$$

---

\*for the Gaussian statistics case

<sup>2744</sup> Of particular interest is the likelihood optimized  $t(z)$ ,<sup>†</sup>  $t^*(z) = \rho_S(z)/\rho_B(z)$ .  $m_{bb}$  windows are  
<sup>2745</sup> chosen separately for each scheme studied to maximize total significances and are summarized in  
<sup>2746</sup> Table B.3.

$$\left(\frac{S}{\delta B}\right)_z = \frac{N_S \epsilon_S}{0.5 + \sqrt{0.25 + N_B (\epsilon_B^2 + \sigma_B^2)}} \quad (B.8)$$

<sup>2747</sup>

$$\left(\frac{S}{\delta B}\right)_{t^*(z)} = \frac{N_S \int_0^1 dz \frac{\rho_S^2(z)}{\rho_B(z)}}{0.5 + \sqrt{0.25 + N_B \int_0^1 dz \frac{\rho_S^2(z)}{\rho_B(z)}}} \quad (B.9)$$

<sup>2748</sup> where  $\epsilon_{S,B}$  are the means of  $\rho_{S,B}(z)$  and  $\sigma_B^2$  is the variance of  $\rho_B(z)$ . Further details can be found in  
<sup>2749</sup> Refs. [36, 47] and Appendix B.6.

**Table B.3:**  $m_{bb}$  windows studied. These windows were chosen to optimize significances over all  $p_T^Z$ .

Analysis Type	$S/\delta B$ Type	Optimal $m_{bb}$ Window
Reconstructed	$\text{anti-}k_t R = 0.4$ $t(z) = z$ $t(z) = \rho_S(z)/\rho_B(z)$ $\text{anti-}k_t R = 0.4$ , telescoping $R = 0.6$	$90\text{--}140 \text{ GeV}$ $110\text{--}155 \text{ GeV}$ $110\text{--}155 \text{ GeV}$ $95\text{--}140 \text{ GeV} (R = 0.4), 105\text{--}160 \text{ GeV} (R = 0.6)$
Truth	$\text{anti-}k_t R = 0.4$ $t(z) = z$ $t(z) = \rho_S(z)/\rho_B(z)$ $\text{anti-}k_t R = 0.4$ , telescoping $R = 0.9$	$100\text{--}130 \text{ GeV}$ $115\text{--}140 \text{ GeV}$ $120\text{--}135 \text{ GeV}$ $100\text{--}130 \text{ GeV} (R = 0.4), 100\text{--}155 \text{ GeV} (R = 0.9)$

<sup>2750</sup> The truth-level distributions  $\rho_S(z)$ ,  $\rho_B(z)$ , and  $\rho_S(z)/\rho_B(z)$  are shown for the  $m_{bb}$  window  
<sup>2751</sup> that optimizes  $(S/\delta B)_{t^*(z)}$  in Figure B.4, and significance improvements as a function of  $p_T^Z$  are  
<sup>2752</sup> summarized in Figure B.5. Uncertainties in Figures B.5 and B.9 are statistical uncertainties. JES sys-

---

<sup>†</sup>Derived under the assumption of Gaussian statistics in Ref [47]

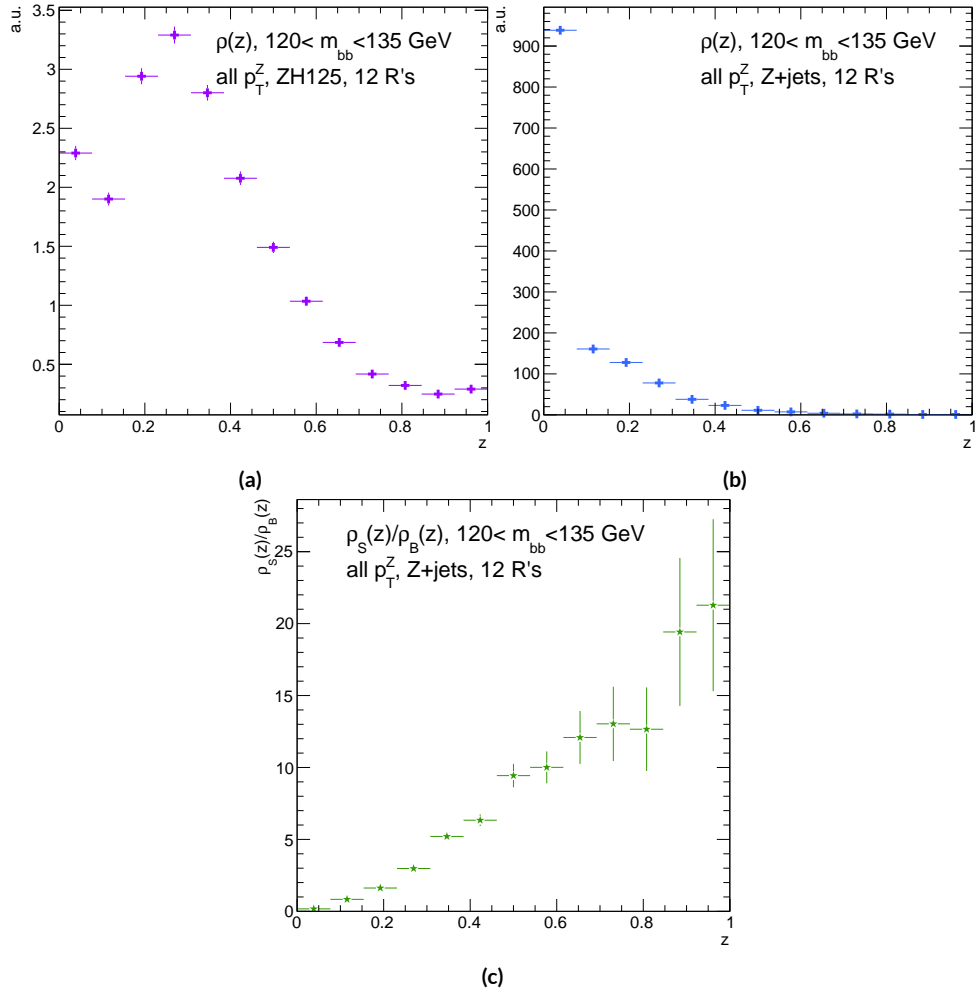


**Figure B.4:** Truth-level  $\rho(z)$  distributions for the  $m_{bb}$  window optimizing  $(S/\delta B)_{r^*(z)}$ .  $\rho_S(z)$  for the signal ZH125 sample is shown in (a), and  $\rho_B(z)$  for the background Z+jets sample is shown in (b). The distribution of  $\rho_S(z)/\rho_B(z)$  for these samples is shown in (c).

2753    tematics will need to be evaluated for different  $R$ 's, as modeling uncertainties is an outstanding is-  
 2754    sue, but these systematics will likely be strongly correlated for the different  $R$ 's and are not antici-  
 2755    pated to be a very large contribution to total uncertainties. While the two dimensional  $m_{bb}$  cut and  
 2756     $t(z) = z$  schemes only showed marginal improvement at truth level at 2.87%<sup>‡</sup> and 1.45%, respec-  
 2757    tively, the likelihood optimized  $t^*(z)$  showed a more substantial 40.7% improvement overall, with  
 2758    a steady increase in improvement with increasing  $p_T^Z$ . Figure B.5 (d) summarizes the improvements  
 2759    with respect to  $p_T^Z$  for the  $t^*(z)$  event weight for five, seven, and twelve telescoping radii (interpreta-  
 2760    tions) per event. Improvements increase with a greater number of interpretations and are more pro-  
 2761    nounced at higher  $p_T^Z$  for this scheme. The optimal  $120 < m_{bb} < 135$  GeV window for  $t^*(z)$  case  
 2762    is among the smallest studied. The benefits of this window's narrowness are suggested in Figure B.4.  
 2763    While the background cut-weight distribution,  $\rho_B(z)$  in Figure B.4 (b) behaves as one might with  
 2764    a marked peak at  $z = 0$ , the signal  $\rho_S(z)$  distribution peaks at a relatively modest  $z = 0.3$ , which  
 2765    indicates that much of the gain at truth level comes from background rejection. This is possible at  
 2766    truth level since there is both truth-level information available and no smearing and since  $\rho_S/\rho_B$  is  
 2767    the relevant quantity (as shown in Figure B.4 (c)).

---

<sup>‡</sup>The limited improvement is provably due to the simplified treatment of the 2D case; better performance with a more sophisticated treatment has been observed in Ref. [39].

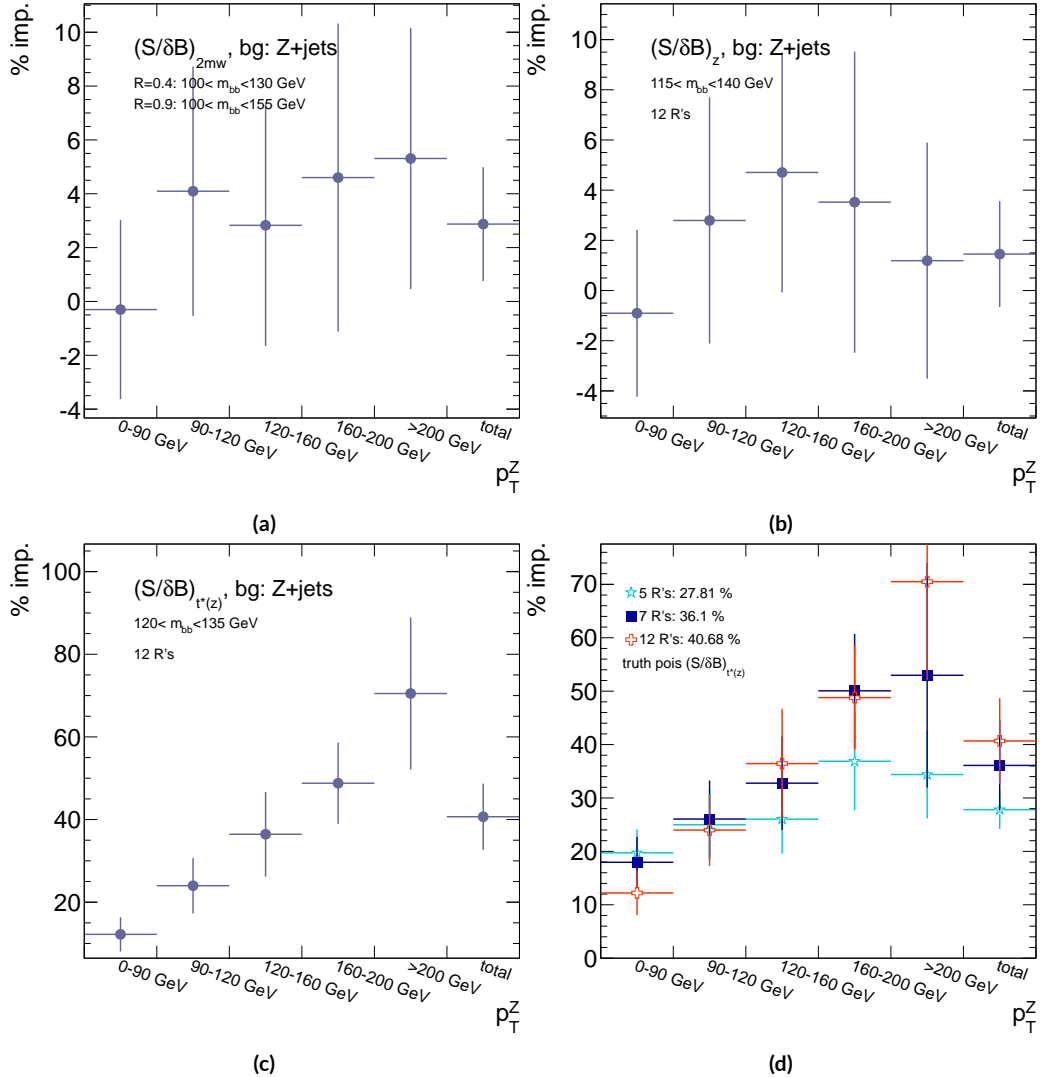


**Figure B.5:** A summary of the improvements for different truth-level telescoping jet cuts and weights is shown in bins of  $p_T^Z$ . The final bin is the total improvement over all  $p_T^Z$ . Shown are improvements for the 2D  $m_{bb}$  cut (a),  $t(z) = z$  (b),  $t(z) = t^*(z)$  with 12 radii (c), and  $t(z) = t^*(z)$  for various radii (d).

2768 B.II RECONSTRUCTED-LEVEL ANALYSIS

2769 At reconstructed level, the same overall effect of introducing a high tail in  $m_{bb}$  distributions with  
2770 increasing  $R$  is evident in comparing Figures B.2 and B.6. The optimal  $m_{bb}$  windows, however, grow  
2771 larger, due to the lack of truth-level information.

2772 Total significance gains at reconstructed level for the two dimensional  $m_{bb}$  cut and the  $t(z) = z$   
2773 case are similar, at 2.87% and 1.45%, respectively. The optimal two-dimensional  $m_{bb}$  cut at recon-  
2774 structed level is  $95 < m_{bb,R=0.4} < 140 \text{ GeV}$ ,  $105 < m_{bb,R=0.6} < 160 \text{ GeV}$ . Just as at truth level,  
2775 the  $R = 0.4$   $m_{bb}$  cut is comparable to the optimal single  $R = 0.4$   $m_{bb}$  cut, and the second  $m_{bb}$  cut is  
2776 at similar values (cf. Table B.3 and Figures B.3 and B.7). However, the optimal second telescoping ra-  
2777 dius is markedly smaller at  $R = 0.6$  versus the optimal truth-level second radius of  $R = 0.9$ , which  
2778 suggests that effects like pileup at reconstructed level obscure correlations between the  $R = 0.4$   
2779 interpretations and limit the usefulness of larger  $R$  interpretations in this particular scheme. The  
2780  $t(z) = z$  case has a wider optimal window and yields about half the improvement it does at truth  
2781 level.

2782 The optimal  $m_{bb}$  window for the  $t^*(z)$  case is also markedly wider at reconstructed level, at  $110 <$   
2783  $m_{bb} < 155 \text{ GeV}$  in comparison to the truth-level optimal  $120 < m_{bb} < 135 \text{ GeV}$ . The  $\rho(z)$  dis-  
2784 tributions for the signal  $ZH125$  and background  $Z+\text{jets}$  as well as the  $\rho_S(z) / \rho_B(z)$  in this window  
2785 are shown in Figure B.8. Compared with the truth-level distributions in Figure B.4, both the sig-  
2786 nal and background optimal  $\rho(z)$  distributions have higher values at higher  $z$ . The peak in  $\rho_S(z)$  at  
2787  $z = 1$  suggests that at reconstructed level, maximizing the number of more “signal-like” events is

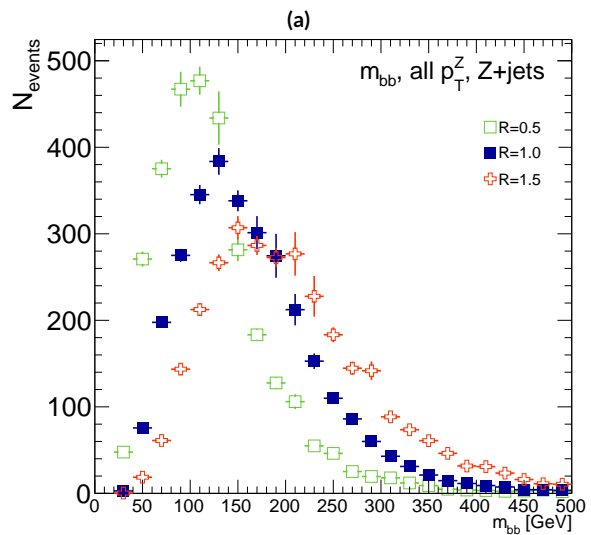
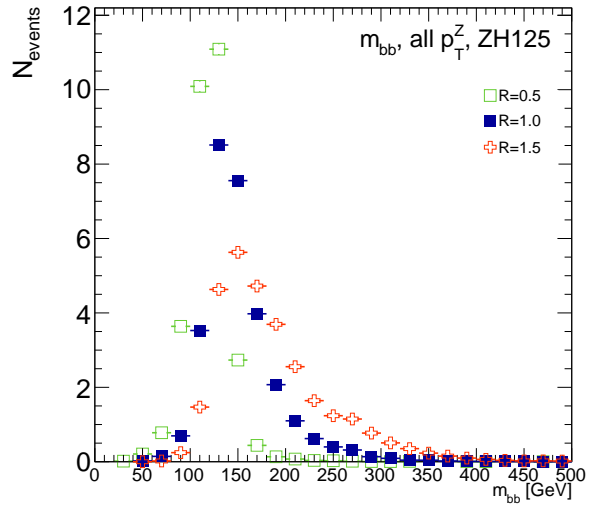


**Figure B.6:** The  $m_{bb}$  distribution for the telescoping jets with  $R = 0.5$ ,  $R = 1.0$ , and  $R = 1.5$  reconstructed-level jets is shown for the signal and background samples in (a) and (b), respectively.

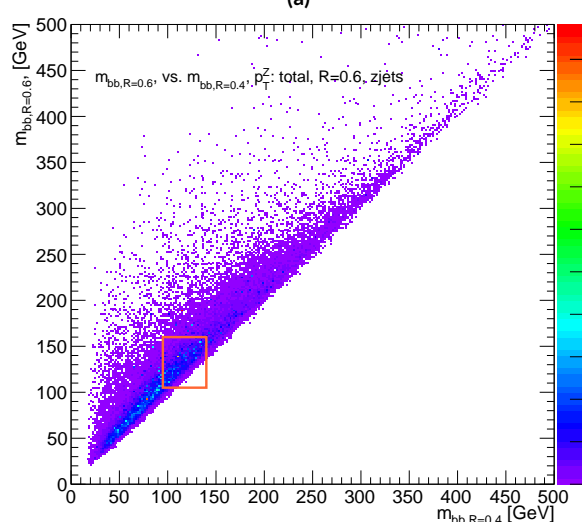
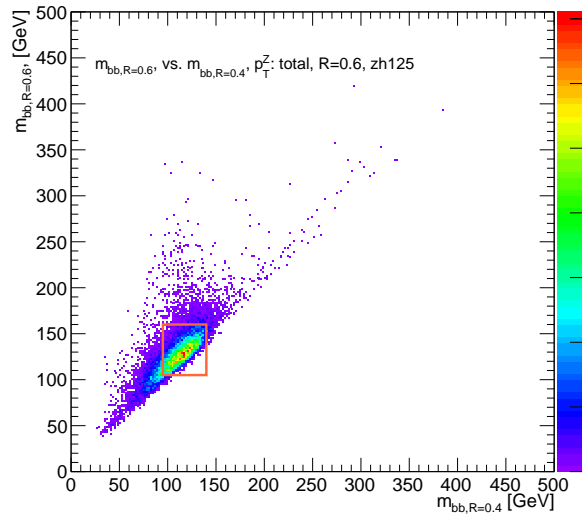


**Figure B.7:** The 2D distribution of  $m_{bb,R=0.8}$  vs.  $m_{bb,R=0.4}$  is shown for signal and background reconstructed-level samples in (a) and (b), respectively. The region chosen for the double  $m_{bb}$  cut is outlined in orange.

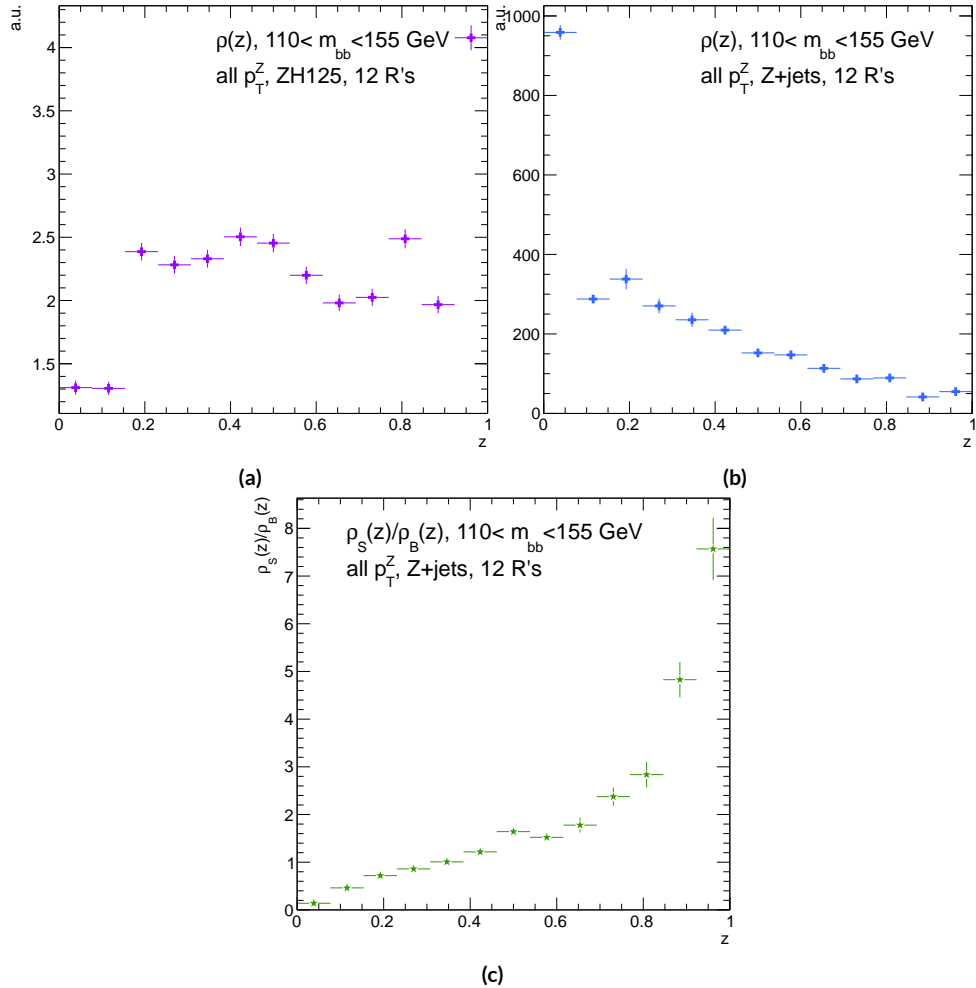


**Figure B.8:** Reconstructed-level  $\rho(z)$  distributions for the  $m_{bb}$  window optimizing  $(S/\delta B)_{t^*(z)} \cdot \rho_S(z)$  for the signal  $ZH125$  sample is shown in (a), and  $\rho_B(z)$  for the background  $Z+jets$  sample is shown in (b). The distribution of  $\rho_S(z)/\rho_B(z)$  for these samples is shown in (c).

2788 the key to optimizing significances, as opposed to the optimal, background suppressing  $\rho(z)$  distri-  
 2789 butions at truth level. The use of a greater number of interpretations per event (telescoping radii)  
 2790 does appear to result in overall greater improvement as at truth level, as twelve radii performed bet-  
 2791 ter than five, but this is less clear at reconstructed level, as shown in Figure B.9 (d). The improve-  
 2792 ment at reconstructed level using an event weight of  $t^*(z)$  is 20.5%, just over half the improvement  
 2793 at truth level but still quite significant. Summaries of improvements as a function of  $p_T^Z$  for all three  
 2794 cases studied and for the  $t^*(z)$  case for different numbers of telescoping radii are shown in Figure  
 2795 B.9.

**Table B.4:** A summary of significances for different weighting schemes and cuts and for reconstructed and truth jets for a luminosity of  $20.3 \text{ fb}^{-1}$ .

Type	0–90 GeV	90–120 GeV	120–160 GeV	160–200 GeV	> 200 GeV	total
anti- $k_t$ , $R = 0.4_{rec}$	0.47492	0.28214	0.28339	0.25748	0.37337	0.76887
anti- $k_t$ , $R = 0.4_{tru}$	0.57414	0.30655	0.37309	0.35042	0.53569	0.98619
$2 m_{bb,rec}$	0.48903	0.2858	0.28812	0.25972	0.38297	0.78611
$2 m_{bb,tru}$	0.5724	0.3191	0.38364	0.36655	0.56414	1.0145
$z_{rec}$	0.50698	0.27962	0.29937	0.25688	0.36846	0.79158
$z_{tru}$	0.56894	0.31511	0.39065	0.36277	0.54206	1.0005
$t^*(z)_{rec}$	0.55085	0.29931	0.33367	0.30107	0.51321	0.92649
$t^*(z)_{tru}$	0.64425	0.38008	0.50904	0.5214	0.91337	1.3873

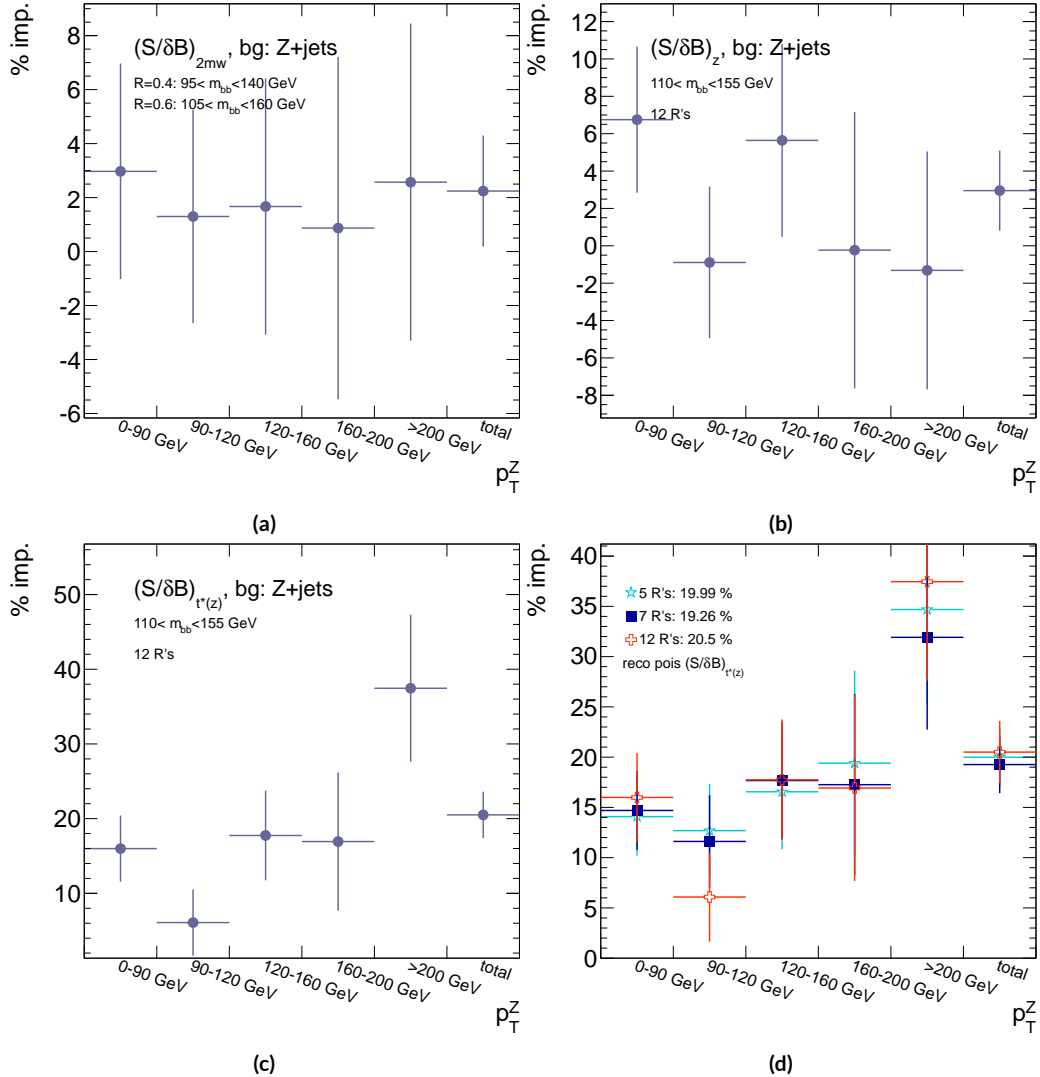


**Figure B.9:** A summary of the improvements for different reconstructed-level telescoping jet cuts and weights is shown in bins of  $p_T^Z$ . The final bin is the total improvement over all  $p_T^Z$ . Shown are improvements for the 2D  $m_{bb}$  cut (a),  $t(z) = z$  (b),  $t(z) = t^*(z)$  with 12 radii (c), and  $t(z) = t^*(z)$  for various radii (d).

2796 B.12 CONCLUSIONS AND PROSPECTS

2797 The use of telescoping jets to provide multiple event interpretations shows promise as an avenue to  
2798 increase significances in the  $H \rightarrow b\bar{b}$  search in ATLAS and make an observation in the systematics-  
2799 limited environment of early Run 2. A preliminary study using the telescoping jets algorithm with  
2800 12 telescoping radii to build 12 event interpretations on 2012 Monte Carlo based on the full, cut-  
2801 based Run 1 analysis yielded a 20.5% improvement in  $S/\delta B$  over using anti- $k_t$  with  $R = 0.4$  alone  
2802 at reconstructed level using a likelihood maximized event weighting to study the  $ZH \rightarrow llb\bar{b}$  pro-  
2803 cess. The jets used in this note at reconstructed level were trimmed in order to guarantee reasonable  
2804 resolution in the large- $R$  interpretations. The algorithm, in particular, showed discriminating power  
2805 at high  $p_T^Z$ , so better performance can be expected in Run 2 with a higher  $\sqrt{s}$  and higher numbers of  
2806 events with large  $p_T^Z$ . Additionally, the many simplifying assumptions regarding jet calibration and  
2807 the relatively basic use of information<sup>§</sup> from multiple invariant masses in this note suggest that even  
2808 further improvements than those quoted are possible. While this note did not explore the corre-  
2809 lations between multiple event interpretations and the variables used in the BDT of the latest mul-  
2810 tivariate version of the  $H \rightarrow b\bar{b}$  analysis[20], new phenomenological studies suggest that such  
2811 correlations are not strong[39]. The corresponding reconstructed-level study, using a BDT, is left  
2812 for future work. Also left for future work are better understanding the effects of jet trimming and  
2813 which interpretations are the most useful.

---

<sup>§</sup>For examples of more sophisticated treatments compared to the treatment in this note, see Ref [39].

*Ah, peut on être heureux?*

*Quand on forme des autres voeux?*

J. P. Rameau, Forêts Paisibles

2814

C

2815

## Progress in Particle Physics and Existential

2816

## Threats to the American World Order

2817 INTERNATIONAL COLLABORATIONS with thousands of scientists like those at CERN's (the Euro-

2818 pean Organisation for Nuclear Research) 27 km circumference Large Hadron Collider (LHC) are

2819 fast becoming the norm in many fields of science, making the past seven decades of discovery in par-  
2820 ticle physics seem a natural part of history's long march of progress. Seemingly arcane terms like dark  
2821 matter and the Higgs boson (the infamous "God particle") even pop up in blockbuster movies and  
2822 primetime television. All of this, however, would have been impossible without the fascist and then  
2823 communist existential threats to the American world order throughout the 20th century.

2824 The Manhattan Project and its atomic arsenal were a direct response to the threat of global fas-  
2825 cism in World War II. They both secured the United States' position as a world power at the end of  
2826 the war and laid the foundations for many particle physics developments for the following three  
2827 decades. High ranking American officials were well aware that this would have been impossible  
2828 without the contributions of particle physicists. Some of these physicists, like Enrico Fermi and  
2829 Arthur Compton, were already Nobel laureates and luminaries in the field. Others, like Richard  
2830 Feynman and Owen Chamberlain, would go on to make their marks in the decades following the  
2831 war. Though a few of these physicists, most notably Edward Teller, would continue their work on  
2832 nuclear weapons, most of these physicists would return to basic science research as the nation turned  
2833 towards the uneasy peace time of the Cold War.

2834 Particle physicists' service and connections made during the war would serve them well in the  
2835 decades to come as the military-controlled Manhattan Project transitioned to the civilian-led Atomic  
2836 Energy Commission (AEC). The AEC was founded in 1946 to oversee the nuclear arsenal, the devel-  
2837 opment of atomic power, and related fundamental research in the United States. Many of those on  
2838 AEC board were former Manhattan Project particle physicists, including Glenn Seaborg, the AEC  
2839 chairman from 1961-1971. Congressional oversight for AEC funding consisted of a single committee,

2840 the Joint Committee on Atomic Energy (JCAE), whose deliberations often took place behind closed  
2841 doors owing to the AEC's sensitive national security mission. Elementary particle physics research  
2842 was clearly central to the AEC mission at its founding, as nuclear fission was the bleeding edge of par-  
2843 ticle physics at the beginning of World War II and represented the culmination of decades of highly  
2844 specialized research that had no immediately obvious practical application. Furthermore, particle ac-  
2845 celerator technology, the main workhorse then as now for basic science research in particle physics  
2846 and the most expensive item on any particle physicist's wish list, had been crucial to many of these  
2847 discoveries. The anticipation of future windfalls as momentous as the power of the atom and the ex-  
2848 emplary performance of particle physicists during the war ensured that experimental particle physics  
2849 and particle accelerators would remain the crown jewel of AEC research throughout the organiza-  
2850 tion's existence.

2851 The AEC's sizable budget (thanks to its crucial mission of securing the nation's nuclear arsenal)  
2852 and lavish support were the biggest contributing factors to the development of particle physics in  
2853 the mid 20th century through its funding of accelerator facilities. Particle accelerators use powerful  
2854 electromagnetic fields to take beams of subatomic particles, usually protons or electrons, as close to  
2855 the speed of light as possible before colliding them into either fixed targets or other beams to pro-  
2856 duce high energy collisions. Physicists use these collisions to test models of the universe that predict  
2857 behavior in these extreme regimes. Without more energetic collisions, progress becomes function-  
2858 ally impossible. While the first such accelerator was smaller than the average human hand, studying  
2859 more complete models of the universe called for more energetic collisions and hence bigger, more  
2860 powerful, and more expensive accelerators.

2861 Soon, these experiments became too big and expensive for individual universities to operate on  
2862 their own. Progress in American particle physics became entirely dependent on the AEC, and hence  
2863 on the continued threat of nuclear annihilation. National laboratories, all under AEC stewardship,  
2864 became regional centers of research for particle physicists. By the late 1960's, Brookhaven National  
2865 Laboratory, Lawrence Berkeley National Laboratory, and the Stanford Linear Accelerator Center  
2866 hosted the majority of cutting edge accelerator facilities in the country alongside a dwindling num-  
2867 ber of single university accelerators. By the decade's end Cornell hosted the only such university op-  
2868 erated facility. The competitive rivalry among these different institutions fostered American success  
2869 and dominance in experimental particle physics through the 1970's. The culmination of AEC pa-  
2870 tronage was the National Accelerator Laboratory (now Fermilab), which began operations in 1967.  
2871 Fermilab's construction was not a foregone conclusion given the economically challenging backdrop  
2872 of the Vietnam War, but an emphasis on cost effective plans for both the laboratory and accelerator  
2873 backed by the full support of the AEC secured Fermilab's funding. Fermilab would ultimately be-  
2874 come home to the Tevatron, the final particle accelerator in the United States to claim the title of the  
2875 world's most powerful.

2876 Particle physics only became more dependent on the existence of a Soviet threat with the end of  
2877 the AEC. Due to budgetary pressures, the AEC was abolished in 1975, and its duties were eventually  
2878 reorganized into the Department of Energy (DOE). Under DOE administration, proposed parti-  
2879 cle physics experiments now had to compete against research projects from the entire range of fields  
2880 germane to American energy instead of only other nuclear and particle physics projects. Moreover,  
2881 DOE leadership had far fewer officials with track records of supporting particle physics research

2882 projects above all others. Nevertheless, there remained one last, great effort to promote collider  
2883 physics in the United States, the Superconducting Supercollider (SSC). The SSC was an incredibly  
2884 ambitious design: a 50 mile ring under the Waxahachie desert with superconducting magnets to ac-  
2885 celerate protons and antiprotons to energies more than three times higher than the LHC's current  
2886 world record. The project was conceived during the Reagan administration and billed as a megapro-  
2887 ject to reassert American dominance as the president took a more aggressive approach to the Soviet  
2888 threat. Unfortunately, the project was perhaps too ambitious and suffered from management prob-  
2889 lems. It is not surprising, then, that the end of the Cold War spelled the end of the SSC. With no  
2890 external threat to American global dominance, there was little impetus to continue funding such an  
2891 expensive and over-budget project. There has not been a single initiative since for the United States  
2892 to recapture its once commanding lead over efforts in Western Europe.

2893 Western Europe was the only other serious center of 20th century particle physics, and successes  
2894 there also depended upon five decades of existential threat to the United States, though in a less di-  
2895 rect fashion. Most obviously, American institutions and physicists have been essential to the devel-  
2896 opment of European particle physics, just as European physicists were crucial to the success of the  
2897 Manhattan Project. Seven of the ten Cold War era CERN Directors General were either educated  
2898 or did research at American universities, and every major particle physics discovery since the end of  
2899 World War II has relied on both American and European talent and infrastructure. Furthermore,  
2900 the European approach to experimental particle physics, epitomized by CERN, emphasized consen-  
2901 sus and cooperation and was emblematic of larger geopolitical currents on the European continent  
2902 in the latter half of the 20th century. Such a culture and its success would have been impossible with-

2903 out the same threats that facilitated American success in particle physics. While limited resources of  
2904 member states were no doubt contributing factors in CERN's genesis, the collaborative culture of  
2905 CERN and other pan-European organizations was a reaction to centuries of competition for conti-  
2906 nental dominance. After the total destruction of the world wars, enough was enough. The relatively  
2907 peaceful prosperity on the Western side of the Iron Curtain made European cooperation possible,  
2908 while the threat at Western Europe's doorstep only heightened the urgency of pan-European desires.  
2909 Hence, the symbolic importance of European unity during the Cold War is hard to underestimate, and  
2910 CERN-facilitated European cooperation made it a forerunner to organizations like the European  
2911 Union and a model to the world. Every major achievement in particle physics after 1940 therefore  
2912 relies on facilities and institutions on both sides of the Atlantic that would never have been formed  
2913 without the back to back threats of global fascism and Soviet Communism.

2914 With the cancellation of the SSC in 1993 and the closing of Fermilab's Tevatron in 2011, CERN  
2915 and its LHC remain the lone laboratory and experiment at the energy frontier. The United States  
2916 is now a mere "observer state" at CERN: American talent and funding are essential to CERN and  
2917 its mission, but the United States does not have a seat on CERN's governing council. It remains  
2918 to be seen whether a legacy of over six decades of international cooperation will provide sufficient  
2919 motivation for particle physics to continue at CERN after the LHC without guarantee of any dis-  
2920 covery at the next experiment. Current nuclear threats, while attention grabbing, are far from exis-  
2921 tential and unlikely to reignite any initiative for distinctly American science megaprojects. The only  
2922 other prospect for a future collider at the energy frontier is China, whose nationalistic desire for su-  
2923 perpower status may prove a sufficiently powerful and lasting motivator for the next generation of

<sup>2924</sup> collider.

# References

2925

- 2926 [1] (2010). Measurement of the  $w \rightarrow l\nu$  and  $z/\gamma^* \rightarrow ll$  production cross sections in proton-  
2927 proton collisions at  $\sqrt{s} = 7$  TeV with the atlas detector. *JHEP*, 1012.
- 2928 [2] (2011a). *ATLAS tunes of PYTHIA 6 and Pythia 8 for MCII*. Technical Report ATL-PHYS-  
2929 PUB-2011-009, CERN, Geneva.
- 2930 [3] (2011b). *New ATLAS event generator tunes to 2010 data*. Technical Report ATL-PHYS-  
2931 PUB-2011-008, CERN, Geneva.
- 2932 [4] (2012a). *b-jet tagging calibration on c-jets containing  $D^{*+}$  mesons*. Technical Report ATLAS-  
2933 CONF-2012-039, CERN, Geneva.
- 2934 [5] (2012b). Electron performance measurements with the atlas detector using the 2010 lhc  
2935 proton-proton collision data. *Eur. Phys. J.*, C72.
- 2936 [6] (2012a). Observation of a new boson at a mass of 125 GeV with the CMS experiment at the  
2937 LHC. *Phys.Lett.*, B716, 30–61.
- 2938 [7] (2012b). Observation of a new particle in the search for the Standard Model Higgs boson  
2939 with the ATLAS detector at the LHC. *Phys.Lett.*, B716, 1–29.
- 2940 [8] (2012). The Proton Synchrotron.
- 2941 [9] (2012). The Proton Synchrotron Booster.
- 2942 [10] (2012). The Super Proton Synchrotron.
- 2943 [11] (2013a). Jet energy measurement with the atlas detector in proton-proton collisions at  $\sqrt{s} = 7$   
2944 TeV *Eur. Phys. J.*, C73.
- 2945 [12] (2013b). *Search for the bb decay of the Standard Model Higgs boson in associated W/ZH*  
2946 *production with the ATLAS detector*. Technical Report ATLAS-CONF-2013-079, CERN,  
2947 Geneva.

- 2948 [13] (2014). *ATLAS Run 1 Pythia8 tunes*. Technical Report ATL-PHYS-PUB-2014-021, CERN,  
 2949 Geneva.
- 2950 [14] (2014). *Electron efficiency measurements with the ATLAS detector using the 2012 LHC*  
 2951 *proton-proton collision data*. Technical Report ATLAS-CONF-2014-032, CERN, Geneva.
- 2952 [15] (2015). *Expected performance of the ATLAS b-tagging algorithms in Run-2*. Technical Report  
 2953 ATL-PHYS-PUB-2015-022, CERN, Geneva.
- 2954 [16] (2015). *Jet Calibration and Systematic Uncertainties for Jets Reconstructed in the ATLAS*  
 2955 *Detector at  $\sqrt{s} = 13 \text{ TeV}$* . Technical Report ATL-PHYS-PUB-2015-015, CERN, Geneva.
- 2956 [17] (2015). *Muon reconstruction performance in early  $\sqrt{s}=13 \text{ TeV}$  data*. Technical Report ATL-  
 2957 PHYS-PUB-2015-037, CERN, Geneva.
- 2958 [18] A. L. Read (2002). Presentation of search results: the  $CL_s$  technique. *J. Phys. G*, 28, 2693–  
 2959 2704.
- 2960 [19] Aad, G. et al. (2014). Measurement of the  $Z/\gamma^*$  boson transverse momentum distribution in  
 2961  $pp$  collisions at  $\sqrt{s} = 7 \text{ TeV}$  with the ATLAS detector. *JHEP*, 09, 145.
- 2962 [20] Ahmadov, F., Alio, L., Allbrooke, B., Bristow, T., Buescher, D., Buzatu, A., Coadou, Y.,  
 2963 Debenedetti, C., Enari, Y., Facini, G., Fisher, W., Francavilla, P., Gaycken, G., Gentil, J.,  
 2964 Goncalo, R., Gonzalez Parra, G., Grivaz, J., Gwilliam, C., Hageboeck, S., Halladjian, G., Jack-  
 2965 son, M., Jamin, D., Jansky, R., Kiuchi, K., Kostyukhin, V., Lohwasser, K., & Lopez Mateos,  
 2966 D, e. a. (2014). *Supporting Document for the Search for the bb decay of the Standard Model*  
 2967 *Higgs boson in associated (W/Z)H production with the ATLAS detector*. Technical Report  
 2968 ATL-COM-PHYS-2014-051, CERN, Geneva.
- 2969 [21] Aliev, M., Lacker, H., Langenfeld, U., Moch, S., Uwer, P., et al. (2011). HATHOR: Hadronic  
 2970 Top and Heavy quarks cross section calculator. *Comput.Phys.Commun.*, 182, 1034–1046.
- 2971 [22] Alwall, J., Frederix, R., Frixione, S., Hirschi, V., Maltoni, F., Mattelaer, O., Shao, H. S.,  
 2972 Stelzer, T., Torrielli, P., & Zaro, M. (2014). The automated computation of tree-level and  
 2973 next-to-leading order differential cross sections, and their matching to parton shower simula-  
 2974 tions. *JHEP*, 07, 079.
- 2975 [23] Alwall, J., Herquet, M., Maltoni, F., Mattelaer, O., & Stelzer, T. (2011). Madgraph 5 : Going  
 2976 beyond.

- 2977 [24] ATLAS Collaboration (2014). *Tagging and suppression of pileup jets with the ATLAS detector*. Technical Report ATLAS-CONF-2014-018, CERN, Geneva.
- 2978
- 2979 [25] ATLAS Collaboration (2015a). MCPAnalysisGuidelinesMC15.
- 2980 <https://twiki.cern.ch/twiki/bin/view/AtlasProtected/MCPAnalysisGuidelinesMC15>.
- 2981 [26] ATLAS Collaboration (2015b). *Performance of missing transverse momentum reconstruction for the ATLAS detector in the first proton-proton collisions at  $\sqrt{s} = 13 \text{ TeV}$* . Technical Report ATL-PHYS-PUB-2015-027, CERN, Geneva.
- 2982
- 2983
- 2984 [27] Ball, R. D. et al. (2013). Parton distributions with LHC data. *Nucl. Phys.*, B867, 244–289.
- 2985 [28] Ball, R. D. et al. (2015). Parton distributions for the LHC Run II. *JHEP*, 04, 040.
- 2986 [29] Botje, M. et al. (2011). The PDF4LHC Working Group Interim Recommendations.
- 2987 [30] Buckley, A., Butterworth, J., Grellscheid, D., Hoeth, H., Lonnblad, L., Monk, J., Schulz, H.,  
2988 & Siegert, F. (2010). Rivet user manual.
- 2989 [31] Buzatu, A. & Wang, W. (2016). *Object selections for SM Higgs boson produced in association with a vector boson in which  $H \rightarrow b\bar{b}$  and  $V$  decays leptonically with Run-2 data: Object support note for  $VH(bb)$  2015+2016 dataset publication*. Technical Report ATL-COM-PHYS-2016-1674, CERN, Geneva. This is a support note for the  $VH(bb)$  SM publication using the 2015+2016 datasets.
- 2990
- 2991
- 2992
- 2993
- 2994 [32] Cacciari, M., G. P. Salam, M. C., & Salam, G. P. (2008). Pileup subtraction using jet areas. *Phys. Lett.*, B659.
- 2995
- 2996 [33] Campbell, J. M. & Ellis, R. K. (2010). MCFM for the Tevatron and the LHC. *Nucl. Phys. Proc. Suppl.*, 205-206, 10–15.
- 2997
- 2998 [34] Capeans, M., Darbo, G., Einsweiller, K., Elsing, M., Flick, T., Garcia-Sciveres, M., Gemme,  
2999 C., Pernegger, H., Rohne, O., & Vuillermet, R. (2010). *ATLAS Insertable B-Layer Technical  
3000 Design Report*. Technical Report CERN-LHCC-2010-013, ATLAS-TDR-19.
- 3001 [35] CERN (2008). LHC first beam: a day to remember.
- 3002 [36] Chan, S., Huth, J., Lopez Mateos, D., & Mercurio, K. (2015a). *ZH  $\rightarrow llb\bar{b}$  Analysis with  
3003 Telescoping Jets*. Technical Report ATL-PHYS-INT-2015-002, CERN, Geneva.

- 3004 [37] Chan, S. K.-w. & Huth, J. (2017). *Variations on MVA Variables in the SM ZH → ℓℓ $b\bar{b}$  Search*. Technical Report ATL-COM-PHYS-2017-1318, CERN, Geneva.
- 3005
- 3006 [38] Chan, S. K.-w., Lopez Mateos, D., & Huth, J. (2015b). *Micromegas Trigger Processor Algo-*  
3007 *rithm Performance in Nominal, Misaligned, and Corrected Misalignment Conditions*. Tech-  
3008 nical Report ATL-COM-UPGRADE-2015-033, CERN, Geneva.
- 3009 [39] Chien, Y.-T., Farhi, D., Krohn, D., Marantan, A., Mateos, D. L., & Schwartz, M. (2014).  
3010 Quantifying the power of multiple event interpretations.
- 3011 [40] Ciccolini, M., Dittmaier, S., & Kramer, M. (2003). Electroweak radiative corrections to asso-  
3012 ciated WH and ZH production at hadron colliders. *Phys. Rev.*, D68, 073003.
- 3013 [41] Clark, B., Lopez Mateos, D., Felt, N., Huth, J., & Oliver, J. (2014). *An Algorithm for Mi-*  
3014 *cromegas Segment Reconstruction in the Level-1 Trigger of the New Small Wheel*. Technical  
3015 Report ATL-UPGRADE-INT-2014-001, CERN, Geneva.
- 3016 [42] Collaboration, A. (2017a). Evidence for the  $h \rightarrow b\bar{b}$  decay with the atlas detector.
- 3017 [43] Collaboration, A. (2017b). Study of the material of the atlas inner detector for run 2 of the  
3018 lhc.
- 3019 [44] Collaboration, T. A., Aad, G., Abat, E., Abdallah, J., & A A Abdelalim, e. a. (2008). The atlas  
3020 experiment at the cern large hadron collider. *Journal of Instrumentation*, 3(08), S08003.
- 3021 [45] Cowan, G., Cranmer, K., Gross, E., & Vitells, O. (2011). Asymptotic formulae for likelihood-  
3022 based tests of new physics. *Eur. Phys. J. C*, 71, 1554.
- 3023 [46] Czakon, M., Fiedler, P., & Mitov, A. (2013). Total Top-Quark Pair-Production Cross Section  
3024 at Hadron Colliders Through  $\alpha(\frac{4}{5})$ . *Phys. Rev. Lett.*, 110, 252004.
- 3025 [47] D. Kahawala, D. Kahawala, D. K. & Schwartz, M. D. (2013). Jet sampling: Improving event  
3026 reconstruction through multiple interpretations.
- 3027 [48] D. Krohn, D. Krohn, J. T. L. W. (2009). Jet trimming.
- 3028 [49] Delmastro, M., Gleyzer, S., Hengler, C., Jimenez, M., Koffas, T., Kuna, M., Liu, K., Liu, Y.,  
3029 Marchiori, G., Petit, E., Pitt, M., Soldatov, E., & Tackmann, K. (2014). *Photon identification*  
3030 *efficiency measurements with the ATLAS detector using LHC Run 1 data*. Technical Report  
3031 ATL-COM-PHYS-2014-949, CERN, Geneva.

- 3032 [50] Evans, L. & Bryant, P. (2008). Lhc machine. *Journal of Instrumentation*, 3(08), S08001.
- 3033 [51] Gleisberg, T. et al. (2009a). Event generation with SHERPA 1.1. *JHEP*, 02, 007.
- 3034 [52] Gleisberg, T., Höche, S., Krauss, F., Schönherr, M., Schumann, S., Siegert, F., & Winter, J.  
3035 (2009b). Event generation with sherpa 1.1. *Journal of High Energy Physics*, 2009(02), 007.
- 3036 [53] Hagebock, S. (CERN, Geneva, 2017). Lorentz Invariant Observables for Measurements of  
3037 Hbb Decays with ATLAS.
- 3038 [54] Heinemann, B., Hirsch, F., & Strandberg, S. (2010). *Performance of the ATLAS Secondary  
3039 Vertex b-tagging Algorithm in 7 TeV Collision Data*. Technical Report ATLAS-COM-CONF-  
3040 2010-042, CERN, Geneva. (Was originally 'ATL-COM-PHYS-2010-274').
- 3041 [55] J. Pumplin, J. Pumplin, D. S. J. H. H. L. P. M. N. e. a. (2002). New generation of parton  
3042 distributions with unvertainties from global qcd analysis. *JEGP*, 0207.
- 3043 [56] Jackson, P. & Rogan, C. (2017). Recursive jigsaw reconstruction: Hep event analysis in the  
3044 presence of kinematic and combinatoric ambiguities.
- 3045 [57] Kant, P., Kind, O., Kintscher, T., Lohse, T., Martini, T., Molbitz, S., Rieck, P., & Uwer, P.  
3046 (2015). Hathor for single top-quark production: Updated predictions and uncertainty esti-  
3047 mates for single top-quark production in hadronic collisions. *Computer Physics Communica-  
3048 tions*, 191, 74 – 89.
- 3049 [58] Lampl, W., Laplace, S., Lelas, D., Loch, P., Ma, H., Menke, S., Rajagopalan, S., Rousseau,  
3050 D., Snyder, S., & Unal, G. (2008). *Calorimeter Clustering Algorithms: Description and Per-  
3051 formance*. Technical Report ATL-LARG-PUB-2008-002. ATL-COM-LARG-2008-003,  
3052 CERN, Geneva.
- 3053 [59] Lavesson, N. & Lonnblad, L. (2005). W+jets matrix elements and the dipole cascade.
- 3054 [60] LHC Higgs Cross Section Working Group, Dittmaier, S., Mariotti, C., Passarino, G., &  
3055 Tanaka (Eds.), R. (CERN, Geneva, 2011). Handbook of LHC Higgs Cross Sections: 1. In-  
3056 clusiv Observables. *CERN-2011-002*.
- 3057 [61] Loch, Peter and Lefebve, Michel (2007). Introduction to Hadronic Calibration in ATLAS.

- 3058 [62] Luisoni, G., Nason, P., Oleari, C., & Tramontano, F. (2013). H<sub>w</sub> ±/hz + o and 1 jet at nlo  
 3059 with the powheg box interfaced to gosam and their merging within minlo. *Journal of High*  
 3060 *Energy Physics*, 2013(10), 83.
- 3061 [63] M. Cacciari, M. Cacciari, G. P. S. & Soyez, G. (2008). The anti- $k_t$  jet clustering algorithm.  
 3062 *JHEP*, 0804.
- 3063 [64] Marcastel, F. (2013). CERN's Accelerator Complex. La chaîne des accélérateurs du CERN.  
 3064 General Photo.
- 3065 [65] Masubuchi, T., Benitez, J., Bell, A. S., Argyropoulos, S., Arnold, H., Amaral Coutinho, Y.,  
 3066 Sanchez Pineda, A. R., Buzatu, A., Calderini, G., & Chan, Stephen Kam-wah, e. a. (2016).  
 3067 *Search for a Standard Model Higgs boson produced in association with a vector boson and de-*  
 3068 *caying to a pair of b-quarks*. Technical Report ATL-COM-PHYS-2016-1724, CERN, Geneva.
- 3069 [66] Patrignani, C. et al. (2016). Review of Particle Physics. *Chin. Phys.*, C40(10), 100001.
- 3070 [67] Robson, A., Piacquadio, G., & Schopf, E. (2016). *Signal and Background Modelling Stud-*  
 3071 *ies for the Standard Model VH, H → b̄b and Related Searches: Modelling support note*  
 3072 *for VH(b̄b) 2015+2016 dataset publication*. Technical Report ATL-COM-PHYS-2016-1747,  
 3073 CERN, Geneva. This is a support note for the VH(b̄b) SM publication using the 2015+2016  
 3074 datasets.
- 3075 [68] S. Alioli et al. (2009). NLO Higgs boson production via gluon fusion matched with shower  
 3076 in POWHEG. *JHEP*, 0904, 002.
- 3077 [69] S. D. Ellis, S. D. Ellis, A. H. T. S. R. D. K. & Schwartz, M. D. (2012). Qjets: A non-  
 3078 deterministic approach to tree-based jet substructure. *Phys. Rev. Lett.*, 108.
- 3079 [70] Salam, G. P. (2009). Towards jetography.
- 3080 [71] Schwartz, M. D. (2014). *Quantum Field Theory and the Standard Model*. Cambridge Uni-  
 3081 versity Press.
- 3082 [72] Sjostrand, T., Mrenna, S., & Skands, P. Z. (2008). A Brief Introduction to PYTHIA 8.1.  
 3083 *Comput.Phys.Commun.*, 178, 852–867.
- 3084 [73] Stancari, G., Previtali, V., Valishev, A., Bruce, R., Redaelli, S., Rossi, A., & Salvachua Fer-  
 3085 rando, B. (2014). *Conceptual design of hollow electron lenses for beam halo control in the*

- 3086        *Large Hadron Collider*. Technical Report FERMILAB-TM-2572-APC. FERMILAB-TM-  
3087        2572-APC, CERN, Geneva. Comments: 23 pages, 1 table, 10 figures.
- 3088 [74] Stewart, I. W. & Tackmann, F. J. (2011). Theory uncertainties for higgs and other searches  
3089        using jet bins.
- 3090 [75] Symmetry Magazine (2015). The Standard Model of Particle Physics.
- 3091 [76] T. Gleisberg et al., T. G. e. a. (2009). Event generation with sherpa 1.1. *JHEP*, 02.
- 3092 [77] T. Sjöstrand, T. Sjöstrand, S. M. & Sands, P. Z. (2008). A brief introduction to pythia 8.1.  
3093        *Comput. Phys. Commun.*, 178.
- 3094 [78] Tully, C. C. (2011). *Elementary particle physics in a nutshell*. Princeton, NJ: Princeton Univ.  
3095        Press.
- 3096 [79] Verkerke, W. & Kirkby, D. (2003). The RooFit toolkit for data modeling. In *2003 Computing*  
3097        *in High Energy and Nuclear Physics, CHEP03*.
- 3098 [80] Watts, G., Filthaut, F., & Piacquadio, G. (2015). *Extrapolating Errors for b-tagging*. Technical  
3099        Report ATL-COM-PHYS-2015-711, CERN, Geneva. This is for internal information only, no  
3100        approval to ever be seen outside of ATLAS.
- 3101 [81] Y. L. Dokshitzer, Y. L. Dokshitzer, G. D. L. S. M. & Webber, B. R. (1997). Better jet cluster-  
3102        ing algorithms. *JHEP*, 9708.